Next Generation Optical Communications for Satellites

EngD Thesis

Jonathan R. Crabb

Center for Doctoral Training for Applied Photonics

Department of Electronic & Electrical Engineering

University of Strathclyde, Glasgow

A thesis submitted to the Department of Electronic & Electrical Engineering

for the degree of Doctor of Engineering (EngD) in Applied Photonics

September 17, 2020

Signed:

Date:

Abstract

The amount of data being generated and communicated in space is ever increasing. With radio frequency systems becoming increasingly strained under technological and regulatory problems, laser communications has been identified as a key technology in leading a paradigm shift within satellite communications. When compared to traditional radio satellite communications, laser communication techniques show greater performance in terms of available data rates, but also improvements in areas such as a reduction in the size, weight and power of the communication subsystem.

Historically, laser communications has been demonstrated on large satellites but their current use upon small satellites ($\leq$ 10 kg) is limited. Within this thesis we address this problem by providing a trade-off analysis for a laser transmitter within space and assess the unique environment in which these laser systems will operate.

3 new classes of optical component not previously assessed for space use are tested. A polarisation maintaining hybrid and non-polarisation maintaining hybrid component are shown to suitable for use within a low-Earth orbit environment whilst a compact 1 µm isolator needs to be assessed further. Additionally, a selection of double-clad ErYb-doped fibers are tested to select the most suitable fiber for use within future high-power applications.

With a new set of parts tested, the thesis turns towards novel module development. The first module presented is a technology readiness level 5/6 design for a 0.2 W, 1 Gbps laser transmitter designed for CubeSat applications. The optical design is modelled and verified over a temperature range of -5 °C to +50 °C. Finally a multi-channel optical amplifier used for photonic-based radio frequency beam-forming is presented. This amplifier utilises a novel photonic-crystal fiber which was then integrated into a

module and performance verified.

Having demonstrated the potential for laser communications in small satellite applications. This thesis has helped to provide a technological base on which the next-generation of compact, optical communication payloads can be built.

Acknowledgements

Firstly and foremost I would like to thank both my academic supervisors, Dr. Craig Michie and Prof. Walter Johnstone, and my industrial supervisors, Dr. Efstratios Kehayas and Dr. Leontios Stampoulidis for their guidance and support over the past 4 and a half years. I am grateful for their broad and deep knowledge of photonics on both a technical and commercial level; which in turn has helped shaped this project and furthered my photonics knowledge and understanding.

Next I would like to acknowledge the funding sources which have made my EngD studies possible. The ESPRC-funded CDT for Applied photonics has enabled my studies and I would like to thank them for their support. Without the wonderful learning and support program, this project would have not been possible. Additionally I would like to thank Gooch & Housego, the sponsor company for hosting me and supporting my studies.

I would also like to thank the whole system technology group (STG) within Gooch & Housego, Torquay, as their help and support has allowed for someone with very little experience in fiber-optics to now be confident in designing, building and testing complex optical communications systems. I would like to especially thank the members of the space photonics team: Dr. G. Stevens, R. Elliott, M. Kechagias, M. Tuci, Dr. M. Welch and Dr. J. Edmunds, to name a few.

I cannot express my gratitude with words to Abigail for the support and love she has shown me over the past four years. She has made Devon feel my home and I cannot wait to see what our future holds.

Finally I would like to thank my family with all my heart for their love and support over this long educational journey.

Contents

List of Figures

List of Tables

Abbreviations

AIT assembly, integration and testing

ASE amplified spontaneous emission

BFM back facet monitor

BPSK binary phase shift keying

CD coherent detection

CME coronal mass ejection

COTS commercial off-the-shelf

CVCM collected volatile condensable material

CW continuous wave

DBR distributed Bragg reflector

DD direct detection

DFB distributed feedback laser

DML directly modulated laser

DPSK differential phase shift keying

E/O electrical-to-optical

EDFA erbium-doped fiber amplifier

EDRS European data relay system

EOL end-of-life

ESA European Space Agency

EYDFA erbium-ytterbium doped fiber amplifier

FSL free-path space loss

GCR galactic cosmic ray

GEO geostationary orbit

HPA high power amplifier

I/L insertion loss

IM/DD intensity modulated/directly detected

ISL inter-satellite link

JAXA Japanese Aerospace Exploration Agency

LED light emmitting diode

LEO low Earth orbit

LNA low noise amplifier

LO local oscillator

LTX laser transmitter

MC-EDFA multi-Channel erbium doped fiber amplifier

MM multi-mode

MOPA master-oscillator power amplifier

MZM Mach-Zehnder modulator

NASA National Aeronautics and Space Administration

NF noise figure

NIEL non-ionizing energy loss

NPRO non-planar monolithic ring oscillator

OOK on-off keying

OSA optical spectrum analyser

PCF photonic crystal fiber

PER polarisation extinction ratio

PIC photonic integrated components

PM polarisation-maintaining

PPM pulse-position modulation

PRBS psuedo-random bit generator

RF radio frequency

RIA radiation induced attenuation

RX receiver

SBS stimulated Brillouin scattering

SM single-mode

SNR signal-to-noise ratio

SOA semi-conductor optical amplifier

SWaP size, weight and power

TEC thermo-electric cooler

TID total ionising dose

TML total mass loss

TRL technology readiness level

TVAC thermal vacuum

TX transmitter

VCSEL vertical cavity surface emitting laser

VOA variable optical attenuator

WDM wave division multiplexing

YDFA ytterbium-doped fiber amplifier

Chapter 1

Introduction and Executive Summary

1.1 Introduction

Since the 1960s, satellite communications has become increasingly important in the modern world. From providing key science data to entertainment, society has become increasingly reliant on this technology. Current trends in the satellite communications industry have led to increasing strains on radio frequency (RF) architectures [1.1]. The first trend is that the RF spectrum is becoming increasingly populated due to more developing countries becoming space-faring nations requiring access to the key parts of the RF spectrum to provide services to their citizens e.g. navigation systems and satellite TV. An additional factor is that a larger amount of private spacecraft are being launched each year for commercial systems with large networks of small satellites becoming increasingly popular, thus further congesting the RF spectrum. The second trend is that the sensors on-board spacecraft are producing ever-larger amounts of data and the ability of them being able to communicate this data is a mission-limiting factor [1.2].

There are multiple solutions to this problem and one of which is space laser communications. Although a multitude of research has previously been completed on high bandwidth RF systems. Space-based laser communications offers improvements in

many sought-after design spaces. Some examples of these improvements include: terminals with a lower size, weight and power (SWaP), higher data rates and more relaxed regulations when compared to state-of-the-art RF systems (see section 2.3 for more details). This need for an increase in data bandwidth and the possible impact that laser communications could provide has been highlighted worldwide by the space community [1.2]–[1.4] emphasising the requirement for research in to this field.

Research into space laser communications has been occurring since the 1970s with the European Space Agency (ESA) leading the way [1.4]. Early attempts were made by the National Aeronautics and Space Administration (NASA) in 1992 when the Galileo spacecraft demonstrated the possibility of optical links with satellites [1.5]. The Japanese Aerospace Exploration Agency (JAXA) became the first agency to demonstrate a geostationary orbit (GEO) to ground, bi-directional link in 1995 with the ETS-VI satellite [1.6], [1.7]. However it was not until 2001 when the first robust laser communications link in space became operational with data rates able to support satellite payloads [1.8], [1.9]. Since 2001, most space agencies have developed systems for more applications such as inter-satellite links (ISLs) [1.9], [1.10] or direct downlink of data from the Moon [1.11].

This thesis describes the development of one of the key technologies and the components needed when building a space-based optical communications network, the laser transmitter (LTX). A large focus will be made on the miniaturisation of the transmitter as the targeted end use of these terminals is to be used in small- (mass < 50 kg) or micro-satellite (mass < 10 kg) communication sub-systems. As already occurred terrestrially, fiber-optics offers many improvements in SWaP when compared to RF systems and has replaced RF in long-distance communications. In turn, this thesis will add to the research in the paradigm shift from RF communications to the optical regime, a key factor in linking up the world through the transfer of data.

1.2 Executive Summary

Laser communications has been identified as a key enabling technology for the next generation of high-data rate communication systems to help alleviate upcoming issues

with RF communications such as spectrum congestion and the capacity of RF networks. However, as described within this thesis, the current qualification status of opto-electronics and fiber amplifiers varies greatly depending on the technology used. The relatively unknown qualification status of these components and systems currently limits their use within space missions and therefore provides an opportunity for it to be addressed.

A broad literature analysis is first presented discussing the background of space-based laser communications, next the building blocks needed for a laser transmitter and the current qualification status for each block is discussed and a trade-off analysis presented. The anticipated operating environment and the challenges this causes is also discussed with a focus upon the erbium and erbium-ytterbium doped fibers and the damage caused by γ-radiation. Finally, a comparison of RF and optical satellite communication systems followed by the status of current state-of-the-art laser communication systems.

The overall aim of this thesis is to assess new components and design new modules for use within a variety of satellite communications applications. This is achieved by first assessing fiber optic components for their use within space through environmental testing. The tested components are a polarisation-maintaining (PM) and non-PM fiber hybrid component which consist of an isolator, tap and wave division multiplexer (WDM) in one package and a compact isolator designed for use at 1064 nm. Additionally, a selection of co-doped ErYb fibers have been assessed to determine the most radiation resilient fiber in terms of both specialist and commercially available fiber.

With a new class of component tested, the first iteration of design for a small form-factor laser transmitter for small- and micro-satellite applications is presented. This laser transmitter is designed for an initial data rate of 1 Gbit/s and output power of 0.2 W. Design and verification testing over temperature is presented, raising the technology readiness level (TRL) of this module to TRL 5/6. Although this does not use the previously tested components, this module will lay the foundation for the next generation of commercially available laser transmitters for space applications.

Finally, the assembly and testing of a multi-channel fiber amplifier for the miniatur-

isation of future RF beam-forming modules is shown. This module utilises a radiation-hardened, erbium-doped photonic crystal fiber (PCF) which can provide amplification across 7 channels. This fiber is also assessed for it's resistance to radiation and a radiation induced attenuation (RIA) of 0.72 dB/100 kRad is reported. This radiation hardness is achieved by co-doping the erbium photonic crystal fiber with Cerium, a known element used for radiation hardening in other fiber types and bulk glasses. With the fiber tested, a 7-channel amplifier module utilising this novel PCF was assembled and tested. Testing showed amplification of over 20 dB in all 7 channels. Following successful testing, the module was then integrated into a demonstrator which showed the first instance RF beam separation via a complete photonic-aided payload. More specifically, this module demonstrated the first use of a multi-channel Er-doped multi-core PCF within an optical beam forming network.

1.3 Thesis Structure

The remaining chapters of this thesis are set out in a portfolio format such that each major body of work commenced as part of this EngD project shall be presented in a single chapter. The exception to this is Chapter 2 which describes the background to the thesis subject matter. The chapters are organised as follows:

- **Chapter 2** introduces the theory behind a space based LTX and performs a trade-off analysis of potential technologies that can be used within space laser communications systems. In addition, the chapter describes the anticipated operational environment; the design challenges it poses and how they are overcome. Finally it discusses the benefits of optical over RF communications and includes examples of current state-of-the-art systems; plus planned missions which in turn provides a context for this thesis.

- **Chapter 3** describes the environmental testing undertaken on various fiber optic components. Test levels have been chosen to simulate the components' anticipated operational environment and results analysed to assess the components'

suitability for space applications. This testing will be completed on both passive and active fiber optic components.

- **Chapter 4** describes the design and development of a 0.2 W, 1 Gbit s^{-1} CubeSat-class laser transmitter. This transmitter is designed to be for use on micro-satellites (mass $<$ 10kg). Two designs will be presented utilising the same optical engine thus showing the versatility of the optical engine.
- **Chapter 5** describes the development and testing of an optical amplifier to be used for intra-satellite communication and RF beam-forming applications. This amplifier was designed to amplify multiple RF channels in a compact format when compared to contemporary RF communication payloads.
- **Chapter 6** will conclude the thesis summarising the key findings and discussing future work and the path towards demonstrating the modules developed in this thesis in orbit.

References

[1.1] J. Farserotu and R. Prasad, "A survey of future broadband multimedia satellite systems, issues and trends," *IEEE Communications Magazine*, vol. 38, no. 6, pp. 128–133, 2000. DOI: 10.1109/35.846084.

[1.2] M. Toyoshima, "Trends in satellite communications and the role of optical free-space communications," *Journal of Optical Networking*, vol. 4, no. 6, p. 300, 2005. DOI: 10.1364/JON.4.000300.

[1.3] F. Lansing, L. Lemmerman, A. Walton, G. Bothwell, K. Bhasin, and G. Prescott, "Needs for communications and onboard processing in the vision era," in *IEEE International Geoscience and Remote Sensing Symposium*, vol. 1, Toronto: IEEE, 2002, pp. 375–377. DOI: 10.1109/IGARSS.2002.1025044.

[1.4] Z. Sodnik, B. Furch, and H. Lutz, "Optical Intersatellite Communication," *IEEE Journal of Selected Topics in Quantum Electronics*, vol. 16, no. 5, pp. 1051–1057, 2010. DOI: 10.1109/JSTQE.2010.2047383.

[1.5] K. E. Wilson, J. R. Lesh, and T.-Y. Yan, "GOPEX: a laser uplink to the Galileo spacecraft on its way to Jupiter," in *Proc. SPIE 1866*, G. S. Mecherle, Ed., Aug. 1993, p. 138. DOI: 10.1117/12.149251.

[1.6] M. Toyoda, M. Toyoshima, T. Takahashi, M. Shikatani, Y. Arimoto, K. Araki, *et al.*, "Ground-to-ETS-VI narrow laser beam transmission," G. S. Mecherle, Ed., vol. 2699, International Society for Optics and Photonics, 1996, p. 71. DOI: 10.1117/12.238436.

[1.7] Y. Arimoto, M. Toyoshima, M. Toyoda, T. Takahashi, M. Shikatani, and K. Araki, "Preliminary result on laser communication experiment using (ETS-VI)," in *Free-Space Laser Communication Technologies VII*, G. S. Mecherle, Ed., vol. 2381, Apr. 1995, p. 151. DOI: 10.1117/12.207423.

[1.8] G. Planche and V. Chorvalli, "SILEX in-orbit performances," in *International Conference on Space Optics — ICSO 2004*, J. Costeraste and E. Armandillo, Eds., Toulouse: SPIE, 2004, pp. 403–410. DOI: 10.1117/12.2500113.

[1.9] Z. Sodnik, B. Furch, and H. Lutz, "Free-Space Laser Communication Activities in Europe: SILEX and beyond," in *LEOS 2006 - 19th Annual Meeting of the IEEE Lasers and Electro-Optics Society*, vol. 1, IEEE, 2006, pp. 78–79. DOI: 10.1109/LEOS.2006.278845.

[1.10] Y. Takayama, T. Jono, Y. Koyama, N. Kura, K. Shiratama, B. Demelenne, *et al.*, "Observation of atmospheric influence on OICETS inter-orbit laser communication demonstrations," in *Proc. SPIE*, A. K. Majumdar and C. C. Davis, Eds., vol. 6709, International Society for Optics and Photonics, Sep. 2007, 67091B. DOI: 10.1117/12.736789.

[1.11] D. M. Cornwell, "NASA's optical communications program for 2015 and beyond," in *Proc. SPIE 9354, Free-Space Laser Communication and Atmospheric Propagation XXVII*, H. Hemmati and D. M. Boroson, Eds., Mar. 2015, 93540E. DOI: 10.1117/12.2087132.

Chapter 2

Introduction to Laser Communications for Satellites

Chapter 2 introduces the field of space laser communications and the design challenges faced in designing such a system. Additionally, a review of contemporary satellite based laser communication systems shall be presented illustrating the state of the field and any opportunities that the research in this thesis can address. Chapter 2 is structured as follows:

- Section 2.1 will discuss laser transmitters for space-based optical communications; discussing potential component technologies and the trade-offs needed for a space-based system.
- Section 2.2 will illustrate the operational environment and potential damage mechanisms of the modules in space. The focus of this section will be that of fiber optic components as the damage mechanisms for this component class have only recently became to be known.
- Section 2.3 surveys the current field of space based optical communications and the potential improvements that optical systems can provide over current RF systems. In addition, state-of-the-art systems will be presented with examples of future space-based optical communications systems.

2.1 Laser Transmitters for Space-Based Optical Communications

To build a free-space optical communications system, it is best to visualise the system as a sequence of blocks through which the signal is passed through. An example block diagram is shown in Figure 2.1. It details the stages required to construct a free-space optical communications link and the key parts of the system. One of the main differences between space-based optical communications as from terrestrially optical communication systems is the lack of a relay amplifier (except the use of a relay satellite) when trying to communicate over long distances. Thankfully, when operating at high optical powers, non-linear effects experienced when communicating over long distances in the atmosphere or in long lengths of optical fiber do not exist in the vacuum of space.

Two of the blocks shown in Figure 2.1, the amplifier blocks (both at the transmitter (TX) and receiver (RX)) and LTX sub-system which are key parts of the link and the main focus for the work presented in this thesis. The aim of this sub-section is to introduce the reader to laser transmitters and optical amplifiers and to discuss the suitability of using these technologies in the space environment and to perform trade-offs when necessary. The key design trade-offs are shown in Table 2.1 and elaborated upon in later sections. As can be seen in Table 2.1, TRL[1] plays a key part in the selection of these components. This is to ensure that the laser transmitters developed as part of this project can be developed quickly and at a low risk. It can be seen from Table 2.1 that the main parameter of each technology is the SWaP. The component selection may vary significantly for different applications. E.g. The technologies used on a laser transmitter for CubeSats could vary greatly from the technology used on a laser transmitter designed for small satellites.

[1]In this thesis the TRLs defined by NASA will be used. This is slightly different from those seen in terrestrial industry as NASA's TRL places more importance on rigorous terrestrial testing before orbital deployment. For more information on the definition of TRL levels see Appendix B.

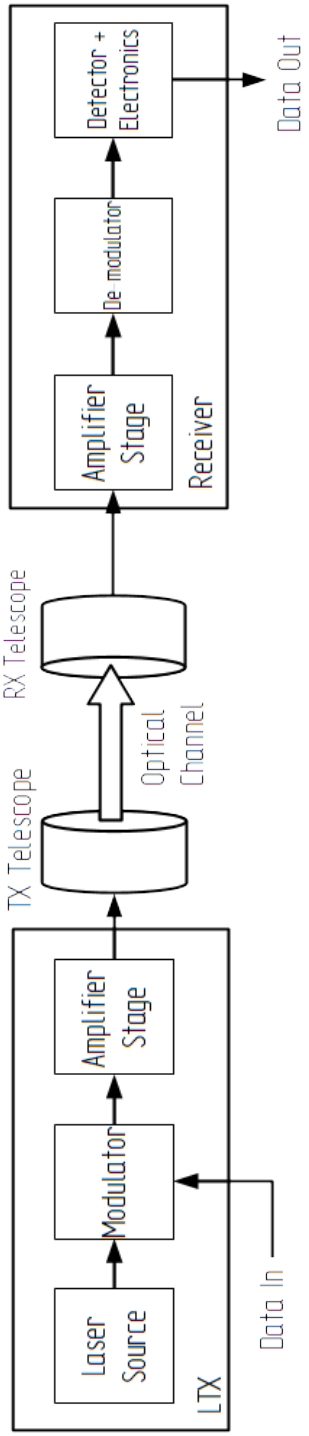

Figure 2.1: A block diagram of a typical free-space optical communications system.

System Parameter	Trade-off Performance Parameters	Feasible Options
Detection Method	Link budget, required optical output power & impact on SWaP.	Direct v Coherent Detection
Operational Wavelength	Interoperability, cost, future-proofing & efficiency.	1550 nm v 1064 nm.
Laser Source	SWaP, cost & noise performance.	Diode laser v Solid-State laser (NPRO).
Transmitter Integration Technology	SWaP & TRL	Fiber Optics v Photonic Integrated Circuits
Modulation Method	Optical power handling & extinction ratio.	DML v Externally Modulated.
Amplifier Technology	Cost, TRL & SWaP.	SOA v Rare-Earth doped amplifier.

Table 2.1: Summary of key trade-offs in space-based laser transmitter design.

2.1.1 Detection Architectures

Optical communications is a technique where light is used to transfer data from a transmitting terminal to a receiving terminal via a wave-guide (such as an optical fiber) or through free space. There are two main principles by which data can be conveyed via light by modulating a property of the light. These modulation principles in-turn drive both the TX and RX system architectures.

Direct Detection

The first principle is that of direct detection (DD) (also known as non-coherent) where the data is conveyed by modulating the intensity of the light. A DD receiver identifies a 1 or zero on the basis of the presence or absence of transmitted light. This is also known as on-off keying (OOK) and an example is shown in Figure 2.2.

As part of the LTX, DD can be implemented either by using directly modulating the source laser through the use of a directly modulated laser (DML) or by using an external modulator. As shown in Figure 2.2 the light is intensity modulated and this technique is commonly used within the communications industry due to it's simplicity. When intensity modulation is combined with DD, as is in most cases, it is known as

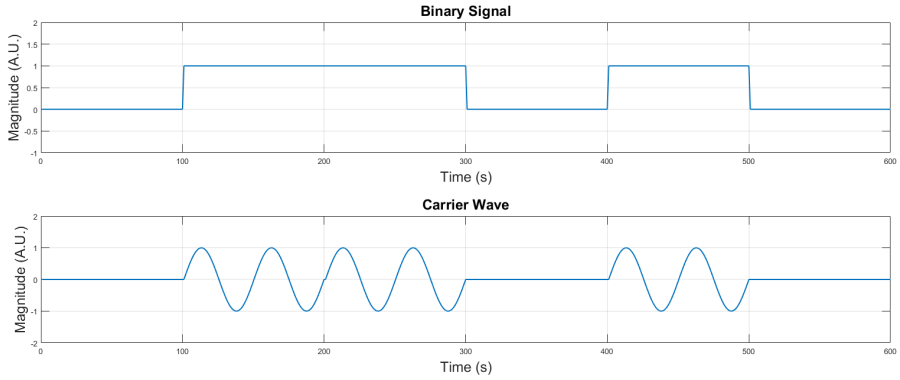

Figure 2.2: Illustrative example of a direct detection modulation scheme (RZ-OOK).

intensity modulated/directly detected (IM/DD).

As discussed previously, DD uses only the amplitude information of the carrier wave. This is the most simple modulation principle and therefore is the easiest to implement. This is usually achieved by focusing the received light onto a photodiode where the amplitude of the light creates a data signal and only a noise signal when no light is present.

IM/DD is attractive as a transmission architecture due to its simplicity and consequently it is commonplace within the optical communications industry (albeit not in modern terrestrial system) and a large amount of effort has taken place in developing IM/DD systems [2.1], [2.2]. The large amount of experience accrued in IM/DD systems leads to two main advantages. Firstly, when designing a new space system architecture, it is easiest to keep the architecture simple. This de-risks the project and allows the focus of development to be on assessing the impact of the space environment on the technology; one of the key themes of this thesis and one of Chan's 'design rules for designing communication subsystems' [2.3]. The second advantage is that because IM/DD is commonplace in the optical communications industry many technologies and components have been developed to meet this market. This leads to a larger selection of technologies to choose from, some of which shall be assessed later on in this section, and therefore a decrease in development cost and time due to specialist components already being developed.

Coherent Detection

The second modulation principle is coherent detection (CD). In this detection scheme, the data is encoded onto the carrier such that the light's amplitude and phase information is used. It offers many advantages over DD including better sensitivity, and therefore access to higher data rates ($\approx>$ 10 Gbit/s) due to improvements in the link budget, and less susceptibility to non-coherent light sources such as background or stray light. An example of a CD scheme is binary phase shift keying (BPSK) where the phase of a carrier wave is modulated to indicate data.

In CD, (amplitude or frequency) of the optical carrier is modulated by the to be transmitted as part of the LTX sub-system. The local oscillator (LO) is combined with the transmitted signal to recover the transmitter phase (or amplitude or frequency). There are three ways in which a CD transmitter can be implemented. The choice of which would depend on a trade-off of specific properties of the communication link architecture. Example trade-off parameters include transceiver/host spacecraft requirements, availability and maturity of key components such as the LO or modulator/demodulator [2.4]. The three architectures in which CD can be implemented are as follows:

1. The use of a high power LO laser with data modulated onto the carrier by a high power, low loss modulator.

2. Use of a medium power LO laser with a medium power modulator. In addition a booster amplifier is used (low gain, high output power) to increase the output power to the desired level. E.g. A semi-conductor bulk amplifier (Nd-doped glass or crystal).

3. Low power LO laser with a low power, low loss modulator and high gain, high output power amplifier. In this regime, the modulator and LO operate at mW levels whilst the amplifier will boost the modulated light to several Watt-level output powers. In this case the transmitter is usually implemented in a all-fiber solution.

The choice of using IM/DD or CD as the detection technique is not always that easy. The main driver of the choice of detection technique is that of overall wall-plug efficiency of the LTX. This is a measure of how much electrical power is required to reach a certain optical output power level. For satellites, this is a key parameter as power generation is always limited through the fixed size of the solar panel arrays and capacity of batteries on-board the spacecraft. It is well known that the main driver of the overall communications system's power budget is that of the required transmitter output power [2.4], [2.5]. As the overall efficiency of the LTX is a key driver in not just the link budget, but also in power budget of the overall spacecraft; the component selection of the LTX is important such that the impact on other systems within the satellite is minimized. This allows for the desired improvement of functionality of other systems such as the payload. For the rest of this section, the focus will be on the components of the LTX system and how a good TX efficiency can be maintained.

2.1.2 Operational Wavelength

The selection of the operational wavelength is a key parameter when designing an optical communications link. This is because it impacts both the link budget but also the optical technologies used in both the transmitter and receiver design.

The first free-space optical links in space operated at a wavelength of 847 nm but the drive towards smaller terminals found that a shift towards operational wavelengths of 1550 nm (C-band[2]), and 1064 nm were needed [2.6].

Although the atmosphere permits the use of many wavelengths to propagate through, the choice of wavelength selection is not necessarily an easy one and a trade-off analysis must be made. The main trade-offs are summarised in Table 2.2 [2.4]. Although historically systems have been designed to operate at 1064 nm this wavelength was chosen at the time as technology operating at 1064 nm was seen to be more mature (in terms of flight qualification) and did not carry the risk photo-darkening of the optical amplifier (see section 2.2 for more information).

Regardless of the wavelength of operation, the operational wavelength must be

[2]The optical C-band have wavelengths between 1530-1565 nm and is not to be confused with the RF C-band.

λ (nm)	Pros	Cons
1064	Higher η_q Typical detectors more efficient[1] Lower diffraction losses	Lower commercial availability of parts Higher quantum noise
1550	Compatible with many fibre optic components Lower Doppler shift Lower atmospheric attenuation	Higher diffraction losses

[1] E.g. InGaAs photodiodes.

Table 2.2: Comparison of Different Operational Wavelengths

tuned to counteract the frequency shift brought forward by the Doppler effect and the relative movements of the two terminals to each other. A typical value for the Doppler shift observed for ISLs is ± 4.8 GHz with a maximum frequency tuning rate of 6 MHz s^{-1} [2.7]. Although these values are for a LEO-GEO link it is anticipated that these values will in fact be lower, as shown in [2.8]. This drift can be overcome by using a tunable laser source (e.g. a distributed feedback laser (DFB)). By using a DFB as the source it is possible to tune the central wavelength by thermally controlling the feedback grating manufactured into the laser diode chip. It is anticipated that this tuning rate can be achieved by controlling a thermo-electric cooler (TEC) which is attached to the diode laser inside the DFB package. I.e. A ± 4.8 GHz drift which require a shift in wavelength of 38 pm at an operational wavelength of 1550 nm, easily achievable with a TEC.

As 1550 nm technology has become the operational wavelength of choice for terrestrial optical communications, development of key components has already been completed. One example of this is the large selection of high-reliability fused components offered by Gooch & Housego and other fiber optic component providers. As these components have been previously designed to operated at an extremely low-rate of failure by being qualified to telecommunications standards such as Telcordia GR-468 [2.9] and Telcordia GR-326 [2.10]; qualification of these components for the space environment is de-risked to a lower level. In a commercial aspect 1550 nm technology is attractive as due to the large industry it supports the market is very competitive in pricing which allows for cost-effective solutions. In addition (as shown in section 2.1.5) the C-band

is very broadband allowing for future-proofing for wave division multiplexing (WDM) systems.

Communications using 1064 nm are more efficient due to a lower quantum defect, however, component availability for 1064 nm is more restricted but becoming less of an issue due to recent advances in the field of fiber lasers [2.11]. In addition some questions remain over the suitability of using fiber amplifiers based at 1064 nm as the radiation hardness of Yb^{3+} ion based fiber amplifiers is still unanswered, however the status of this is discussed in detail in section 2.2. In addition, through the availability of more sensitive detectors and reduction in free-path space loss (FSL) a 1064 nm will see an improvement in a link budget when compared to a similar 1550 nm link. Finally, 1064 nm is the incumbent technology through it's demonstration in the European data relay system (EDRS) [2.12] the European data relay system and is the technology of choice by ESA moving forward [2.6], [2.13].

In the case where the laser transmitter is designed to be compatible with EDRS, the operational wavelength is already 1064 nm. However, interest in the C-band is still active as some space optical communications are adopting 1550 nm due to the availability of low-cost, high-reliability components [2.14] or when considering high-throughput WDM systems. Therefore when designing LTXs for space applications, both wavelengths must be considered when designing the laser transmitter sub-system.

2.1.3 Laser Sources

Historically, optical fibers were originally designed to operate in the region of 0.7-0.9 µm [2.15] due to optical sources available at the time being mostly composed of $Al_xGa_{x-1}As$ (aluminium gallium arsenide) [2.1]. However, it quickly became apparent that transmission in the 1550 nm region was more efficient due to lower absorption losses and dispersion limiting potential communications bandwidth [2.16] and because of these advantages 1550 nm technology quickly became the dominant technology in industry.

Throughout the historical development of low-loss optical fiber, light sources have always been developed to match the research in optical fibers. Initially, this led to the first class of light emmitting diodes (LEDs) which were incoherent but could be

Source	**Pros**	**Cons**
Laser Diodes	Compact & efficient	Difficult to achieve high data rate (> 10 Gbit s^{-1}) at high optical output powers (> 1W)
Diode-Pumped Solid State Lasers (e.g. Nd:YAG)	Multi-Watt power levels possible Provide good coherence	Inefficient when compared to other sources. IM/DD rates are limited Heat dissipation an issue
Rare-Earth Doped Fiber Amplifiers	Scaling to powers > 10 W possible 10's of Gbit s^{-1} modulation bandwidth possible in one fiber mode	Susceptible to non-linear effects Radiation Degradation
semi-conductor optical amplifiers (SOAs)	Small size & mass	Output power limited Large loss for coupling to fiber Larger noise figure than other sources

Table 2.3: Different laser source technologies and their pros and cons.

used in multi-mode (MM) fibre links [2.1]. However, as fiber technology matured the use of single-mode technology became more apparent and LEDs became unsuitable for long-haul communications due to the poor temporal coherence and inefficiency of focusing the light into a single-mode fiber. As single-mode became the dominant technology for long-haul communications, lasers became the light source of choice due to the excellent spatial qualities of the beam exiting the laser along with the improved temporal coherence of the light, thus making it suitable for coherent communications. Therefore when using fiber optics to guide light or when a highly collimated beam is needed, lasers are the light source of choice. Previously, the laser source was seen as a limiting factor in the development of space optical communications [2.17] thus highlighting the need for careful source selection.

Table 2.3 shows the potential feasible laser source technologies and their pros and cons. Although fiber amplifiers and semi-conductor optical amplifiers (SOAs) can be thought as high power laser sources, they require some seed light to amplify and will not be discussed in this section. More information on optical amplifiers can be found in section 2.1.5. However, the pros and cons of typical seed sources (laser diodes and

solid-state lasers) need to be addressed and a trade-off analysis performed.

Laser Diodes

Laser diodes operate by converting electrical power into light by the combination of electrons and holes across a forward biased p-n junction through the process of stimulated emission. Laser diode design is a large topic by itself and won't be discussed, however the engineering impact of using laser diodes in LTXs will be considered.

For optical communication systems, single frequency operation is a must. This is so that optical noise, caused by either the TX, RX or channel, in the optical channel can be easily filtered out and the system is as efficient as possible. In addition single frequency operation becomes essential in DWDM systems as an excellent discrimination between wavelengths channel is needed. Single wavelength operation in modern laser diodes is achieved through the use of a DFB or distributed Bragg reflector (DBR) laser. The schematic of both a DFB and DBR is shown in Figure 2.3. Both devices utilise a periodic grating (Bragg grating) in the laser cavity to stabilise the operational wavelength through the mechanism of constructive/destructive interference.

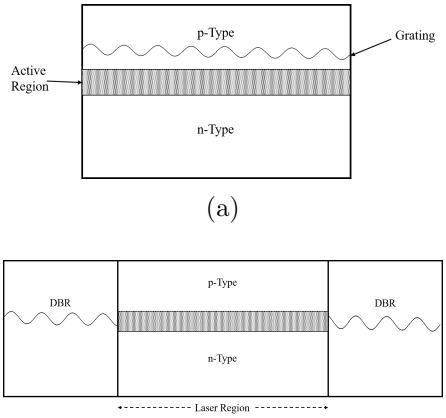

Figure 2.3: Schematic of two different classes of feedback laser:
(a) DFB laser & (b) DBR laser.

The use of the Bragg grating along with tight control of the cavity length allows for the selection of a single wavelength by setting the wavelength-dependent loss of the laser cavity over the active medium's gain bandwidth. The loss is set such that only

one wavelength is selected over the laser's gain profile and all other longitudinal modes are suppressed. As seen in Figure 2.3 there are differences between the DFB and DBR lasers. For a DFB laser, the grating is etched into the actively pumped region; whilst for a DBR the grating is etched onto the ends of the active region and can be thought to be analogous to the feedback mirrors found in traditional Fabry-Pérot laser cavities. Although using a DBR gives the user the advantage of placing the feedback mechanism outside the active region, thus making it more stable, it is more lossy than a DFB due to optical absorption in the unpumped regions [2.1].

In the initial designs of DFBs the grating was placed in the light-generating part of the laser diode, it was found that the reliability of these devices was extremely poor. However, moving the grating structure into a passive part of the wave-guide greatly improved the reliability of the device as the grating is not subject to the recombination of carriers [2.1]. Wavelength selection is achieved by selecting a grating period, Λ such that the Bragg condition is met. The wavelengths, λ_B, selected by the Bragg filter is given by the equation 2.1

$$\lambda_B = 2n_e l\Lambda \tag{2.1}$$

Where n_e is the effective refractive index and l is the grating order. From equation 2.1 it can be seen that many wavelengths (or side-modes) can be selected as the order of the grating, l, is increased. This leads to issues in terms of reducing the efficiency of the laser as the side-modes will use some of the gain present in the active medium, not at the desired wavelength. In addition it shows that the λ_B can be actively tuned by adjusting Λ. This can be achieved in two ways: The first and most common is to thermally control the grating by using a TEC which is placed below the laser diode and substrate. The second method which is applicable to DBRs only, is that the end Bragg reflectors can be mechanically deformed to adjust their transmissive properties. The tuning properties of these laser diodes allow for the constant de-tuning caused by effects such as Doppler shift and thermal instability which caused by an always changing thermal environment on-board the spacecraft, making this class of laser diode an attractive choice.

Another laser diode topology for wavelength tuning is that of a vertical cavity surface emitting laser (VCSEL). This topology can be easily discounted as the technology is not mature enough to provide heritage in high-reliability applications. Although, this issue is currently being addressed by the research community for the 1.55 µm wavelength [2.18] with some VCSELs already passing Telecordia test standards at 1.3 µm [2.19]. Performance data on extended life time operation is presently not available therefore these devices are not suitable due to a low qualification status at this time.

For coherent and narrowband communications, the phase noise and line width of the source laser is of major importance as this adds unwanted noise at the receiver. The line-width of a laser is inversely proportional to the length of the laser cavity [2.20] and therefore an increase in the laser cavity will reduce the phase noise exhibited by the source. For laser diodes this is achieved through the use of an external cavity which can be either integrated into the laser wave-guide or completely external to the chip. Recent development into external cavity laser diodes has produced commercially available laser diodes with a line-width in the region of 15 kHz and a noise performance similar to solid-state laser systems [2.21]–[2.23].

Although both DFBs and DBRs have been demonstrated to be tunable across the C-band and have had use in telecommunications [2.24], the choice of which topology to use for space optical communications is simple. As mentioned earlier, single wavelength operation is needed so that the noise bandwidth can be reduced to as small as possible. It is known that DFBs are known to have improved stability in single wavelength operation [2.25] through the use of a longer cavity along with only one active tuning element to control. In addition, most feedback lasers on the market are currently DFBs thus making them an attractive choice for the development of laser transmitters due to a lower cost and broader range of component models to choose from. Therefore DFBs are the laser diode topology of choice when designing non-coherent optical links. For coherent communications, using a laser diode with an external cavity would be suitable due it's inherent narrow line width.

Diode Pumped Solid-State Lasers

The most common solid-state laser used in optical communications is based on a Nd:YAG crystal. It uses the Nd^{3+} ion as its active ion hosted in yttrium-aluminium-garnet ($Y_3Al_5O_{12}$) crystal. The Nd^{3+} ion is a four-level gain medium with it's most common transition emitting at a wavelength of 1064 nm [2.1]. Nd:YAG has previously been selected for its' good optical and thermal properties when compared to other solid-state lasers. In addition Nd:YAG is radiation resistant to a degree but extra co-dopants can be added to improve the radiation response of the crystal, for more information on radiation effects see section 2.2.3. However, its main drawback is the sharp pump absorption peaks which are present. This causes issues in pump diode selection as they need to be stable over temperature and life [2.4]. Solid-state lasers rely on being optically pumped by laser diodes meaning that they cannot take advantage of the package sizes of laser diodes and will be much bigger. Typically, because of this size differential the cost of a Nd:YAG laser will be higher when compared to a laser diode.

As mentioned above the solid-state laser is larger than a laser diode. One of the smallest ways in which to integrate a Nd:YAG crystal is through using non-planar monolithic ring oscillator (NPRO) topology. This allows for a very compact laser as the majority functional optics (e.g. $\lambda/2$ wave-plate, polariser, & Faraday rotator) used in the laser cavity are integrated into the geometry of the NPRO crystal [2.26]. An example of the NPRO geometry is shown in Figure 2.4. When a magnetic field is present, the Nd:YAG crystal acts as a Faraday rotator, therefore the surfaces of the facets inside the cavity act as wave-plates which in-turn achieves omni-directional travel around the optical cavity. The coating used on the input/output facet provides polarisation selection if needed.

Hermetically sealed NPRO lasers have already been demonstrated in-orbit and gained a good level of space heritage, currently being used as the source laser in the laser terminals in EDRS and other lasers developed by TESAT [2.4], [2.6], [2.27]–[2.29]. In addition these types of lasers are currently being used in remote sensing applications such as in the ICESat-2 mission [2.30]. A summary of one of the laser sources developed by TESAT is shown in Table 2.4. In addition to these specifications it has

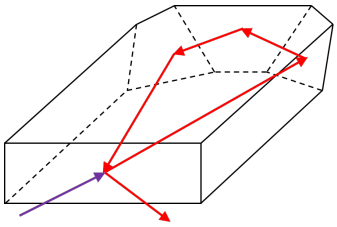

Figure 2.4: A Non-Planar Ring Oscillator laser cavity. The pump light (808 nm) is shown in purple and output light (1064 nm) shown in red.

Specification	**Value**
Operational λ	1064 nm
Continuous frequency tuning range	30 GHz
Output power	50 mW
Volume	20 x 25 x 18 mm
Mass	80 g

Table 2.4: Typical performance parameters of a space qualified Nd:YAG NPRO laser developed by TESAT [2.27].

been previously reported that line-widths of 10 kHz have been achieved for this class of laser [2.31]. The pump light is provided by using a 100 µm MM fiber and redundant 808 nm laser diodes which have been proven to have an excellent level of reliability. The output of the NPRO laser is then coupled out of the NPRO cavity via a PM fiber [2.27].

Trade-off Analysis of Diode Lasers & Diode Pumped Solid-State Lasers

As shown above solid-state NPRO technology provides a superior performance when compared to diode lasers. However, recent research has shown that with an external cavity laser diode technology can match or even better NPRO lasers at a wavelength of 1064 nm [2.22], [2.23]. When comparing the cost of the two laser technologies (in both monetary and system terms) laser diodes are the preferable technology. As the size and mass contribution of laser diode technology will be less than NPRO lasers, laser diodes are the preferable technology as the LTXs produced as part of this project are envisaged to be place on-board small- ($<$ 50 kg) and micro- ($<$ 10kg) satellites. In a

commercial sense, the main market for this kind of LTX would be a high volume/low price market. This would exclude NPRO lasers due to their high recurring cost. For example, Numata et al. estimates a diode laser would cost approximately 10 times less than a solid-state or bulk laser [2.23].

2.1.4 Modulation Technologies

To transmit information by continuous wave (CW) laser, data must be mixed onto the carrier light. This is achieved through the process of optical modulation. There are two major modulator schemes which are commonly used. These are: Directly Modulated Lasers and External Modulation.

The modulation scheme chosen for the optical link influences the modulator choice and only some modulator families can perform certain modulation techniques. Although the polarisation and frequency of the light can be modulated to convey data, the main method in which light is modulated is through amplitude and phase modulation. Optical modulators can be characterized by 5 key parameters [2.4]. These are:

- Bandwidth;
- Insertion loss;
- Extinction ratio;
- Power consumption;
- Optical power handling.

Direct Modulation

The easiest way to modulate data onto an optical carrier is through directly modulating the output power of the laser source. In most telecommunication systems this is achieved by modulating the drive current feeding a laser diode. The laser diode drive current is modulated by driving the laser diode at a bias current and then adding on a 'data' current level through the use of a bias-T. The bias-T works by adding a DC

current, I_{DC}, by passing through the signal through a inductor (therefore blocking any AC noise) and the AC signal, I_{AC}, is added through a resistor and capacitor. Care must be taken to ensure that $I_{DC} > I_{AC}$, as reverse biasing the laser diode will cause irreparable damage to the device.

The modulation of the laser diode makes DMLs highly attractive for IM/DD applications, as a good extinction ratio is available if the laser diode is modulated near threshold. Typical modulation schemes used by DMLs are OOK and pulse-position modulation (PPM) and have been shown to be suitable for optical communications in space [2.32]–[2.34]. The main disadvantage of DMLs is that the maximum modulation bandwidth available for low-cost, high-reliability parts is limited. Although Winzer [2.2] reports that some research demonstrations have reached data rates of up to 40 Gbit s^{-1} most commercially available parts in the C-band have a maximum modulation bandwidth of 12.5 GHz (see G&H AA0701/EM65X series). However, most contemporary space optical communications using have data rates operating in the 1-10 Gbit s^{-1} regime or lower [2.4], [2.6], [2.13]. Therefore using DMLs when developing DD LTXs for data rates under 10 Gbit s^{-1} is a possibility as this will improve the SWaP and reduce module cost.

External Modulation

When a higher data rate or coherent communications is required, the CW light exiting the laser source must be externally modulated. For both coherent and DD optical communications this is typically achieved through the use of a lithium niobate ($LiNbO_3$) modulator. Lithium niobate modulators work on the principle of the electro-optic effect. By splitting the beam and applying a voltage across two electrodes the refractive index of the crystal will change and therefore the phase of the light wave of one arm which can then cause constructive or destructive interference when the beams are recombined.

For intensity modulated applications, a device known as a Mach-Zehnder modulator (MZM) is used and a schematic of this device is shown in Figure 2.5 with the active crystal shown in the hatched area. MZMs operate through the interference of two waves, unlike direct modulation [2.35]. The incoming light is split into two paths with one arm

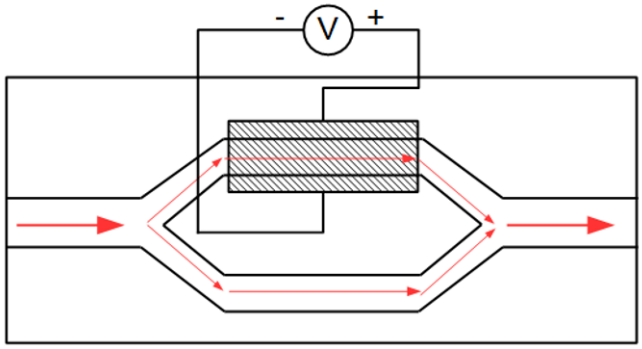

Figure 2.5: Schematic of a Mach-Zehnder Modulator. Light travelling through the device is shown in red.

experiencing a phase delay (although it is common for both arms to experience this through using phase modulators on both arms) determined by a voltage being applied to the crystal. When the light exiting the device is set such that light is at a minimum, the voltage across the crystal is set such that the phase offset between the two arms is $\phi = \pi$ at V_π. Therefore the two arms destructively interfere and an intensity minimum exits the device, denoting an 'off' state. When a maximum transmission is needed the voltage across the crystal is set to zero, the two arms constructively interfere and lights exits the device at an intensity maximum denoting an 'on' state. However, there is a loss of light through the device as some of the light will be absorbed by the $LiNbO_3$ crystal.

In most modern communications systems, MZMs operated use phase modulators on both arms and can be operated in one of two modes [2.1], [2.35]. The first mode is that of Push-Push Operation where the applied voltage across both arms is equal. This is typically used in applications where pure phase modulation is needed, i.e. coherent communications. The second mode is that of push-pull operation (also known as balanced driving) [2.2] where the voltage across each arm has the same magnitude but opposite polarity. This mode of operation is used when amplitude modulation is needed. When operating in push-pull operation, the biasing voltage is set to $V_{Bias} = V_\pi/2$, the quadrature point. It is set at this point because it is easy to control by using either a lock-in amplifier or RF pilot tone [2.36].

Commercially available devices developed for space applications show that modu-

lation bandwidths of up to 20 Gbit s^{-1} are available [2.37], [2.38]. Terrestrial lithium niobate devices have been shown to reach data rates up to 40 Gbit s^{-1} [2.35]. To increase the terrestrial devices' TRL, they could be investigated by passing them through a qualification campaign to assess their suitability for space applications. However, currently the need for data rates higher than 10 Gbit s^{-1} is not prevalent enough [2.14], [2.39], [2.40] therefore no research into qualifying higher speed devices is currently occurring. These devices have already been assessed for operation in harsh terrestrial environments (e.g. underwater/defence applications) [2.38] so the only outstanding concern comes from the device's radiation response. Research into the radiation response has been completed by Thomes Jr. et al. and it shows that the performance of the device does not degrade for a total ionising dose (TID) of up to 52 kRad [2.41].

So far in this discussion only lithium niobate has been considered as the material to be used. However, another potential material is GaAs (gallium arsenide) which is also shown to exhibit the electro-optic effect [2.42]. GaAs have been demonstrated to operate with high modulation bandwidths since 1993 [2.43] and has even been demonstrated at data rates up to 100 Gbaud [2.44], rivalling and improving on lithium niobate technology. GaAs devices can be realised such that they can exhibit lower SWaP than $LiNbO_3$ devices as they are compatible with production on low-loss, low-cost substrates. This makes GaAs devices highly attractive for small form factor, high data rate applications for both terrestrial and space-based applications.

One final material to mention is indium phosphide (InP). Although it is starting to appear in integrated photonic devices for high speed applications [2.45]. InP devices are still at a too low a TRL level to be considered for use in space.

Trade-Off Analysis of Modulation Technology

For low-data rate applications (less than 2.5 Gbit s^{-1}) using direct modulation is preferable due to the simplicity offered. This allows for systems with lower SWaP and developmental effort. For small form-factor laser transmitters suitable for CubeSats and other small satellites, direct modulation would be the preferred technology

When data rates exceed 2.5 Gbit s^{-1} external modulation becomes the dominant

technology for two reasons. The first is that when at these data rates, external modulators offer a better extinction ratio. This is because as the modulation frequency increases, the extinction ratio for directly modulated lasers decreases because of the lasers' relaxation oscillations [2.46], the amount of frequency chirp allowed in the system and other practical electronic defects such as stray capacitance in the device. Secondly for space systems, external modulation has already been extensively used in terrestrial applications at higher data rates [2.2] and have been proven to operate in a harsh environment when high-reliability is needed. This gives greater confidence in developing a robust system suitable for the harsh environment of space when volume and mass is not such a stringent requirement.

As discussed above the two main materials to be used in external modulators are lithium niobate and GaAs. The main trade-off of these materials for space systems is the current TRL of technology. As shown by Winzer and Essiambre [2.2], MZMs based on lithium niobate have long be used in terrestrial systems for both commercial and more specialist applications [2.41]. Consequently, lithium niobate already has flight heritage [2.4], [2.38], [2.47]. Meanwhile GaAs modulator technology has not yet been demonstrated in space, although the material has been used in other applications such as in RF electronics [2.44]. Although research is active in developing GaAs modulators for space [2.48], the current TRL is not currently sufficiently high to be considered for use in this thesis.

2.1.5 Optical Amplifiers

master-oscillator power amplifier (MOPA) architectures require optical amplifiers to increase the output to a suitable power level so it can be either transmitted or received. As with traditional RF telecommunications amplifiers, optical amplifiers are designed differently depending on the situation where they will be used in either the TX or RX sub-system. In either a TX or RX sub-system it is typical for more than one amplifier of differing types to be used. There are three main classes of optical amplifier:

1. low noise amplifiers (LNAs) – In RX sub-systems these are the first amplifier in the chain and as such are designed to operate at very low input powers. The

main aim of LNAs is to amplify the received signal to an intermediary power level whilst adding as little noise as possible. i.e. Minimizing the noise figure (NF).

2. Booster amplifiers – These are used to increase a small signal input into a suitable output power. This type of optical amplifier is designed such that it can provide a good amount of gain whilst also providing a good level of noise management. These are typically used in RXs after the LNA and as the pre-amplifier in TXs.

3. high power amplifiers (HPAs) – Used in TX subsystems to increase the output power to Watt levels. These amplifiers are designed to provide as much gain as possible. Noise performance is usually considered as a secondary design parameter.

Each amplifier class has its own design difficulties which will become apparent throughout this thesis and will be addressed when needed. Because as with any engineering system, the design space is greatly influenced by the operational environment.

There are two main optical amplification technologies which can be used and compared in Table 2.5. Although bulk crystal optical amplifiers have previously been considered by Hemmati for space systems [2.4]; for compact applications this type of optical amplifier can be discarded due to concerns over it's potential SWaP requirements. Both SOAs and fiber amplifiers (typically based on either erbium or ytterbium) offer the opportunity of designing a compact system suitable for small- and micro-satellites and comparison of the two technologies is shown in Table 2.5.

There is very little difference in the optical performance between either erbium-doped fiber amplifiers (EDFAs) or SOAs, apart from the worse NF of SOAs. The main differences lies in their impact on the overall system. EDFAs operate at a lower total power consumptions than SOAs and power is a key performance parameter when being used on board spacecraft where power generation is limited. This difference arises from the need of a TEC needed to keep the device at an operational temperature, however the electo-optical efficiency of the SOA without a TEC is quite high. Hemmati (section 4.2.2.2.1) [2.4] also lists other advantages of fiber amplifiers being the high-beam quality exiting the amplifier, mechanical requirements, thermal requirements and redundancy

Parameter	**Booster-EDFA**	**SOA**
Typical Output Power (dBm)	> 15	> 13
Gain (dB)	> 24[1]	> 25
Noise Figure (dB)	< 6	< 8
Max. Gain Variation (dB/nm)	< 0.75	< 0.1
Polarisation Dispersion (dB)	< 0.3	< 0.5
Typical Size (mm)	45x70x12	30x12.5x12.5
Typical Power Consumption (W)	< 1	< 5

[1] The maximum gain available is largely dependent on the application. As shown later, EDFA gain is limited at higher output powers due to gain saturation.

Table 2.5: Comparison of comparative optical amplifier technologies [2.49]

implementation [2.4].

One other point to note is the TRL of each technology. Fiber amplifiers have already a high level of TRL through previous development by Tesat [2.29] and G&H [2.50]–[2.52]. However, SOAs are yet to be proven in a space environment and little thought has been put into using SOAs in space application when compared to fiber amplifiers [2.4].

Therefore, in conclusion fiber amplifiers are the technology of choice for optical amplification. Although using SOAs offer the opportunity of making more compact transmitters, the current TRL of the technology makes it unsuitable for this project.

Rare-Earth Doped Fiber Amplifiers

Optical amplification in fibers is achieved by co-doping the glass with a rare earth metal. Depending on the operational wavelength, the co-dopant used will change on the specific use, much like conventional bulk lasers. For operation at 1064 nm the active element is the Yb^{3+} ion (ytterbium-doped fiber amplifier (YDFA)). Whilst for operation in the C-band the active element is the Er^{3+} ion (erbium-doped fiber amplifier (EDFA)). For high power operation over the C-band a co-doped fiber of both Yb^{3+} and Er^{3+} is used. This is known as a erbium-ytterbium doped fiber amplifier (EYDFA). Shown in Figure 2.6 are the energy-level diagrams for both the Yb^{3+} and Er^{3+} ions, showing the

lasing mechanisms used for the amplification of light at both 1064 nm [2.53] and the C-band [2.54]. Although other lasing transitions are available within these systems the transitions shown are most commonly used due to their high transition cross-sections. As in this thesis only EDFAs and EYDFAs will be developed, discussion on YDFAs and their lasing transitions will be kept to a minimum.

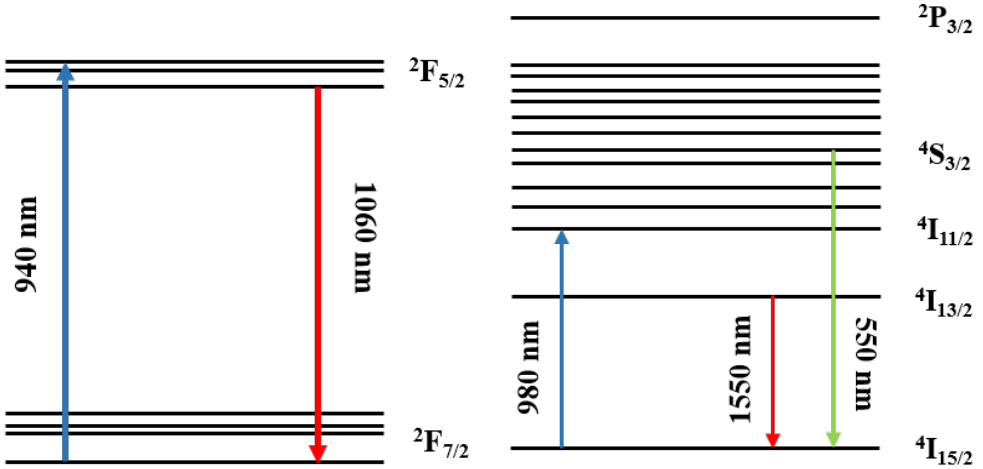

(a) Yb^{3+} (b) Er^{3+}

Figure 2.6: Energy level diagrams for the active elements commonly used in fiber amplifiers: (a) Yb^{3+} and (b) Er^{3+} [2.53], [2.54]. Note: The gaps between energy levels are not to scale.

Optical amplifiers dependent on the Yb^{3+} lasing transition for operation at 1064 nm or at high power over the C-band depend only on two energy levels, $^2F_{5/2}$ and $^2F_{7/2}$, which split into three and four sub-levels respectively. Typically these sub-levels are not resolved for Yb_3^+ ions in a glass matrix at normal operation temperatures due to level broadening (homogeneous and inhomogeneous). The impact of this broadening means that a large amount of wavelengths can be used for both the signal and pump wavelength. Primarily this impacts the laser dynamics by providing two windows for the pump wavelength: one centred on 976 nm as a sharp peak and a broader although less efficient window at 875 to 950 nm with a peak at 915 nm [2.53].

EDFAs can be co-doped with other rare metals to influence the lasing properties. The most common pairing for erbium is with ytterbium. The process on which this relies is sensitized fluorescence, in which the ytterbium ion acts as an energy donor to

a nearby erbium ion [2.54], [2.55]. This process is made possible by the $^2F_{5/2}$ level of the Yb^{3+} ion being in close resonance with the $^4I_{11/2}$ level of the Er^{3+} ion [2.55]. This allows for the energy which is absorbed by the pumping of an Yb^{3+} ion able to be transferred efficiently to an Er^{3+} ion which can then be stimulated to emit light.

Typically a pump wavelength of 940 nm is used for EYDFAs for three reasons: pump laser diode stability due to environmental changes, reliability in operation and availability of components. The first reason is a trade-off between the much more efficient absorption peak at 976 nm versus the wavelength stability of the laser diode. As the 976 this is counteracted with temperature control of the laser diode through the use of a TEC. This lowers the overall wall-plug efficiency of the amplifier due to the power draw of the TEC. Although using a pump wavelength of 976 nm is optically more efficient due to a high quantum efficiency, this is not always the case due to the wall-plug efficiency and if a TEC is used.

The second reason is due to the reliability of the laser diode and it's resilience to the creation of dark-line defects, a major failure mechanism. For devices which operate at a longer wavelength they do not reach the activation energy needed to create the point defects which cause the creation of dark line defects [2.56], [2.57]. Historically, the telecommunications industry has chosen 976 nm as a pump wavelength and that become standard throughout the industry due to cost. However at the time high power MM laser diodes were hard to come by due them not being able to lock to 976 nm via a fiber-Bragg grating. Therefore more reliable MM high-power laser diodes have been developed at 940 nm then at 976 nm such that the pump laser market for high-power EYDFAs could be addressed.

The final and most important reason is a consequence of the previous point. The component availability of 940 nm high power laser diodes is quite high when compared to other wavelengths. Another benefit of 940 nm laser diode technology becoming dominant in the telecommunications industry is that they were developed for high-reliability applications. This previous work in reliability studies can be leveraged into space application where heritage is a key design parameter. Leveraging high-reliability components developed by the telecommunications industry is a key theme throughout

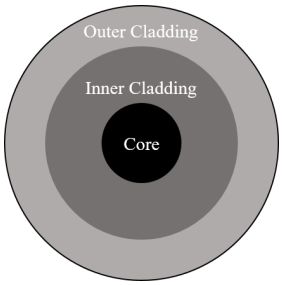

Figure 2.7: Structure of a core-centred double-clad fiber.

this thesis and this can be seen in later chapters.

For high output power applications (> 1W), a double clad fiber structure is typically used and is shown in Figure 2.7. This differs from standard fiber by the use of an additional cladding layer in which the pump light is guided overlapping the core where the signal is guided. This is beneficial for high power applications for three reasons. The first is that a large cladding area allows for a multi-modal structure in which the capture angle for the pump light is increased; in turn the amount of pump power can be increased through improved coupling efficiency to a laser diode. Secondly, the use of a cladding structure improves the surface-area to volume ratio which improves the thermal management of the fiber even if pump powers are scaled to the kW level [2.58]. In addition, the use of a larger surface area increases the threshold at which optical damage and unwanted non-linear effects such as stimulated Brillouin scattering (SBS) (a major output power limiter in narrow line-width systems) becomes apparent along with avoiding the dielectric breakdown of the material through the use of a larger area, thus increasing the maximum pump power level. Finally, the use of a multi-mode (MM) pump guide structure allows for the use of higher power laser diodes which only operate in a MM fashion. However, the only drawback of using cladding pumped fiber is a reduction of the pumping efficiency as a consequence of the fact that not all of the fiber is being inverted, thus causing signal re-absorption in a three-level system (e.g. in YDFAs/EYDFAs). The engineering impact of this is that longer Yb-doped fiber lengths are needed which increases the amplifier's susceptibility to SBS.

For optical amplification over the C-band an EDFA is used. Originally reported on in 1987 [2.59], [2.60] for use in the telecommunications industry, EDFAs depend on the

Er^{3+} ion with energy levels split ranging from $^4I_{5/2}$ to $^2P_{3/2}$ as shown in Figure 2.6 (b). Although the optical transitions and properties of EDFA's have been studied in great detail in the past [2.54], [2.61] there are three main optical transitions.

The first key and main pump transition is that of $^4I_{15/2}$ to $^4I_{13/2}$ which corresponds to a wavelength of 980 nm and is known as the ground state absorption transition. The ions excited to the $^4I_{11/2}$ then relax to the $^4I_{13/2}$ level through multi-phonon, non-radiative decay when hosted in a oxide (e.g. SiO_2) matrix [2.61]. Although pumping to the $^4I_{11/2}$ is possible at 1480 nm through in-band pumping, the absorption of this wavelength is slightly less than at 980 nm [2.54], [2.62]. The selection of 980 nm as a pump wavelength for EDFAs has led to the development of many high-reliability laser diodes, leading to a wide range of components becoming available. Therefore 980 nm is the chosen pump wavelength because a larger number of commercially available, high-reliability components along with the option of scaling to higher output powers.

The lasing transition of interest is from $^4I_{13/2}$ to $^4I_{15/2}$ which is centred on 1530-1540 nm. To amplify signals across the whole C-band, homogeneous and inhomogeneous broadening assist in providing a large gain bandwidth. The main causes of this are the temperature of the EDFA, phonon interaction in the glass and the Stark effect which arises from the local electric field present in the host matrix around the ion [2.54]. One other important factor which affects the wavelength dependence on the emission cross-section of this transition is the co-dopant (e.g. Al_2O_3, GeO_2 or P_2O_5) used in the glass matrix to increase the Er^{3+} concentration [2.54], [2.61]. As shown later, the choice of co-dopant is a key parameter when designing radiation hardened EDFAs. Ions excited to the $^4I_{13/2}$ level can also randomly decay without any stimulation to the ground state. This process is known as spontaneous emission and is the main source of noise in fiber amplifiers. This spontaneously emitted light can then be amplified through stimulated emission in the process described above. This light is known as amplified spontaneous emission (ASE) and is known to limit both the gain and noise performance of optical amplifiers. This is due to the amplified spontaneous emission (ASE) light extracting some of the gain which could possibly be used to amplify the signal. As this noise is amplified through the system, this raises the noise of the EDFA and thus degrades the

signal-to-noise ratio (SNR).

The final process of interest is the transition from $^4S_{3/2}$ to $^4I_{15/2}$. This process arises from multi-photon absorption in which the $^4I_{13/2}$ level is excited by an extra pump photon to the $^4F_{7/2}$ level and then decays non-radiatively to the $^4S_{3/2}$ level [2.61]. From this level the ion can relax to the ground state emitting visible green light at 550nm resulting in the characteristic green light of EDFAs.

EDFAs do not suffer from photodarkening like YDFAs do, however they do suffer from photodarkening induced by gamma radiation (known as radiation induced attenuation (RIA)). As this effect is extremely important to this thesis, it is covered specifically in Section 2.2.3.

At a wavelength of 980 nm the Yb^{3+} ion has a cross-section approximately 10 times greater than the Er^{3+} ion [2.55]. This leads to a higher pump absorption per unit length and is more power efficient when compared to pure EDFAs. This paves the way for a more efficient high power optical amplifier to be used over the C-band [2.53], [2.54], [2.61]. In practice this increased power efficiency and gain per unit length leads to shorter devices which helps in terms of creating compact systems. In addition because of the reduced device length, non-linear effects such as SBS become less of an issue. Therefore for a high output power, $P_{out} >= 500$ mW, over the C-band a co-doped fiber EYDFA should be used.

Performance Characteristics of Fiber Amplifiers

Designing a communication system containing optical amplifiers requires effect models that describe the amplifier operation. Amplifiers are describes using three main figures of merit: The Gain and noise figure (NF), both which are commonly expressed in dB, and P_{Sat}, the maximum power that the amplifier can deliver (usually defined as the point as which the gain is reduced by 3 dB). The gain of an amplifier is defined as a ratio of the output power, P_{out}, to input power, P_{in}. Gain is commonly defined to also normalise the output power for ASE by subtracting the ASE power P_{ASE} from the signal power. The definition of gain in units of dB is given in Equation 2.2, with output powers expressed linearly.

$$G(\lambda) = 10\log_{10}\left(\frac{P_{out}(\lambda) - P_{ASE}(\lambda)}{P_{in}(\lambda)}\right) \qquad \text{[dB]} \tag{2.2}$$

A figure of merit for the noise performance of an optical amplifier is either output SNR or noise figure (NF), both of which are interrelated. The definition of NF has previously been a topic of much debate within the optical amplifier research community with many definitions not being consistent as definitions of NF define the parameter in such a way that it can be difficult measure easily [2.63]–[2.65]. However work by the telecommunications industry has led to many different methods of measuring the NF of an optical system [2.65]. Noise figure is traditionally defined as the ratio of input SNR to output SNR at a specific wavelength [2.66]. i.e.

$$NF(\lambda) = 10\log_{10}\left(\frac{SNR_{in}(\lambda)}{SNR_{out}(\lambda)}\right) \qquad \text{[dB]} \tag{2.3}$$

To redefine Equation 2.3 in terms of measurable parameters, a derivation of Equation 2.4 is needed. This derivation is shown in Appendix C and the result of which is given in Equation 2.4 using the source-subtraction method and assuming a shot-noise limited system.

$$NF(\lambda) = 10\log_{10}\left(\frac{P_{ASE}\lambda^3}{Ghc\Delta\lambda} + \frac{1}{G} - \frac{P_{SSE}\lambda^3}{hc\Delta\lambda}\right) \qquad \text{[dB]} \tag{2.4}$$

Where P_{ASE} is the output ASE power, P_{SSE} is the source spontaneous emission power (source noise level), G is the amplifier's gain (in linear form), h is Planck's constant, λ is the signal wavelength, c is the speed of light and $\Delta\lambda$ is the optical spectrum analyser (OSA) bandwidth (for EDFA measurements this ranges from $0.1 - 0.5$ nm).

Although there are more precise and accurate ways to measure NF, such as the time-domain extinction (TDE) method[3]. The choice of source-subtraction allows for quick and easy measurements which in turn allows for faster system development which is needed in this project.

[3]The TDE method is more accurate due to it suppressing more P_{SSE} than source-subtraction. This is achieved by pulsing the signal off and measuring the ASE before the amplifier recovers to a new steady state.

Influence of Pump Light Direction

It is well known that the direction of pump light greatly affects the NF and gain performance of an amplifier. For NF this arises from the absorption of pump light and the generation of ASE along the fiber. Desurvire (p. 113-114) [2.54] provides a good explanation of this effect by showing that for fiber amplifiers in which the pump light decreases over length (noise density increases due to ASE generation), that in terms of noise generation (and therefore NF) co-propagating pump light provides a better performance than counter-propagating light. This is achieved by describing the fiber amplifier as a system of cascaded infinitesimally small amplifiers which have different levels of medium inversion.

The pay-off of having a higher NF in a counter-pumped amplifier over a co-pumped amplifier is that a higher gain can be extracted from the fiber when operating at a fixed input power and pump power. For counter-pumped amplifiers this arises from the fact that at the exit of the fiber, the ions are inverted meaning that the signal is being amplified all the way to the exit and no signal re-absorption occurs; thus increasing efficiency. For co-pumped amplifiers this may not be the case and the signal can undergo re-absorption in the later parts of the fiber amplifier.

The two effects described above depend on the ion inversion profile along the fiber amplifier. For a saturated amplifier (i.e. all ions present in the fiber are inverted and no more gain can be extracted) the difference between co-pumping and counter-pumping becomes less pronounced [2.54]. Thus for operation in which the optical amplifier needs to operate with a good level of gain and NF, a homogeneous level of inversion, provides the best pay-off in performance between gain and NF. This is best achieved through bi-directionally pumping the amplifier in which pump light is injected from both ends of the amplifier. Bi-directional pumping is more efficient than pumping from one direction as this allows for easy inversion along the whole length of the fiber.

Influence of wavelength

As shown above in Equation 2.2 and 2.3, both gain and NF are dependent on wavelength. This is due to both the inhomogeneous absorption and emission cross-section

profiles of the active ions. The emission and absorption profiles for both EDFAs [2.54], [2.61] and YDFAs [2.53] are well known as they are key to the operation of fiber amplifiers when used in dense WDM configurations in high-speed communications. The wavelength dependence of gain and NF will become evident later on in this thesis and will not be discussed further.

2.1.6 Integrated Photonics

With the advent of photonic integrated components (PIC) in recent times offering more compact and efficient photonic systems, they must be suitably assessed for use in the next generation of space optical communications systems. As shown earlier on in this section and later in Section 2.3, most current baseline designs operate on either bulk lasers and more recently fiber optics but the benefits that PICs offer cannot be ignored. Integrated photonics offer improvements in areas such as more compact and efficient systems through the inherently smaller packaging. For space-specific applications PICs can offer a high level of resilience against the operational environment due to the compact design and materials used [2.67].

Although there has been significant recent advances in integrated photonics through improvements of fabrication and packaging processes [2.67], there are still improvements to be made in terms of commercial availability. Current disadvantages of PICs include the lack of low-loss, hermetic packaging, power dissipation (both electrical and optical), the need for tight thermal control and therefore a need for a TEC decreases overall efficiency and more specific for the space environment, integration of components using low-outgassing materials and range of operational/survival temperatures [2.67].

One example of this is the recent research in miniaturising key components of laser transmitters. Recent research into developing transmitters has been completed in the USA but with limited success in terms of generating BER curves [2.68] due to excess noise. Another example is the exciting developments in miniaturising lithium niobate MZMs [2.69]. This research shows clear improvements in using integrated photonics by providing a low loss, miniature device which can be easily interfaced to by using CMOS components.

Both of these exciting pieces of research show that although there is the potential for the use of these components in the space environment, their current TRL makes it problematic to use at the moment as they are currently have a TRL of 1-3. As the modules developed in will be at a TRL of 5-7, PIC devices are not currently suitable to be used in this project. However, it should be noted that a big shift in space photonics is near as the TRL of PIC are raised and the benefits they bring are realised.

2.1.7 Trade-Off Summary

Shown in Table 2.6 is a summary of the key technological trade-offs discussed, highlighting the key technologies to be used in the development of the laser transmitters developed in this project. This is the result of the earlier discussion of the trade-offs given in Table 2.1 and now sets the technological baseline for the space laser transmitters to be developed as part of this project.

System Parameter	**Chosen Option**	**Comments**
Detection Architecture	Dependent of link requirements	Also dependent on overall LTX SWaP requirements.
Operational Wavelength	1550 nm preferable	1550 nm can leverage high-rel telecommunications components. Also dependent on EDRS/ground segment compatibility.
Laser Source	DFB for DD & external cavity diode laser for CD	Laser diodes offer smaller packages & can leverage heritage high-rel telecomms components.
Modulation Method	Dependent of data rate	For data rates $> 10\text{Gbit}\,\text{s}^{-1}$ use external modulation
Amplification Method	Fiber Amplifier	EDFA TRL is high, no TEC is needed.
Integration level	Don't use PICs	PIC TRL is too low.

Table 2.6: Summary of key space laser transmitter design trade-offs.

2.2 Damage Mechanisms of Fiber Optic Components in the Space Environment

Now that a technological baseline has been established for the development of space laser transmitters, the operational environment must be considered. This poses a major challenge not just to the optics inside the laser transmitter but to the whole satellite.

The aim of this section is to provide an introduction to the space environment and the challenges it poses in the design of space laser transmitters. The key damage mechanisms which degrade the performance of the components identified in Section 2.1 will also be surveyed along with techniques for providing mitigation against the operational environment.

2.2.1 The Space Environment

For many engineering systems, the Earth can be a highly protective place to operate when compared to the space environment. However, space-based optical systems are unique due to the design challenges posed by the potential operating environment. Therefore, when transferring terrestrial technology to the space domain large design modifications are required to provide a reliable and efficient system. The space environment can be broadly split into three themes in which the system will be operating. These are:

- The pre-launch environment - This is important during assembly, integration and testing (AIT) such that the system can operate reliably and avoid any issues due to contamination.
- The launch environment - This environment poses the greatest challenge to the device's mechanical parameters through high levels of shock and vibration.
- The in-orbit environment - This is the environment in which the spacecraft will spend a large majority of its lifetime. Reliability is a key parameter here as it is very unusual for a satellite to be serviced in-orbit[4].

[4]However, in-orbit servicing is possible. Most famously the Hubble Space Telescope has been serviced four separate times in-orbit.

Pre-Launch Environment

The pre-launch environment concerns the assembly, integration and testing (AIT) phase of the spacecraft's life cycle. To ensure the optimal performance of electronic, electromechanical and most importantly optical systems; manufacturing facilities must be kept as clean as possible so that any contamination which can affect performance or reliability can be avoided.

For electronic systems it is well known that a clean room of at least class 10,000 (less than 10,000 particles with diameter greater than 0.5 µm per cubic ft) is needed to provide a 'clean' environment [2.5], [2.70]. For fiber-optic components this clean environment already exists due to high-reliability requirements. A clean environment is needed as this greatly increases the reliability of any fiber optic component where the glass core or cladding is exposed (e.g. during splicing). Any dust that is present on the bare fiber can cause the coupling of light out the fiber or cause issues in fiber optic splices, where any dust can cause a loss and in turn can burn or reduce the mechanical strength of the fiber.

Another important pre-launch environmental issue is that of storage. Because of the length of time it can take to integrate a whole spacecraft, it might be necessary to store certain subsystems for many months or years before launch. Therefore, to avoid degradation of any components, Fortescue et al. recommends that tight environmental controls are needed [2.5]. This can usually be achieved by controlling storage room properties such as temperature and humidity.

Launch Environment

Currently the only way to reach orbit is via a multi-stage rocket and although research is currently ongoing to develop a single-stage-to-orbit system, it is still many years away from completion [2.71]. Although rockets are well known for the acoustic noise during launch, other mechanical stresses are present such as high levels of shock and vibration. Other environmental conditions such as thermal gradients and de-pressurisation are present. Although literature [2.5], [2.70] provides rough values for these environments, the conditions observed during launch will be unique due to variance of launcher and

payload mass. The best source for launch conditions are the launcher user manuals which provide specific values for spacecraft designers to use.

The sources of vibrational energies come in a variety of sources but mostly consist of launch vehicle acceleration and aerodynamic buffering as the launch vehicle moves up through the atmosphere [2.5], [2.70]. Two peak vibration levels occur during launch. The first peak occurs at lift off where the noise and vibrational energy generated by the rocket motors and the exhaust gases released by the motors reaches it's peak. The second peak occurs when the vehicle passes into super sonic flight in which the launch vehicle is stimulated by the irregular airflow around the nose of the vehicle. At this point it is known for peak levels to reach slightly above 10^{-1} g^2/Hz [2.70].

Static loading to the launch vehicle payloads occur due to the constant acceleration of the rocket moving through the atmosphere. The loads experienced by the spacecraft during launch depends on the kind of launcher used. For launchers which have a low payload mass, the peak loads exhibited are generally greater due to short motor firing times. For Ariane launches (one of the main launchers used by ESA), the loads experienced can reach above 4.55 g_0[5] [2.72].

Mechanical shocks can occur when latches are opened, pyrotechnic bolts are fired, when motors are fired, or when vehicle separation occurs during landing or docking. These events are characterised by high acceleration loads lasting a few milliseconds which translates to a characteristic frequency spectrum of high frequency components. For example, one of the largest of these shocks can be found in the Ariane 5 launcher where the peak level occurs at above 3 kHz where the design requirement is that the spacecraft survives a shock at 10^4 g_0 [2.72].

The thermal environment observed during launch is mainly determined by the temperature reached by the nose of the spacecraft being heated up due to aerodynamic frictional heating. This is largely dependent on the specific heat capacity of the shroud's material and the payload within the vehicle experiences a temperature rise due to radiative and conductive heat transfer between the nose of the vehicle and the payload, but is usually of no concern.

[5] g_0, acceleration due to gravity

As the launch vehicle ascends through the atmosphere, the ambient pressure declines during launch. The rate by which the pressure drops within the launcher is largely dominated by the venting of the launcher which can be fixed by including venting ports to the launcher structure. For example, the Ariane launcher de-pressurisation rate is 10^3 kPa s^{-1} [2.5]. Both venting of the spacecraft structure and of electrical housing is generally required to avoid unwanted static loads due to pressure differentials.

As discussed previously the main impact this has on space optical systems is on the opto-mechanical design. This can manifest itself in fiber optic systems in both the module, through design of support structures, and on a component level where the construction of the device is important. One example on a device level is that of free-space optical alignment in laser diodes and fiber-optic isolators utilising micro-optics as any perturbation of the optical path can lead to unit failure. Therefore, these devices must be qualified to a suitable level before launch.

In-Orbit Environment

The in-orbit environment is the place where the spacecraft will spend all of it's operational lifetime and is highly influential in determining the design of the spacecraft and its' subsystems. The space environment is known to be a very hostile place to operate a system and must be engineered to make sure that these problems are overcome. These design challenges can be broadly broken up into five themes:

- The thermal environment;
- The vacuum environment;
- The microgravity environment;
- The upper atmospheric environment;
- The radiation environment.

For space-based fiber-optic systems the main challenges faced come from the radiation environment and the thermal environment. For more comprehensive reviews of the space environment, the author points the reader towards Fortescue et al. [2.5]

Surface finish	**White Paint** $\alpha = 0.15$ $\epsilon = 0.9$	**Black Paint** $\alpha = 0.9$ $\epsilon = 0.9$	**Electroplated Gold** $\alpha = 0.25$ $\epsilon = 0.04$
No eclipse	-61 °C	+20 °C	+176 °C
Maximum eclipse	-70 °C	-2 °C	+138 °C

Table 2.7: Equilibrium temperatures for a spacecraft operating at LEO with different surface finishes. From: [2.5]

and Wertz & Larson [2.70]. For a more specific review on the radiation environment Holmes-Siedle & Adams [2.73] offers a far-reaching review.

Space is well known for being a vacuum and very cold, thus proving a challenging thermal environment. Surfaces are typically characterised by their absorbance, α, and emittance, ϵ. Table 2.7 shows typical system equilibrium temperatures for spacecraft operating at low Earth orbit (LEO) with different surface finishes showing the large thermal fluctuations that a system will need to survive. From this it can be seen that good thermal control over optical systems is needed otherwise they will be susceptible to damage through thermal stress or the expansion/contraction of the optical media as temperature is varied.

Optical components which are at risk for fiber optic systems are laser diodes due to their delicate facet coatings on the end of the laser cavity. Large thermal fluctuations can lead to thermal shock and progressive reduction of the output power through a degrading output facet. Other important issues in laser diode stability is that changes in the temperature can lead to junction fluctuations which can cause reliability issues both electrically and optically through wavelength changes. Temperature changes can also effect the alignment of free-space optical components (e.g. in optical isolators) adding an unwanted additional temperature dependent loss to the device. In addition, through expansion and contraction of opto-mechanics, the properties of fiber optic components can change or mechanically stress bonds. i.e. coupling ratio in fiber couplers.

The vacuum of space poses design challenges in designing the thermal path of components, due to the loss of convection to transport heat; but more specifically for optical systems, avoiding contamination due to out-gassing. This poses a problem when bulk

optics is used as contamination can cause aberrations in telescope optics which can then greatly degrade performance. Typically the ambient pressure at spacecraft altitudes ranges between $100^{-11} - 10^{-15}$ Pa which causes sublimation when the vaporisation pressure of the material is reached. Thin plastic layers and organic materials are typically sensitive to out-gassing [2.5] which are quite common in the use of fiber-optics e.g. Acrylate is used as the main buffer material of optical fiber. However, out-gassing is not typically a concern as the amount of volatile material is quite low (even with a large amount of fiber present) and the venting of volatile materials can be controlled via providing a venting hole on the equipment which is pointing away from sensitive equipment.

The radiation environment plays a key role in the design of a spacecraft as without proper design a lot of unnecessary weight will be added as metallic shielding. The radiation environment is known to produce many affects on space systems which must be countered to ensure good reliability of the spacecraft and any subsystems. These affects are well known and are surveyed greatly in literature [2.5], [2.70], [2.73]. These damage mechanisms and consequences are discussed later in Section 2.2.2 and 2.2.3.

Only the LEO environment will be discussed as the LTXs designed as part of this thesis will mostly be deployed at this altitude. However, components and modules can be tested with harsher conditions to simulate higher altitudes e.g. GEO.

Non-ionizing radiation is of no concern when developing spacecraft due to the ease of which it can be shielded from [2.5], [2.74]. Ionizing radiation however is of greater concern as shielding will only provide a certain level of protection before diminishing returns take hold. There are three main sources of ionizing radiation at LEO: The Van Allen belts, the Sun and galactic cosmic rays (GCRs).

The Van Allen radiation belts contain highly energetic particles and exist at various altitudes. Shown in Figure 2.8 are the radiation measurements made by Pioneer 3 in 1959 [2.75]. Although these are rough measurements it clearly shows the structure of the two Van Allen belts and at what altitudes they exist at. The inner belt is typically characterised by large amounts of high energy protons being present [2.76]. These protons have energies that range between $0.01 - 400$ MeV with fluxes of $\approx 100 - 600$

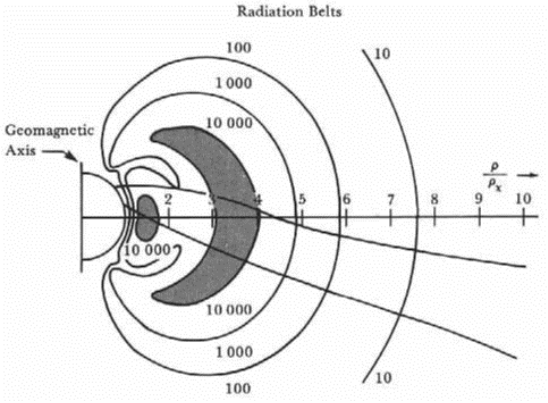

Figure 2.8: Radiation measurements made upon Pioneer 3, showing the structure of the Van Allen belts. From: [2.75]

$\mathrm{cm}^2\,\mathrm{s}^{-1}$ [2.5].

The Sun contributes to the radiation environment in three ways: the solar wind, coronal mass ejections (CMEs) and solar flares. The solar wind is a stream of constant energetic particles originating from the Sun's surface (slow solar wind) or from coronal holes (fast solar wind) [2.77] and carry an energy of $\approx$ 100 keV and have a flux of $< 10^{12}\mathrm{cm}^2\,\mathrm{s}^{-1}$ [2.73]. For spacecraft which orbit around planets which exhibit a strong magnetic field (Earth, Jupiter, Saturn etc...) and are at an altitude to be within the magnetosphere of the planet i.e. LEO, the effects of the solar wind can only be felt at the magnetic poles. This is because a lot of energetic particles are streamed to the poles due to the structure of a planet's magnetic field being approximately a dipole field in shape.

A coronal mass ejection is a large amount of energetic plasma is released into the solar wind when a magnetic field and a large amount of plasma erupts from the Sun's corona. It can contain a mass of plasma slightly larger than 10^{13} kg and can achieve velocities to the order of thousands of $\mathrm{km\,s}^{-1}$. However, a typical CME has a mass of around $10^{11} - 10^{12}$ kg and travels at a speed between $400 - 1000\ \mathrm{km\,s}^{-1}$ [2.78]. CMEs consist of a mixture of helium ions and high oxidation states of oxygen as well as heavier metals such as iron as well as cooler ions of magnesium and neon [2.79], [2.80]. Because of the high energy of these particles, spacecraft electronics may suffer severe degradation or failure (e.g. memory corruption), there must be proper shielding

or mitigation to avoid these effects.

The last solar event is a solar flare. A solar flare occurs when a bright flash of light is observed on the Sun's surface and a large amount of energy is released. It might be inferred that a CME might follow a solar flare, especially a large solar flare, but this is not always the case [2.81]. A solar flare ejects energy mostly in the x-ray region of the electromagnetic spectrum and emit charged particles such as electrons, protons and ions into interstellar space [2.81]. It also takes approximately one to three days for the particles released by a solar flare to reach the Earth and then start to interact with the geomagnetic field. Upon interaction with the geomagnetic field, the solar flare starts to warp the geomagnetic field which can put spacecraft lying at GEO in polar and highly inclined orbits at risk as the spacecraft will be subject to a unusually high radiation dose.

GCRs are defined by Fortescue et al. to be high energy radiation rays that propagate through space that is occupied by low-density matter [2.5]. Although the origins of GCRs are still well debated in literature [2.82]; the current consensus is that they originate from neutral pion decay within supernovae with each supernova releasing approximately 10^{44} J [2.83]. GCRs consist of approximately 83% protons, 13% α-particles, 3% electrons and then a small abundance of heavier ions (1%) [2.5]. Primary cosmic rays are GCRs which are directly incident upon the Earth and are therefore the most important rays to think about in terms of space system design. When travelling towards Earth, GCRs interact with the stellar medium it is travelling through, causing GCR fragmentation. This means that the abundance of higher energy nuclei is decreased and the abundance of lower energy nuclei is increased. This causes the detected fluxes to vary (especially the lower energy regions), modulated by the solar-cycle [2.70] and decreasing by 40% in sharp drops occurring at solar maximum [2.5]. Therefore in terms of the impact that GCRs have upon space systems; GCRs add to the background radiation but can also cause some problems with single strikes. GCR strikes are known to cause problems with electronics [2.5], [2.70] but this typically will only be a problem for spacecraft in a high altitude or inclined orbit (i.e. at GEO or polar orbit).

2.2.2 Damage Mechanisms due to Displacement Damage

When highly energetic particles travel through a pure semi-conductor material, the semi-conductor can become damaged by displacing atoms from the semi-conductor's lattice [2.74]. Through the wide use of electronics in harsh radiation environments such as in the space environment or in the nuclear industry, the effects of radiation on silicon electronics is well known [2.5], [2.73], [2.74]. Although a short introduction to the mechanism behind displacement damage is presented here, for more information the author points the reader towards the textbooks by Holmes-Siedle & Adams [2.73], Fortescue et al. [2.5] and Larson & Wertz [2.70] and short course presented by the IEEE [2.74].

Displacement damage occurs when a highly energetic particle collides or primary recoil atoms collide with atoms in the target material's lattice. This causes the formation of a Frenkel Pair (the displaced atom and lattice vacancy) [2.73], [2.74]. With the formation of Frenkel pairs, this introduces unwanted energy states in the band gap of the material which in turn can lead to changes in both the mechanical and electrical performance of devices. In summary, displacement damage is known to contribute towards degradation of performance in transistors, electronic memory and opto-electronic devices where the light-to-current ratios are important [2.74], [2.84].

Previous work by Dale et al. [2.85] has shown that for energies less than 1000 MeV protons are the dominant particle in causing displacement damage as protons exhibit the highest non-ionizing energy loss (NIEL) for these energies. As protons are the dominant energetic particle at LEO, it can be hard to distinguish displacement damage from ionizing damage [2.5]. Displacement damage of opto-electronic components must be considered as they are integral to the laser transmitters developed in this thesis.

As discussed earlier the main threat that displacement damage poses is in the creation of Frenkel pairs which generate allowed energy levels in the material's band-gap. Opto-electronic components which are used in laser transmitters are all based on diodes. Diodes are classified as minority carrier devices and it is known that displacement damage can effect these devices through the creation of bulk traps in the lattice. Bulk traps are known to reduce carrier lifetimes and therefore increase carrier recombination across

the p-n junction.

For laser diodes and LEDs, an increase in carrier recombination will lead to lower efficiencies in light generation as different energy levels can now be accessed to cross the band gap of the material. This would reduce the electrical-to-optical (E/O) efficiency and increase in threshold current of a laser diode which is shown in literature [2.86]. Previous work by G&H has shown the levels of damage that laser diodes see through proton bombardment. For a 60 MeV fluence of 10^{12} p/cm^2, a proton fluence shown at LEO, for non-PM pumps there was no degradation in output power and a negligible increase in threshold current [2.87]. For high-power MM pumps a degradation of 50 mW (2.3%, within measurement error) was observed at a pump current of 3 A and same proton fluence [2.87]. Thus showing that for space applications that these laser diodes (and therefore many more through qualification by similarity) are resistant to displacement damage caused by protons.

For photodiodes literature suggests that an increase in dark current and decrease in photo-sensitivity will be present after proton irradiation [2.88]–[2.90]. This is due to the same mechanism described above in which Frenkel pairs inhibit the movement of carriers across the p-n junction. Literature has shown that a large increase in dark current is observed although it is from pA to nA [2.91]–[2.93]. In some cases a large decrease of 25%-40% is seen in the E-O efficiency of the back facet monitor (BFM) in both single-mode (SM) and MM laser diode packages [2.92] and PIN photodiodes [2.93] but is not present in other work [2.91]. This would suggest the photodiodes being used by Gonthier et al. are being saturated or there are other effects present in the system effecting the results (i.e. single event effects impacting drive electronics).

One caveat about the studies described above [2.86], [2.88], [2.89], [2.91]–[2.93] is that they cannot distinguish between the damage caused by ionizing and non-ionizing radiation (displacement damage). Therefore, damage due to ionizing radiation cannot be ignored and is discussed in Section 2.2.3. However, through recognising that these devices are p-n junctions, they are analogous to both diodes and transistors and the damage to this component class is well known for both displacement damage [2.74], [2.84] and ionizing radiation [2.5], [2.70], [2.74].

2.2.3 Damage Mechanisms due to Total Ionising Dose

Damage through the ionisation of a material is achieved via bombardment by high energy protons, electrons and photons. Although interactions with photons are not of a concern, the space environment consists of highly energetic protons and electrons [2.5], [2.84]. However, when characterising ionisation damage it is typical for laboratories to use γ-ray sources. γ-rays interact with matter in one of three ways [2.74]:

- The Photoelectric effect (for energies $\leq$ 100 keV) - A bound electron is ejected from an atom and is filled by an electron from the outer electron shells.
- The Compton effect (for energies from 100 keV to a few MeV) - A γ-ray is scattered by an electron in the outer electron shells and is then ejected from the atom.
- Pair production (for energies $\geq$ a few MeV) - A photon is absorbed by an atomic nucleus with an electron and positron pair created.

As ionizing radiation interacts with the target material, charge is built up within the material through the process of generating e-h pairs in which some kinetic energy of the radiation particle is lost. It is known that the amount of e-h pairs generated is dependent on the energy band-gap of the material. For SiO_2 the amount of e-h pairs generated per rad is typically 8.1×10^{12} p/cm^3 [2.74].

The e-h pairs generated across the band-gap of the material will attempt to recombine. However, some e-h pairs will escape the recombination process and will leave a defect within the material lattice. It is at these points where charge can become trapped within the lattice of the material and in turn degrade both the material's electrical and optical properties.

Although the mechanism of total ionising dose damage is well known within electronic components such as diodes and transistors [2.5], [2.70], [2.74]. The effects of gamma radiation on fiber optics, especially rare-Earth doped fibers are known or not as well understood when compared to electronic components.

Radiation Induced Effects in Optical Fibers

After the advent of EDFAs in optical communications, a large amount of research has been undertaken to study the effect of radiation on different classes of optical fibers: passive fibers and active fibers (EDFAs, YDFAs and EYDFAs). Although a a large majority of this research is for the nuclear industry, in-flight, on-board testing confirms that EDFAs degrade quickly in the space environment [2.94], [2.95]. The work by Girard et al. [2.96] defines the two main effects due to gamma-radiation observed in optical fibers as:

- **radiation induced attenuation (RIA)** - This is an increase in the attenuation of the glass due to radiation effect. This is dependent on both wavelength, time [2.97] and dose rate [2.98].
- **Radiation Induced Emission (RIE)** - This corresponds to a sharp increase in emission of the optical fiber due to radiation. This is typically produced by the luminescence of already existing or radiation induced point-defects.

Girard et al. [2.96] identifies RIA as the main limiting factor effecting the performance of active fibers within a radiative environment. RIE only has an effect when radiation tolerant fibers are used at high doses and only degrades the SNR by increasing the spontaneous noise [2.99].

The radiation response of both passive and active optical fibers are governed by the co-dopants used in the silica host matrix. Typical dopants in passive fibers include: germanium, phosphorus and aluminium; all of which allow the modification of the refractive index of either the glass core or cladding. All of these co-dopants generate colour centres which effect the spectral absorption of the fiber and in turn it's optical efficiency. Each colour centre generated is centered on a single wavelength and then is broadened depending on the energy structure [2.96].

In Telecom-grade commercial off-the-shelf (COTS) optical fibers, Ge-doped optical fibers are the most common. With this in mind a large amount of effort has been focused on assessing Ge-doped fibers for a variety of applications to empirically determine the effect of radiation [2.96], [2.100]. Early on it was identified that Ge-doped glasses

showed a high level of RIA when compared to pure silica glasses [2.101]. This implies that the co-dopant interactions are the main source of RIA within optical fibers, not Si−Si or Si−O interactions found within pure silica fibers [2.101] and this assumption holds for all other co-dopants [2.96]. Girard [2.96] and Neustuev [2.101] show that RIA occurs mostly in the UV and blue part of the visible spectrum (200-700 nm) meaning that for applications at NIR wavelengths Ge-doped glasses can be used without fear of high-levels of RIA. However for applications where RIA is detrimental to the overall system, RIA must be fully characterised. The main absorption bands are found at energies of 1.97 eV to 6.8 eV [2.96] and are mostly attributed to unpaired electrons present in the crystal lattice [2.99], [2.101], [2.102].

Phosphorus is commonly used within EYDFAs to increase the rate of energy transfer between the Yb^{3+} and Er^{3+} ions [2.54] and also to increase the solubility of rare-Earth ions within glass [2.96]. A comprehensive piece of work by Griscom et al. [2.103] characterises and explains the origins of P-based colour centres and the process attributed to them. In terms of the main impact of telecommunications using NIR wavelengths the main colour centres of concern are those generated by Phosphorus-Oxygen-Hole Centres which cause absorption at pump wavelength (900 nm to 1 µm). These colour centres are classed as a hole type defect as a net positive charge is left in the silica matrix as an electron is ejected from the lattice. The process of this charge generation is shown in Figure 2.9 in which an electron is ejected out of the phosphate molecule which can then move freely. The resultant molecule's charge is net positive and the unpaired spin is shared between 2 p-orbitals of neighbouring non-bridging Oxygen atoms [2.103]. Although known to have high RIA at shorter wavelengths than the wavelengths of interest, Phosphorus is not the main contributor to RIA observed in EDFAs, YDFAs and EYDFAs

Typically found in EDFAs and EYDFAs aluminium is used to co-dope the core to prevent clustering of Er^{3+} ions due to Er^{3+} ions having a coordination number[6] of 6 (typical) and it's position within the tetrahedral silica matrix [2.104]. Aluminium-related point defects have in the past been identified as the main cause RIA within

[6]Coordination number is a measure of how many atoms that can be bound to a central atom.

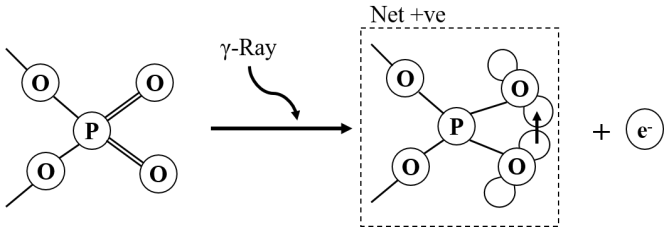

Figure 2.9: Phosphorus-Oxygen-Hole Centre formation process.

EDFAs [2.94], [2.104]. It has been shown that the presence of aluminium-doping causes RIA within optical fibers not the concentration or presence of Er^{3+}.

Girard [2.104] showed that the process by which this occurs is that the Al_2O_3 which is used as the co-dopant forms an ionic shell around the rare-Earth ion. This would then reduce efficiency of the ion being influenced by external electric fields and therefore it's ability to contribute to spontaneous emission. Previous work has shown that in Al-doped fibers that the level of Er^{3+} concentration does not effect the level of RIA [2.104]–[2.107]. Therefore it can be said that the host matrix is the cause of RIA of Al-codoped rare-Earth doped optical fibers.

Highlighted above are the known key causes of RIA within active-optical fibers. Although the effects of RIA are well known within EDFAs, YDFAs and EYDFAs this is still an active research field for other doped fibers; as recently lanthanum and thulium doped fibers have been shown to show strong levels of RIA [2.99]. As such it is not recommended to use thulium doped fiber amplifiers as the effects of RIA are still unknown. RIA can be hardened for by altering the fiber design or through component testing. Hardening strategies against RIA are discussed in sub-section 2.2.4.

Dose rate (flux) and the total dose (fluence) has previously been found to vary the RIA of an optical fiber. Intuitively the RIA of an optical fiber increases as the total dose is increased [2.108], [2.109]. However, work has shown that RIA is not a linear process. Early work by Griscom et al. [2.108] showed that RIA can be modelled as a power law growth process, a model which still mostly holds today for non-PM fibers [2.99]. The dose rate influences the RIA response by increasing the RIA at a higher dose rate for a fixed total dose [2.108], [2.109]. This occurs as the generation of defects is increased at higher dose rates and has been always been a constituent part of modelling RIA

[2.108].

With regards to the irradiation particle type previous work has found that particle type only effects absorption in optical wavelengths [2.102]. Differences arise when looking at transients in the system as it is known that pulsed x-rays will cause unstable defects which will temporarily increase the RIA observed [2.99], [2.102]. For steady state irradiation little difference was found in RIA when irradiating with γ-rays or highly energetic protons [2.110]. In terms of this thesis, the main particle that will be seen in operation in the space environment are constant γ-rays. Therefore when testing the radiation response of a component or module, a source that produces a constant source of γ-rays should be used to simulate the environment as similarly as possible to the actual environment.

The final extrinsic factor is that the temperature of the optical fiber when irradiated has been shown to influence the level of RIA observed. A change in temperature influences the rate at which colour centres are created and the rate at which photo-bleaching occurs [2.99], [2.111]. Although initially thought a rise in temperature would only positively influence the RIA [2.111], work by Girard in 2013 shows that for different co-doped fibers, the temperature can effect fibers in different ways [2.112]. For example, for P-doped fibers temperature has no influence, Ge-doped fibers exhibit a reduction in RIA at higher temperatures and pure-silica fibers can see an increase in RIA due to the conversion of an unstable defect into a more stable colour centre [2.112]. Girard in 2013 explains that this is a complex relationship and that for practical applications, an empirical approach is needed [2.112]. In fact, the same author in 2018 remarks that is still the case and further work is needed to understand this relationship [2.99].

2.2.4 Hardening Strategies

As discussed in the previous three sub-sections, the space environment is a harsh place to operate for fiber optics. Although fiber optics has flown and been operated in space before, this have been typically used for confidential applications and end user's/part vendors are reluctant to share qualification data due to disclosure agreements such as

ITAR[7].

As such, European researchers have developed recent guidelines [2.113], [2.114] which have been able to guide researchers and engineers in assessing optical components for their suitability in space. However, no real standard has yet emerged from either the USA, Europe or Japan for the qualification of opto-electronics and fiber optic components for the space environment.

Opto-electronics & Passive Fiber Optics

For opto-electronics and fiber optic components a lot of work, has previously been undertaken in the terrestrial telecommunications industry to assess and understand fiber optic failure modes and reliability models [2.115]. As a response, industrial standards by Telcordia [2.9], [2.10] have been developed to test product reliability so that end user can use components with confidence in high-reliability applications such as sub-sea communications.

In terms of use within aerospace products, previous guidance has come from microelectronic high-reliability test specifications such as MIL-STD-883 [2.116]. These offer stringent test requirements in areas such as mechanical vibration, shock, thermal and humidity environmental testing. This specification also sets out important test procedures that are to be followed when assessing components.

As already mentioned, effort by ESA and partner companies has led to the development of component testing guidelines for space-applications [2.113], [2.114]. Although these standards are designed for laser diodes they can be extended to other opto-electronic and fiber-optic components to some degree. In fact, these ESA guidelines frequently refer the reader to MIL-STD-883 and the Telcordia standards mentioned. If specific tests are required the ESA guideline uses MIL-STD-883 and Telcordia test processes but change the test conditions such that it suits the anticipated environment i.e. mechanical vibration/shock is much higher at launch than seen by a plane on take-off. Therefore, it can be concluded that using industrial high-reliability standards for

[7]ITAR - International Traffic in Arms Regulations, is a US regulation that prohibits the export of defence technologies. Sadly, any space component used in a US satellite, even when used in a civilian application, is covered by ITAR and as such reduces the data available for engineers to use.

component screening can give a good understanding on the component's response to the space environment and can be used a component hardening strategy.

Although qualifying a component by prior Telcordia or MIL-STD-883 certification does not guarantee survivability of the component in space, further testing of these components on a single lot level is needed to ensure that workmanship is kept high and consistent. This is similar to the current approach by the space industry to electronic components in terms of qualifying lots of components for flight use.

Radiation Hardening of Active Fibers

Section 2.2.3 discusses the main threat faced by active fibers is that of γ-radiation. As this fiber class are a key component within space-based laser transmitters, a radiation hardened optical fiber is key. There are many approaches to hardening active fibers to radiation which will be discussed below. A large amount of work has provided the background for the commercialisation of radiation hardened active fiber for optical amplifiers by manufactures such as IxBlue [2.117]–[2.119] and Draka [2.120].

One of the major drawbacks of commercial radiation hardened fibers is that the cost of these top performing specialist fibers is extremely high ($\approx$ 1000-1500 €/m), not necessarily suitable for cost sensitive applications. To provide a survey of COTS fibers which can be used to assess the fiber's response to expected radiation levels (typically 100 kRad) is highly beneficial. From this survey the fiber with the lowest RIA can be selected. Although this means a poorer performance when compared to rad-hard fibers, the cost is a lot lower and can be scalable in a commercial context, making COTS fibers more suitable for volume applications such as for satellite constellations.

For both COTS and specialist fibers, a known effect on RIA response is that of photobleaching of the active fiber by the input power to the active fiber. It is known that photo-bleaching will decrease the RIA seen during irradiation as well as increase the recovery of the fiber post-irradiation. The effect of photo-bleaching is known to be dependent on both the fiber composition and therefore the type of defect generated [2.121]. In addition it is known that the level of photo-bleaching is dependent on the operational environment (e.g. wavelength and temperature) [2.99] of the fiber showing

that this effect is application specific. In testing of fibers usually low or no input power is used to assess the worst-case RIA of a fiber.

Another strategy to avoid RIA is to adjust the operational wavelength of the fiber amplifier. For the space-environment, the minimum RIA can be found in the 1-1.2 µm window for most optical fibers [2.99]. However, IR-RIA is still not understood fully and unknown absorption bands must be investigated. In addition other wavelengths, such as 1.5 µm can be used if the RIA can be hardened for in another way. Although the RIA performance at 1.5 µm is worse, it might be selected for other reasons such as the availability of commercial components. The other wavelength to consider is the pump wavelength. For EDFA RIA it has been shown that pumping at 1480 nm is more efficient than at 980 nm when photobleaching is not present [2.122]. However, this is not the case and with photobleaching present, the gain recovered when pumping at 980 nm is 30 times more than at 1480 nm [2.122].

The main approach to radiation hardening active fibers is that of altering the fiber composition. The approach of which depends on the type of amplifier.

For EDFAs and EYDFAs, there are differing approaches to this problem. The first approach is to remove the aluminium through specialist doping techniques such as with nano-particles [2.123]. This approach by Draka Communications has led to the development of a EDFA which shows a reduction in RIA to 3.75 dB/100 kRad, which is significantly lower than standard telecoms fibers which show a RIA of $\sim$ 10 dB/100 kRad [2.99], [2.123]. For this class of fiber, the pay-off of reducing the amount of aluminium present is an increase in the measured NF of 1.5 dB [2.123]. This is due to the lack of aluminium which in turn broadens the noise spectra. As a result this will increase the noise power density and therefore degrade the NF. Because of the complex preform doping procedure, it is unclear whether this doping technology can be transferred to EYDFAs.

A different approach, relying on traditional glass radiation hardening techniques, is to co-dope the glass with cerium-ions. Known to provide radiation-hardness since the 1960s [2.124], co-doping glass with cerium ions allows for two oxidation states of cerium to form, Ce^{3+} and Ce^{4+}. The Ce^{3+} ion has been shown to act as trap for

holes, thus addressing the Phosphorus related defects, whilst the Ce^{4+} ion has been shown to act as an electron trap for high energy colour centres found in the UV [2.124]. Co-doping with cerium has been shown to provide no detrimental effects to the spectral performance of either the Er^{3+} or Yb^{3+} ions [2.125], [2.126] suggesting that it can be used in conjunction with EDFAs and EYDFAs.

At the same time as the work completed by Draka, IxFiber (a division of IxBlue Photonics) developed a cerium co-doped EDFA and EYDFA. This fiber has been shown to provided an RIA of 1.6 dB/100 kRad [2.127] for γ-ray irradiation which is an improvement of 2.15 dB/100 kRad when compared to the nano-particle technique.

The final method of co-doping that has been explored is to load the fiber with molecular hydrogen. When the fiber is irradiated and colour centres are formed, the hydrogen atoms can form bonds where the broken bonds lie which have been created by radiation damage. Initially, developed for harsh terrestrial environments such as the nuclear industry, H_2 loaded fibers have been developed by two competing groups in Russia and France [2.127]–[2.130]. Initial work in 2012 showed an improvement in RIA performance, such that an observed RIA of 0.44 dB/100 kRad for a H_2 loaded fiber and 0.22 dB/100 kRad for a H_2 loaded and cerium co-doped fiber was reported [2.127], thus showing an extremely radiation tolerant EDFA and EYDFA.

The major problem of loading fibers with H_2 is that the H_2 will diffuse out of the fiber over time [2.128], [2.129]. To counteract this the use of a hermetic coating of the fiber is suggested. This is a good solution but can now pose a problem in providing a mechanism for the H_2 to be loaded into the fiber at normal temperatures [2.99]. To ensure that the H_2 does not diffuse from the fiber and to ensure homogeneous loading in the fiber, the IxFiber group developed a hole-assisted carbon coated (HACC) fiber [2.130]. A cross section of a HACC fiber is shown in Figure 2.10 showing the holes placed in the cladding to allow loading of the hydrogen from the ends of the fiber preform. This fiber has been shown to provide an RIA of 0.22 dB/100 kRad when being irradiated in an active configuration [2.127] and 1.1 dB/100 kRad whilst not active when being irradiated (worst case scenario)[2.130].

Another way of mitigating RIA is to shorten the fiber length at the expense of

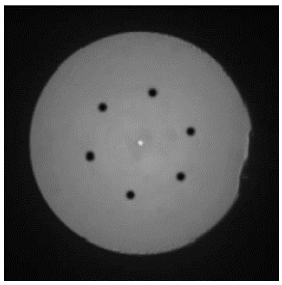

Figure 2.10: Cross-section of a hole-assisted carbon coated fiber. From: [2.130]

amplifier gain [2.97], [2.131]. This occurs due to less fiber being irradiated and therefore a lower amount of colour centres being formed [2.97]. Although this shows a possible way forward it is hard to integrate into a system. One approach presented by Li et al. suggest using EDFAs or different lengths and to switch lengths and pump powers when the fiber becomes irradiated [2.132]. This shows an improvement of reducing RIA by 8 dB when compared to a fixed length and pump power. However, this is not always easy to implement in SWaP constrained systems, such as on small satellites, as this method would require the duplication of components which would greatly damage the SWaP performance of the system.

One final way to reduce the RIA during the operational lifetime of the fiber is to pre-irradiate the fiber. It has been shown that pre-irradiating fiber before it's intended use greatly reduces the RIA when the fiber is irradiated at a later date [2.133]. Although this is a potential technique to use it is not recommended as the fiber would have already degraded from it's performance when pristine; a non-ideal situation. Therefore it would be better to use a radiation hardened fiber.

2.3 Contemporary Satellite Optical Communications Systems

2.3.1 Comparison of RF and Optical Systems

As with terrestrial communications, optical communications has overtaken RF communications as the technology of choice. The main differences between optical and RF communications can be found in the link equation with the inherent shorter wavelength

used by optical communications. The link equation is well known and is given as:

$$P_R = P_T G_T L_{FS} L_{atm} G_R \tag{2.5}$$

Where P_T is the transmitted power, P_R is the received power, G_T and G_R are the transmit and receive antenna gain, L_{FS} and L_{atm} are the free-path space loss and atmospheric loss, respectively. The equation to calculate L_{FS} and both G_T and G_R are given by:

$$G_{(T/R)} = \frac{4\pi A_{(T/R)}}{\lambda_s^2} \tag{2.6}$$

$$L_{FS} = \left(\frac{\lambda_s}{4\pi Z}\right)^2 \tag{2.7}$$

If you combine equation 2.5 with equations 2.6 and 2.7 it can be seen that, $P_R \propto 1/\lambda_s^2$, showing that using shorter signal wavelengths is beneficial to the overall system performance if the other link parameters are kept similar. The ramifications of this result are such that the required transmitter power is lowered, telescope diameters reduced and an increase in data rate is possible if optical communications are chosen over RF communications. Thus showing where improvements in SWaP can be made.

To see the impact this has on overall system performance, it is useful to compare RF and optical systems. A comparison of the technical limitations are shown in Table 2.8. In terms of direct impact on the spacecraft bus in terms of laser terminal SWaP and scenario of a LEO-LEO 2.5 Gbit s^{-1} link; Toyoshima predicts that by using a state-of-the-art RF link would increase the system mass and power consumption by a factor of 2.1-2.4 [2.134] when compared to an optical system.

2.3.2 State-of-the-Art Space-Based Optical Communications Systems

As already mentioned in Section 1.1 research into space laser communications has been occurring since the 1970s [2.6]. More modern activities have been undertaken by three main space agencies: ESA, NASA and JAXA (Japan). This section shall mention some of the key historical systems and current state-of-the-art systems such that a

Parameter	RF	Optical
Wavelength	Typ. 1 cm (Ka-Band)	Typ. 1.5 nm (Optical C-band)
RX noise limitation	Thermally limited, $k_b T = -174$ dB Hz^{-1}	Shot-noise limited, $h\nu = -159$dB Hz^{-1}
Spectrum Regulations	Regulated	Unregulated[1]
Amplifier Technology		
Technology Basis	Transistor or Travelling-Wave Tube	EDFA/EYDFA
Typical Gain	10 dB	50 dB
Bandwidth	$\sim$ 50 GHz	$\sim$ 50 THz
Modulation Formats	Complicated (High order PSK & QAM)	Basic (OOK, PPM, DBPSK)
Waveguide Attributes		
Type	Co-axial Cable	Optical Fiber
Bandwidth	$\sim$ 20 GHz	$\sim$ 50 THz
Loss	100 dB km^{-1}	0.2 dB km^{-1}
Channel Characteristics		
Antenna Gain[1]	30 dB	106 dB
Free-path Space Loss [2]	188 dB	264 dB
Diffraction Angle	10^{-2}/D	10^{-6}/D
Cloud Attenuation	Low	High

[1] Calculated gain in the main beam. Assuming an aperture of 1 cm and wavelengths shown above.
[2] Assuming the wavelengths described above and a link distance of 2000 km (LEO to ground at zenith).
[3] Attempts on a world-wide level are being made to standardise space laser communications. However they are not yet finalised and work is continuing [2.135].

Table 2.8: Comparison of RF and free-space optical communication systems. Adapted from: [2.136].

background to this thesis can be formed.

From Asia, the main push in space laser communications research has come from Japanese institutes such as JAXA and NICT. NICT were the first to demonstrate a GEO to ground, bi-directional link in 1995 at a data rate of 1 Mbit s^{-1} using wavelengths of 800 nm and 500 nm [2.137], [2.138]. The next mission from Japan was a joint mission from JAXA and NICT called the Optical Intersatellite Communication Engineering Test Satellite (OICETS) which was built in partnership with ESA's SILEX program (see below). In 2006, OICETS performed LEO-GEO links with ESA's ARTEMIS laser terminal [2.6] as well as direct downlinks to ground from LEO. OICETS operated at a wavelength of 847 nm and used IM/DD modulation at a data rate of 50 Mbit s^{-1} [2.139], [2.140]. Following the success of OICETS NICT moved forwards in 2014 with the launch of the Small Optical TrAnsponder (SOTA) on-board the micro-satellite, Space Optical Communication Research Advanced Technology Satellite (SOCRATES). SOTA started to show the miniaturisation of space optical terminals with a mass of 5.9 kg and total power consumption of 12.6 W [2.141], thus showing the path forward for future systems. SOTA operated at a wavelength of 1550 nm and 976 nm, using IM/DD modulation formats and a data rate of 10 Mbit s^{-1}. In addition to this, the SOCRATES spacecraft and SOTA terminal provided the capability of providing quantum key distribution, which in turn produced the world first quantum space communications experiment [2.142] in 2017. The work in providing quantum key distribution was quickly followed in the same year by a further demonstration by a Chinese group who successfully generated entangled photons in orbit. The MICIUS experiment demonstrated the distribution via satellite of entangled photon pairs to two separate ground stations via a wavelength of 810 nm from LEO [2.143]. The link operated on wavelengths of 532 nm, 671 nm as beacon channels for tracking such that the pointing and tracking of both the ground station and transmitter could be kept [2.143]. As recently launched in January 2019, NICT has developed the Very Small Optical TrAnsponder (VSOTA). Based on IM/DD modulation at a data rate of 1-100 kbit s^{-1} this LEO to ground downlink demonstrates a very small optical unit (mass < 1 kg and power consumption < 10 W) [2.144] which is encouraging. However, the data rate provided is very low to

be of practicable application, but this is limited by the transmitting telescope which is small for this particular system.

Efforts in the USA have been mostly led by NASA, albeit with some military and commercial interest. Although NASA were involved in demonstrating a GEO-ground link with ETS-VI to the USA through the GOLD program [2.145]; no more demonstrations from the USA came until 2008 with the NFIRE (Near Field InfraRed Experiment) spacecraft. Operating at a wavelength of 1064 nm and modulation scheme of BPSK, this satellite provided a 5.6 Gbit s^{-1} LEO-LEO ISL with the ESA satellite, TerraSAR-X [2.6], as well as LEO downlinks at a later date [2.146]. The next major demonstration held by NASA was the ambitious project of the Lunar Laser Communications Demonstrator (LLCD). Operating in lunar orbit on-board the LADEE spacecraft in 2013, this program demonstrated the first lunar to ground, duplex laser link. This link operated at a wavelength of 1550 nm and provided a 16-PPM 622 Mbit s^{-1} signal [2.147]. One interesting demonstration showed NASA sending files from Massachusetts to New Mexico via the Moon, whilst another demonstration showed the streaming of HD video from the Moon. NASA also pioneered the use of using up-screened COTS components for space optical communications through the demonstrator mission, OPALS, launched in 2014. A demonstrator based on the International Space Station, it provided a 50 Mbit s^{-1}, OOK downlink from LEO at a wavelength of 1550 nm using a mix of previously commercial and space qualified parts, showing the potential of using terrestrial parts in fiber optic space systems [2.148], [2.149].

With a growing interest in space laser communications, commercial entities in the USA started to design and launch their own systems. The Aerospace Corp. have developed two programs for CubeSat based laser communications, a key topic for this thesis, with mixed success. The two programs known as OCSD-A and OCSD-B developed CubeSat LTXs with a wavelength of 1064 nm, output power of up to 4 W, modulation format of OOK and data rate up to 200 Mbit s^{-1} [2.150]. The initial satellite, AeroCube-7A was launched in 2015 but the laser transmitter was not tested due to an attitude control system failure [2.151]. The second wave of spacecraft, AeroCube-7B/7C were launched in 2017 and a successful link at a data rate of 100 Mbit s^{-1}, demonstrat-

ing the world's first laser link from a CubeSat [2.150]. However, this came with a disappointing BER of 10^{-6} [2.150]. This shows that although laser communications via CubeSat is possible, a lot more work is needed to improve the BER of the link. This could be achieved through either improving the link budget, such as through using a larger transmitting or receiving telescope, or changing modulation formats (and therefore decreasing the data rate).

European research into space laser communications has been mostly been pushed forwards by ESA and the German space agency, DLR. European efforts stem from the SILEX program originally set up in 1985. From this program the ARTEMIS laser terminal was developed to be placed on-board the host spacecraft, SPOT-4. It was not until 2001 that a GEO to ground link was demonstrated [2.39] using ARTEMIS; and a GEO-LEO link demonstrated with OICETS in 2005 [2.39]. SILEX was based at a wavelength of 800 nm and used IM/DD (OOK) to provide a data rate of 50 Mbit s^{-1}.

However, the SILEX terminal had a large mass of 157 kg and yet provided an alternative to RF communications, therefore the push for smaller terminals to be used in ISLs were made by ESA [2.6]. With this imperative, ESA in partnership with TESAT Spacecom developed the laser terminal that was placed on the NFIRE satellite (already mentioned) and the German satellite TerraSAR-X to provide a LEO-LEO ISL and also a LEO downlink to ground, all of which were demonstrated in 2008 [2.12]. The link is based upon a wavelength of 1064 nm, BPSK modulation and at a data rate of 5.6 Gbit s^{-1} [2.6], [2.12], [2.146], [2.152]. The laser source was a NPRO Nd:YAG laser providing suitable frequency stability with a high reliability [2.152]. Due to the success of this terminal ESA approved this technology to be the basis for European data relay system (EDRS). Based on the need to provide a high-speed data relay link from ground-LEO-GEO, EDRS was designed to transmit up to 6 Tbit from space to ground per day as European missions previously relied on non-European ground stations to downlink data [2.6]. The EDRS terminals were based upon those used in NFIRE and TerraSAR-X but slightly modified to provide a longer link length (link distance from GEO to ground is $\sim 4.5 \times 10^5$ km). The main differences between the two terminals types are summed up in Table 2.9. Note that only the differences between the two terminal generations

Parameter	**TerraSar-X, NFIRE (Gen 1)**	**Alphasat, EDRS (Gen 2)**
Rx/TX Diameter ($1/e^2$)	125 mm	135 mm
Data rate	5.6 Gbit s^{-1}	1.8 Gbit s^{-1}
Tx Power	1 W	5 W
Link Distance	6000 km	45000 km
Terminal Mass	35 kg	45 kg
Power Consumption	120 W	140 W

Table 2.9: Technical Comparison of the two TESAT LCT generations

are shown, not the whole specification. The first satellite to be launched with this new generation of terminal was Alphasat in 2013. The laser communications terminal was a secondary payload on a GEO communications satellite and was intended to act as the GEO downlink node. The link from Alphasat was tested in 2013 and provided a 1.8 Gbit s^{-1} data rate from GEO orbit [2.153]. Alphasat's partner LCTs were launched upon Sentinel-1A/1B satellites part of ESA's Copernicus program and to be placed into LEO. The first Sentinel satellite was launched in 2014 and link established with Alphasat later that year. No errors were detected in the GEO to LEO link at a data rate of 1.8 Gbit s^{-1} [2.154], [2.155]. Since the successful operation of the terminals on-board Alphasat and Sentinel-1A, further laser terminals have been launched on-board Sentinel-1B and the EDRS-A node on-board the commercial satellite Eutelsat-9B. All EDRS terminals have been in operation and over 17000 successful links have been made, supplying a link availability of $> 99.8\%$ since the start of operations [2.156].

The final European program of note is that of DLR's OSIRIS program. Currently two OSIRIS optical communications terminals are in orbit. Based on a IM/DD modulation scheme and wavelength of 1550 nm, the first terminal OSIRIS-1 has been shown to provide a downlink from LEO at a data rate of 200 Mbit s^{-1} with the capability of scaling the data rate to 1 Gbit s^{-1} [2.157]. The second terminal has not been able to demonstrate a downlink to ground due to problems with the host spacecraft's pointing capabilities [2.157].

Upcoming Space-Based Optical Communications Missions

With the previous success that space-based laser communications has enjoyed, space agencies are planning more missions to provide high speed communications from space. Previously, these laser terminals have been a secondary payload but are now becoming the primary communication method for some of these spacecraft.

In Japan, a new focus is being made on building the Japan Data Relay System (JDRS) with the first terminal currently planned to be launched in 2019 [2.158]. JDRS is designed in a similar way to ESA's EDRS in that it will consist of a LEO-GEO ISL and optical feeder links from GEO to ground [2.159]. The main difference between two systems is that JDRS will operate in the C-band and use differential phase shift keying (DPSK) at a data rate of 1.8 $\mathrm{Gbit\,s^{-1}}$ [2.158]. In addition to JDRS, JAXA are planning to launch a high-throughput satellite in which a 10 $\mathrm{Gbit\,s^{-1}}$ optical GEO-ground feeder link is to be demonstrated; thus facilitating the next generation of high speed laser communications from space [2.160]. This work is currently in the early stages with an anticipated launch in 2021.

American efforts have also been focusing on LEO-GEO ISLs with the Laser Communications Relay Demonstration (LCRD). To be launched on-board a US defence satellite in 2019 [2.40], the LCRD terminal will supply users with a 1.244 $\mathrm{Gbit\,s^{-1}}$ DPSK channel with error coding [2.161]. In addition to improving near-Earth communications, NASA are interested in deep space communications. The Deep Space Optical Communication (DSOC) program will develop a laser communications terminal such that a link can be achieved between an asteroid and Earth. This is not the final aim however, as it is envisioned that this system can then be expanded for supporting 125 $\mathrm{Mbit\,s^{-1}}$ links from Martian orbit [2.162]. Based at 1550 nm (downlink) and 1064 nm (uplink), the initial demonstration is to take place on the PYSCHE mission in which a 200 $\mathrm{Mbit\,s^{-1}}$ link from an asteroid will be provided using PPM [2.163]. Although a lot of effort is being placed in the transmitter development, the main focus is being placed on the development of an advanced photon counting receiver [2.162], [2.163] which are needed to receive extremely low photon counts.

European future missions have mostly been focusing on completing the EDRS sys-

tem and demonstrating high data links from both LEO and GEO. The second EDRS terminal, EDRS-C, is to be launched in 2019 and will operate in the say way as the other EDRS nodes from a GEO orbit [2.164]. DLR are also expanding the OSIRIS program in launching two new terminals: OSIRIS-3 which will be based upon the International Space Station and CubeSat laser transmitter OSIRIS-4, developed in partnership with TESAT [2.157]. Both terminals are designed to operate at 1550 nm with OSIRIS-3 operating with a data rate of 10 Gbit s^{-1} and OSIRIS-4 providing an output power of 100 mW and data rate of 100 Mbit s^{-1} [2.157]. Finally, ESA have embarked on the SeCure and Laser communication technology (Scylight) program in which the High Throughput Optical Network (HydRON) aims to provide Tbit s^{-1} data links from GEO and LEO [2.165]. The first demonstration of HydRON is anticipated to launch in 2022 with the project still currently in the planning and early design stage with no requirements currently available [2.165].

2.4 Summary

In summary this chapter has introduced the key components needed to create a space-based optical communications system and has provided a trade-off analysis based on component suitability for on-board a satellite. The challenges faced by these components are also shown, describing potential damage mechanisms which become important in the later chapters of this thesis. Particular attention has been made on radiation induced attenuation (RIA) and the effect is has on both rare-earth doped fiber optic amplifiers. Some hardening strategies have been introduced which are used within this thesis to assess the suitability of different optical components which could be potentially used within a laser transmitter.

The current status and future for space-based optical communications is very bright, with multiple successful demonstrations and interest not just growing from national space agency but also from commercial entities. Through the miniaturization of laser communication terminals, in the case of this thesis by focusing on the transmitter, this will not just improve the overall SWaP of the system but also push forward the possibilities of what can be achieved in this field.

Based on this work, the rest of this thesis addresses the miniaturization of laser communication terminals through assessing new classes of components for space applications. In addition this thesis will present novel laser communication terminals for space applications up to a TRL level of 5 such that in future work the TRL level can be raised and in turn qualify the units for flight.

References

[2.1] J. M. Senior and M. Y. Jamro, *Optical Fiber Communications Principles and Practice*, Third. Pearson Education, 2009.

[2.2] P. Winzer and R.-J. Essiambre, "Advanced Optical Modulation Formats," *Proceedings of the IEEE*, vol. 94, no. 5, pp. 952–985, 2006. DOI: 10.1109/JPROC.2006.873438.

[2.3] V. Chan, "Optical space communications," *IEEE Journal of Selected Topics in Quantum Electronics*, vol. 6, no. 6, pp. 959–975, 2000. DOI: 10.1109/2944.902144.

[2.4] H. Hemmati, *Near Earth Laser Communications*. CRC Press, 2009, p. 418.

[2.5] P. Fortescue, J. Stark, and G. Swinerd, *Spacecraft Systems Engineering*, 4th. Wiley, 2003.

[2.6] Z. Sodnik, B. Furch, and H. Lutz, "Optical Intersatellite Communication," *IEEE Journal of Selected Topics in Quantum Electronics*, vol. 16, no. 5, pp. 1051–1057, 2010. DOI: 10.1109/JSTQE.2010.2047383.

[2.7] S. Betti, V. Carrozzo, and E. Duca, "Optical Intersatellite System Based on DPSK Modulation," in *2005 2nd International Symposium on Wireless Communication Systems*, IEEE, 2005, pp. 817–821. DOI: 10.1109/ISWCS.2005.1547823.

[2.8] Q. Yang, L. Tan, and J. Ma, "Doppler characterization of laser inter-satellite links for optical LEO satellite constellations," *Optics Communications*, vol. 282, no. 17, pp. 3547–3552, 2009. DOI: 10.1016/j.optcom.2009.05.058.

[2.9] Telcordia, "GR-468 - Generic Reliability Assurance Requirements for Optoelectronic Devices Used in Telecommunications Equipment," Telcordia, Tech. Rep., 2004.

[2.10] Telcordia, "GR-326-CORE - Generic Requirements for Singlemode Optical Connectors and Jumper Assemblies," Telcordia, Tech. Rep., 1999.

[2.11] M. N. Zervas and C. A. Codemard, "High Power Fiber Lasers: A Review," *IEEE Journal of Selected Topics in Quantum Electronics*, vol. 20, no. 5, pp. 219–241, 2014. DOI: 10.1109/JSTQE.2014.2321279.

[2.12] F. Heine, H. Kampfner, R. Czichy, R. Meyer, and M. Lutzer, "Optical inter-satellite communication operational," in *2010 - MILCOM 2010 MILITARY COMMUNICATIONS CONFERENCE*, IEEE, 2010, pp. 1583–1587. DOI: 10.1109/MILCOM.2010.5680175.

[2.13] F. Heine, D. Troendle, C. Rochow, K. Saucke, M. Motzigemba, R. Meyer, *et al.*, "Progressing towards an operational optical data relay service," in *Free-Space Laser Communication and Atmospheric Propagation XXIX*, H. Hemmati and D. M. Boroson, Eds., vol. 10096, International Society for Optics and Photonics, 2017, p. 100960X. DOI: 10.1117/12.2252703.

[2.14] S. Yamakawa, Y. Chishiki, Y. Sasaki, Y. Miyamoto, and H. Kohata, "JAXA's optical data relay satellite programme," in *2015 IEEE International Conference on Space Optical Systems and Applications (ICSOS)*, IEEE, 2015, pp. 1–3. DOI: 10.1109/ICSOS.2015.7425056.

[2.15] K. Kao and G. Hockham, "Dielectric-fibre surface waveguides for optical frequencies," *Proceedings of the Institution of Electrical Engineers*, vol. 113, no. 7, pp. 1151–1158, 1966. DOI: 10.1049/piee.1966.0189.

[2.16] T. Miya, Y. Terunuma, T. Hosaka, and T. Miyashita, "Ultimate low-loss single-mode fibre at 1.55 μm," *Electronics Letters*, vol. 15, no. 4, p. 106, 1979. DOI: 10.1049/el:19790077.

[2.17] S. G. Lambert and W. Casey, *Laser Communications in Space*. Artech House, 1995, p. 390.

[2.18] K. H. Rhew, S. C. Jeon, D. H. Lee, B.-S. Yoo, and I. Yun, "Reliability assessment of 1.55-μm vertical cavity surface emitting lasers with tunnel junction using high-temperature aging tests," *Microelectronics Reliability*, vol. 49, no. 1, pp. 42–50, 2009. DOI: 10.1016/j.microrel.2008.10.008.

[2.19] A. Sirbu, G. Suruceanu, V. Iakovlev, A. Mereuta, Z. Mickovic, A. Caliman, *et al.*, "Reliability of 1310 nm Wafer Fused VCSELs," *IEEE Photonics Technology Letters*, vol. 25, no. 16, pp. 1555–1558, 2013. DOI: 10.1109/LPT.2013.2271041.

[2.20] C. Henry, "Theory of the linewidth of semiconductor lasers," *IEEE Journal of Quantum Electronics*, vol. 18, no. 2, pp. 259–264, 1982. DOI: 10.1109/JQE.1982.1071522.

[2.21] M. Alalusi, P. Brasil, S. Lee, P. Mols, L. Stolpner, A. Mehnert, *et al.*, "Low noise planar external cavity laser for interferometric fiber optic sensors," in *Proceedings Volume 7316, Fiber Optic Sensors and Applications VI*, E. Udd, H. H. Du, and A. Wang, Eds., vol. 7316, 2009, p. 73160X. DOI: 10.1117/12.828849.

[2.22] K. Numata, J. Camp, M. Krainak, and L. Stolpner, "Performance of planar-waveguide external cavity laser for precision measurements," *Optics Express*, vol. 18, no. 22, p. 22 781, Oct. 2010. DOI: 10.1364/OE.18.022781.

[2.23] K. Numata, M. Alalusi, L. Stolpner, G. Margaritis, J. Camp, and M. Krainak, "Characteristics of the single-longitudinal-mode planar-waveguide external cavity diode laser at 1064 nm," *Optics Letters*, vol. 39, no. 7, p. 2101, Apr. 2014. DOI: 10.1364/OL.39.002101.

[2.24] L. Coldren, "Monolithic tunable diode lasers," *IEEE Journal of Selected Topics in Quantum Electronics*, vol. 6, no. 6, pp. 988–999, Nov. 2000. DOI: 10.1109/2944.902147.

[2.25] Y. Kotaki and H. Ishikawa, "Wavelength tunable DFB and DBR lasers for coherent optical fibre communications," *IEE Proceedings J Optoelectronics*, vol. 138, no. 2, p. 171, 1991. DOI: 10.1049/ip-j.1991.0030.

[2.26] T. J. Kane and R. L. Byer, "Monolithic, unidirectional single-mode Nd:YAG ring laser," *Optics Letters*, vol. 10, no. 2, p. 65, Feb. 1985. DOI: 10.1364/OL.10.000065.

[2.27] F. Heine, T. Schwander, R. Lange, and B. Smutny, "Space qualified laser sources," no. April 2006, p. 61892I, 2006. DOI: 10.1117/12.678601.

[2.28] M. Gregory, "Commercial optical inter-satellite communication at high data rates," *Optical Engineering*, vol. 51, no. 3, p. 031 202, Mar. 2012. DOI: 10.1117/1.OE.51.3.031202.

[2.29] G. Baister, T. Dreischer, E. Rugi Grond, L. Gallmann, B. Thieme, and K. Kudielka, "The OPTEL Terminal Development Programme - Enabling Technologies for Future Optical Crosslink Applications," in *AIAA Space 2003 Conference & Exposition*, Reston, Virigina: American Institute of Aeronautics and Astronautics, Sep. 2003. DOI: 10.2514/6.2003-6229.

[2.30] N. W. Sawruk, P. M. Burns, R. E. Edwards, T. Wysocki, A. VanTuijl, V. Litvinovitch, *et al.*, "ICESat-2 laser technology readiness level evolution," in *Solid State Lasers XXIV: Technology and Devices*, W. A. Clarkson and R. K. Shori, Eds., vol. 9342, Feb. 2015, p. 93420L. DOI: 10.1117/12.2080531.

[2.31] K. Nicklaus, N. Beller, O. Fitzau, M. Giesberts, G. P. Barwood, R. A. Williams, *et al.*, "High stability laser for next generation gravity missions," in *International Conference on Space Optics — ICSO 2014*, B. Cugny, Z. Sodnik, and N. Karafolas, Eds., vol. 10563, SPIE, Nov. 2014, p. 101. DOI: 10.1117/12.2304161.

[2.32] E. Clements, R. Aniceto, D. Barnes, D. Caplan, J. Clark, I. del Portillo, *et al.*, "Nanosatellite optical downlink experiment: design, simulation, and prototyping," *Optical Engineering*, vol. 55, no. 11, p. 111 610, Sep. 2016. DOI: 10.1117/1.OE.55.11.111610.

[2.33] R. Kingsbury, "Optical Communications for Small Satellites," Ph.D. dissertation, Massachusetts Institute of Technology, 2015.

[2.34] T. S. Rose, S. W. Janson, S. LaLumondiere, N. Werner, D. H. Hinkley, D. W. Rowen, *et al.*, "LEO to ground optical communications from a small satellite platform," H. Hemmati and D. M. Boroson, Eds., vol. 9354, Mar. 2015, p. 93540I. DOI: 10.1117/12.2087275.

[2.35] E. Wooten, K. Kissa, A. Yi-Yan, E. Murphy, D. Lafaw, P. Hallemeier, *et al.*, "A review of lithium niobate modulators for fiber-optic communications systems," *IEEE Journal of Selected Topics in Quantum Electronics*, vol. 6, no. 1, pp. 69–82, 2000. DOI: 10.1109/2944.826874.

[2.36] Y. Fu, X. Zhang, B. Hraimel, T. Liu, and D. Shen, "Mach-Zehnder: A Review of Bias Control Techniques for Mach-Zehnder Modulators in Photonic Analog Links," *IEEE Microwave Magazine*, vol. 14, no. 7, pp. 102–107, Nov. 2013. DOI: 10.1109/MMM.2013.2280332.

[2.37] IXblue, *Analog LiNbO3 modulators and matching components*, Paris, 2016.

[2.38] H. Porte and P. Le Roux, "LiNbO3 for Space Environment," iXblue, Paris, Tech. Rep., 2016.

[2.39] Z. Sodnik, B. Furch, and H. Lutz, "Free-Space Laser Communication Activities in Europe: SILEX and beyond," in *LEOS 2006 - 19th Annual Meeting of the IEEE Lasers and Electro-Optics Society*, vol. 1, IEEE, 2006, pp. 78–79. DOI: 10.1109/LEOS.2006.278845.

[2.40] D. M. Cornwell, "NASA's optical communications program for 2015 and beyond," in *Proc. SPIE 9354, Free-Space Laser Communication and Atmospheric Propagation XXVII*, H. Hemmati and D. M. Boroson, Eds., Mar. 2015, 93540E. DOI: 10.1117/12.2087132.

[2.41] W. J. Thomes Jr., F. V. LaRocca, M. N. Ott, X. L. Jin, R. F. Chuska, S. L. MacMurphy, *et al.*, "Investigation of hermetically sealed commercial LiNbO3 optical modulator for use in laser/LIDAR space-flight applications," *Proceedings of SPIE*, vol. 6713, no. 1, 67130T, 2007. DOI: doi:10.1117/12.732525.

[2.42] J. G. Mendoza-Alvarez, R. H. Yan, and L. A. Coldren, "Contribution of the band-filling effect to the effective refractive-index change in double-heterostructure GaAs/AlGaAs phase modulators," *Journal of Applied Physics*, vol. 62, no. 11, pp. 4548–4553, Dec. 1987. DOI: 10.1063/1.339048.

[2.43] C. Rolland, R. Moore, F. Shepherd, and G. Hillier, "10 Gbit/s, 1.56 μm multiquantum well InP/InGaAsP Mach–Zehnder optical modulator," *Electronics Letters*, vol. 29, no. 5, p. 471, 1993. DOI: 10.1049/el:19930315.

[2.44] R. G. Walker, M. F. O'Keefe, N. Cameron, H. Ereifej, and T. Brast, "Gallium Arsenide Electro-Optic Modulators," *2014 IEEE Compound Semiconductor Integrated Circuit Symposium (CSICS)*, pp. 1–4, 2014. DOI: 10.1109/CSICS.2014.6978557.

[2.45] Y. Ueda, Y. Ogiso, and N. Kikuchi, "InP PIC technologies for high-performance Mach-Zehnder modulator," in *Optical Metro Networks and Short-Haul Systems IX*, A. K. Srivastava, B. B. Dingel, and Y. Akasaka, Eds., vol. 10129, International Society for Optics and Photonics, Jan. 2017, p. 1 012 905. DOI: 10.1117/12.2253492.

[2.46] K. Petermann, *Laser Diode Modulation and Noise*, Illustrate. Dordrecht: Springer Netherlands, 1988, pp. 88–91. DOI: 10.1007/978-94-009-2907-4.

[2.47] B. Edwards, "Overview of the Laser Communications Relay Demonstration Project," in *SpaceOps 2012 Conference*, Reston, Virigina: American Institute of Aeronautics and Astronautics, Jun. 2012, pp. 1–11. DOI: 10.2514/6.2012-1261897.

[2.48] R. G. Walker, N. Cameron, Y. Zhou, and S. Clements, "Electro-optic modulators for space using gallium arsenide," in *International Conference on Space Optics — ICSO 2016*, N. Karafolas, B. Cugny, and Z. Sodnik, Eds., SPIE, Sep. 2017, p. 185. DOI: 10.1117/12.2296173.

[2.49] D. R. Zimmerman and L. H. Spiekman, "Amplifiers for the Masses: EDFA, EDWA, and SOA Amplets for Metro and Access Applications," *Journal of*

Lightwave Technology, vol. 22, no. 1, pp. 63–70, 2004. DOI: 10.1109/JLT.2003.822144.

[2.50] L. Stampoulidis, J. Edmunds, M. Kechagias, G. Stevens, J. Farzana, M. Welch, *et al.*, "Radiation-resistant optical fiber amplifiers for satellite communications," in *SPIE 10096, Free-Space Laser Communication and Atmospheric Propagation XXIX*, H. Hemmati and D. M. Boroson, Eds., Feb. 2017, 100960H. DOI: 10.1117/12.2252086.

[2.51] L. Stampoulidis, E. Kehayas, M. Kehayas, G. Stevens, L. Henwood-Moroney, P. Hosking, *et al.*, "Radiation-hard Mid-power Booster Optical Fiber Amplifiers for High-speed Digital and Analogue Satellite Laser Communication Links," in *International Conference on Space Optics*, 2014.

[2.52] E. Kehayas, J. Edmunds, M. Welch, M. Tuci, C. Palmer, K. Simpson, *et al.*, "Space qualification of multi-channel optical fiber amplifier for low Earth orbit satellite-to-ground direct downlinks," in *Free-Space Laser Communication and Atmospheric Propagation XXX*, H. Hemmati and D. M. Boroson, Eds., San Francisco: SPIE, Feb. 2018, p. 35. DOI: 10.1117/12.2289664.

[2.53] R. Paschotta, J. Nilsson, A. Tropper, and D. Hanna, "Ytterbium-doped fiber amplifiers," *IEEE Journal of Quantum Electronics*, vol. 33, no. 7, pp. 1049–1056, 1997. DOI: 10.1109/3.594865.

[2.54] E. Desurvire, *Erbium-doped fiber amplifiers: principles and applications*, Illustrate. Wiley-Interscience, 2002.

[2.55] A. Polman and F. C. J. M. van Veggel, "Broadband sensitizers for erbium-doped planar optical amplifiers: review," *Journal of the Optical Society of America B*, vol. 21, no. 5, p. 871, May 2004. DOI: 10.1364/JOSAB.21.000871.

[2.56] M. Ott, "Capabilites and Reliability of LEDs and Laser Diodes," *Internal NASA Parts and Packaging Publication*, 1996.

[2.57] S. L. Yellen, A. H. Shepard, R. J. Dalby, J. A. Baumann, H. B. Serreze, T. S. Guido, *et al.*, "Reliability of GaAs-Based Semiconductor Diode Lasers: 0.6–1.1 µm," *IEEE Journal of Quantum Electronics*, vol. 29, no. 6, pp. 2058–2067, 1993. DOI: 10.1109/3.234469.

[2.58] J. Koponen, M. Söderlund, H. J. Hoffman, D. a. V. Kliner, J. P. Koplow, and M. Hotoleanu, "Photodarkening rate in Yb-doped silica fibers," *Applied Optics*, vol. 47, no. 9, pp. 1247–1256, 2008. DOI: 10.1364/AO.47.001247.

[2.59] E. Desurvire, J. R. Simpson, and P. C. Becker, "High-gain erbium-doped traveling-wave fiber amplifier," *Optics Letters*, vol. 12, no. 11, p. 888, Nov. 1987. DOI: 10.1364/OL.12.000888.

[2.60] R. J. Mears, L. Reekie, I. M. Jauncey, and D. N. Payne, "High-gain rare-earth-doped fiber amplifier at 1.54 μm," in *Optical Fiber Communication*, Washington, D.C.: OSA, 1987, WI2. DOI: 10.1364/OFC.1987.WI2.

[2.61] J. Bradley and M. Pollnau, "Erbium-doped integrated waveguide amplifiers and lasers," *Laser & Photonics Reviews*, vol. 5, no. 3, pp. 368–403, May 2011. DOI: 10.1002/lpor.201000015.

[2.62] C. Giles and E. Desurvire, "Modeling erbium-doped fiber amplifiers," *Journal of Lightwave Technology*, vol. 9, no. 2, pp. 271–283, 1991. DOI: 10.1109/50.65886.

[2.63] H. Haus, "The noise figure of optical amplifiers," *IEEE Photonics Technology Letters*, vol. 10, no. 11, pp. 1602–1604, Nov. 1998. DOI: 10.1109/68.726763.

[2.64] E. Desurvire, "Comments on "The noise figure of optical amplifiers"," *IEEE Photonics Technology Letters*, vol. 11, no. 5, pp. 620–621, May 1999. DOI: 10.1109/68.759418.

[2.65] D. M. Baney, P. Gallion, and R. S. Tucker, "Theory and Measurement Techniques for the Noise Figure of Optical Amplifiers," *Optical Fiber Technology*, vol. 6, no. 2, pp. 122–154, Apr. 2000. DOI: 10.1006/ofte.2000.0327.

[2.66] BSI, *BS EN IEC 61291-1:2018*, 1st ed. BSI, 2018, pp. 13–14.

[2.67] M. A. Krainak, M. A. Stephen, E. Troupaki, S. A. Tedder, B. Reyna, J. Klamkin, *et al.*, "Integrated photonics for NASA applications," in *Components and Packaging for Laser Systems V*, A. L. Glebov and P. O. Leisher, Eds., SPIE, Mar. 2019, p. 14. DOI: 10.1117/12.2509808.

[2.68] J. Fridlander, S. Pinna, V. Rosborough, S. Estrella, L. Johansson, and J. Klamkin, "RZ-DPSK photonic integrated transmitter for space optical communications," in *Free-Space Laser Communication and Atmospheric Propagation XXX*, H. Hemmati and D. M. Boroson, Eds., vol. 10524, SPIE, Feb. 2018, p. 34. DOI: 10.1117/12.2287557.

[2.69] C. Wang, M. Zhang, X. Chen, M. Bertrand, A. Shams-Ansari, S. Chandrasekhar, *et al.*, "Integrated lithium niobate electro-optic modulators operating at CMOS-compatible voltages," *Nature*, p. 1, Sep. 2018. DOI: 10.1038/s41586-018-0551-y.

[2.70] W. Larson and J. R. Wertz, *Space Mission Analysis and Design*, 2nd, ser. Space Technology Library. Springer Netherlands, 1991.

[2.71] R. Longstaff and A. Bond, "The SKYLON Project," in *17th AIAA International Space Planes and Hypersonic Systems and Technologies Conference*, ser. International Space Planes and Hypersonic Systems and Technologies Conferences, American Institute of Aeronautics and Astronautics, Apr. 2011. DOI: doi:10.2514/6.2011-2244.

[2.72] Arianespace, "Ariane 5 User's Manual," Arianespace, Evry-Courcouronnes, Tech. Rep. 5, 2016.

[2.73] A. Holmes-Siedle and L. Adams, *Handbook of radiation effects*, 2nd Ed. New York, NY (United States); Oxford University Press Inc., 2002.

[2.74] H. Barnaby and M. Marinella, "Total Ionizing Dose and Displacement Damage Effects in Embedded Memory Technologies," *RADECS 2013 Short Course*, 2013.

[2.75] J. A. Van Allen and L. A. Frank, "Radiation Around the Earth to a Radial Distance of 107,400 km.," *Nature*, vol. 183, no. 4659, pp. 430–434, Feb. 1959. DOI: 10.1038/183430a0.

[2.76] E. Fiandrini, "Protons with kinetic energy E 70 MeV trapped in the Earth's radiation belts," *Journal of Geophysical Research*, vol. 109, no. A10, A10214, 2004. DOI: 10.1029/2004JA010394.

[2.77] D. M. Hassler, "Solar Wind Outflow and the Chromospheric Magnetic Network," en, *Science*, vol. 283, no. 5403, pp. 810–813, Feb. 1999. DOI: 10.1126/science.283.5403.810.

[2.78] T. Howard, *Coronal Mass Ejections*, ser. Astrophysics and Space Science Library. New York, NY: Springer New York, 2011, vol. 376. DOI: 10.1007/978-1-4419-8789-1.

[2.79] G. Borrini, J. T. Gosling, S. J. Bame, and W. C. Feldman, "Helium abundance variations in the solar wind," *Solar Physics*, vol. 83, no. 2, pp. 367–378, Mar. 1983. DOI: 10.1007/BF00148286.

[2.80] E. E. Fenimore, "Solar wind flows associated with hot heavy ions," en, *The Astrophysical Journal*, vol. 235, p. 245, Jan. 1980. DOI: 10.1086/157628.

[2.81] S. W. Kahler, "Solar Flares and Coronal Mass Ejections," en, *Annual Review of Astronomy and Astrophysics*, vol. 30, no. 1, pp. 113–141, Sep. 1992. DOI: 10.1146/annurev.aa.30.090192.000553.

[2.82] O. Adriani and E. al., "PAMELA measurements of cosmic-ray proton and helium spectra.," en, *Science (New York, N.Y.)*, vol. 332, no. 6025, pp. 69–72, Apr. 2011. DOI: 10.1126/science.1199172.

[2.83] M. Ackermann, M. Ajello, A. Allafort, and E. al., "Detection of the characteristic pion-decay signature in supernova remnants.," en, *Science (New York, N.Y.)*, vol. 339, no. 6121, pp. 807–11, Feb. 2013. DOI: 10.1126/science.1231160.

[2.84] P. Canon, M. Angling, L. Barclay, C. Curry, C. Dyer, R. Edwards, *et al.*, "Extreme Space Weather: Impacts on engineered systems and infrastructure," Royal Academy of Engineering, London, Tech. Rep., Feb. 2013.

[2.85] C. Dale, P. Marshall, E. Burke, G. Summers, and E. Wolicki, "High energy electron induced displacement damage in silicon," *IEEE Transactions on Nuclear Science*, vol. 35, no. 6, pp. 1208–1214, 1988. DOI: 10.1109/23.25441.

[2.86] A. Johnston, B. Rax, L. Selva, and C. Barnes, "Proton degradation of light-emitting diodes," *IEEE Transactions on Nuclear Science*, vol. 46, no. 6, pp. 1781–1789, 1999. DOI: 10.1109/23.819154.

[2.87] J. MacDougall, P. Henderson, P. Naylor, J. Elder, A. Norman, I. Turner, *et al.*, "Transmission and pump laser modules for space applications," H. Hemmati and D. M. Boroson, Eds., Feb. 2017, p. 100960I. DOI: 10.1117/12.2252150.

[2.88] M. A. Cappelletti, A. P. Cédola, and E. L. Peltzer Y Blancá, "Simulation of silicon PIN photodiodes for use in space-radiation environments," *Semiconductor Science and Technology*, vol. 23, no. 2, 2008. DOI: 10.1088/0268-1242/23/2/025007.

[2.89] J. Bogaerts, B. Dierickx, G. Meynants, and D. Uwaerts, "Total dose and displacement damage effects in a radiation-hardened CMOS APS," *IEEE Transactions on Electron Devices*, vol. 50, no. 1, pp. 84–90, 2003. DOI: 10.1109/TED.2002.807251.

[2.90] D. Nikolić, A. Vasić, I. Fetahović, K. Stanković, and P. Osmokrović, "Photodiode Behavior in Radiation Environment," *Scientific Publications of the State University of Novi Pazar Series A: Applied Mathematics, Informatics and mechanics*, vol. 3, no. 1, pp. 27–34, 2011.

[2.91] F. Gonthier, V. Poenariu, J. Chu, D. Snejko, J. Lavoie, P. Murzionak, *et al.*, "1550 Nm Combined Transmission Booster Amplifier and Receiver Preamplifier for Satellite To Satellite Laser Communication," in

International Conference on Space Optics (ICSO) 2018, Z. Sodnik and B. Cugny, Eds., Chania: European Space Agency (ESA), 2018.

[2.92] J. Barbero and E. Cordero, "ITT 7524 Space validation of Rad-Hard Erbium Optical Fibre," Alter Technology, Madrid, Tech. Rep., 2017.

[2.93] J. J. Jiménez, J. Sánchez-Páramo, M. T. Álvarez, J. A. Domínguez, J. M. Oter, I. Arruego, *et al.*, "Proton radiation effects on medium/large area Si PIN photodiodes for Optical Wireless Links for Intra-Satellite Communications (OWLS)," *IEEE Radiation Effects Data Workshop*, pp. 73–79, 2007. DOI: 10.1109/REDW.2007.4342543.

[2.94] B. P. Fox, K. Simmons-Potter, D. A. Kliner, and S. W. Moore, "Effect of low-earth orbit space on radiation-induced absorption in rare-earth-doped optical fibers," *Journal of Non-Crystalline Solids*, vol. 378, pp. 79–88, 2013. DOI: 10.1016/j.jnoncrysol.2013.06.009.

[2.95] J. Lee, K. Lee, Y. S. Jang, H. Jang, S. Han, S. H. Lee, *et al.*, "Testing of a femtosecond pulse laser in outer space," *Scientific Reports*, vol. 4, pp. 4–10, 2014. DOI: 10.1038/srep05134.

[2.96] S. Girard, J. Kuhnhenn, A. Gusarov, B. Brichard, M. Van Uffelen, Y. Ouerdane, *et al.*, "Radiation effects on silica-based optical fibers: Recent advances and future challenges," *IEEE Transactions on Nuclear Science*, vol. 60, no. 3, pp. 2015–2036, Jun. 2013. DOI: 10.1109/TNS.2012.2235464.

[2.97] A. Gusarov, M. Van Uffelen, M. Hotoleanu, H. Thienpont, and F. Berghmans, "Radiation sensitivity of EDFAs based on highly Er-doped fibers," *Journal of Lightwave Technology*, vol. 27, no. 11, pp. 1540–1545, 2009. DOI: 10.1109/JLT.2009.2014255.

[2.98] B. Brichard, A. F. Fernandez, H. Ooms, and F. Berghmans, "Gamma dose rate effect in erbium-doped fibers for space gyroscopes," *Proc. of the 16th International Conference on Optical Fiber Sensors*, pp. 336–339, 2003.

[2.99] S. Girard, A. Morana, A. Ladaci, T. Robin, L. Mescia, J.-J. Bonnefois, *et al.*, "Recent advances in radiation-hardened fiber-based technologies for space applications," *Journal of Optics*, vol. 20, no. 9, p. 093 001, Sep. 2018. DOI: 10.1088/2040-8986/aad271.

[2.100] M. N. Ott, "Radiation effects data on commercially available optical fiber: Database summary Update 2008," Tech. Rep., 2008.

[2.101] V. B. Neustruev, "Colour centres in germanosilicate glass and optical fibres," *Journal of Physics: Condensed Matter*, vol. 6, no. 35, pp. 6901–6936, Aug. 1994. DOI: 10.1088/0953-8984/6/35/003.

[2.102] S. Girard, J. Baggio, and J. Bisutti, "14-MeV Neutron, Gamma-Ray, and Pulsed X-Ray Radiation-Induced Effects on Multimode Silica-Based Optical Fibers," *IEEE Transactions on Nuclear Science*, vol. 53, no. 6, pp. 3750–3757, Dec. 2006. DOI: 10.1109/TNS.2006.886222.

[2.103] D. L. Griscom, E. J. Friebele, K. J. Long, and J. W. Fleming, "Fundamental defect centers in glass: Electron spin resonance and optical absorption studies of irradiated phosphorus-doped silica glass and optical fibers," *Journal of Applied Physics*, vol. 54, no. 7, pp. 3743–3762, 1983. DOI: 10.1063/1.332591.

[2.104] S. Girard, B. Tortech, E. Regnier, M. Van Uffelen, A. Gusarov, Y. Ouerdane, *et al.*, "Proton- and Gamma-Induced Effects on Erbium-Doped Optical Fibers," *IEEE Transactions on Nuclear Science*, vol. 54, no. 6, pp. 2426–2434, Dec. 2007. DOI: 10.1109/TNS.2007.910859.

[2.105] T. Rose, D. Gunn, and G. Valley, "Gamma and proton radiation effects in erbium-doped fiber amplifiers: active and passive measurements," *Journal of Lightwave Technology*, vol. 19, no. 12, pp. 1918–1923, 2001. DOI: 10.1109/50.971685.

[2.106] M. Ott, "Radiation Effects Expected for Fiber Laser/Amplifier Rare Earth Doped Optical Fiber," NASA, Tech. Rep., 2004.

[2.107] B. Tortech, Y. Ouerdane, S. Girard, J.-P. Meunier, A. Boukenter, T. Robin, *et al.*, "Radiation effects on Yb- and Er/Yb-doped optical fibers: A micro-luminescence study," *Journal of Non-Crystalline Solids*, vol. 355, no. 18-21, pp. 1085–1088, Jul. 2009. DOI: 10.1016/j.jnoncrysol.2009.01.055.

[2.108] D. L. Griscom, M. E. Gingerich, and E. J. Friebele, "Model for the Dose, Dose-Rate and Temperature Dependence of Radiation-Induced Loss in Optical Fibers," *IEEE Transactions on Nuclear Science*, vol. 41, no. 3, pp. 523–527, Jun. 1994. DOI: 10.1109/23.299793.

[2.109] T. Wijnands, L. K. De Jonge, J. Kuhnhenn, S. K. Hoeffgen, and U. Weinand, "Optical absorption in commercial single mode optical fibers in a high energy physics radiation field," in *IEEE Transactions on Nuclear Science*, vol. 55, 2008, pp. 2216–2222. DOI: 10.1109/TNS.2008.2001859.

[2.110] S. Girard, Y. Ouerdane, B. Tortech, C. Marcandella, T. Robin, B. Cadier, *et al.*, "Radiation Effects on Ytterbium- and Ytterbium/Erbium-Doped Double-Clad Optical Fibers," *IEEE Transactions on Nuclear Science*, vol. 56, no. 6, pp. 3293–3299, Dec. 2009. DOI: 10.1109/TNS.2009.2033999.

[2.111] A. T. Ramsey, W. Tighe, J. Bartolick, and P. D. Morgan, "Radiation effects on heated optical fibers," *Review of Scientific Instruments*, vol. 68, no. 1, pp. 632–635, Jan. 1997. DOI: 10.1063/1.1147670.

[2.112] S. Girard, C. Marcandella, A. Morana, J. Perisse, D. Di Francesca, P. Paillet, *et al.*, "Combined High Dose and Temperature Radiation Effects on Multimode Silica-Based Optical Fibers," *IEEE Transactions on Nuclear Science*, vol. 60, no. 6, pp. 4305–4313, Dec. 2013. DOI: 10.1109/TNS.2013.2281832.

[2.113] European Space Agency (ESA), "ESCC Basic Specification No. 23202 - Validation and Lot Acceptance Testing Guidelines for Laser Diodes," 2018.

[2.114] European Space Agency (ESA), "ESCC Basic Specification No. 23201 - Evaluation Test Programme Guidelines for Laser Diode Modules," 2014.

[2.115] F. Berghmans, S. Eve, and M. Held, "An Introduction to Reliability of Optical Components and Fiber Optic Sensors," in *Optical Waveguide Sensing and Imaging*, ser. NATO Science for Peace and Security Series August 2014, W. J. Bock, I. Gannot, and S. Tanev, Eds., Dordrecht: Springer Netherlands, 2008, pp. 73–100. DOI: 10.1007/978-1-4020-6952-9_4.

[2.116] United States Department of Defense, "MIL-STD-883K Test Method Standard Microcircuits," 2017.

[2.117] B. Cadier, R. Montron, T. Gotter, P. Guitton, A. Laurent, A. Barnini, *et al.*, "Evidence of photo-darkening in co-doped erbium-ytterbium double-clad fibers operated at high-output power," in *Optical Components and Materials XV*, M. J. Digonnet and S. Jiang, Eds., vol. 10528, SPIE, Feb. 2018, p. 42. DOI: 10.1117/12.2290947.

[2.118] A. Ladaci, S. Girard, L. Mescia, T. Robin, A. Laurent, B. Cadier, *et al.*, "Optimized radiation-hardened erbium doped fiber amplifiers for long space missions," *Journal of Applied Physics*, vol. 121, no. 16, p. 163 104, Apr. 2017. DOI: 10.1063/1.4981532.

[2.119] A. Ladaci, S. Girard, L. Mescia, T. Robin, A. Laurent, B. Cadier, *et al.*, "Optimization of rare-earth-doped amplifiers for space mission through a hardening-by-system strategy," in *SPIE 10096, Free-Space Laser Communication and Atmospheric Propagation XXIX*, H. Hemmati and D. M. Boroson, Eds., vol. 10096, Feb. 2017, 100960F. DOI: 10.1117/12.2249284.

[2.120] E. Haddad, V. Poenariu, K. Tagziria, W. Shi, C. Chilian, N. Karafolas, *et al.*, "Comparison of gamma radiation effect on erbium doped fiber amplifiers," in *International Conference on Space Optics — ICSO 2016*, N. Karafolas, B. Cugny, and Z. Sodnik, Eds., SPIE, Oct. 2016, p. 202. DOI: 10.1117/12.2296186.

[2.121] E. J. Friebele and M. E. Gingerich, "Photobleaching effects in optical fiber waveguides," *Applied Optics*, vol. 20, no. 19, p. 3448, Oct. 1981. DOI: 10.1364/AO.20.003448.

[2.122] K. V. Zotov, M. E. Likhachev, A. L. Tomashuk, A. F. Kosolapov, M. M. Bubnov, M. V. Yashkov, *et al.*, "Radiation Resistant Er-Doped Fibers: Optimization of Pump Wavelength," *IEEE Photonics Technology Letters*, vol. 20, no. 17, pp. 1476–1478, Sep. 2008. DOI: 10.1109/LPT.2008.927909.

[2.123] J. Thomas, E. Burov, P. Signoret, G. Mélin, A. Pastouret, M. Sotom, *et al.*, "Radiation-resistant erbium-doped-nanoparticles optical fiber for space applications," *Optics Express*, vol. 20, no. 3, p. 2435, 2012. DOI: 10.1364/oe.20.002435.

[2.124] J. S. Stroud, "Color Centers in a Cerium-Containing Silicate Glass," *The Journal of Chemical Physics*, vol. 37, no. 4, pp. 836–841, Aug. 1962. DOI: 10.1063/1.1733170.

[2.125] M. Vivona, S. Girard, C. Marcandella, T. Robin, B. Cadier, M. Cannas, *et al.*, "Influence of Ce codoping and H2 pre-loading on Er/Yb-doped fiber: Radiation response characterized by Confocal Micro-Luminescence," *Journal of Non-Crystalline Solids*, vol. 357, no. 8-9, pp. 1963–1965, Apr. 2011. DOI: 10.1016/j.jnoncrysol.2010.10.039.

[2.126] M. Vivona, S. Girard, T. Robin, B. Cadier, L. Vaccaro, M. Cannas, *et al.*, "Influence of Ce3+ Codoping on the Photoluminescence Excitation Channels of Phosphosilicate Yb/Er-Doped Glasses," *IEEE Photonics Technology Letters*, vol. 24, no. 6, pp. 509–511, 2012. DOI: 10.1109/LPT.2011.2182644.

[2.127] S. Girard, M. Vivona, A. Laurent, B. Cadier, C. Marcandella, T. Robin, *et al.*, "Radiation hardening techniques for Er/Yb doped optical fibers and amplifiers for space application," *Optics Express*, vol. 20, no. 8, pp. 8457–8465, Apr. 2012. DOI: 10.1364/OE.20.008457.

[2.128] K. V. Zotov, M. E. Likhachev, A. L. Tomashuk, M. M. Bubnov, M. V. Yashkov, and A. N. Gur'yanov, "Radiation-resistant erbium-doped

silica fibre," *Quantum Electronics*, vol. 37, no. 10, pp. 946–949, Oct. 2007. DOI: 10.1070/QE2007v037n10ABEH013660.

[2.129] K. V. Zotov, M. E. Likhachev, A. L. Tomashuk, M. M. Bubnov, M. V. Yashkov, A. N. Guryanov, *et al.*, "Radiation-Resistant Erbium-Doped Fiber for Spacecraft Applications," *IEEE Transactions on Nuclear Science*, vol. 55, no. 4, pp. 2213–2215, Aug. 2008. DOI: 10.1109/TNS.2008.2001834.

[2.130] S. Girard, A. Laurent, E. Pinsard, T. Robin, B. Cadier, M. Boutillier, *et al.*, "Radiation-hard erbium optical fiber and fiber amplifier for both low- and high-dose space missions," *Optics Letters*, vol. 39, no. 9, p. 2541, May 2014. DOI: 10.1364/OL.39.002541.

[2.131] R. Dardaillon, J. Thomas, M. Myara, S. Blin, A. Pastouret, C. Gonnet, *et al.*, "Broadband Radiation-Resistant Erbium-Doped Optical Fibers for Space Applications," *IEEE Transactions on Nuclear Science*, vol. 64, no. 6, pp. 1540–1548, 2017. DOI: 10.1109/TNS.2017.2701550.

[2.132] Mi Li, Wenxiang Jiao, Yuejiang Song, Xuping Zhang, and Lingqian Chang, "Self-Adaptive High Anti-Radiation EDFA for Space Optical Communication Systems," EN, *Journal of Lightwave Technology*, vol. 33, no. 21, pp. 4513–4516, Nov. 2015. DOI: 10.1109/JLT.2015.2478805.

[2.133] D. L. Griscom, "Radiation hardening of pure-silica-core optical fibers: Reduction of induced absorption bands associated with self-trapped holes," *Applied Physics Letters*, vol. 71, no. 2, pp. 175–177, Jul. 1997. DOI: 10.1063/1.119493.

[2.134] M. Toyoshima, "Trends in satellite communications and the role of optical free-space communications," *Journal of Optical Networking*, vol. 4, no. 6, p. 300, 2005. DOI: 10.1364/JON.4.000300.

[2.135] B. L. Edwards, R. Daddato, K. J. Schulz, C. Schmidt, J. Hamkins, D. Giggenbach, *et al.*, "An update on the CCSDS optical communications working group," *2017 IEEE International Conference on Space Optical*

Systems and Applications, ICSOS 2017, pp. 1–9, 2018. DOI: 10.1109/ICSOS.2017.8357202.

[2.136] D. O. Caplan, "Laser communication transmitter and receiver design," *Journal of Optical and Fiber Communications Reports*, vol. 4, no. 4-5, pp. 225–362, Sep. 2007. DOI: 10.1007/s10297-006-0079-z.

[2.137] Y. Arimoto, M. Toyoshima, M. Toyoda, T. Takahashi, M. Shikatani, and K. Araki, "Preliminary result on laser communication experiment using (ETS-VI)," in *Free-Space Laser Communication Technologies VII*, G. S. Mecherle, Ed., vol. 2381, Apr. 1995, p. 151. DOI: 10.1117/12.207423.

[2.138] M. Toyoda, M. Toyoshima, T. Takahashi, M. Shikatani, Y. Arimoto, K. Araki, *et al.*, "Ground-to-ETS-VI narrow laser beam transmission," G. S. Mecherle, Ed., vol. 2699, International Society for Optics and Photonics, 1996, p. 71. DOI: 10.1117/12.238436.

[2.139] T. Jono, Y. Takayama, K. Shiratama, I. Mase, B. Demelenne, Z. Sodnik, *et al.*, "Overview of the inter-orbit and the orbit-to-ground laser communication demonstration by OICETS," in *Free-Space Laser Communication Technologies XIX and Atmospheric Propagation of Electromagnetic Waves*, S. Mecherle and O. Korotkova, Eds., vol. 6457, Feb. 2007, p. 645 702. DOI: 10.1117/12.708864.

[2.140] Y. Takayama, T. Jono, Y. Koyama, N. Kura, K. Shiratama, B. Demelenne, *et al.*, "Observation of atmospheric influence on OICETS inter-orbit laser communication demonstrations," in *Proc. SPIE*, A. K. Majumdar and C. C. Davis, Eds., vol. 6709, International Society for Optics and Photonics, Sep. 2007, 67091B. DOI: 10.1117/12.736789.

[2.141] D. Kolev, H. Takenaka, Y. Munemasa, M. Akioka, N. Iwakiri, Y. Koyama, *et al.*, "Overview of international experiment campaign with small optical transponder (SOTA)," in *2015 IEEE International Conference on Space Optical Systems and Applications (ICSOS)*, IEEE, Oct. 2015, pp. 1–6. DOI: 10.1109/ICSOS.2015.7425060.

[2.142] H. Takenaka, A. Carrasco-Casado, M. Fujiwara, M. Kitamura, M. Sasaki, and M. Toyoshima, "Satellite-to-ground quantum-limited communication using a 50-kg-class microsatellite," *Nature Photonics*, vol. 11, no. 8, pp. 502–508, 2017. DOI: 10.1038/nphoton.2017.107. arXiv: 1707.08154.

[2.143] J. Yin, Y. Cao, Y.-H. Li, S.-K. Liao, L. Zhang, J.-G. Ren, *et al.*, "Satellite-based entanglement distribution over 1200 kilometers," *Science*, vol. 356, no. 6343, pp. 1140–1144, Jun. 2017. DOI: 10.1126/science.aan3211.

[2.144] T. Kuwahara, K. Yoshida, Y. Sakamoto, Y. Tomioka, K. Fukuda, M. Fukuyama, *et al.*, "Satellite-to-ground optical communication system on Low Earth Orbit micro-satellite RISESAT," *2012 IEEE/SICE International Symposium on System Integration, SII 2012*, pp. 939–944, 2012. DOI: 10.1109/SII.2012.6427336.

[2.145] K. E. Wilson, J. R. Lesh, K. Araki, and Y. Arimoto, "Overview of the Ground-to-Orbit Lasercom Demonstration (GOLD)," in *Proc. SPIE 2990, Free-Space Laser Communication Technologies IX*, G. S. Mecherle, Ed., vol. 2990, International Society for Optics and Photonics, 1997, pp. 23–30. DOI: 10.1117/12.273703.

[2.146] R. Fields, D. Kozlowski, H. Yura, R. Wong, J. Wicker, C. Lunde, *et al.*, "5.625 Gbps bidirectional laser communications measurements between the NFIRE satellite and an Optical Ground Station," in *2011 International Conference on Space Optical Systems and Applications (ICSOS)*, IEEE, May 2011, pp. 44–53. DOI: 10.1109/ICSOS.2011.5783708.

[2.147] D. M. Boroson, B. S. Robinson, D. V. Murphy, D. A. Burianek, F. Khatri, J. M. Kovalik, *et al.*, "Overview and results of the Lunar Laser Communication Demonstration," in *Free-Space Laser Communication and Atmospheric Propagation XXVI*, H. Hemmati and D. M. Boroson, Eds., vol. 8971, Mar. 2014, 89710S. DOI: 10.1117/12.2045508.

[2.148] M. J. Abrahamson, B. V. Oaida, O. Sindiy, and A. Biswas, "Achieving operational two-way laser acquisition for OPALS payload on the International Space Station," in *Free-Space Laser Communication and Atmospheric Propagation XXVII*, H. Hemmati and D. M. Boroson, Eds., vol. 9354, Mar. 2015, p. 935 408. DOI: 10.1117/12.2182473.

[2.149] M. W. Wright, M. W. Wilkerson, and R. Renyong, "Qualification testing of fiber-based laser transmitters and on-orbit validation of a commercial laser system," in *International Conference on Space Optics (ICSO)*, 2014, pp. 1–20.

[2.150] T. S. Rose, D. W. Rowen, S. D. LaLumondiere, N. I. Werner, R. Linares, A. C. Faler, *et al.*, "Optical communications downlink from a 1.5U cubesat: OCSD program," in *Free-Space Laser Communications XXXI*, H. Hemmati and D. M. Boroson, Eds., vol. 10910, SPIE, Mar. 2019, p. 28. DOI: 10.1117/12.2513963.

[2.151] T. S. Rose, D. W. Rowen, S. Lalumondiere, N. I. Werner, R. Linares, A. Faler, *et al.*, "Optical Communications Downlink from a 1.5U CubeSat: OCSD Program," in *32nd Annual AIAA/USU Conference on Small Satellites*, 2018.

[2.152] R. Lange and B. Smutny, "Homodyne BPSK-based optical inter-satellite communication links," *Proceedings of SPIE*, vol. 6457, pp. 645703–645703–9, 2007. DOI: 10.1117/12.698646.

[2.153] S. Seel, D. Troendle, F. Heine, H. Zech, M. Motzigemba, and U. Sterr, "Alphasat laser terminal commissioning status aiming to demonstrate Geo-Relay for Sentinel SAR and optical sensor data," in *2014 IEEE Geoscience and Remote Sensing Symposium*, IEEE, Jul. 2014, pp. 100–101. DOI: 10.1109/IGARSS.2014.6946365.

[2.154] F. Heine, P. Martin-Pimentel, H. Kaempfner, G. Muehlnikel, D. Troendle, H. Zech, *et al.*, "Alphasat and sentinel 1A, the first 100 links," *2015 IEEE*

International Conference on Space Optical Systems and Applications, ICSOS 2015, pp. 1–4, 2016. DOI: 10.1109/ICSOS.2015.7425059.

[2.155] D. Tröndle, P. Martin Pimentel, C. Rochow, H. Zech, G. Muehlnikel, F. Heine, *et al.*, "Alphasat-Sentinel-1A optical inter-satellite links: run-up for the European data relay satellite system," in *Free-Space Laser Communication and Atmospheric Propagation XXVIII*, H. Hemmati and D. M. Boroson, Eds., vol. 9739, International Society for Optics and Photonics, Mar. 2016, p. 973 902. DOI: 10.1117/12.2212744.

[2.156] F. F. Heine, A. Sánchez-Tercero, P. Martin-Pimentel, N. Höpcke, D. Hasler, and H. Zech, "Operational experience of the Alphasat and EDRS laser communication system," in *Free-Space Laser Communications XXXI*, H. Hemmati and D. M. Boroson, Eds., SPIE, Mar. 2019, p. 29. DOI: 10.1117/12.2510721.

[2.157] C. Fuchs, C. Schmidt, J. Keim, F. Moll, B. Rödiger, M. Lengowski, *et al.*, "Update on DLR's OSIRIS program and first results of OSIRISv1 on Flying Laptop," *Free-Space Laser Communications XXXI*, no. March, p. 27, 2019. DOI: 10.1117/12.2514349.

[2.158] Y. Satoh, Y. Miyamoto, Y. Takano, S. Yamakawa, and H. Kohata, "Current status of Japanese optical data relay system (JDRS)," in *2017 IEEE International Conference on Space Optical Systems and Applications (ICSOS)*, IEEE, Nov. 2017, pp. 240–242. DOI: 10.1109/ICSOS.2017.8357398.

[2.159] Y. Chishiki, S. Yamakawa, Y. Takano, Y. Miyamoto, T. Araki, and H. Kohata, "Overview of optical data relay system in JAXA," in *Free-Space Laser Communication and Atmospheric Propagation XXVIII*, H. Hemmati and D. M. Boroson, Eds., vol. 9739, Mar. 2016, p. 97390D. DOI: 10.1117/12.2217552.

[2.160] D. R. Kolev, A. Carrasco-Casado, H. Takenaka, Y. Munemasa, P. V. Trinh, Y. Saito, *et al.*, "Satellite Laser Communication Activities in NICT," in *2018*

Progress in Electromagnetics Research Symposium (PIERS-Toyama), IEEE, Aug. 2018, pp. 1680–1685. DOI: 10.23919/PIERS.2018.8597762.

[2.161] D. J. Israel, B. L. Edwards, and J. W. Staren, "Laser Communications Relay Demonstration (LCRD) update and the path towards optical relay operations," in *2017 IEEE Aerospace Conference*, IEEE, Mar. 2017, pp. 1–6. DOI: 10.1109/AERO.2017.7943819.

[2.162] D. M. Cornwell, "NASA's optical communications program for 2017 and beyond," in *2017 IEEE International Conference on Space Optical Systems and Applications (ICSOS)*, IEEE, Nov. 2017, pp. 10–14. DOI: 10.1109/ICSOS.2017.8357203.

[2.163] A. Biswas, M. Srinivasan, R. Rogalin, S. Piazzolla, J. Liu, B. Schratz, *et al.*, "Status of NASA's deep space optical communication technology demonstration," in *2017 IEEE International Conference on Space Optical Systems and Applications, ICSOS 2017*, IEEE, Nov. 2018, pp. 23–27. DOI: 10.1109/ICSOS.2017.8357206.

[2.164] R. Migliore, J. Duncan, V. Pulcino, D. Bourne, S. Voegt, and G. Perez, "Outlook on EDRS-C," in *International Conference on Space Optics — ICSO 2016*, N. Karafolas, B. Cugny, and Z. Sodnik, Eds., vol. 10562, SPIE, Sep. 2016, p. 169. DOI: 10.1117/12.2296160.

[2.165] H. Hauschildt, C. Elia, L. Moeller, and J. M. Perdigués Armengol, "HydRON: High throughput optical network," in *Free-Space Laser Communications XXXI*, H. Hemmati and D. M. Boroson, Eds., SPIE, Mar. 2019, p. 18. DOI: 10.1117/12.2511391.

Chapter 3

Environmental Testing of Fiber Optic Components for Space Applications

As discussed in Chapter 2, qualifying components for their anticipated environment is of utmost importance when designing fiber optic systems to be based in the space environment. As an early stage in the design process, these components must be tested to a rigorous standard such that it can be ascertained if they will survive. As shown in section 2.2.4, standardised space qualification standards for fiber optic components do not exist and must be modified from ESCC test standards for laser diodes [3.1], [3.2]. One important point to note from the ESCC test standards is that they reference terrestrial test standards such as MIL-STD-883 [3.3] and Telcordia standards [3.4], [3.5] with modified test conditions. This approach has been used to devise the tests outlined in section 3.3 and are suitable for enabling the initial assessment of the components tested for their use within space systems. This chapter is structured as follows:

- Section 3.1 will introduce the objectives of the test campaign and types of component tested.
- Section 3.2 describes the components to be tested.
- Section 3.3 presents the test plan and with it the methods and conditions used.

- Test results for each component type are presented in section 3.4
- The test campaign on irradiated ErYb-doped fibers is treated separately and is presented in section 3.5
- Section 3.6 summarises and provides a conclusion of the test campaign.

3.1 Aims & Objectives

To meet the overall aim of this thesis which is to demonstrate the miniaturisation of satellite optical communications technology. The primary aim of the test campaign described in this chapter is to provide an initial assessment into the suitability of a new class of optical component that has not yet been tested (to the author's current knowledge). In addition to this, ErYb-doped active fibers will be tested such that a suitable fiber can be selected to provide the best radiation response at a reasonable cost.

The components to be tested are shown below. For specific information on each component type see section 3.2 for the passive optical parts and section 3.5 for specific information on the ErYb-doped fiber tested.

1. Hybrid components, in which multiple parts can be merged into one part, in both a PM and non-PM configuration.
2. A compact, high-power isolator designed to operate at a wavelength of 1 µm.
3. Er/Yb-doped fiber designed for high-power ($>$ 1W) operation.

3.2 Description of Components

3.2.1 1 µm High-Power Isolator

These components are designed to operate at a signal wavelength of 1064 nm and as such are inherently different from components designed for use over the C-band. Shown in figure 3.1 is the component layout and mechanical dimensions of the device to be

Parameter	Value
Centre Wavelength	1064 nm
Operating Wavelength Range	±5 nm
Typ. Isolation	35 dB
Min. Isolation	28 dB
Typ. insertion loss (I/L) (@25 °C)	1.7 dB
Max. I/L (@0 – +50 °C, 2 W)	3 dB
Min. polarisation extinction ratio (PER)	20 dB
Max. Optical Power (CW)	2 W
Operating Temperature	0 – +70 °C
Storage Temperature	−40 – +85 °C

Table 3.1: Summary of 1 µm isolator specification.

tested. Care was taken in component selection to find an optical isolator which operates at 1 µm, provides a suitable power handling (approx. 2W) and is of a compact size. A summary of the specification of the 1 µm isolator selected is shown in table 3.1.

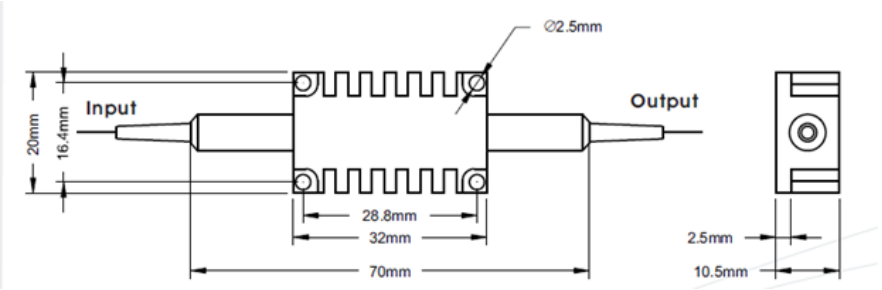

Figure 3.1: 1 µm fiber-optic isolator schematic.

3.2.2 Hybrid Components

This class of fiber optic component act as multi-functional passive optical devices incorporating a tap, WDM and isolator (or any other combination). Hybrid passive components are designed to be used on either the input or output of an active fiber which is providing amplification whilst reducing the component count. Therefore these devices come in two configurations, forward pumping (to be placed on the input of the

active fiber) and backward pumping (to be placed on the output of the active fiber). When a tap is present in the device, these devices have 4 ports and the typical configuration is shown in figure 3.2. A summary of the specification for this class of part is shown in tables 3.2 and 3.3.

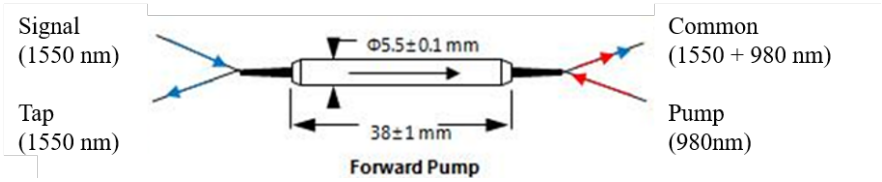

Figure 3.2: Schematic of a forward-pumped hybrid fiber-optic component.

Parameter	**λ = 1550/980 nm**
Isolator Stages	Dual Stage
Signal Wavelength (nm)	1528-1564 (C-band)
Pump Wavelength (nm)	965-1000
Signal Isolation @ 23 °C (dB)	≥ 45
I/L - Pump Channel (dB)	≤ 0.6
I/L - Signal Channel (dB)	≤ 1.4
Tap Ratio (dB)	$19.0 - 20.8$
Extinction Ratio (dB)	≥ 22
Return Loss (dB)	≥ 50
Optical Power (mW)	≤ 300
Operating Temperature (°C)	$0 - +70$
Storage Temperature (°C)	$-40 - +85$
Package Dimensions (mm)	$\psi 5.5 \times 35$

Table 3.2: Typical performance characteristics for PM hybrid optical components.

Parameter	**λ = 1550/980 nm**
Isolator Stages	Dual Stage
Signal Wavelength (nm)	1528-1564 (C-band)
Pump Wavelength (nm)	965-1000
Signal Isolation @ 23 °C (dB)	≥ 45
I/L - Pump Channel (dB)	≤ 0.6
I/L - Signal Channel (dB)	≤ 1.4
Tap Ratio (dB)	$19.0 - 20.8$
Return Loss (dB)	≥ 50
Optical Power (mW)	≤ 300
Storage Temperature (°C)	$-40 - +85$
Package Dimensions (mm)	$\psi 5.5 \times 35$

Table 3.3: Typical performance characteristics for non-PM hybrid optical components.

3.3 Test Conditions

This section will outline the tests and measurements to be conducted on the hybrid optical components and 1µm isolator as part of this test campaign. The tests defined in this document will be conducted to ECSS standards [3.1], [3.2] if applicable. When not applicable, other high-reliability standards [3.3]–[3.5] will be used.

3.3.1 Test Flow

30 components are to be tested in test batches of 10 components (30 components total). The type of hybrid component selected to be tested is the forward pumped, 4 port device. This type of device has been selected for two reasons. The first, is the pumping direction. These types of devices are constructed such that the optical path will be similar such that the forward pumping and backward pumping devices are almost identical; the difference being how the optical elements are ordered in the device. Therefore the backward pumping parts can be qualified through similarity. The second reason is that 4 port devices are the most complicated due to them including a

tap port along with the isolator and WDM found in the 3 port devices. These devices are similar but the 4 port devices are slightly more complicated. Although the 3 port devices cannot be qualified through similarity, they can through analysis by them being more resilient to the environment by being a simpler component.

The test flow for one batch of evaluation tests to be completed are shown in figure 3.3. The testing is broken up into 4 groups. These are:

- Control Group (2) – These devices will be used as reference components to ensure the measurements made are precise. The results for these components will not be shown unless there is a large discrepancy between measurements.
- Thermo-mechanical (4) – This group will focus on the thermo-mechanical performance of the devices. There are three test legs making up this group. The precise conditions for each test of this leg can be found in figure 3.4 and tests will be conducted according to ESCC Basic Specification No. 23201 [3.1] with some modifications.

  Mechanical leg

  Thermal cycling and humidity

- Vacuum group (2) – This will assess the devices' performance under vacuum conditions. Namely rapid depressurisation and thermal vacuum (TVAC) conditions.
- Radiation (2) – In this test group the devices will be irradiated with gamma radiation to assess the component's radiation hardness.

The test conditions for the vacuum group are shown in tables 3.4 and 3.5 and shall take place according to ESCC Basic Specification No. 23201 [3.1] clause 6.4.2.4.

Parameter	**Condition**
Starting Pressure	Atmospheric
Finish Pressure	$\leq$ 1333 Pa
Time for depressurisation	$\leq$ 5 s

Table 3.4: Rapid Depressurisation Test Conditions.

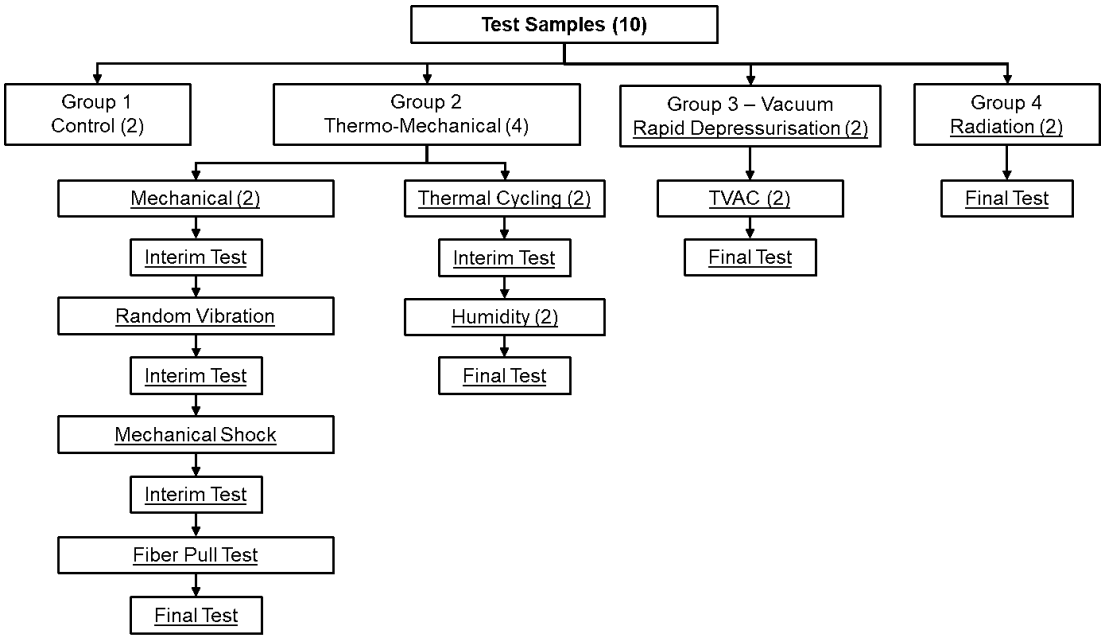

Figure 3.3: Generic test flow for passive component testing. The number in brackets denotes the number of devices to be tested.

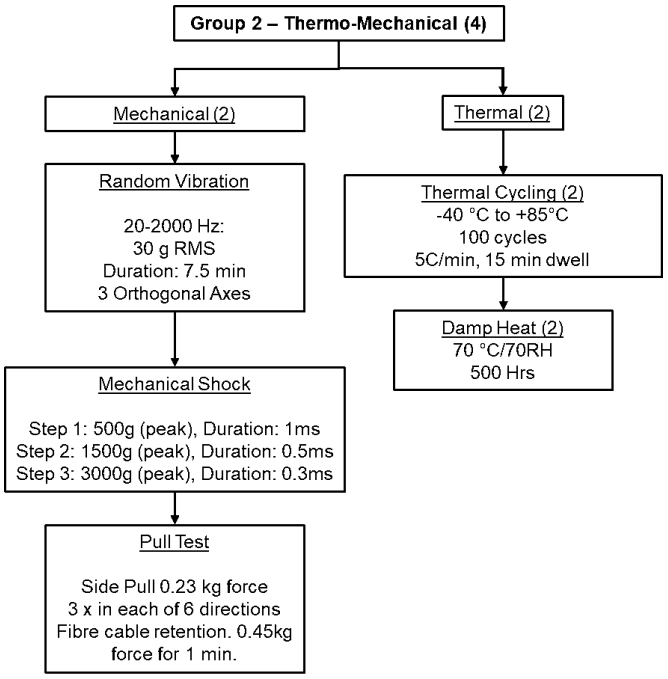

Figure 3.4: Overview and detailed test conditions of Thermo-Mechanical Test Group

Parameter	Condition
Duration	1000 h
Pressure	$\leq 10^{-6}$ torr
Temperature	+60 °C

Table 3.5: TVAC Test Conditions.

Dose Step	Dose (kRad)
A	30
B	100

Table 3.6: Radiation Test Conditions.

The radiation testing shall be completed according to ESCC Basic Specification No. 22900 [3.6] using the standard dose rate (0.36 to 180 kRad (Si) / hour). The only exception is the dose steps chosen which are shown in Table 3.6.

3.3.2 Required Measurements

In between each test step, the measurements according to Table 3.7 shall be taken. These shall also be completed on the control units at each stage to verify the status of the measurement system. All measurements for the hybrid components will be completed at $\lambda = 1550$ nm (signal)/ 980 nm (pump) and room temperature (approx. +23 °C). The 1 µm isolator measurements will be taken at a $\lambda = 1064$ nm. Only signal path I/L, signal isolation and signal PER measurements are applicable for the 1 µm isolator. The signal and common ports for the 1 µm isolator are denoted as the input port and the output port respectively.

In addition, the pass/fail conditions have been included in Table 3.7. The value for the allowed Δ has been chosen to reflect current high-reliability standards suitable for fiber-optic components [3.4], [3.5].

Parameter	Measurement Ports	Allowed Δ	Unit
Signal Path I/L	Signal → Common	±0.5	dB
Pump Path I/L	Signal → Common		
Signal Tap Ratio	Signal → Tap		
Signal Isolation	Common → Signal	> 30	
Signal PER[1]	Signal → Common	> 20	

[1] Only applicable to measurements on PM components.

Table 3.7: Test Campaign Required Measurements.

3.4 Results

3.4.1 Mechanical

The devices were mounted on separate plates such that it would simulate the expected mounting conditions. Figure 3.5 shows how the devices mounted before mechanical testing. The vibration tests were completed at PARC, Bideford, Devon and the devices were shaken in an order of: Y-axis, X-axis then Z-axis. The test setup and axis orientation is shown in Figure 3.6.

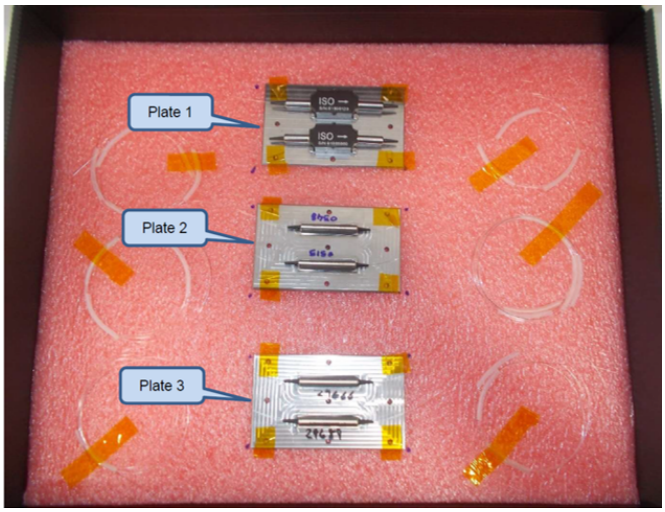

Figure 3.5: Fiber optic devices mounting before vibration testing.

Shock tests were completed at Alter Technology, Madrid and test setup for the +Y-axis shock is shown in Figure 3.7. After each shock level and shock axis, each fiber optic component tested was checked to ensure that the signal path was still intact by

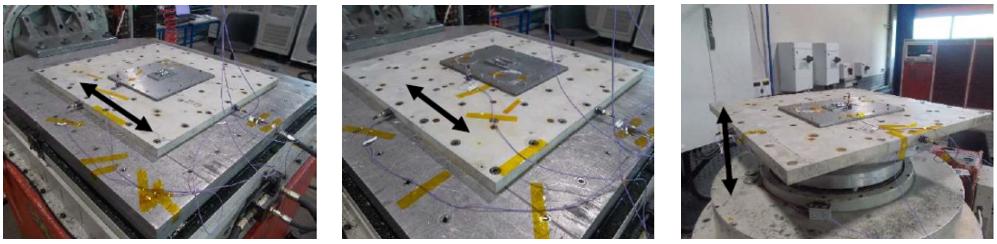

(a) X-axis (b) Y-axis (c) Z-axis

Figure 3.6: Vibration test setup on shaker and axis orientation.

a signal path I/L measurement. This was completed at the test house to reduce the test time. A summary of the results of the interim shock measurements is shown below in Table 3.8. Shown are the Δ values for signal path insertion loss. All measurements were based off an initial value measured before each shock was applied. Based off the data shown in Table 3.8, it can be seen that all components survived the shock test. However, significant variation in the 1 µm data can be seen suggesting that some degradation has occurred to both tested units. This variation is not enough to fail the test but is of a sufficient value to point towards some problem with the part, thus the conclusion of a partial pass for the 1 µm isolator (Table 3.21). Upon return to G&H, the 1 µm isolator S/N: 81805129 failed the post-shock measurement (Table 3.9) . When comparing the data in Table 3.8 and 3.9 this would suggest that the part became damaged during shipping the part back to G&H. As shown below during the fiber pull test this is not the first time parts became damaged during shipping, although at the time it was thought that the part was damaged during the shock test.

When the units were returned from the shock test, it was found that S/N: 81805060 had a shortened fiber due to problems with the connectorisation process completed at the test house. This is shown in Figure 3.8 and this became a problem when testing the isolator for the fiber pull test. Because of the short fiber in addition to the potentially damaged part S/N: 81805129, the fiber pull test could not be completed so it was decided that this set of parts would be replaced by the parts which underwent the vacuum leg. Although it does not test the mechanical strength after a shock test, a TVAC test can be thought of to be just as rigorous due to the high temperatures and low pressures that the part faced.

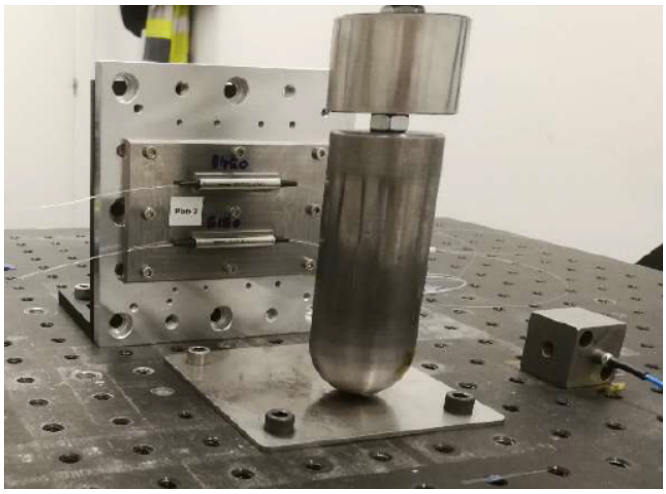

Figure 3.7: Photo showing the test setup for the +Y axis shock. Photo credit: Alter Technology.

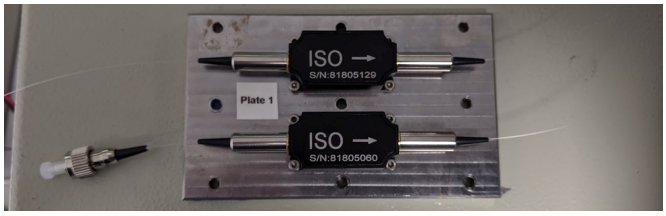

Figure 3.8: Photo of the returned 1 µm isolators, post-shock test.

Following the shock test, the final fiber pull test was completed at Alter technology, Madrid, Spain. The setup for the fiber pull test is shown in Figure 3.9; more specifically, the test shown is the side-pull test for the PM hybrid components. As discussed previously, the parts tested for the fiber pull test for the 1 µm isolator were changed after the shock test due to the short fiber of S/N: 81805060 and potentially damaged part S/N: 81805129. The results for this test are shown in Table 3.15 as this test was completed on the vacuum leg parts, after the TVAC test. The results of the 1µm isolator pull test were mixed. It can be seen from Figure 3.10 that the part S/N: 81804734 has been damaged as the stress relief boots have become loose. This would suggest that the fiber has become loose inside and damaged during the test. This can be seen by the increase in I/L of 2.67 dB through the component in Table 3.15. However, the part S/N: 81804721 passed the fiber pull test. Therefore, a partial-pass for the mechanical leg for this component can be reported.

Shock Level	Axis	PM Hybrid		Non-PM Hybrid		1 µm Isolator	
		29666	29688	1710015	17100348	81805129	81805060
500g	+X	-0.10	0.00	0.00	0.00	-0.44	0.13
	-X	-0.18	0.01	-0.04	-0.10	-0.08	0.05
	+Y	-0.01	-0.03	0.04	0.02	0.14	0.46
	-Y	-0.08	0.04	0.00	0.02	-0.46	0.32
	+Z	-0.02	0.08	0.01	0.02	-0.08	-0.15
	-Z	0.00	0.01	0.00	0.00	-0.30	-0.07
1500 g	+X	-0.08	0.00	0.00	0.01	-0.26	0.11
	-X	-0.15	0.00	-0.01	0.00	0.03	0.26
	+Y	0.00	0.00	-0.01	0.00	0.34	-0.3
	-Y	-0.04	0.13	0.00	0.00	-0.43	-0.09
	+Z	-0.12	0.01	0.01	0.00	0.11	0.37
	-Z	-0.10	-0.01	0.01	0.00	0.29	-0.14
3000 g	+X	-0.04	0.00	0.01	0.00	0.40	-0.46
	-X	0.06	0.00	0.01	0.00	0.44	0.01
	+Y	0.00	-0.03	0.00	0.00	0.17	-0.34
	-Y	-0.19	-0.04	0.00	0.00	-0.33	0.36
	+Z	-0.07	-0.01	0.01	-0.01	-0.02	0.04
	-Z	0.04	0.00	0.00	-0.01	-0.46	-0.41

Table 3.8: Measured change in insertion loss between shock axes at levels of 500 g, 1500 g, and 3000 g for the passive optical components tested. Units: dB

The PM hybrid part, S/N: 29688 was damaged during shipping to the test house. The result of this damage can be seen in the lower part of Figure 3.11, where only two small stubs of fiber remain on the input side. The test was still completed on the output fibers. Following the test, the pump fiber and output fiber were still intact meaning that a pump port I/L could be recorded and reported. It was found that the pump port functioned correctly, adding further evidence to that the part S/N: 29688 became damaged during shipping and not a result of the pull or shock tests.

During the fiber side-pull test of the non-PM hybrid part, S/N: 17100515, more than 12 N of force (specified amount: 2.25 N) was applied to the fiber due to an error with the test fixture. This caused pump fiber to be pulled out of the package. The extent of the damage can be seen in Figure 3.12. The result was that the pump insertion loss could not be measured. Additionally, this over load of the fiber would cause damage within the package of the device and would misalign any optics inside the package due

Figure 3.9: Photo of the fiber pull test setup. Photo credit: Alter Technology

Figure 3.10: Photo of the pull-test failed isolator. It can be clearly seen that the strain relief boots have become loose (circled).

to a fiber being pulled out of the system. Therefore the increase in signal I/L and signal tap ratio shown in the post-pull measurement in Table 3.11 can be attributed to the over loading of the pump fiber. This conclusion is further evidenced by the fact that measurements made for the other non-PM hybrid part (S/N: 17100348) showed no degradation in any test parameter following the fiber pull test.

A summary of the pre- & post-measurements of each test are shown in Tables 3.9-3.11 with all units in dB. Each measurement is shown along with a Δ between

Figure 3.11: Photo of the returned PM hybrid components, post-fiber pull test.

Figure 3.12: Photo of the returned non-PM hybrid components, post-fiber pull test.

each test showing the degradation of the parts from the initial measured value. No Δ has been included for isolation or PER as these values are not used as part of the pass/fail criteria. Where isolation measurements are the same as the initial value, the isolation measurement was not successful as too low a signal was passed from the common $\rightarrow$ signal port to be measured using the same power meter. This indicates a high isolation and if the signal path was broken, then this would be shown in the signal path I/L measurement. The same calibrated power meter was used through the test campaign to provide consistency in the data and reduce drift in the measured values.

S/N	Test	Sig. I/L	Sig. Iso	Sig. PER
81805129	Initial	1.5	34.00	34.0
	Post Vib.	1.89	34.00	32.6
	Δ	0.39	-	-
	Post Shock	12.87	34.00	29.1
	Δ	**11.37**	-	-
	Post Fiber-Pull		N/A[1]	
81805060	Initial	1.3	32.00	39
	Post Vib.	1.55	32.00	34.4
	Δ	0.25	-	-
	Post Shock	1.75	34.00	27.0
	Δ	0.45	-	-
	Post Fiber-Pull		N/A[1]	

[1] Pull test not completed on these parts. See TVAC components for pull test result.

Table 3.9: Result summary of the mechanical leg for the 1 µm isolator. All units are in dB.

S/N	Test	Sig. I/L	P. I/L	Sig. Tap	Sig. Iso	Sig. PER
29666	Initial	0.72	0.31	22.26	58.00	37.9
	Post Vib.	0.98	0.21	22.61	72.66	40.6
	Δ	0.26	-0.10	0.35	-	-
	Post Shock	1.22	0.42	22.68	58.00	39.3
	Δ	0.50	0.11	0.42	-	-
	Post Pull	0.95	0.12	22.57	66.25	35.9
	Δ	0.23	-0.19	0.31	-	-
29688	Initial	0.97	0.33	22.22	56.00	32.3
	Post Vib.	1.31	0.41	22.37	56.00	31.3
	Δ	0.34	0.08	0.15	-	-
	Post Shock	1.27	0.17	22.47	56.00	35.4
	Δ	0.30	-0.16	0.25	-	-
	Post Pull	N/A[1]	0.01		N/A[1]	
	Δ		-0.32			

[1] Measurements not made due to damage during shipping.

Table 3.10: Result summary of the mechanical leg for the PM hybrid components. All units are in dB.

S/N	Test	Sig. I/L	P. I/L	Sig. Tap	Sig. Iso
17100515	Initial	1.00	0.41	20.55	56.00
	Post Vib.	1.19	0.17	20.57	58.72
	Δ	0.19	-0.24	0.02	-
	Post Shock	1.41	0.28	20.74	56.00
	Δ	0.41	-0.13	0.19	-
	Post Pull	2.87	N/A[1]	27	56.00
	Δ	**1.86**		**6.45**	-
17100348	Initial	0.84	0.50	20.4	60.00
	Post Vibration	0.48	0.50	20.4	55.20
	Δ	-0.36	-0.39	0.00	-
	Post Shock	1.10	0.28	20.50	57.40
	Δ	0.26	-0.22	0.10	-
	Post Pull	0.67	0.14	20.29	60.00
	Δ	-0.17	-0.36	-0.11	-

[1] 12 N of force loaded onto fiber which caused breakage. See commentary for more details.

Table 3.11: Result summary of the mechanical leg for the non-PM hybrid components. All units are in dB.

3.4.2 Thermal

Shown in Tables 3.12-3.14 are the results for the thermal leg of the test campaign. These tests were completed internally at G&H Torquay. Figure 3.13 shows the devices in the test chambers for the tests completed in this leg. Both devices were tested before and after each test and Δ calculated between each test.

It was found that little or no degradation in performance was found in these components after test. Therefore, it can be said that all the parts passed this test leg and are suitable for the anticipated thermal and storage humidity environment.

(a) (b)

Figure 3.13: Parts placed in the (a) thermal & (b) humidity chamber.

S/N	Test	Sig. I/L	Sig. Iso	Sig. PER
61802169	Initial	1.33	33.00	38.3
	Post Thermal	1.51	33.00	35.7
	Δ	0.25	-	-
	Post DH	1.65	32.08	32.10
	Δ	0.32	-	-
81804859	Initial	2.20	34.00	36.6
	Post Thermal	1.73	34.00	33.2
	Δ	-0.47	-	-
	Post DH	2.07	30.22	32.7
	Δ	-0.13	-	-

Table 3.12: Result summary of the thermal leg for the 1 µm isolator. All units are in dB.

S/N	Test	Sig. I/L	P. I/L	Sig. Tap	Sig. Iso	Sig. PER
29630	Initial	0.77	0.37	21.99	55.00	33.7
	Post Thermal	1.21	0.33	22.00	55.00	30.7
	Δ	0.44	-0.04	0.01	-	-
	Post DH	1.07	0.27	22.20	65.73	38.7
	Δ	0.30	-0.10	0.21	-	-
29632	Initial	1.03	0.37	21.99	57.00	34.5
	Post Thermal	1.31	0.34	22.01	57.00	32.8
	Δ	0.28	-0.03	0.02	-	-
	Post DH	1.45	0.81	22.06	66.58	26.4
	Δ	0.42	0.44	0.07	-	-

Table 3.13: Result summary of the thermal leg for the PM hybrid components. All units are in dB.

S/N	Test	Sig. I/L	P. I/L	Sig. Tap	Sig. Iso
17100571	Initial	0.95	0.42	20.59	57.68
	Post Thermal	1.34	0.20	20.46	52.66
	Δ	0.39	-0.22	-0.13	-
	Post DH	1.44	0.11	20.38	53.09
	Δ	0.49	-0.31	-0.21	-
17100507	Initial	0.93	0.56	20.80	54.50
	Post Thermal	0.74	0.48	20.34	61.64
	Δ	-0.19	-0.08	-0.46	-
	Post DH	0.75	0.10	20.35	59.04
	Δ	-0.18	-0.46	-0.45	-

Table 3.14: Result summary of the thermal leg for the non-PM hybrid components. All units are in dB.

3.4.3 Vacuum

Shown in Tables 3.15-3.17 are the results for the vacuum leg of the test campaign. The vacuum leg of the test campaign was completed at Alter Technology, Madrid and the same chamber was used for both the rapid depressurisation test and TVAC test. Figure 3.15 shows the parts placed within the TVAC chamber before the test leg was commenced.

Upon return from TVAC testing fibers on all of the devices were found to be yellow (see Figure 3.15). When the fiber is stripped it shows a clear glass cladding and core (Figure 3.15 (bottom)) illustrating that the discolouration has occurred in the acrylate buffer of the fiber. This is a well known problem for fiber being used in long-lifetime applications and is a common observation when accelerated life tests at high temperatures are commenced.

Based on the data shown in Tables 3.15-3.17, all parts pass the vacuum leg of the test campaign. The only failure was observed in the 1 µm isolator part S/N: 81804734 after the pull test. This failure has been addressed in Section 3.4.1.

S/N	Test	Sig. I/L	Sig. Iso	Sig. PER
81804734	Initial	1.70	32.00	31.1
	Post Rap. Depres.	1.75	36.11	27.40
	Δ	0.05	-	-
	Post TVAC	2.07	32.00	31.6
	Δ	0.37	-	-
	Post Pull	4.39	32.00	36.8
	Δ	**2.67**	-	-
81804721	Initial	1.67	33.00	36.5
	Post Rap. Depres.	1.99	33.10	42.7
	Δ	0.32	-	-
	Post TVAC	2.14	33.00	37.2
	Δ	0.47	-	-
	Post Pull	1.85	33.00	36.1
	Δ	0.18	-	-

Table 3.15: Result summary of the vacuum leg and fiber pull test for the 1 µm isolator. All units are in dB.

S/N	Test	Sig. I/L	P. I/L	Sig. Tap	Sig. Iso	Sig. PER
29625	Initial	1.15	0.27	22.14	50.00	36.9
	Post Rap. Depres.	1.20	0.46	22.33	66.30	32.4
	Δ	0.05	-0.05	0.19	-	-
	Post TVAC	1.17	0.17	22.40	50.00	34.1
	Δ	0.02	-0.34	0.26	-	-
29623	Initial	1.23	0.44	22.12	45.00	34.7
	Post Rap. Depres.	1.18	0.44	22.12	65.80	32.0
	Δ	-0.05	-0.06	-0.16	-	-
	Post TVAC	1.71	0.12	22.33	45.00	27.1
	Δ	0.48	-0.32	0.21	-	-

Table 3.16: Result summary of the vacuum leg for the PM hybrid components. All units are in dB.

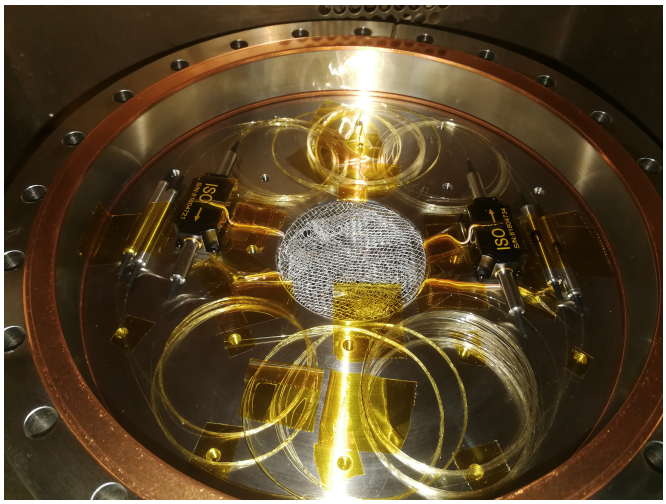

Figure 3.14: Photo of the tested parts in the TVAC chamber prior to 1000 hour life test. Photo credit: Alter Technology

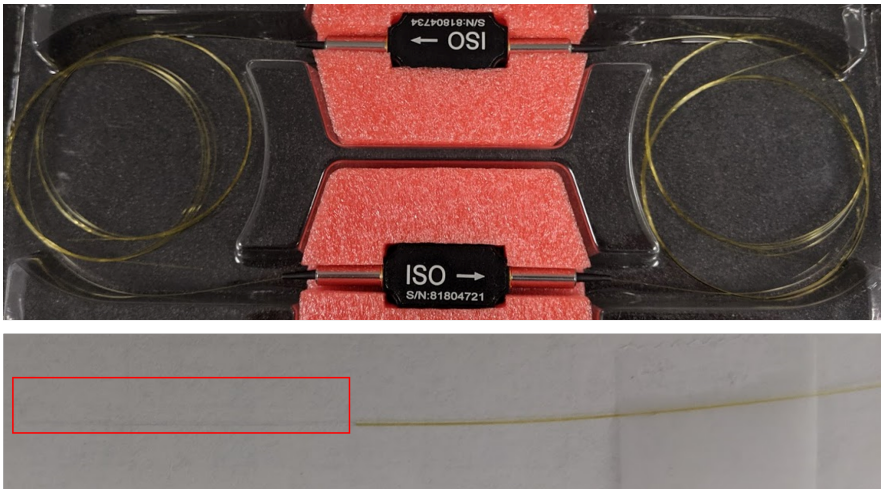

Figure 3.15: (Top) Photo of the 1 µm isolators post-TVAC showing the discoloured fiber. (Bottom) Photo of stripped discoloured fiber. Glass cladding and core is shown boxed in red.

3.4.4 Radiation

The radiation testing was completed at Alter Technology, Seville. Photos of the test setup are shown in Figure 3.16. Only one component of each type was tested at a dose of 30 and 100 kRad for it's radiation response. The results are summarised in Tables 3.18-3.20.

It can be seen that for both the PM and non-PM components, that failures occur

S/N	Test	Sig. I/L	P. I/L	Sig. Tap	Sig. Iso
17100526	Initial	0.94	0.38	20.31	54.60
	Post Rap. Depres.	1.19	0.12	20.67	61.07
	Δ	0.25	-0.26	0.36	-
	Post TVAC	1.26	0.24	20.60	61.07
	Δ	0.32	-0.14	0.29	-
17100363	Initial	0.98	0.37	20.43	53.61
	Post Rap. Depres.	1.12	0.10	20.60	54.49
	Δ	0.14	-0.27	0.17	-
	Post TVAC	1.16	0.20	20.71	57.82
	Δ	0.18	-0.17	0.28	-

Table 3.17: Result summary of the vacuum leg for the non-PM hybrid components. All units are in dB.

at doses of 100 kRad but pass at 30 kRad, thus providing a result of a partial-pass. Failures are found in the pump path I/L for the PM component and all I/Ls for the non-PM component. This would suggest that the output stage of the hybrid component is affected by radiation as the pump part of the hybrid will be after any losses caused by damage to the tap or isolator parts.

Although this failure mode is unknown, it shows that these devices are suitable for use at LEO (lower radiation dose). This is important as hybrid components would typically be used in applications where the SWaP is limited which is almost exclusively in spacecraft operating at LEO, not GEO where a larger rocket and spacecraft is common. For satellites operating at LEO, they are designed with SWaP in mind to reduce both spacecraft and launch cost. Typically these are commercial spacecraft used in satellite constellations where a large number of satellites are manufactured and launched so cost is important.

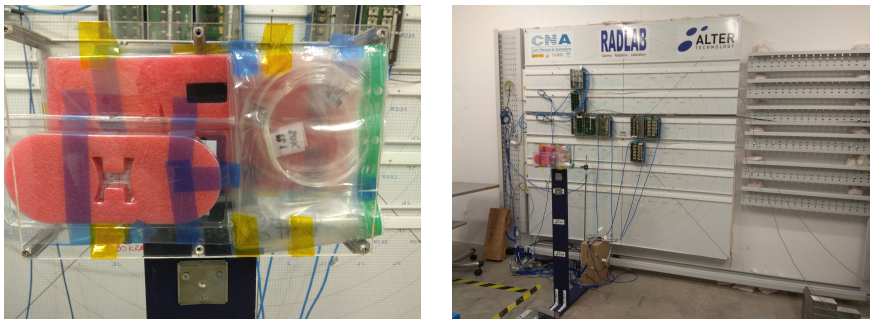

(a) (b)

Figure 3.16: Photos of the radiation test setup. Shown are the part packaged (a) before being placed in the test chamber (b).

S/N	Dose	Test	Sig. I/L	Sig. Iso	Sig. PER
81804733	100 kRad	Initial	1.91	32.00	22.9
		Post Radiation	2.11	41.48	30.5
		Δ	0.20	-	-
81805042	30 kRad	Initial	1.45	34.00	34.1
		Post Radiation	1.69	27.82	36.2
		Δ	0.24	-	-

Table 3.18: Result summary of the radiation leg for the 1 µm isolator. All units are in dB.

S/N	Dose	Test	Sig. I/L	P. I/L	Sig. Tap	Sig. Iso
1710056	30 kRad	Initial	0.78	0.39	20.30	52.00
		Post Rad.	0.82	0.64	20.65	63.34
		Δ	0.04	0.25	0.35	-
17100325	100 kRad	Initial	1.10	0.42	20.42	63.87
		Post Rad.	2.17	1.39	21.53	65.76
		Δ	**1.07**	**0.97**	**1.11**	-

Table 3.20: Result summary of the radiation leg for the non-PM hybrid components. All units are in dB.

3.4.5 Summary and Discussion of Results

Based on the results shown in the previous sub-sections, a summary of the reported results is shown in Table 3.21. All tests were a pass apart from the 1 µm isolator mechanical leg, where one part failed the fiber pull test, and the 100 kRad test on both

S/N	Dose	Test	Sig. I/L	P. I/L	Sig. Tap	Sig. Iso	Sig. PER
29684	30 kRad	Initial	1.17	0.68	22.05	58.00	39.6
		Rad.	0.88	0.68	21.94	65.8	31.5
		Δ	-0.29	0.00	-0.11	-	-
29653	100 kRad	Initial	1.19	0.73	22.21	50.00	30.9
		Rad.	1.43	1.88	21.96	67.45	37.1
		Δ	0.24	**1.15**	-0.25	-	-

Table 3.19: Result summary of the radiation leg for the PM hybrid components. All units are in dB.

classes of hybrid component.

Test Leg	Result		
	1 µm Isolator	PM Hybrid	Non-PM Hybrid
Mechanical	**Partial-Pass**	**Pass**	**Pass**
Thermal	**Pass**	**Pass**	**Pass**
Vacuum	**Pass**	**Pass**	**Pass**
Radiation	**Pass**	**Partial-Pass**	**Partial-Pass**

Table 3.21: Summary of Passive Component Testing.

For LEO applications, this data shows that both classes of hybrid component are suitable for space applications and can be incorporated in future designs. However, their use in GEO applications is limited as additional radiation shielding would be required. The trade-off between the additional mass required for the shielding versus using traditional fused fiber components and isolators would be needed, with the most likely outcome being that traditional parts being used due to the risk-averse nature of the space industry.

The 1 µm isolator testing is inconclusive due to two reasons. The first is that only one part (S/N: 17100515) failed the shock testing which conflicts with the data provided immediately after the shock test. This leads to the conclusion that the part became damaged during shipping, however this cannot be confirmed. The second reason is that one part (S/N: 81804734) failed the fiber pull test. Because of this the mechanical leg is a partial-pass and inconclusive. Future work would focus on re-testing this part using

a larger sample size for the pull-test to discern whether this failure was due to poor build quality or is an anomalous result. At this stage the 1 µm isolator tested can be still be considered to be used in space but must be re-tested before qualification or a lot-validation test used for the part.

3.5 Double Clad Er/Yb-Doped Optical Fiber Testing

For optical amplifiers, double clad fibers are typically used in high power applications due to their higher efficiencies (see section 2.1.5 for more details). As space-based laser communications as a field is maturing, a shift towards amplifiers providing an output power $\geq$ 1 W to provide higher data rates is occurring. Therefore, the impact of the space environment on this class of fiber must be considered. As discussed previously in section 2.2.3, the main threat to Er/Yb-doped optical fibers is that of γ-radiation.

To test these fibers to a suitable level, radiation levels of 30 kRad and 100 kRad were chosen as this reflects a 10-year lifetime in the two most common orbit environments, LEO and GEO, respectively. The radiation dose rate used was 0.21 kRad/h. The fibers selected were chosen such that a mix of COTS and rad-hard fibers were chosen. A summary of the fibers chosen is shown in Table 3.22 and cross-sectional photos of each 6 µm fiber are shown in Figure 3.17 confirming that all 4 fibers tested were of a PANDA-PM variety. ErYb#5 is also a PANDA-PM fiber based on the design of ErYb#1 but with a larger core diameter of 12 µm.

3.5.1 6 µm EYDF Testing and Results

Test Setup

The fiber amplifier setup which was used to test fibers ErYb#1, #2 & #3 is shown in Figure 3.18. It shows that these fibers were tested in a co-propagating scheme with the output power and spectra collected through the use of an power meter and OSA, respectively. The fiber lengths tested were kept to a set length of 7 m to provide comparative measurements. The input power was fixed to +10 dBm and signal wavelength swept via the use of a tunable laser and variable optical attenuator (VOA). ErYb#4

Fiber ID	**Fiber Description**	**Key Parameters**
ErYb#1	6/130 PM ErYb co-doped with cerium	Clad. abs. @ 915 nm = 0.82 dB/m Core abs. @ 1536 nm = 34.2 dB/m
ErYb#2	PM 6/128 ErYb	Clad. abs. @ 915 nm = 0.67 dB/m Core abs. @ 1535 nm = 62.7 dB/m
ErYb#3	PM 6/125 ErYb	Clad. abs. @ 915 nm = 0.51 dB/m Core abs. @ 1535 nm = N/A
ErYb#4	PM 6/125 ErYb	Clad. abs. @ 915 nm = 0.82 dB/m Core abs. @ 1535 nm = 40.0 dB/m
ErYb#5	PM 12/130 ErYb	Clad. abs. @ 915 nm = 1.8 dB/m Core abs. @ 1536 nm = $>$ 30.0 dB/m

Table 3.22: ErYb fibers selected along with their key parameters.

was tested in a similar manner with the only change being that it was pumped in a counter-propagating fashion. The reason for counter-pumping ErYb#4 was that the output power was trying to be maximised in the 0 kRad test. Therefore, to keep RIA data consistent, the same pumping scheme was kept for the irradiated fibers.

Results

Before the irradiated active fibers were placed in an active configuration, a cross-sectional image, shown in figure 3.19 was taken to provide a quantifiable understanding of any macroscopic changes to the fiber. When compared to the images in 3.17 there are little differences between the pre- and post-radiation images. The majority of differences between the images are a result of a variation of fiber illumination. The one main change is the slight red tint seen across the fiber, especially so in ErYb#4, which is a result of short wavelength RIA in the 600-800 nm region. This is typical for non-rad hard EYDFAs [3.7] with the tail of the absorption region effecting pump wavelengths in the 915-940 nm regime and therefore the amplifier performance. From these results it would appear that ErYb#4 would provide the worst radiation response in an amplifier configuration. It is most likely a result ErYb#4 having a larger proportion of Yb-doping, as shown by the cladding and core absorption measurements.

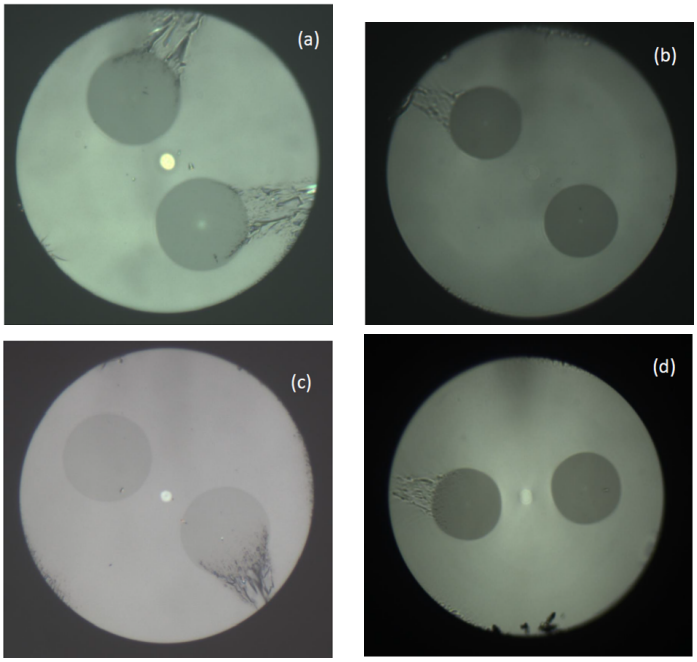

Figure 3.17: Cross-sectional images of the 6 µm fibers to tested. ErYb#1,#2,#3 & #4 are shown in (a), (b), (c) & (d) respectively.

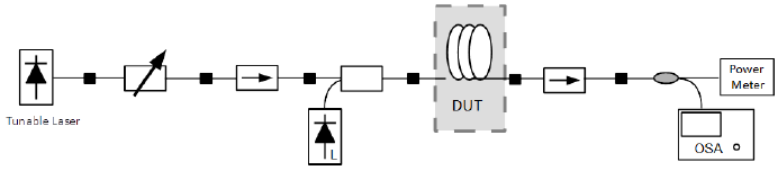

Figure 3.18: Amplifier test setup for testing of ErYb1, 2 & 3.

RIA results for ErYb#1-ErYb#4 are shown in Figures 3.20-3.23, respectively. It shows the amplifier performance for each ErYb fiber with measurements completed at a dose of 30 kRad and 100 kRad for all 4 fibers and at 0 kRad for ErYb#2 and ErYb#4. The reason for this was a problem with the test setup damaging ErYb#1 fiber loops at 0 kRad. The source for this damage was a damaged isolator, causing spurious lasing to occur in the fiber and therefore unwanted power spikes. The cause of this damage is most likely due to pumping the ErYb fiber at a gain of over or near 20 dB, increasing the power observed at 1064 nm which could then damage the isolator. The length of each fiber is 7.3 m for ErYb#1,#2,#3 and 8 m for ErYb#4.

A summary of the ErYb#1 results is shown in Table 3.23 for ErYb#1. The amplifier

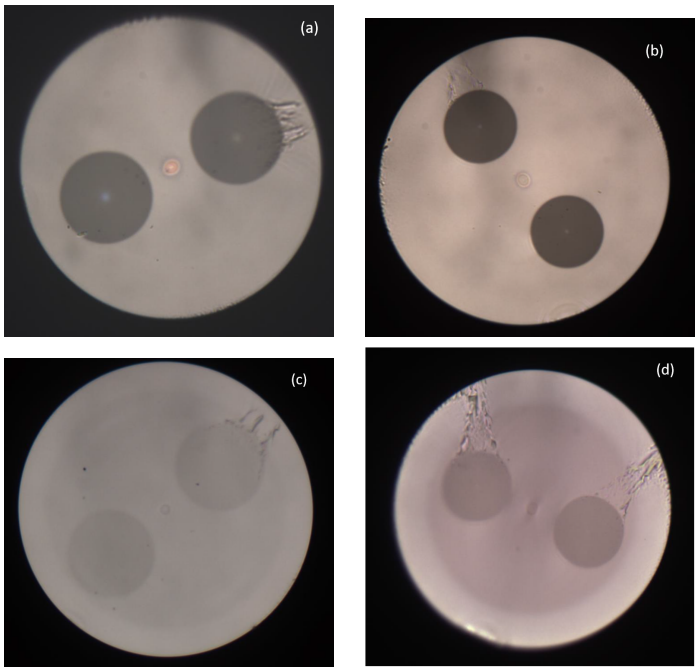

Figure 3.19: Cross-sectional images of the 6 µm fibers irradiated to a dose of 100 kRad. ErYb#1,#2,#3 & #4 are shown in (a), (b), (c) & (d) respectively.

exhibited a drop in gain of 1.67 dB at 1550 nm between doses of 30 kRad and 100 kRad. As no data was available for the same fiber at 0 kRad, the data was extrapolated assuming linear degradation, to provide an initial output power of 30.02 dBm.

With a gain degradation of 2.38 dB/100 kRad, it is expected that the evident radiation drop can be recovered by increasing the pump power and pumping the amplifier at a higher inversion level. This may only be possible when pumping the amplifier below pump powers of 11.3 W. Therefore for low power applications ErYb#1 may be suitable. However, for higher output power ($\geq$ 1 W) applications a different ErYb fiber or multiple stage of ErYb#1 must be used. This due to problems caused by 1064 nm parasitic lasing and limited output power due to a small core and low amount of ErYb doping to avoid RIA.

A summary of ErYb#2's results is shown in Table 3.24. ErYb#2 shows promise as a ErYb-doped fiber to be used in space applications. With a drop of 1.78 dB at 1550 nm from 0 kRad to 30 kRad, this is similar to ErYb#1 (a rad-hard fiber by design). However, performance worsens when approaching 100 kRad with a total gain drop of

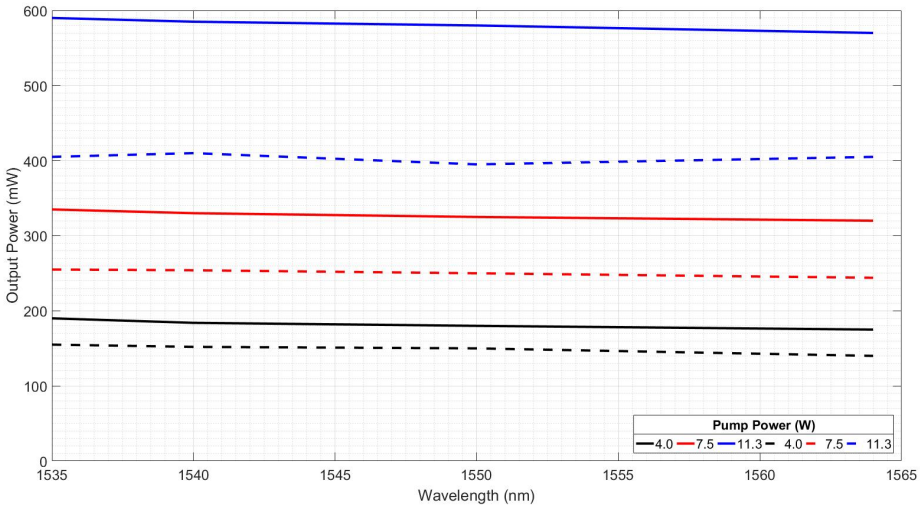

Figure 3.20: Amplifier performance of ErYb#1 after irradiation at 30 kRad (solid) and 100 kRad (dashed).

λ (nm)	ΔG_{30-100}	$\Delta G/100$ kRad
1535	1.63	2.33
1540	1.54	2.21
1550	1.67	2.38
1564	1.48	2.12

Table 3.23: Summary of gain degradation of ErYb#1 at a pump power of 11.3 W. Units: dB.

5.11 dB from 0 kRad, which is over double the loss seen by ErYB#1. Therefore, this fiber is suitable for low dose applications, such as for use at LEO, or for high dose applications with some spot shielding being provided by aluminium casing and the pump power being adjusted to fully invert the fiber to avoid signal re-absorbtion and help with reducing RIA by photobleaching.

A summary table for ErYb#3 is shown in 3.25 with extrapolated 0 kRad values. It shows that ErYb#3 performed poorly with an induced gain drop of 11.48 dB/kRad. Because of this high measured RIA ErYb#3 can be discounted as a suitable fiber to use in space applications. This would still be the case if spot shielding was used to reduce the dose, even at low radiation environments such as LEO.

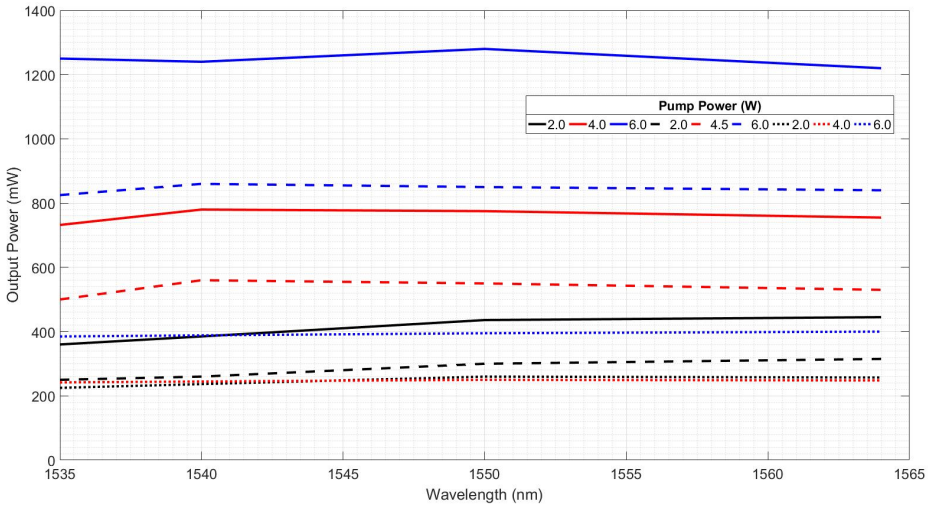

Figure 3.21: Amplifier performance of ErYb#2 after irradiation at 0 kRad (solid), 30 kRad (dashed) and 100 kRad (dotted).

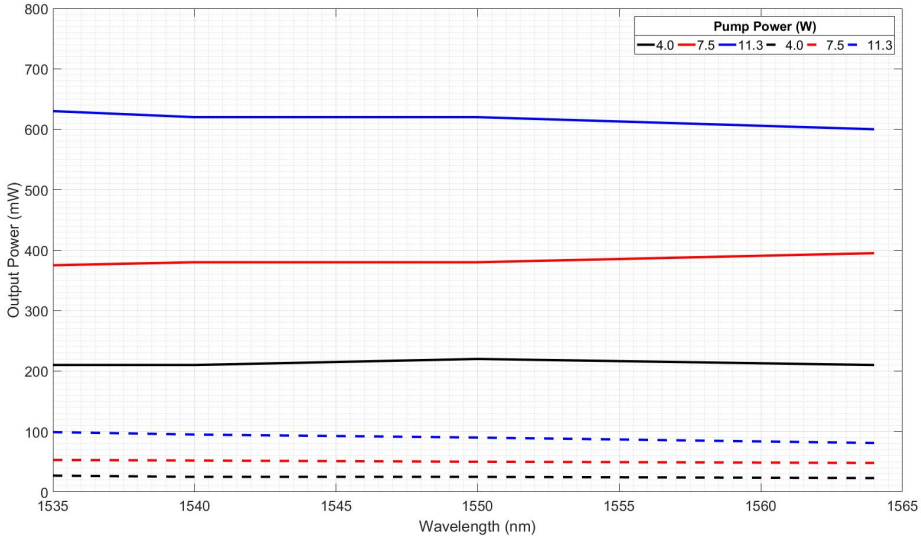

Figure 3.22: Amplifier performance of ErYb#3 after irradiation at 30 kRad (solid) and 100 kRad.

λ (nm)	ΔG_{0-30}	ΔG_{30-100}	ΔG/100 kRad
1535	1.80	3.31	5.11
1550	1.78	3.33	5.11
1564	1.62	3.22	4.84

Table 3.24: Summary of gain degradation of ErYb#2 at a pump power of 6.0 W. Units: dB.

λ (nm)	ΔG_{30-100}	ΔG/100 kRad
1535	8.04	11.48
1540	8.15	11.64
1550	8.38	11.97
1564	8.70	12.42

Table 3.25: Summary of gain degradation of ErYb#3 at a pump power of 11.3 W. Units: dB.

Table 3.26 shows a summary of the observed RIA for ErYb#4. It shows that ErYb#4 is not suitable for use in the space environment, even a low dose orbit or by using spot shielding. This is because is shows worst degradation than ErYb#2 at a dose of 30 kRad and although it can be reduced by using shielding, the amount of shielding needed makes using this fiber infeasible. In addition, this conclusion is in agreement with other data suggesting that this fiber is not suitable for space applications [3.8].

λ (nm)	ΔG_{0-30}	ΔG_{30-100}	ΔG/100 kRad
1535	2.78	1.76	4.54
1540	2.91	2.43	5.34
1550	3.40	3.35	6.75
1564	4.08	2.51	6.59

Table 3.26: Summary of gain degradation of ErYb#4 at a pump power of 6.0 W. Units: dB.

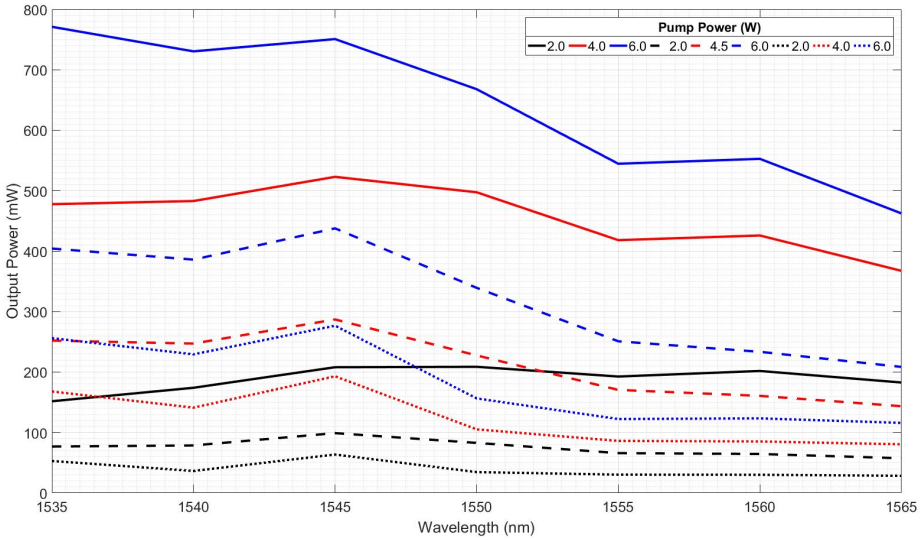

Figure 3.23: Amplifier performance of ErYb#4 after irradiation at 0 kRad (solid), 30 kRad (dashed) and 100 kRad (dotted).

3.5.2 12 µm EYDF Testing and Results

To develop laser transmitters with an output power > +30 dBm, a larger core , double-clad fiber was used to increase the gain available to the signal. Typically, a larger core, double clad fiber is used as the second (or later) stage of a HPA with the first stage typically being core-pumped only. Figure 3.24 shows the optical schematic of the test setup. The fiber length was fixed at 5.5 m, the input power at 35 mW and signal wavelength at 1550 nm, although measurements were made at 1540 nm and 1560 nm. The output power was monitored via both an OSA and power meter (not shown). Care was taken on the output fiber as it was a bare fiber, an angle cleave was used such that back-reflected light was minimised.

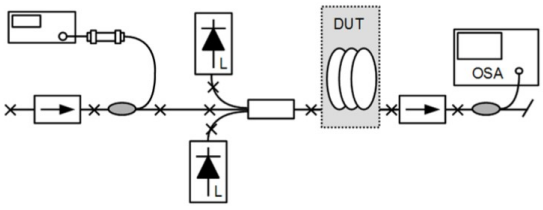

Figure 3.24: Test setup used to assess ErYb#5's amplifier performance.

Results showing the amplifier performance of ErYb#5 is given in Figure 3.25. It shows that for a dose of 100 kRad an output power of 35.05 dBm (3.2 W) is achievable. More interestingly, Figure 3.25 shows an average degradation in gain of 0.15 dB/100 kRad, showing hardness to radiation which is encouraging. The reason for this that at this point the fiber is being operated at high pump powers which are providing a source of photobleaching to the RIA, thus reducing it's effect on the gain performance of the fiber [3.9], [3.10].

Due to the nature of this surprising result and on reporting this result to ESA a repeat set of the measurements at a wavelength of 1560 nm was completed and results given in Figure 3.26. Both measurements were completed on fiber that had been irradiated at 100 kRad with the data presented for the repeat set shown as 'Re-Run' in Figure 3.26.

It must be noted that the output power of the test conducted in this section only reaches a value of 33.2 dBm and not 35.02 dBm as previously achieved. This was due to the fiber Q-switching due to SBS. SBS is a non-linear effect, which limits high-power fiber amplifier/laser operation, where acoustic waves form in the fiber due to photons scattering within the fiber core. This can cause a large power build up and cause fiber damage.

No SBS events occurred on the previous characterization as the input source was a tunable laser that had a broader spectral bandwidth than the narrow linewidth DFB source used for the repeated set of measurements. As SBS is related to the acoustic vibration of the glass lattice it has a narrow resonant frequency/bandwidth of approximately 50 MHz. Stimulated energy transfer only occurs effectively if the driving and frequency shifted light are precisely separated in frequency by the resonant frequency of the lattice. To this end if a broadband signal is used then this coupling does not happen efficiently with the driving optical power being averaged over the creation of acoustic phonons with different frequencies.

In laser transmitters, typically a DFB would be used as a source laser – which if operated unmodulated typically would have a bandwidth < 50 MHz increasing the risk of SBS, but would be broadened if modulated. The modulated linewidth depends on the

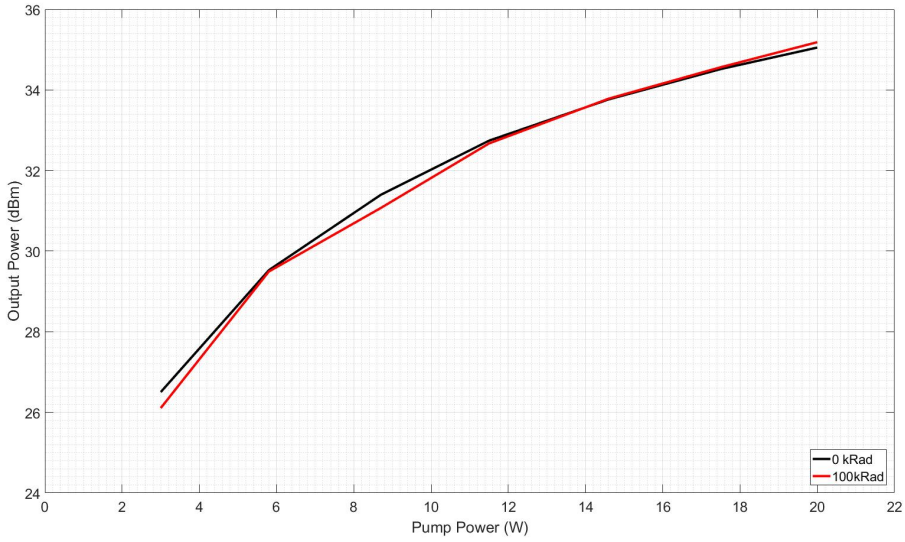

Figure 3.25: Amplifier performance of ErYb#5 as a function of pump power at a fixed wavelength of 1550 nm and input power of 35 mW.

modulation frequency/scheme, but the threshold is at least doubled if the modulation frequency is > 50 MHz [3.11]. Therefore Watt-level laser transmitters/amplifiers should not be used in an unmodulated manner.

From Figure 3.26 it can be clearly seen that the two tests both show similar values, thus supporting the conclusions that were previously made. As a measure of comparing the two results, linear fits were made on the two lines, yielding the fiber efficiency, and the gradient of each line compared. The efficiency for the original test was 15.26 % while the efficiency for the re-run test was 14.22 %. This equates to a percentage difference in the two efficiencies of 6.82 %, well within the measurement error for the two tests. Measurement error is typically 5 % but in this case the error was increased for three reasons:

- Components differences between the tests such as the source, optical isolators and optical combiners and pumps.
- Variations in component attributes such as coupling ratios in the combiners and variations in insertion loss in both the optical isolators and combiners

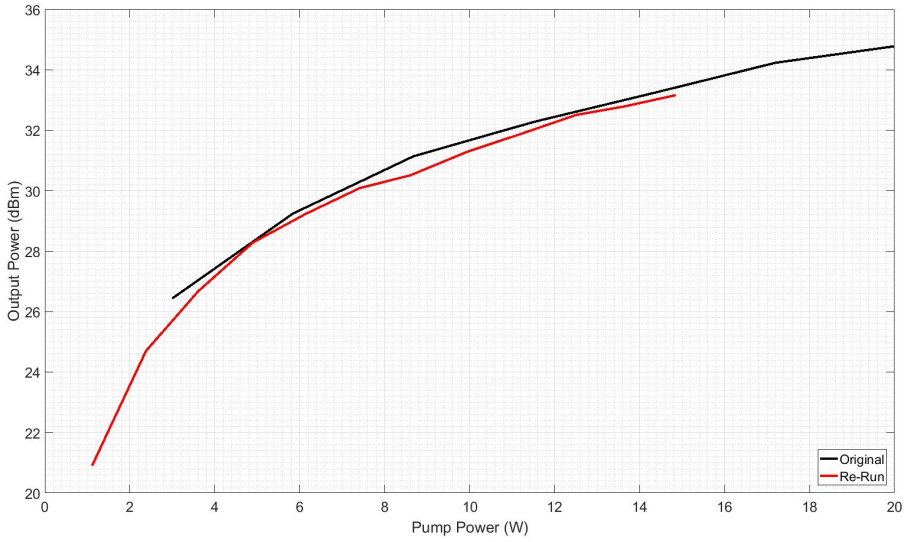

Figure 3.26: Amplifier performance and re-run data of ErYb#5 at a wavelength of 1560 nm and irradiated dose of 100 kRad. Fiber failure occurred at an output power of 33.2 dBm.

- Process variability, such as splice losses including PER loss, fiber coiling losses and viability in pump absorption, power meter imprecision and power supply/driver imprecision.

In terms of conclusions to be drawn from this testing, it can be said that the previous results hold true for this batch of fiber irradiated at 100 kRad. This is because in the two tests that have been carried out a high amount of similarity between the two data sets is shown with some variation due to measurement error. This repeated measurement does highlight the difficult in accurately measuring the gain change of the radiation hardened EYDFAs under γ-irradiation – especially when running in the high gain operation outlined in this section that may mask RIA.

3.5.3 Comparison of results

A comparison of the each tested ErYb fibers' RIA is given in Table 3.27 for a fixed signal wavelength of 1550 nm, the baseline signal wavelength for a C-band based system. Its shows that ErYb#5 is the best fiber in terms of RIA performance (0.15 dB/ 100 kRad).

Fiber	ΔG_{30-100}	ΔG/100 kRad
ErYb#1	1.67	2.38
ErYb#2	1.78	5.11
ErYb#3	8.38	11.97
ErYb#4	3.35	6.75
ErYb#5	-	0.15

Table 3.27: Comparison of tested ErYb fibers at a signal wavelength of 1550 nm. Units: dB

However, ErYb#5 is designed with a larger core and is of a specialist, radiation-hardened nature. This therefore raises two issues. The first is that because it is a specialist fiber, the cost of this fiber is high when compared to the other fibers (including ErYb#1). The second is issue is that of it having a 12 µm core. This is because for operation in the 1 W regime, there are more efficient ways of reaching the output power and reducing the ASE noise generated by the amplifier.

In the case of the 1 W regime, ErYb#1 shows the best RIA performance (2.38 dB/100 kRad) of the 4, 6 µm core diameter ErYb fibers tested. Once again, this is a radiation hardened ErYb fiber co-doped with cerium and has a higher cost when compared to ErYb#2,#3 and #4. For commercial applications, the use of a specialist fiber can be not feasible due to cost constraints. A trend which is becoming more commonplace in the space industry as more satellite constellations are being built and flown. Therefore for commercial applications, the COTS fiber ErYb#2 is most suitable as it displays the lowest RIA of the 3 COTS ErYb fibers. Although an unacceptable amount of RIA is reported for a dose of 100 kRad, the degradation of gain at 30 kRad is comparable to ErYb#1. This means the same performance as a specialist fiber can be achieved in low dose environments such as LEO or in higher dose environments when spot shielding can be used to reduce the dose observed by the fiber.

3.6 Conclusion

To conclude, 3 new classes of passive optical component were tested to assess their suitability for space applications. These were a compact 1 µm isolator, PM hybrid and non-PM hybrid components. These passive components underwent a test campaign to assess their mechanical, thermal, vacuum and radiation performance to levels comparable to those seen in the space and launch environment. It is reported that for LEO applications that both classes of hybrid component are suitable for space applications and can be considered for further use within space laser transmitter designs. The status of the 1 µm isolator is unclear however due to a failure of one part in the fiber-pull test and another single part failure in the shock test. These can still be considered for future use yet must be assessed further before incorporation into any design.

In addition, 5 ErYb-doped fibers were assessed for their use in space by characterising their RIA at steps of 30 kRad and 100 kRad. For operation in the 30 dBm regime, it can be concluded ErYb#1 was the most resilient. However, this is a specialist radiation-hardened fiber which is very costly so is not suitable for low-cssost applications. ErYb#2 shows promise of being used up to doses of 30 kRad, making it suitable for use in LEO. For amplifiers in the multi-Watt regime, it has been shown that ErYb#5 was resilient to radiation with a reported loss of 0.15 dB/100 kRad and that any change in output power is within measurement error.

With these results, it gives confidence into designing the systems which are presented in later chapters as some of the parts to be used have now been proven to be at a TRL 4. The next steps would be to integrate them into a larger amplifier/transmitter system such that their TRL level can be raised further to TRL 5/6.

References

[3.1] European Space Agency (ESA), "ESCC Basic Specification No. 23201 - Evaluation Test Programme Guidelines for Laser Diode Modules," 2014.

[3.2] European Space Agency (ESA), "ESCC Basic Specification No. 23202 - Validation and Lot Acceptance Testing Guidelines for Laser Diodes," 2018.

[3.3] United States Department of Defense, "MIL-STD-883K Test Method Standard Microcircuits," 2017.

[3.4] Telcordia, "GR-326-CORE - Generic Requirements for Singlemode Optical Connectors and Jumper Assemblies," Telcordia, Tech. Rep., 1999.

[3.5] Telcordia, "GR-468 - Generic Reliability Assurance Requirements for Optoelectronic Devices Used in Telecommunications Equipment," Telcordia, Tech. Rep., 2004.

[3.6] European Space Agency, "ESCC Basic Specification No. 22900, Total Dose Steady-State Irradiation Test Method.," 2016.

[3.7] S. Girard, Y. Ouerdane, B. Tortech, C. Marcandella, T. Robin, B. Cadier, *et al.*, "Radiation Effects on Ytterbium- and Ytterbium/Erbium-Doped Double-Clad Optical Fibers," *IEEE Transactions on Nuclear Science*, vol. 56, no. 6, pp. 3293–3299, Dec. 2009. DOI: 10.1109/TNS.2009.2033999.

[3.8] S. Gupta, D. Engin, D. Pachowicz, J.-L. Fouron, J. Lander, X. Dang, *et al.*, "Development, testing, and initial space qualification of 1.5-μm high-power (6W) pulse-position-modulated (PPM) fiber laser transmitter for deep-space laser communication," in *Free-Space Laser Communication and Atmospheric Propagation XXVIII*, H. Hemmati and D. M. Boroson, Eds., vol. 9739, Mar. 2016, p. 97390V. DOI: 10.1117/12.2213661.

[3.9] E. J. Friebele and M. E. Gingerich, "Photobleaching effects in optical fiber waveguides," *Applied Optics*, vol. 20, no. 19, p. 3448, Oct. 1981. DOI: 10.1364/AO.20.003448.

[3.10] S. Girard, A. Morana, A. Ladaci, T. Robin, L. Mescia, J.-J. Bonnefois, *et al.*, "Recent advances in radiation-hardened fiber-based technologies for space applications," *Journal of Optics*, vol. 20, no. 9, p. 093 001, Sep. 2018. DOI: 10.1088/2040-8986/aad271.

[3.11] Y. Aoki, K. Tajima, and I. Mito, "Input Power Limits of Single-Mode Optical Fibers due to Stimulated Brillouin Scattering in Optical Communication Sys-

tems," *Journal of Lightwave Technology*, vol. 6, no. 5, pp. 710–719, 1988. DOI: 10.1109/50.4057.

Chapter 4

Low-Power Laser Transmitters for CubeSat-class Applications

4.1 Introduction

With the emergence of the CubeSat, a micro-satellite standard originally designed for low-cost and rapid prototyping by both universities and private organisations, there is great commercial interest in using these class of satellite to provide cheap access to space. Since 1998 there has been a total of 966 nano-satellites launched with a forecast of over 3000 nano-satellites to be launched in the next 6 years. The main driver for this is CubeSat constellations making up a large majority of the launches. The main applications for CubeSat constellations can be the same as traditional LEO satellite constellations (e.g. communications, Earth observation and internet of things). However, because of the CubeSat's inherent smaller size, a larger number of satellites is needed to accomplish the same task.

As is with small satellites, there is becoming an increasing strain on traditional RF communications there has been investigation into using lasercom as a communication technique. Currently, the main method of downlink is through RF technologies as lasercom for CubeSat platforms has still not been demonstrated to a good enough level to warrant usage of RF systems.

Academic research into laser transmitters for CubeSats originated from MIT [4.1].

Which has provided some solutions to lasercom from CubeSats but has not yet been proven in-orbit. Commercial research through NASA's OCSD program in partnership with Aerospace Corp. has demonstrated a link at 100 Mb/s using 1064 nm technology [4.2]. Meanwhile, Fibertek Inc. have shown research into developing a C-band laser transmitter for CubeSats but this only in the developmental stage [4.3], [4.4]. For more information on these systems see Section 2.3.2.

This chapter will describe the efforts in designing a low-power, CubeSat LTX so that this problem can be addressed. It will focus upon the LTX design in the areas of:

- Optical architecture and design;
- Mechanical design;
- Electrical architecture and design (where applicable);
- Thermal design.

In addition to presenting the design, the assembly and integration of the LTX will be shown along with testing with a aim to verify the design. At the end of this chapter, the LTX will be at a TRL of 5-6, paving the pathway towards qualification and flight.

4.1.1 The CubeSat

Originally developed in 1999 by California Polytechnic University and Stanford University [4.5], the CubeSat was originally conceived to provide a standard such that the cost and effort of launching and operating a mission in space was greatly reduced. This has since evolved and as of 2014 over 100 organisations are currently developing CubeSat missions [4.6].

Shown in Figure 4.1 is the typical layout of a CubeSat. A CubeSat consists of a 1000 cm^3 cube weighing 1.33 kg. This is known as 1U and is the typical size of most CubeSats. However, more recently, 3U (10 x 10 x 30 cm) CubeSats are becoming more prevalent for commercial missions due to the extra volume and surface area, for solar power generation, available over 1 U CubeSats. The actual workable space for 1U as defined by the design specification [4.6] is 96 x 96 x 96 mm with the extra space

taken up by the mechanical support structure. PCBs are typically arranged in a stack configuration which allows for 'plug-and-play' modules to be developed, in-turn reduces developmental efforts as developers can focus on the payload of the spacecraft.

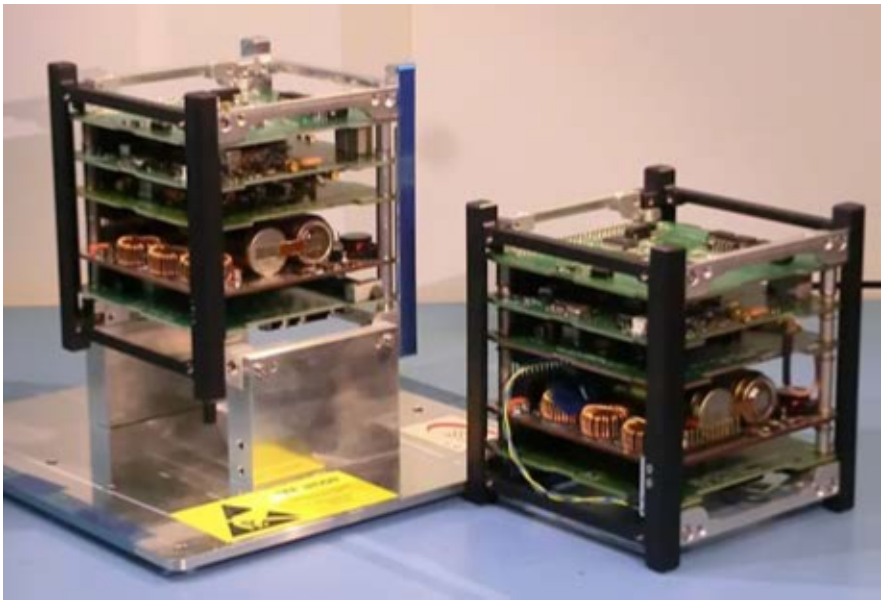

Figure 4.1: Photos showing the typical structure of 2 typical CubeSats (FUNcube). From: [4.7]

4.1.2 CubeSat Capabilities

Power Generation

Power generation on-board CubeSats is limited and is now becoming a limiting factor in designing missions. Currently, CubeSat power is generated via solar panels and is limited by the solar panel surface area and the presence of any batteries on-board. For a 3 U CubeSat with deployable solar panels, it can typically provide an average power of approximately 10 - 20 W with the ability peak power generation 60 W if a battery is used [4.8].

Pointing and Tracking

Pointing and tracking, provided via the attitude, determination and control system, greatly limits applications where telescopes are used due to their small divergence/light

collection angle. Previously, a pointing accuracy of 2.0° has been demonstrated in orbit consistently [4.9]. Aerospace Corp.'s OCSD mission has been shown to provide a greatly improved pointing accuracy of 0.024° [4.2] but this is still in the early stages of the mission and has been only demonstrated once.

For optical communications, if suitable pointing of the spacecraft cannot be achieved via the attitude control system, then the beam must be pointed via another method. For a 1000 km downlink from LEO it has been shown that a telescope using a fine-steering mirror can achieve the necessary pointing accuracy [4.10].

Communications

As CubeSats are becoming increasingly complex, communication sub-systems have been moving to shorter wavelengths. The shift from UHF to Ku-band and then S/X-band transmitters is driven by the need to provide larger bandwidths so that more data from the spacecraft can be downlinked [4.11].

State-of-the-art CubeSat communications sub-systems provide a link in the S or X-band. For example ClydeSpace, a major supplier to CubeSat missions, currently offer a X-band transmitter which outputs a QPSK signal at a data rate of up to 50 Mbit s^{-1} and power of 2 W. This transmitter has a mass of 150 g and a power consumption of 10 W.

Although for CubeSats 50 Mbit s^{-1} is a good data rate, optical communications, as shown in this thesis, can easily provide data rates of up to 200 times this, up to a rate of 10 Gbit s^{-1}, without having to compromise on many of these SWaP parameters.

4.2 Laser Transmitter Target Specifications

Shown in Tables 4.1-4.4 are the target system requirements for the low-power CubeSat laser transmitter. To achieve TRL 5-6 the module is required to undergo testing on the lab bench. However, for this thesis environmental testing at temperatures of -5 and +50 °C shall take place to investigate the thermal performance of the LTX.

Parameter	Value	Unit	Notes
Operational wavelength	1535-1560	nm	-
Source intrinsic linewidth	< 500	MHz	CW-operation
Min. output power	200	mW	-
Modulation depth	> 20	dB	At 1.0 GHz
Data encoding scheme	Amplitude	-	Initially OOK
Fiber type	SM	-	Non-PM
SNR	> 20	dB	-
Output interface	Bare Fiber	-	CubeCAT only
Output fiber type	SMF28e+	-	-
Rise time Fall time	500	ps	10-90%
TX reflection isolation	-23	dB	-
Side Mode Suppression Ratio	30	dB	-

Table 4.1: Low-power CubeSat LTX optical specification.

Parameter	Value	Unit	Notes
Volume	Custom	-	Specific to CubeCAT laser terminal
Mass	≈ 150	g	TBD during AIT
Mechanical interface	Bolted to laser terminal structure		Exact interfacing TBD during AIT

Table 4.2: Low-power CubeSat LTX mechanical specification.

Parameter	Value	Unit	Notes
Operating temp. range	-5 to +50	°C	-
Survival temp. range	-45 to +85	°C	-
Vacuum	10^{-8}	Pa	-
Vent rate	4	kPa/s	-
Cooling Mechanism	Heat sink via spacecraft structure.		
Humidity	20 to 80	%	-
Vibration	TBD	-	-
Shock	TBD	-	-
Static loading	TBD	-	-
Outgassing	TML < 0.1 CVCM< 0.01 %	- -	Waivers needed for some components
Ionising radiation	20	kRad	-
Non-ionising radiation	10 MeV, 1.7e10 p/cm^2	-	-

Table 4.3: Low-power CubeSat LTX environmental specification.

Parameter	Specification			Unit	Notes
	Min.	Typ.	Max.		
Wall plug efficiency	10	-	20	%	w/o TEC
Electrical interface	16-way high-rel connector			-	-
RF input impedance	-	50	-	Ω	-
Modulation bandwidth	0.1	-	1.25	GHz	Target: 2.5 GHz
Source forward voltage	-	2.3	3.0	V	-
Source drive current	-	375	500	mA	CW @ 100 mW
Source TEC voltage	-	0.1	4.0	V	-
Source TEC current	-	0.1	4.0	A	-
Pump drive current Pump forward voltage	- -	- 3.7	1.0 4	A V	Set point TBD
Pump current transient	-	-	1.2	A	Time = 1 µs max.
Thermistor resistance	9.5	10.0	10.5	kΩ	T= 25°C

Table 4.4: Low-power CubeSat LTX electrical specification.

4.3 Laser Transmitter Design

This section shall describe the LTX design and any simulations or breadboard testing completed to preliminarily assess the design. A summary design process has also been covered in a paper by the author: [4.12].

The LTX designed was done so in the remit of the CubeCAT project, a joint project between G&H (UK), TNO and Hyperion Technologies B.V. (both NL). For the work presented in this thesis, the LTX is fully designed by the author and focused upon the light generation and amplification. TNO's focus was on the telescope and supporting mechanics. Hyperion B.V. developed the control electronics for providing a digital interface to the LTX. Shown in Figure 4.2 is the CubeCAT terminal. It has a size of 2 U (10x10x20 cm), a mass of 1 kg and has a total peak power of 10 W during communications.

The LTX's exact location and mechanical interfacing points are shown in Figure 4.3. It can be seen that that the mechanical volume is extremely limited and not of a standard shape. This poses a design challenge in the fact that the opto-electronics and fiber must fit within this volume whilst complying to the design rules given by G&H for fiber routing.

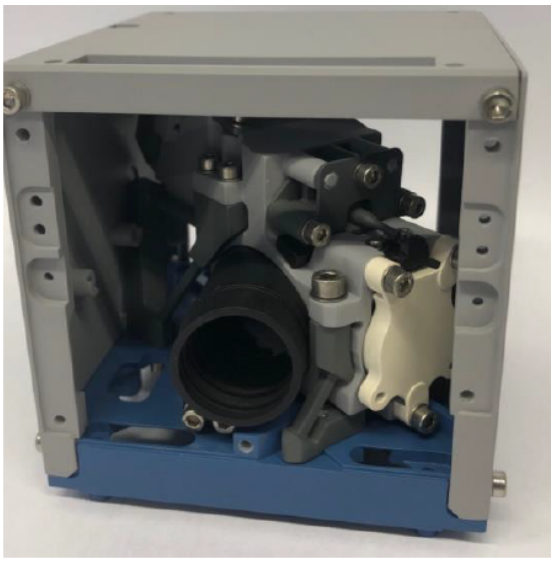

Figure 4.2: 3-D printed mechanical fit check of the CubeCAT terminal. Image provided by TNO.

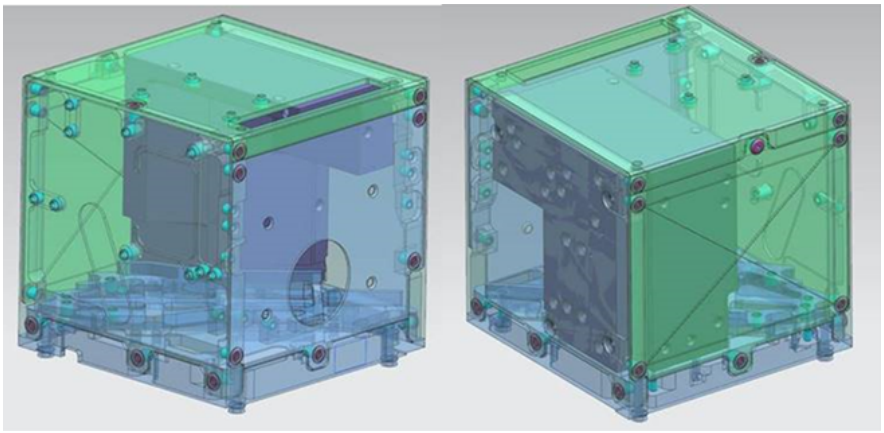

Figure 4.3: CAD image of the LTX's location within the CubeCAT terminal.

4.3.1 Optical Architecture

Based on the system requirements an initial optical architecture was generated and is shown in Figure 4.4. The optical architecture is based on a master-oscillator power amplifier (MOPA) design consisting of the laser source (DFB) and a bi-directionally pumped single stage EDFA.

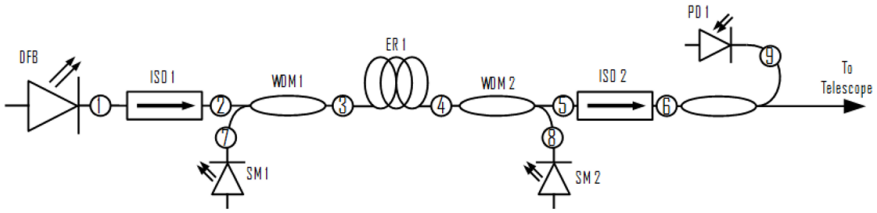

Figure 4.4: CubeCAT Optical Architecture. Splices are shown with circled numbers.

A single stage EDFA design was chosen as the required output power (min. 23 dBm) suggests that only 1, core-pumped EDFA stage is needed to provide the required amplification from a DFB that outputs 10 dBm, CW power. Therefore a minimum gain of 13 dB is needed, well within the operating capabilities of a core-pumped EDFA which can typically provide gains of up to 20 dB. A bi-directional pumping scheme was selected as this provides the best trade-off between output power and noise performance when compared to a purely co-pumped or counter-pumped scheme.

A monitor PD has been chosen such that the CW power of the LTX can be moni-

tored in-situ. As this is a CW measurement, the bandwidth of the PD must be lower than the modulation bandwidth of the system (100's of MHz).

Based on feedback from the end user (TNO) a bare fiber output will be provided such that easy integration with a telescope can be facilitated by fitting a ferule to the bare fiber at a later date. For future modules, depending on the application, a fiber interface such as a mini-AVIM bulkhead can be considered to be used.

4.3.2 Optical Simulations

Optical simulations based on the optical architecture shown in Figure 4.4 were completed to assess its potential performance. The simulations were broken up into two stages of investigation. These are:

- Continuous Wave Operation – Assessment of the LTX when operating in a CW mode. These simulations will be able to conclude whether one amplification stage is necessary to provide the correct output power over the wavelength range. In addition, the noise and gain performance over wavelength will be investigated.
- Dynamic Operation – These simulations will assess the LTX performance in the pulsed regime. I.e. when the DFB is being modulated with data. From this simulated eye diagrams will be generated which can then be analysed.

To meet the output power requirements set out in Table 4.1, a simulation was completed of the CW performance of the optical amplifier section. The simulation tool (OASiX, supplied by the active fiber manufacturer OFS) was selected such that it would provide the most accurate results for the active fiber to be selected; the tool was provided by the manufacturer with a correct set of Gilles' parameters of the fiber type and lot for the amplifier stage to be simulated. Baseline design parameters of an input power to the amplifier was set to +10 dBm, wavelength of 1545 nm, doped fiber loop length of 6m and bi-directional pump power of 500 mW selected. These were selected as these are the operational parameters for the first engineering model to be developed. Three sets of simulations were completed such that the amplifier block can be properly simulated:

- CW output power v pump power - Figure 4.5;
- CW output power & NF v wavelength - Figure 4.6;
- CW output power & NF v input power - Figure 4.7.

Figure 4.5 shows the simulated CW output power performance against a varying, bi directional pump power. Input power and wavelength were fixed at +10 dBm and 1545 nm. The output requirement of 200 mW (+23 dBm) is shown with the red, dotted line. Figure 4.5 shows that the output power specification is easily met at a value of 445 mW (approx. half the maximum available pump power of 1W. In addition it shows that with increasing the pump currents that an output power margin of 3.33 dB is allowed to be lost over life through mechanisms such as component degradation and radiation induced absorption, whilst still meeting the output power requirement of +23 dBm. Thus it can be concluded that the use of a COTS-grade fiber is suitable for use within the amplifier as a RIA of 3.33 dB is a large enough margin for the gain degradation observed by the active fiber.

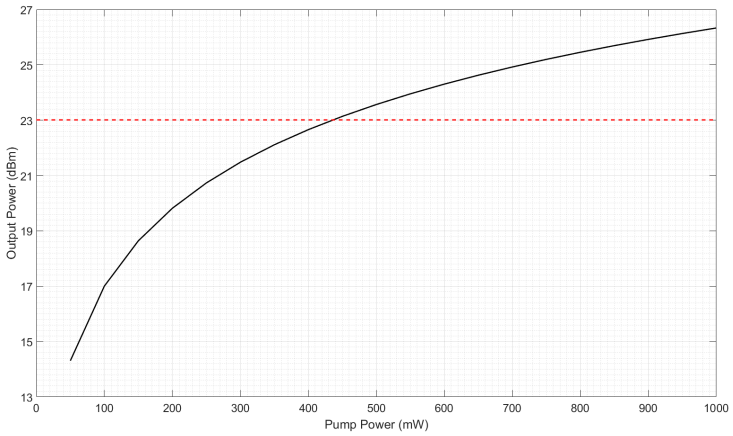

Figure 4.5: Simulated CubeCAT LTX CW output power performance against pump power for a fixed input power of +10 dBm, wavelength of 1545 nm and bi-directional pumping scheme.

The simulated performance of the amplifier block over the optical C-band (1525-1565 nm) is presented in Figure 4.6. The input power and pump power was fixed at +10 dBm and 500 mW, respectively. Figure 4.6 predicts stable performance across the

C-band (0.48 dB stability) and an output power always above the requirement of 200 mW. The NF performance is as expected for a booster amplifier operating with the active fiber in a fully inverted condition.

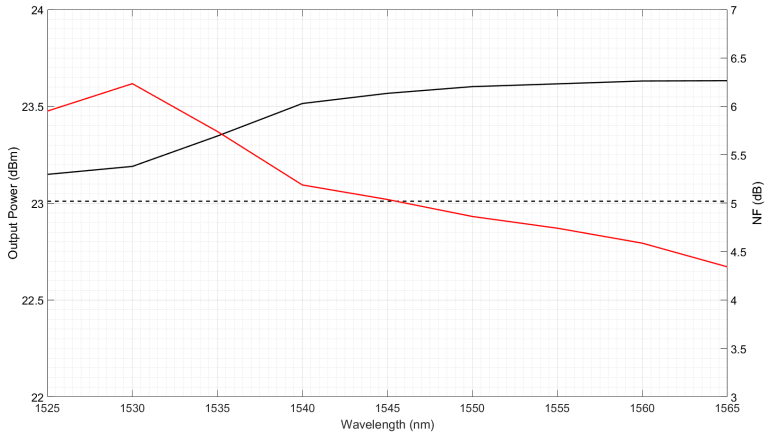

Figure 4.6: Simulated CubeCAT LTX CW output power (black, solid) and NF (red, solid) over the C-band for a fixed input power of +10 dBm and bi-directional pump power of 500 mW.

The influence of input power to the amplifier block was simulated and results are shown in Figure 4.7. The total bi-directional pump power and wavelength were set to 500 mW and 1545 nm, respectively. As the active fiber is near full inversion it is expected that the input power should scale linearly with input power but on a small scale. I.e. The amplifier is saturated with respected to the input power. This shows that as the DFB degrades over life. The CW output power of the LTX will not be effected to a large degree. As the baseline operation point is near +10 dBm, it is expected that the output power will not degrade below the EOL power requirement of +23 dBm (200 mW) unless the DFB laser diode suffers a failure.

The dynamic operation of the system is due to the operation of the laser source, in this case a DFB laser diode. The main purpose of this simulation was to find a suitable modulation and bias current level to operate the DFB laser at 1 Gbps as this data rate was given as the target data rate by the end user (TNO).

The baseline design is to modulate the laser diode to a power of +10 dBm from near threshold current as this would provide the best extinction ratio between the '0'

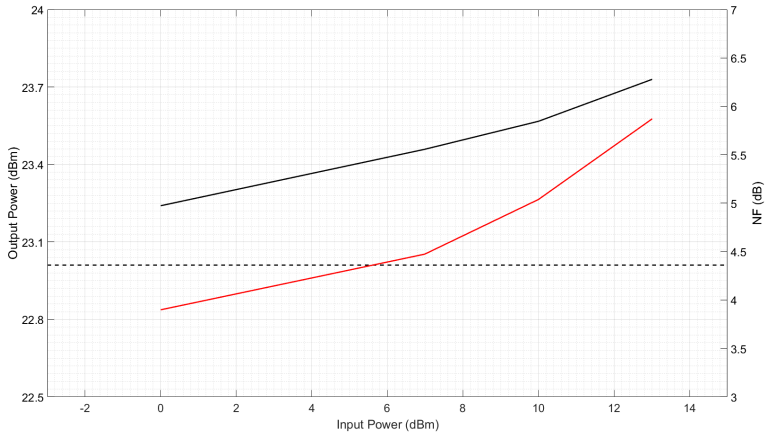

Figure 4.7: Simulated CubeCAT LTX CW output power (black, solid) and NF (red, solid) against input power for a fixed wavelength of 1545 nm and bi-directional pump power of 500 mW.

and '1' levels. However, after speaking to component suppliers, the 50 Ω resistor used in the bias-T of the DFB laser is only rated to 35 mW of RF power. With this in mind this would limit the modulation current to pass through the resistor to be 24.5 mA. As the degradation of the resistor over life has to be taken in to account, a maximum modulation current value of 20 mA is suggested which corresponds to a 7 mW (+8.45 dBm). By comparing this value to the curve shown in Figure 4.7 it can be seen that this value is acceptable to the system without degrading the performance of the LTX.

To assess the effect of modulation current, eye diagram analysis through OptiSystem simulations were used to assess the effect of modulation current on the eye opening. Three example eye diagrams are shown in Figure 4.8 at modulation currents of 4 mA (red), 10 mA (dark yellow) and 20 mA (blue/grey). The simulation was set such that the DFB DC bias was set at 45 mA and threshold current at 50 mA. This was to provide a large enough extinction ration between the '1' and '0' bit would be present such that a sensible bit discrimination level could be set. This can be seen in Figure 5 between the red (still below I_{th}) and dark yellow (above I_{th}) curves.

To quantitatively assess the impact of modulation current, a graph of eye opening factor, a ratio of the eye height (vertical opening of eye) to eye amplitude (difference between mean values of '1' and '0' values) versus modulation current can be plotted

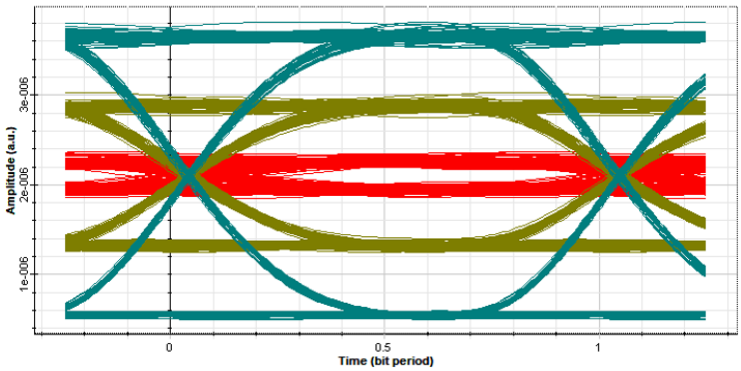

Figure 4.8: Simulated Eye diagrams for a DFB modulation current of 2 mA (red), 10 mA (dark yellow) and 20 mA (grey/blue) with a DFB I_{bias} = 45 mA and I_{th} = 50 mA.

(Figure 4.9). It can be seen that as the modulation current is increased, the eye becomes more open as the modulation current is increased as expected. No measurement was able at 2 mA due to the eye being too closed due to too much time jitter. However, what is surprising is the increase in eye opening from 4mA to 10 mA. As this appear to be a non-linear operating region, operation is not recommended in this location.

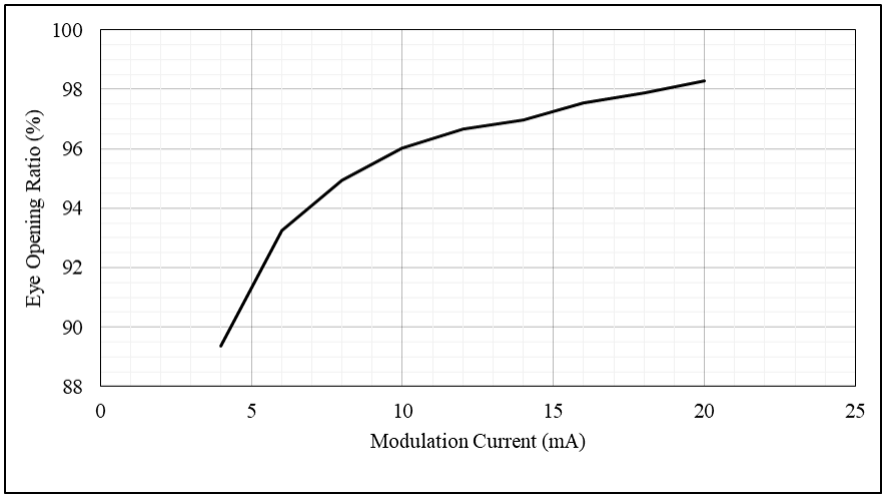

Figure 4.9: A graph of simulated eye opening factor as a function of modulation current.

In an ideal situation, as high a value of modulation current should be selected but in practice this is limited by the drive electronics. Based off external driver requirements a modulation current of 10 mA is allowed. This in turn leads to an eye opening ratio of 96% which is acceptable on a system level. With a modulation current of 10 mA

selected, the DFB is predicted to output approximately 5 mW (+6.98 dBm). Based off the results shown in Figure 4.7, the output power requirement is met even though the input power to the amplifier stage has dropped. Based on the simulations discussed, the current levels for the '1' and '0' bit can be set according to the diagram shown in Figure 4.10.

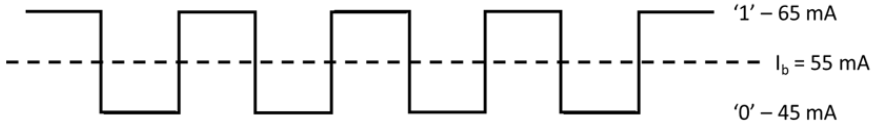

Figure 4.10: Proposed drive current levels of the DFB laser.

4.3.3 Optical Breadboarding

To verify the optical design simulations, optical breadboarding took place. The breadboard was built using the baseline components such that it would be representative of the finished module. It focused on the two major optical blocks of the LTX. The source laser was characterised through:

- The spectral performance of the source will be investigated via a OSA scan. This will highlight the presence of any side modes or any other spectral issues.
- The dynamic performance will be investigated in which eye diagrams will be generated at 100 and 500 Mbit s^{-1}.

The optical engine (source and amplifier) were characterised by the four tests:

- Output power v pump current – A L-I curve for the optical engine will be measured, showing the required pump currents needed to operate the engine at the required output power.
- Output power & NF v input Wavelength – As the laser used in this test operates at 1550 nm (not 1545 nm), the performance of the optical engine over the C band must be characterized to see if the results can be used to verify the performance of the optical engine at 1545 nm.

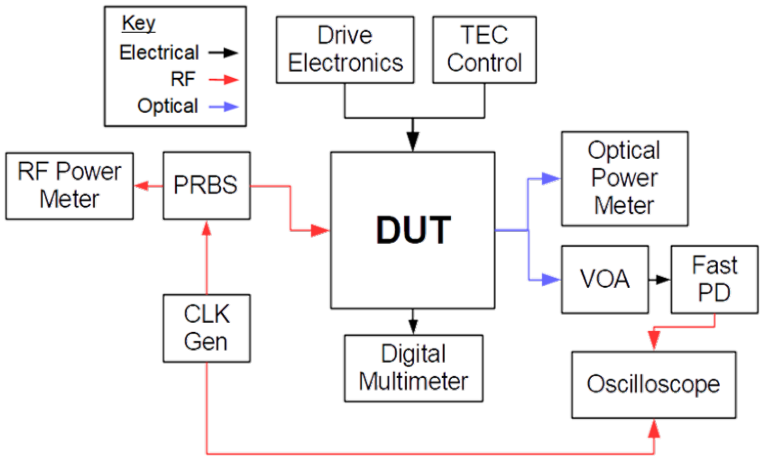

Figure 4.11: Schematic of CubeCAT test-bed.

- Output power v input power – The performance of the optical engine for a varied input power will be investigated. A good performance at lower input powers allows for a lower modulation current of the seed laser.

Test Setup

A schematic of the test kit is shown in Figure 4.11. It consists of three main parts: the laser drive electronics, the high frequency generation and detection scheme. The CW bias current to both the pump and DFB laser were supplied through constant current drivers. A psuedo-random bit generator (PRBS) was used along with a high speed sine-wave generator (as the clock) to generate the required pulse shape which will be then passed to the DFB laser and provide the AC modulation. The clock signal, provided by a sine wave generator was used to trigger the PRBS such that a external clock could be fed into the PRBS and the data modulation rate changed. The clock/16 signal exiting the PRBS was used for triggering the oscilloscope when characterising the pulse shapes.

The location of sensitive equipment on the test bench is important as to avoid crosstalk between the high speed RF lines. To this end the oscilloscope was placed as far as possible from the clock signal generator and PRBS as it was found that this crosstalk caused the instabilities shown in Figure 4.13. To avoid any impedance

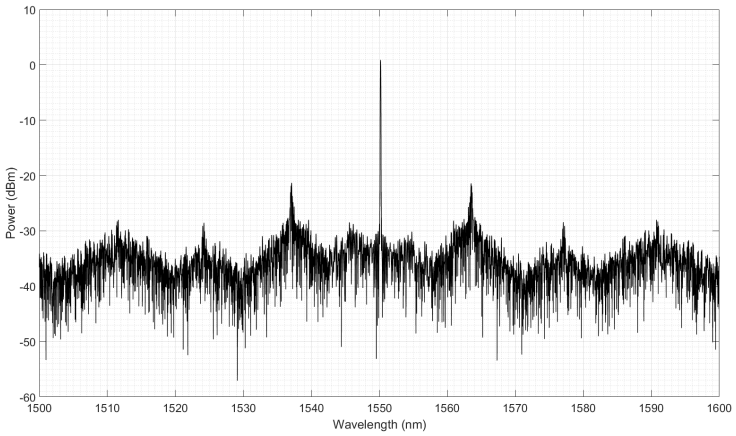

Figure 4.12: Output spectra of the CubeCAT breadboard source laser. NB: Output power has not been adjusted to account for monitor tap.

mismatching in the system, all impedances were kept to 50 Ω.

In the optical output, a VOA was used to avoid saturation of the detection photodiode. Although Figure 4.11 shows an optical connection to both a power meter and VOA at the same time, this was never the case as the LTX was operated in either the CW or pulsed regime.

The output spectra of the source laser used in the breadboard testing is shown in Figure 4.12. It has a central wavelength of 1550 nm, however the LTX which was built has a central wavelength of 1545 nm. However, the DFB used to create the spectrum in Figure 4.12 was of the same chip and housing family as the part used within the product. Figure 4.12 has not taken into account normalising the power for the input tap and coupling losses, but the output power of the laser diode is +10 dBm .

The dynamic performance was simulated via eye diagram testing at data rates of 100 Mbit s^{-1} and 500 Mbit s^{-1}. Figure 4.13 shows the construction of an eye diagram on an oscilloscope based on the received light levels with individual traces (representing one 'bit') overlaid on one another.

Although a good eye opening is seen in Figure 4.13, thus indicating a suitable modulation level of 10 mA, significant ringing is present suggesting that there is a problem with the RF driving circuit or signal distortion caused by a mismatched interface. The time jitter present is thought to be from the measurement system and improper syn-

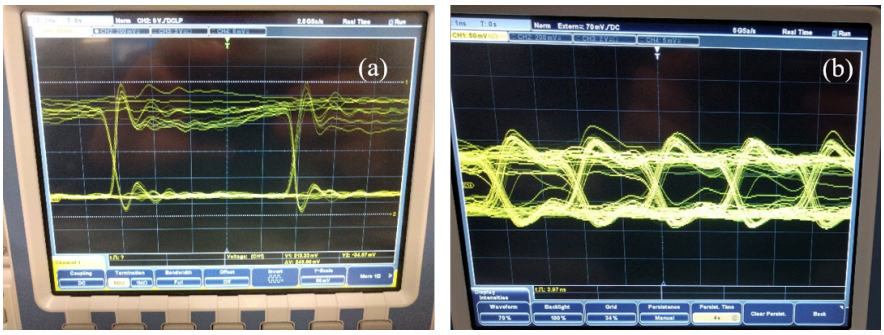

Figure 4.13: Photo of an Eye Diagram generated on an oscilloscope at 100 Mbps (a) and 500 Mbps (b) on the CubeCAT breadboard.

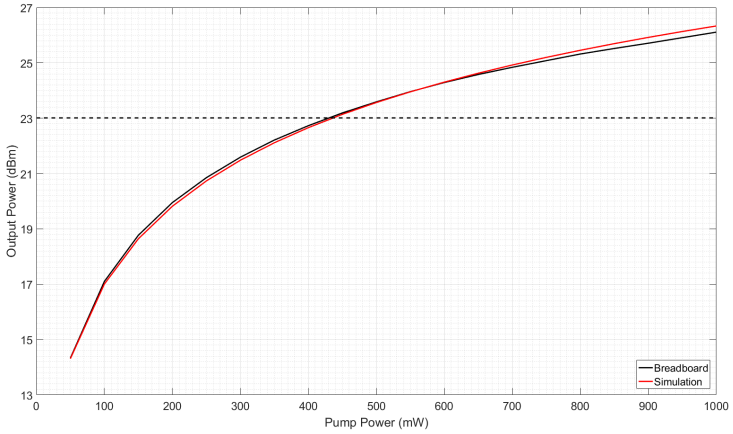

Figure 4.14: P_{out} v I_{pump} for the CubeCAT breadboard. Shown are the breadboard result (black) and simulated result (red).

chronization between the clock and received signal. From this data no realistic eye measurements and therefore BER measurements could be made due to ringing. However, the modulation of the laser source has been demonstrated. With this in mind, further work is needed to provide better electrical interfacing to reduce the level of ringing observed and to maintain signal integrity.

Figure 4.14 shows the relationship between the output power and the pump currents. The input power to the optical engine was +9.97 dBm, which is representative of the predicted input power. The signal wavelength used was 1550 nm (the same laser was used as shown in Figure 2).

Figure 4.14 shows that the output power specification (dashed line) is easily met

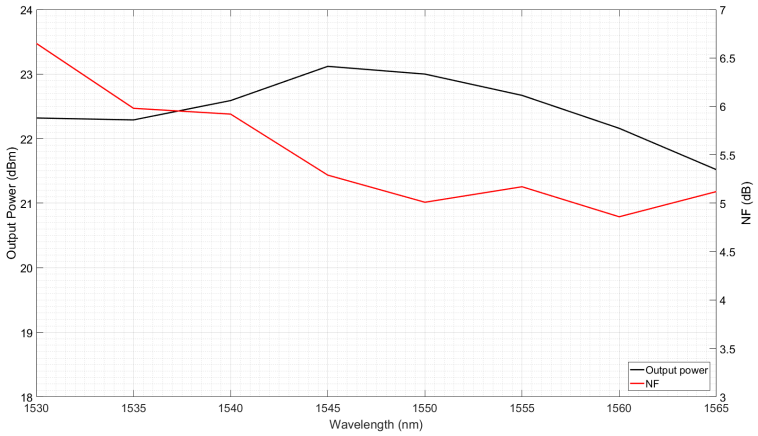

Figure 4.15: CubeCAT Output Power & Noise Figure against Signal Wavelength.

with a pump current of just over 400 mA. The result of an output power of 200 mW against a pump current of 400 mA results in an E/O efficiency of 13.5% (excluding seed laser). This result is encouraging as it shows that the output power can be increased if needed. One example would be if an increase in data rate or if atmospheric conditions worsen and an increase in output power is needed.

In addition, also shown is the simulated data (red), as presented in Figure 4.5. There is little variation between the simulated and breadboard values with a maximum difference observed of 0.22 dB at high pump drive currents. This is well within the margin of error (±0.5 dB). Thus it can be concluded that the simulation holds for a real system. Giving confidence in developing a system operating at 1545 nm.

Figure 4.15 shows the wavelength dependency of the laser engine over the c-band. The test was set such that an input power of +4.43 dBm was used and a total pump current of 935.5 mA was used. It shows that the output power is similar over the C-band meaning that the results shown in Figure 4.12 and 4.14 can be assumed to apply at the operational wavelength of 1545 nm.

In addition, the NF characteristics are as expected for this laser engine. With a maximum NF of 5.98 dB at 1535 and a NF of 5.29 at 1545nm (NF for a typical booster amplifier is approx. 6-7 dB), the laser engine is performing as required. These results are encouraging as it shows that the laser engine is operating in a fully inverted

$\mathbf{P_{in}}$ **(dBm)**	$\mathbf{P_{Out}}$ **(dBm)**
2.99	22.04
5.04	22.69
10.00	23.09

Table 4.5: Values for P_{in} v P_{out} for the CubeCAT breadboard

state even at a reduced pump power, therefore reducing the amount of noise which is generated by the laser engine. This in turn will improve the link budget by having a larger OSNR than originally anticipated.

Table 4.5 shows the variation of the output power as a function of the input power. It clearly shows that even at low input powers of approx. 3 and 5 dBm, the output power does not vary as quickly. This implies that the amplifier is saturated and a reduction in input power to the amplifier stage shall not greatly affect the performance of the laser engine.

These results are beneficial as it means that the modulation current to the laser diode can be decreased to a safe operational level. In the past some concern was had as the resistor used in the seed laser package was rated to only 30 mW, which corresponded to a modulation current of 24.5 mA; smaller than the previously proposed modulation current of 27.5 mA. These results show that a reduction of the modulation current to 20 mA (which corresponds to an input power of 8.45 dBm) will have little impact on the overall output power performance of the laser engine whilst vastly improving the reliability of the laser engine.

4.3.4 Mechanical Design

As previously mentioned, at the start of this design process, the CubeCAT module was originally envisaged to follow the standard CubeSat footprint (95 mm x 95 mm). However, the end user (TNO) required a custom volume to allow for integration with the drive electronics and telescope, such that the whole laser terminal fits within 2U. Shown in Figure 4.16-4.18 is the CubeCAT mechanical design. The baseline material chosen is 6082 T651 AL.AL. with a Alcorom 1200 finish. Alocrom 1200 was chosen

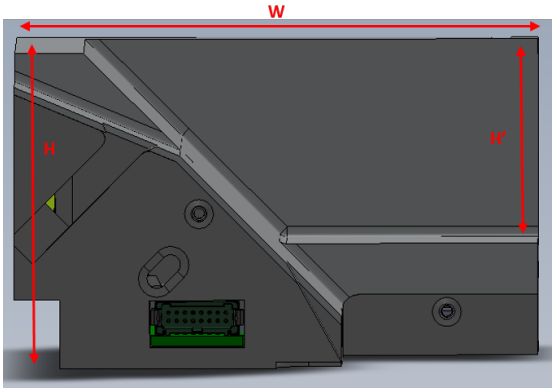

Figure 4.16: CubeCAT laser engine mechanical casing side view.

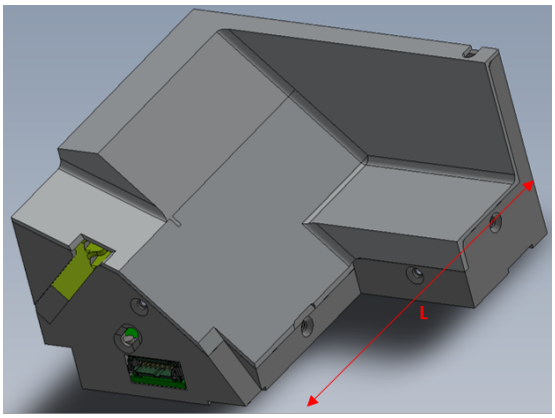

Figure 4.17: CubeCAT laser engine mechanical casing top view.

for the aluminium finish as it provides corrosion resistance whilst providing a conductive coating for grounding the case to the spacecraft bus. In addition, it allows the metalwork to have a long lifetime for AIT, which is not possible to Alocrom 1000.

The design displayed in 4.16-4.18 is modelled such that it is predicted to occupy a volume of 24.75 cm^3 and have a total mass of approximately 130 g. The displayed dimensions are as follows: H= 46 mm, L = 77 mm, W, 79.6 mm, H' = 30 mm. Fixing to the spacecraft structure is provided via 4 x M3x10 mm screws (shown circled in red in Figure 4.18). A thermal interface is provided to the spacecraft bus via the face on which the mounting points sit. This face is where all the opto-electronics are secured to, thus providing a thermal path through which the heat generated by the DFB and pump lasers is dumped. The thermal interfacing material chosen is THERM-A-GAP

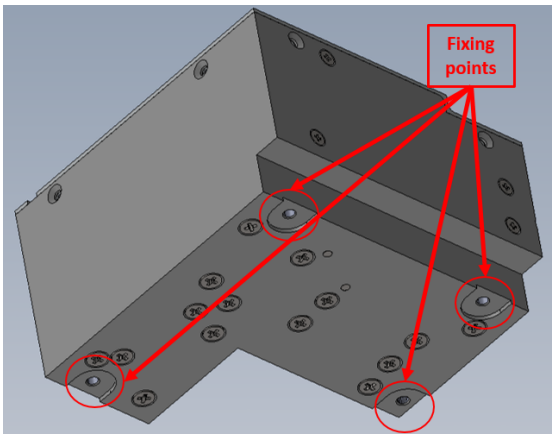

Figure 4.18: CubeCAT laser engine mechanical casing bottom view.

CH6642, a material qualified for space use.

To ensure high-reliability performance of fiber optic components, component layout is key to ensure that the minimum bend radius encountered by the optical fiber was kept within G&H design rules, and to minimize the volume. Figure 4.19 shows the internal layout of the LTX showing the position of the opto-electronics and tray in which the fiber optic components shall be glued in place. Fiber routing will be provided on the blank internal face. Not shown is the RF data interface. This is supplied via a flying U.FL 50 Ω lead which passes through the slot shown circled in green in Figure 4.19.

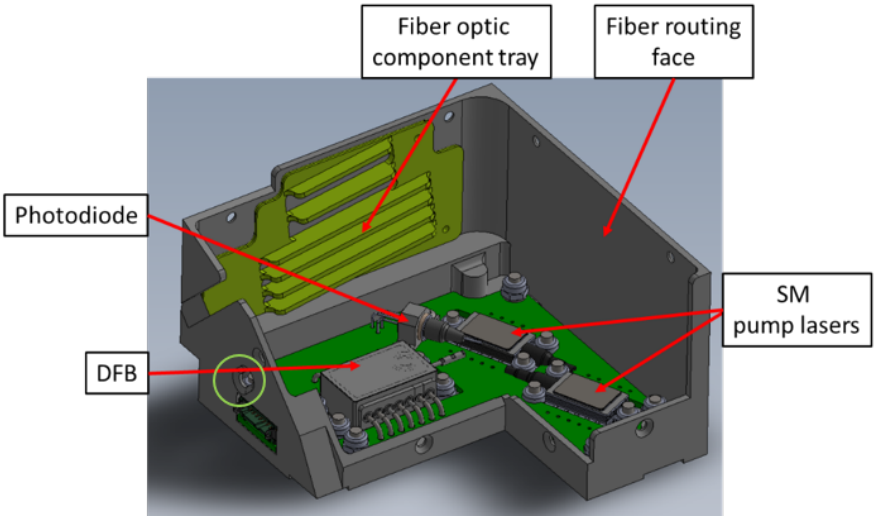

Figure 4.19: CubeCAT laser engine mechanical casing internal view.

4.3.5 Electrical Design

The purpose of the electronics in the CubeCAT laser engine is twofold. Provide mechanical support to the opto-electronic components; and provide a simple electrical interface to external driving circuits. Electrical interfacing is provided via a male, 16-way Gecko connector (G125 series). A RF interface is provided via a 50 Ω U.FL flying lead with a connector placed upon the PCB to reduce the RF path line and avoid any unnecessary signal distortion.

Pin No.	Pin ID	Description
1	GND	Ground (connected to case)
2	DFB_LDCB	DFB laser cathode (DC bias)
3	NC	-
4	DFB_LDA	DFB laser anode
5	P_LDA	Pump laser anode
6	P_LDC	Pump laser cathode
7	TEC+	TEC Anode
8	TEC-	TEC Cathode
9	DFB_T	DFB thermistor
10		
11	O_MON_+14	Output power monitor
12	O_MON_RTN	
13	DFB_MA	DFB monitor anode
14	DFB_MC	DFB monitor cathode
15	MOD_TH+	Module thermistor
16	MOD_TH-	

Table 4.6: CubeCAT laser engine electrical pin-out.

To provide mechanical support and interfacing to the opto-electronics a PCB was designed. The PCB was designed such that the pump lasers operate in a series configuration to avoid using too many pins on the electrical output connector at the expense of a higher operational voltage. Monitoring of the DFB output power, DFB temperature and monitor photodiode photocurrent are also available to be read from the module. A TEC is provided within the DFB package to control the temperature of the DFB

laser to ensure that the DFB laser can be warmed/cooled to an initial operational temperature.

Figures 4.20 & 4.21 show the PCB design of the laser engine. To ensure good signal isolation, correct impedance matching and due to the small footprint available, a 4-layer PCB was used to route the signals. The region in which all the multi-layer routing occurs is shown in Figure 4.21.

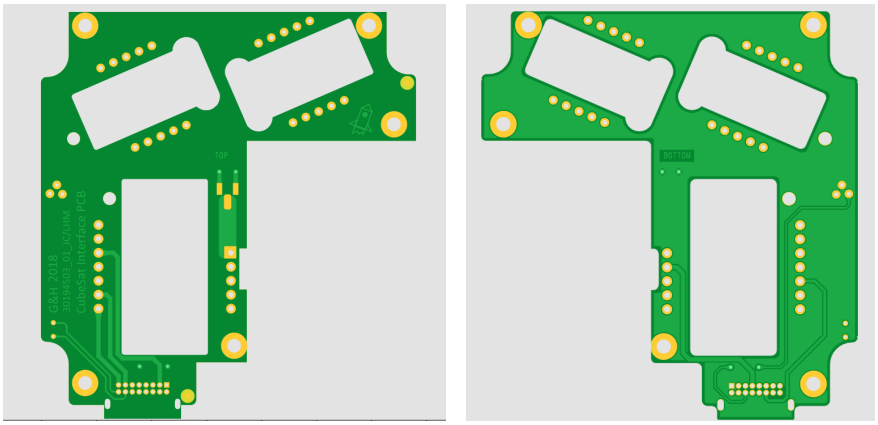

(a) (b)

Figure 4.20: CubeCAT laser engine PCB top view (a) & bottom view (b).

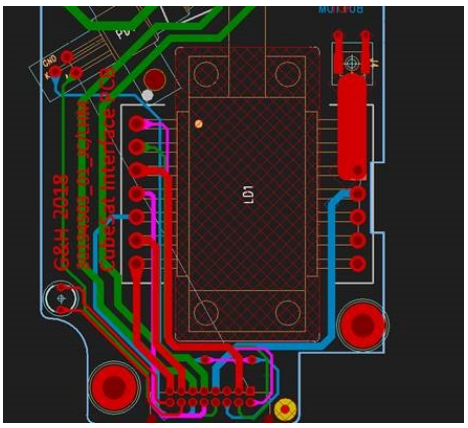

Figure 4.21: CubeCAT laser engine PCB multilayer view. The top layer is shown in red, bottom layer in blue and middle layers in green and pink.

4.3.6 Estimated Efficiencies

Based on baseline part selection, the efficiency of the laser engine can be calculated. The values shown are based on an output power of 200 mW and DFB drive current of 75 mA. It is worth noting that the TEC would not be used in normal operation, only during start-up.

Mode of Operation	**Power Consumption**	**Calculated Efficiency**
Optical-optical efficiency	-	44.0 %
Amplifier only	1.69 W	12.0 %
Wall-plug (w/o TEC)	1.89 W	10.6%
Wall-plug (w/ TEC @ nom. operation)	3.09 W	6.5%

Table 4.7: CubeCAT laser engine estimated power consumption and efficiencies for various modes of operation.

As can be seen in Table 4.7, the efficiency required specification is met at normal operating conditions. During laser warm-up, the main power draw is the TEC which would heat the DFB laser diode such that thermal shocks are avoided when the LTX starts transmitting data.

4.3.7 Thermal Analysis

Presented below is a concise thermal analysis of the main heat sources within the laser engine. At this stage of the product design process this amount of analysis is appropriate to make the product reach TRL 5. A more thorough analysis would be completed in the next phase of development if this laser engine is taken forward towards qualification and flight. The areas of interest within the module are the main heat generators which are:

- Fiber-optic splices observing the highest optical power. These are found on the splices from the pump lasers.

- DFB laser: there is a large contribution from both the TEC and heat generation caused by light generation.
- Pump laser: heat is generated by the generation of pump light.

Model

By utilising the standard equation 4.1 for conductive heat transfer, the temperature rise at the base of the heat source for a certain heat load can be calculated.

$$Q = \frac{\kappa A}{L} \Delta T \tag{4.1}$$

Where κ is the thermal conductivity of the material, A is the area through which the heat will conduct and L is the thickness of the barrier. The case has been modelled to have a thickness of 2.5 mm and aluminium is known to have a thermal conductivity of $\kappa = 220$ W/mK.

Pump Laser Splices

The highest optical power to be found with the fiber optic network is 500 mW, the maximum optical power given by the pump laser diode at the output of the pump fiber (PM980). By assuming a maximum splice loss of 0.2 dB and that any lost light is converted into heat, the amount of heat generated by a splice loss of 0.2 dB is 23.5 mW. This amount of heat generation is said to be not a problem, as it can be dispersed by thermal radiation and is of no further concern as this has never been an issue at this power level in previous G&H modules designed and qualified for space [4.13].

DFB Laser

To assess the amount of heat generated by the DFB the following assumptions have been made. A CW drive current of 100 mA and a worse case TEC condition with a TEC drive current and voltage of 4 A and 4V, respectively.

At a drive current of 100 mA and voltage of 2.55 V, the DFB laser is known to provide an output power of 16.1 mW. By assuming unconverted electrical energy is

wasted as heat, the DFB would provide a heat load of 239 mW without the TEC active. With the TEC active in worst case conditions the overall heat generated would be 16.239 W.

As the overall base area of the DFB laser is 30 x 12.7 mm, this will provide an area of 3.81×10^{-4} m^2 for the heat to flow through into the aluminium casing. The casing currently has a depth of 2.5 mm and a thermal conductivity is 220 W/m K. With these assumptions and worst case conditions it shows that an expected temperature rise of 0.48 K is expected on the base of the DFB laser. This is of no concern currently as this temperature rise would not cause any thermal runaway effects to happen within the DFB laser, causing the heat load to increase. When operating in a vacuum environment the use of a thermal pad is key as conduction will be the main method for dissipating heat and good thermal contact is needed to the base of the DFB.

Pump Laser

At an output power of 500 mW, it is known from the part data sheet that this would need a drive current and voltage of 1 A and 2 V, respectively. By continuing the same assumption about wasted electrical power, the pump lasers will both each output 1.5 W of heat. The pump lasers have a base area of 2.40×10^{-4} m^2. With these assumptions it can be calculated that the temperature rise would be 71.0 mK which is of no concern to the overall thermal design of the laser engine.

4.4 Assembly and Integration

The CubeCAT laser engine was assembled in two stages. First the PCB was assembled, tested and then a conformal coat was applied. The second stage was the assembling of the fiber optic network. Once fully assembled the laser engine underwent testing on the module level to validate the design.

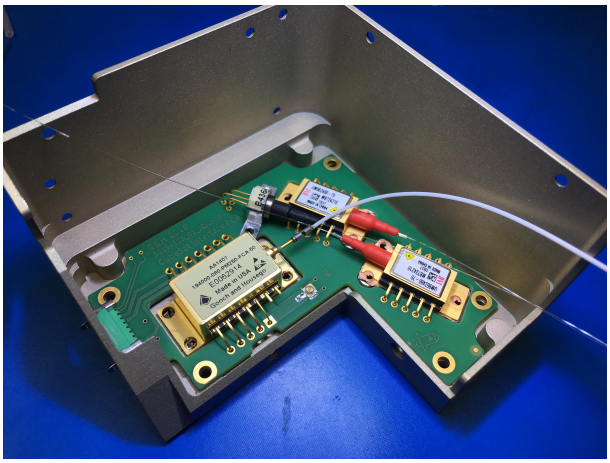

Figure 4.22: Dry fit of all CubeCAT opto-electronic components onto PCB.

4.4.1 PCB Assembly

Before assembly onto the PCB the opto-electronics and PCB undertook a fit check on both the PCB and metalwork. The result of which can be seen in Figure 4.22. It can be seen that space is at a premium for routing fiber and that care must be taken during assembly of the module to avoid damage to the opto-electronics. This is highlighted by the tight fit of the pump lasers. In addition, some modifications were needed around the hole for the Gecko connector as originally in the CAD model only a 2-layer PCB was anticipated. The modification was made by a file and then the board was fit checked again. When assembling the PCB actions must be taken to avoid ESD damage to the opto-electronics as they are especially susceptible to damage caused by static discharge. This was achieved through using ESD safe assembly tools and processes.

Once the fit check was completed the board was assembled to ECSS soldering standards [4.14]. Next the PCB was tested for functionality. For more information on the PCB testing see Section 4.5.1.

With testing complete a conformal coating (MAPSIL 213-B) was applied to both sides of the PCB. The conformal coat provides a protective and non-conductive layer on the PCB surface to ensure long-term reliability. Figure 4.24 shows the fully assembled PCB fitted into the metalwork with the initial fiber routing completed to tidy the module for further assembly.

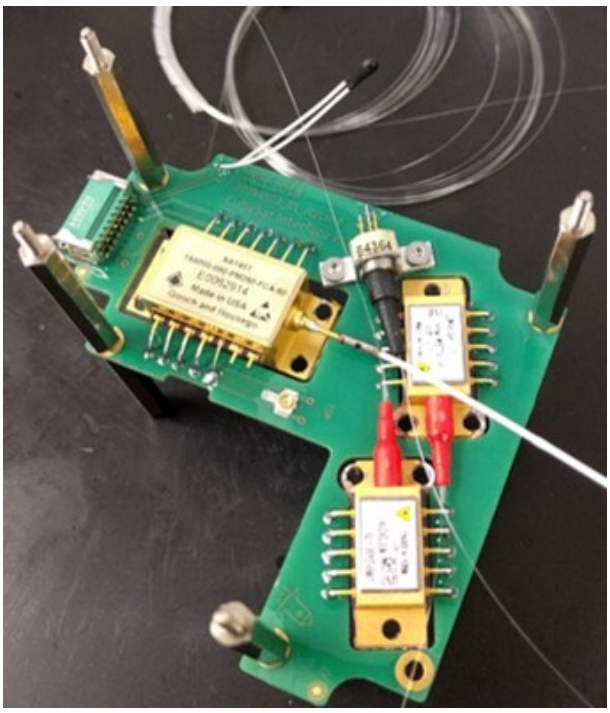

Figure 4.23: Photos of the fully assembled CubeCAT PCB ready for testing.

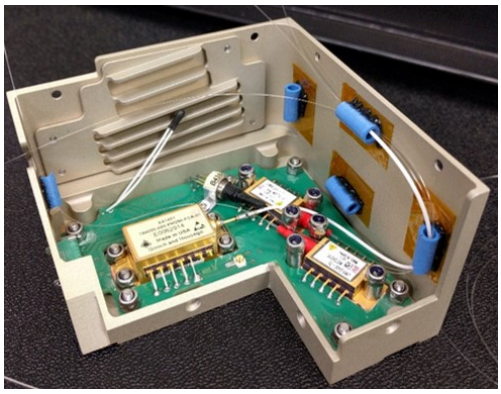

Figure 4.24: Photo of the fitted CubeCAT PCB ready for optical network assembly.

4.4.2 Optical Assembly

With the PCB assembled and tested, the optical network was assembled through the process of splicing optical fibers. Initially, the passive optical components were placed onto a separate carrier and then Scotch-Weld 2216 adhesive was applied to secure the components in place (Figure 4.25). Scotch-Weld 2216 (NASA database entry GSC35727) was chosen as it is known to be a low-outgassing adhesive with a total mass loss (TML) of 0.99 % and collected volatile condensable material (CVCM) of 0.02 % which is approved by NASA[1]. Once the Scotch-Weld was dry the fiber optic component carrier was then secured to a side wall (side wall location is shown in Figure 4.19).

One key change between the optical design presented previously and the design built is the tap ratio on the output coupler, C1. The decision was made to increase the tap ratio from 10% to 20% such that the amount of light coupled to the monitor photodiode was increased. This is because the photocurrent provided by the monitor photodiode would need to be at a level such that the monitor provides a large dynamic range but also allows for easy measurement of the photocurrent. Too low a level could lead to an erroneous reading caused by external electrical noise. The driving factor for this was that from the system level, biasing of the photodiode was no longer being provided.

As seen in Figure 4.25, not all of the components were orientated in the same direction. This was intentional as the component orientation would dictate the complexity of the fiber routing. Because of the limited volume inside the module, the fiber routing was kept as simple as possible to reduce the risk of over-bending a fiber which would apply stress and induce an optical loss.

During the splicing process, care was taken to ensure that the splices were located such they were not in a bend of the main fiber bundle. This was to avoid and any losses at the splice caused by misalignment induced by mechanical stress. The location of each splice was set by winding in the fiber to the fiber bundle twice and marking the point where the fiber reached the top straight. Once this was completed for both

[1]For more information on the properties of low-outgassing materials, the reader is pointed towards `https://outgassing.nasa.gov/`.

Figure 4.25: Fiber optic components fitted to CubeCAT fiber optic component carrier.

fibers in a splice, each relevant fiber was unwound fully as the fiber length when splicing would be quite short due to the nature of the small fiber optic bundle length, and the module would be placed close to the splicer ready for completing the splice.

Once the splice was completed in the fusion splicer, the splice was then re-coated using a UV-curable, low-index resin such that the splice would be protected from the assembly and testing environment such that cleanliness could be achieved. A re-coat process was chosen over the traditional splice tube due to the lack of space available for splice protector tubes and the fact that re-coated splices can be wound into the main fiber bundle if positioned correctly.

Table 4.8, with each splice number being referenced to in Figure 4.4, shows the results of each splice loss showing minimal loss throughout the splice process for the whole module. Some errors were detected such as in the PM-SM splices but this error is normal for this kind of splice. A hot spot was detected in splice 6 which would reduce the mechanical strength of the splice; and if present in the core of the fiber, would cause a loss. From the estimated splice loss of splice 6 this is not the case and it was concluded that this splice would not need to be reworked.

Following the assembly of the optical network, the fiber guides were removed and fiber taped into place using Kapton tape. Kapton tape was used as the rubber fiber guides are not suitable for space applications and Kapton tape is well known for it's low out-gassing properties. Once the fiber was secured in place, the module was tested to verify it's operation. The finished module whist operating is shown in Figure 4.26. With the module now assembled, the module's optical design can now be verified through optical testing. The optical design verification testing is described in Section 4.5.2. The

Splice No.	Splice Type	Est. Loss (dB)
1	PM → SM	0.00*
2	SM → SM	0.00
3	SM → SM	0.00
4	SM → SM	0.00
5	SM → SM	0.00
6	SM → SM	0.00†
7	PM → SM	0.02*
8	PM → SM	0.02*
9	SM → SM	0.00

* Bubble in fiber detected.
† Hot spot in splice detected.

Table 4.8: Summary of fiber-optic splices in CubeCAT AIT process.

final total mass with the module shown in Figure 4.26 and fitted lid was measured to be approximately 165 g, 10 % over the original mass budget which is acceptable on a system level.

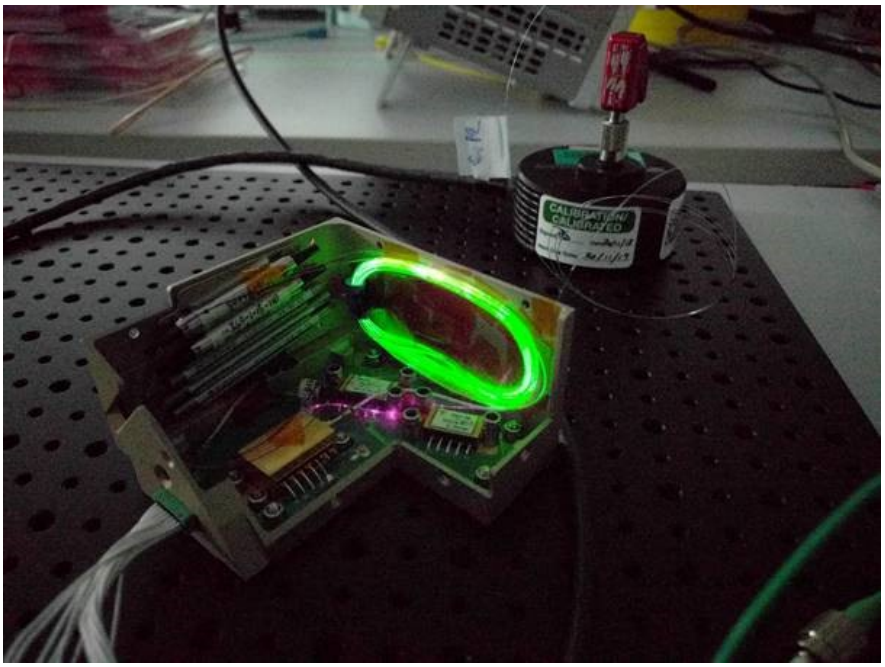

Figure 4.26: Fully assembled and operational CubeCAT laser engine.

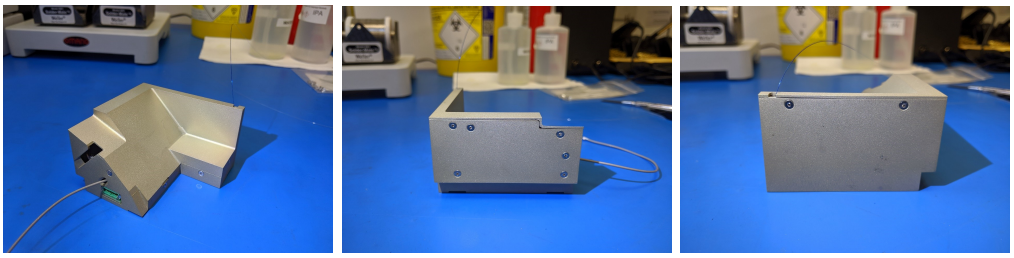

(a) (b) (c)

Figure 4.27: Fully assembled CubeCAT laser transmitter with lid fitted.

4.5 Design Verification

4.5.1 PCB Testing

The CubeCAT PCB was tested in two stages. The first stage was to assess the module's CW performance. This was completed to ensure that all the opto-electronics was operational before applying a RF signal. The DFB source laser's L-I and monitor photodiode characteristics were investigated. The pump L-I curve was also generated to observe if the pump lasers had become damaged during assembly; a distinct possibility considering their proximity on the PCB. Finally the monitor photodiode was characterised such that the data can be used for calibration of the photodiode. NB: All pump current values quoted are for both pump laser diodes as they are wired in series.

The second stage is to assess the dynamic performance, in which the pulse exiting the DFB laser whilst under modulation will be investigated. In addition, an eye diagram will be generated to assess the overall transmission characteristics of the DFB. From this testing the PCB's performance can then be verified before releasing the board further into the AIT process.

The test setup was as shown in Figure 4.11. For CW testing, the output of the DFB laser was connected to a power meter. For the dynamic performance testing, the output was then connected to a fast PD and connected to a Rohde & Schwartz HMO 3004 oscilloscope.

CW performance

The DFB power-current characteristics along with the monitor photodiode response was measured to ensure no damage to the laser diode took place during assembly onto the board. The results are given in Figure 4.28 which show that the DFB is operational. The output power is as expected with a threshold current found at 47 mA. The monitor photodiode varies from what is shown in the part data sheet but is no concern as it shows a linear response over the drive current range. This variance can arise from alignment variances within the laser diode package between the rear facet of the laser cavity and monitor photodiode.

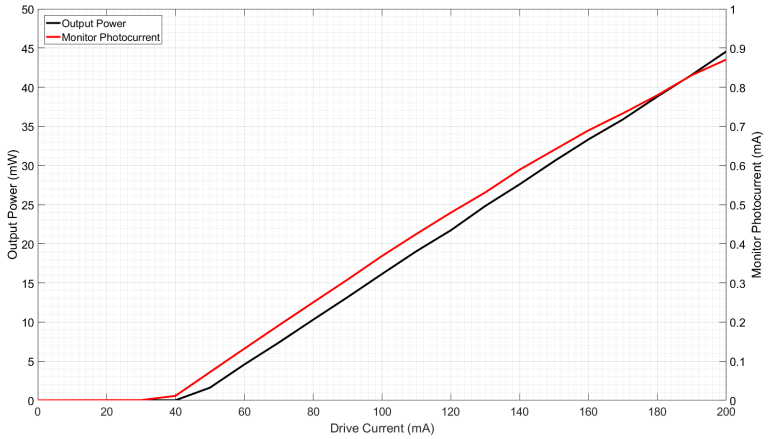

Figure 4.28: CubeCAT laser engine DFB output power & monitor photo-current as a function of drive current.

Shown in Figure 4.29 is the fitted pump laser diodes' output power at 976 nm as a function of drive current. Also shown are the pump lasers' output power-current characteristics used at the breadboarding stage to provide a comparison. One point to note about this test is that the values shown in Figure 4.29 for the fitted pump lasers have been averaged. This is because the measurement was made with the output power of both pumps as they were run in series and would output power at the same time.

It can be seen in Figure 4.29 that the fitted pumps are operational and are more efficient than the the laser diodes used at the breadboard stage. In addition it can be seen that the threshold current for the laser diodes are all the same. With the similarity

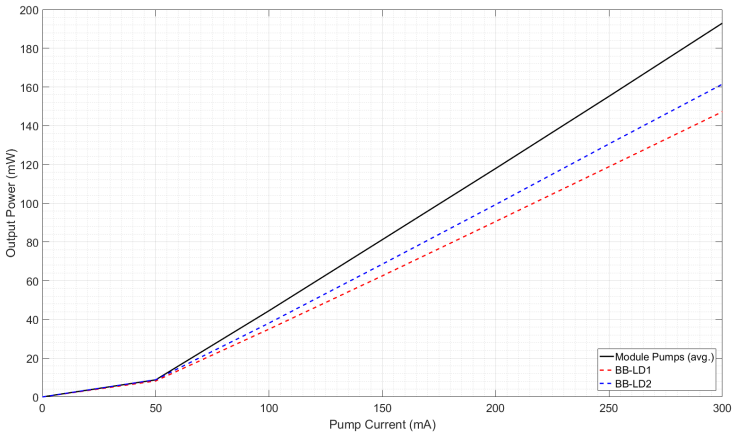

Figure 4.29: CubeCAT module pump output power as a function of drive current. Also shown for comparison are the pump laser diodes used when breadboarding.

between the pump laser diode threshold currents it can be concluded that the pump lasers can be released into later stages of the AIT process.

The monitor photodiode's responsivity characteristics at 23 °C is shown in Figure 4.30. The baseline responsivity for the part according to it's datasheet is 0.9 A/W which is in agreement with what is presented in Figure 4.30. Therefore it can be concluded that the photodiode and monitor circuit of the PCB is operating as intended.

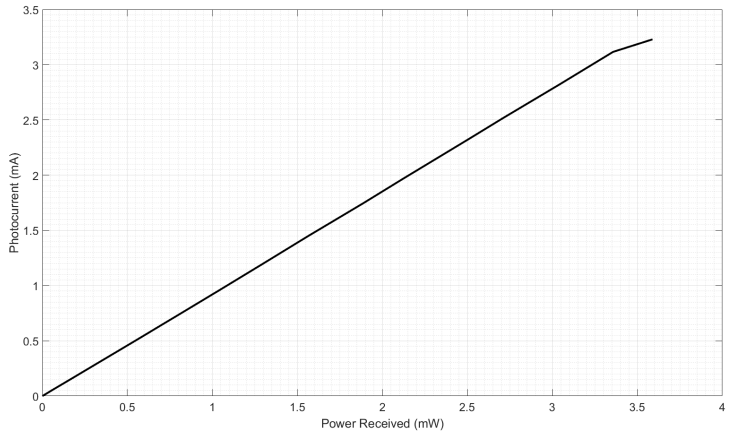

Figure 4.30: CubeCAT laser engine monitor photodiode photocurrent as a function of received power.

Dynamic Performance

The aim of the dynamic performance testing at this stage was to investigate if the signal quality would have been degraded by the PCB. To assess the signal quality the DFB laser source was modulated and the pulse shape observed. In addition, an eye diagram was generated to assess it's use for communications.

Figure 4.31 shows the pulse exiting the DFB at a data rate of 500 Mbit s^{-1}. At this point the signal was a square wave, i.e. not a random bit sequence, as the aim of the test was to observe the shape of the pulses. A square pulse has been used as in the actual system at a data rate of 200 Mbit s^{-1} it would require a continuous sequence 2×10^6 '0' bits before spiking in the output power would become a problem due to gain build-up in the EDFA. This is because the Er^{3+} transition has an upper state lifetime in the order of 10 ms [4.15] and if modulation is occurring in the Mbit s^{-1} regime the system will effectively see a CW signal.

However, Figure 4.31 also shows that relaxation oscillations still degrade both the '1' and '0' bit level shapes. This is because as the DFB is being directly modulated, it is gain-switching the laser diode and some relaxation oscillations can not be avoided. However, the majority of this effect can be filtered out by a low pass filter, a common technique in optical communications receivers [4.16]. This has been applied to Figure 4.31 which cleans any higher frequency noise caused by either crosstalk or relaxation oscillations and makes the signal much more acceptable to detect.

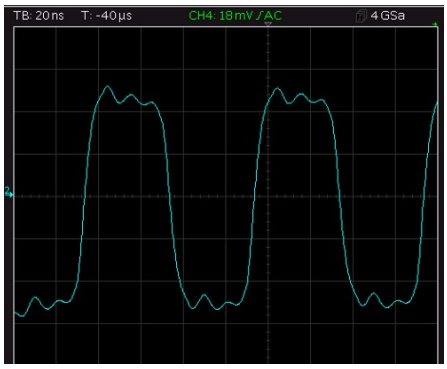

Figure 4.31: CubeCAT laser engine output pulse trace at a data rate of 500 Mbit s^{-1}.

An eye pattern was generated at a data rate of 200 Mbit s^{-1} and is shown as the

blue trace in Figure 4.32. The eye diagram shown is a screen shot of the the oscilloscope screen with trace hold set to 'on'. Some time jitter is present in the eye but it can be seen that this is due to jitter being present in the clock signal (green). The crossing point of approximately 50 % increases the evidence that the time jitter present is caused by a drift in the clock.

The noise levels around the '1' and '0' levels is caused by relaxation oscillations (as described previously). This may cause some degradation in SNR when the modulation level is decreased (e.g. to save power) but currently this is not an issue as a clear opening of the eye can be seen.

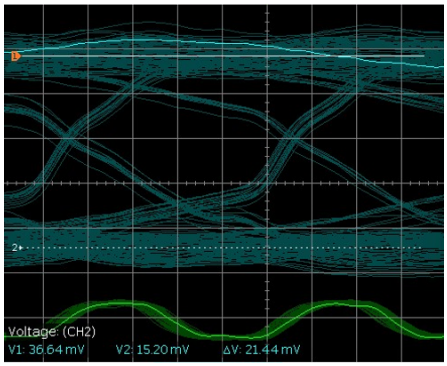

Figure 4.32: CubeCAT laser engine constructed eye diagram at a data rate of 200 Mbit s^{-1}.

At this time only an eye diagram at 200 Mbit s^{-1} was generated due to the oscilloscope being bandwidth limited. Based on pulse shapes shown in Figure 4.31 it can be extrapolated that the eye diagram will be similar at 500 Mbit s^{-1} as no signal distortion can be seen. However, other issues in the test setup such as the bandwidth of the PRBS might become a problem at higher data rates (Gbit s^{-1}). This is due to the output from the PRBS rolls-off and the eye opening decreases due to a smaller modulation signal not due to the DFB laser being bandwidth limited at this modulation frequency.

4.5.2 Optical Testing

This section of the test campaign was completed once the module was fully assembled (see Figure 4.26). This section of testing is split up into 3 parts:

- Output Power v Drive Current - This is to assess the overall efficiency of the module and compare it against breadboard results.
- Output spectrum at an output power of 200 mW - The output spectrum will be recorded via an OSA scan so that the noise performance in the CW regime can be measured.
- Finally an eye diagram will be measured to assess how the signal is distorted when passing through amplifier block.

Output Power v Drive Current

Shown in Figure 4.33 is the CW output power-drive current curve for the fully assembled CubeCAT laser engine. It shows the drive DFB laser set to a drive current of 65 m A and at room temperature (23 °C). The results of Figure 4.33 show that the output power target of 200 mW can be reached easily at a drive current of ≈ 575 mA. Although at this point the amplifier is starting to roll off as the output power starts to become limited by the available gain in the amplifier. In addition to this, for the reasons outlined in Section 4.4.2, the tap ratio for the output coupler was changed at the expense of excess power margin.

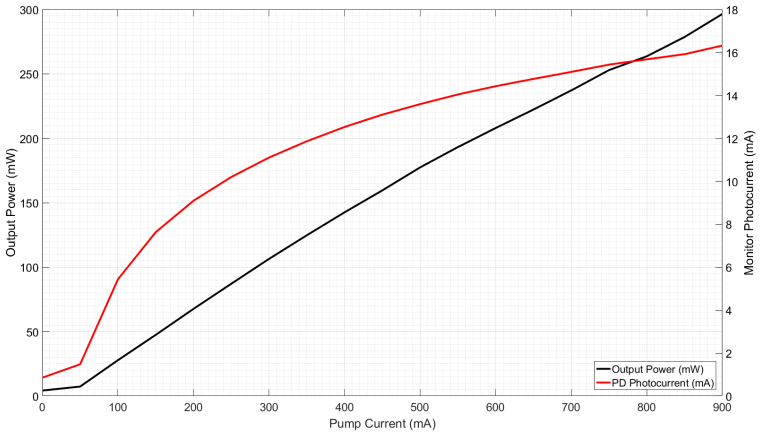

Figure 4.33: Output power and monitor photocurrent as a function of pump drive current of the fully assembled CubeCAT module.

Optical Spectrum

The output spectrum at an output power of 200 mW and temperature of 23 °C is shown in Figure 4.34. Note that the y-axis has not been scaled to reflect the output power. It shows that the output spectrum is stable and that the optical signal to noise ratio is of a good value (50.33 dB). For the measurement of optical signal to noise, an estimated ASE power level is estimated and is shown as the red line in Figure 4.34. With the optical signal-to-noise ratio at a value of 50.33 dB, this far exceeds the target value of 20 dB and it can be said that the module performs well optically.

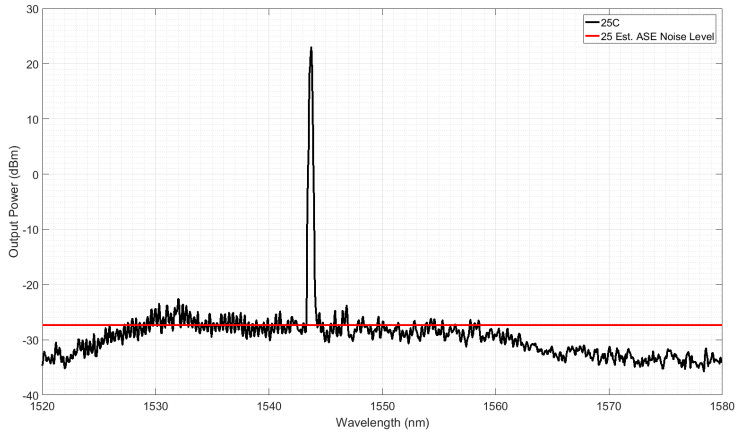

Figure 4.34: CW optical spectrum of the assembled CubeCAT module at P_{Out} = 200 mW.

Figure 4.35 shows the output spectrum of the LTX whilst being operated at an output power of 200 mW, data rate of 1.25 Gbps and temperature of 23 °C. Shown are the side modes of the LTX which are not present in Figure 4.34. From the side mode power given in Figure 4.35, the side mode suppression ratio (SMSR) can be calculated. The calculated value of SMSR is 49.68 dB.

Eye Diagram

An eye diagram was generated at a data rate of 500 Mbit s^{-1} and is displayed in Figure 4.36. The eye diagrams shown in Figure 4.36, 4.43 and 4.44 were generated by recording a time-domain signal on a Rohde & Schwartz HMO 3004 oscilloscope and

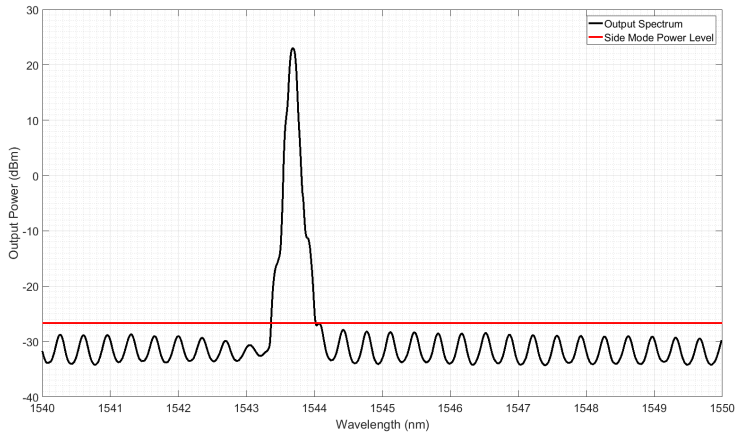

Figure 4.35: Optical spectrum at an output power of 200 mW and temperature of +23 °C. Shown are the side bands of the LTX which are generated when modulation to the DFB is applied at 1.25 Gbit s^{-1}.

using the 'eyediagram' function within MATLAB. Although the eye diagram generated shows significant noise on the '1' and '0' bit through filtered relaxation oscillations, it is believed that the eye can be opened further through adjustment of the DC bias current of the DFB laser diode. However, as an initial assessment this eye diagram is encouraging as it shows very little time jitter, with a large eye opening or little noise in the waveform itself. Based on the eye diagram shown below, it can be said that this laser engine is operable at a temperature of 23 °C and a data rate of 500 Mbit s^{-1}.

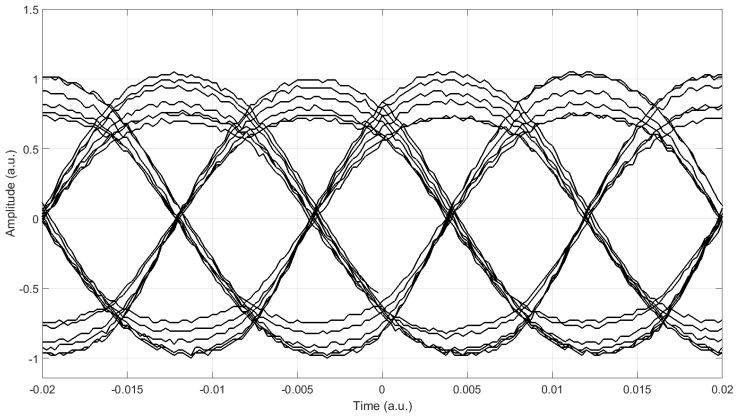

Figure 4.36: Eye Diagram generated at 500 Mbit s^{-1} and temperature of 23 °C.

Operation at 1 Gbit s^{-1} is shown in Figure 4.37. The eye digram shown in Figure 4.37 and 4.38 was generated by using the internal eye diagram function on a Keysight MSO-X 6004A oscilloscope, note that the oscilloscope previously used to eye diagrams was only limited to 500 MHz. The Keysight oscilloscope was used as it had a bandwidth of up to 1.5 GHz. The eye diagram in Figure 4.37 shows some jitter on the falling edge (as seen in Figures 4.32 and 4.36) and some over/undershoot of the pulse. However, it is thought that both of these effects are due to relaxation oscillations being observed. These oscillations can be filtered out by applying a low-pass filter on the receiver. With these relaxation oscillations removed, the eye diagram will appear much cleaner. I.e. More similar to the eye diagram presented in Figure 4.36.

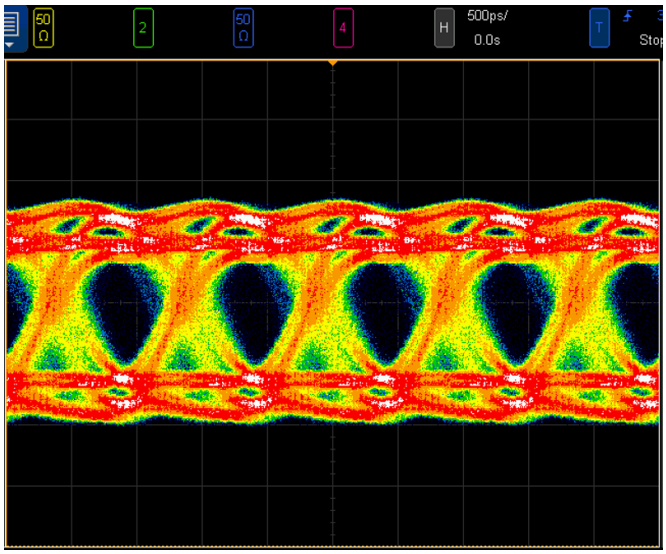

Figure 4.37: Eye Diagram generated at 1 Gbit s^{-1} and temperature of 23 °C.

It is worth noting that when operating the LTX near 1 Gbit s^{-1}, that the amplitude of the relaxation oscillations increase. This is a known effect where the modulation frequency is approaching the resonant frequency of the relaxation oscillations. For DFB laser diodes this is typically a few GHz [4.17], so therefore relaxation oscillations become a large problem when being modulated in the GHz regime. Although this is an inherent problem which cannot be avoided, it can be mitigated by changing the either the design of the DFB itself [4.17], which is not practical, bias or modulation current [4.18]. Another approach is to also fine-tune the input pulse shape by one of two ways

[4.18]. The first is to either artificially increase the rise time of the signal which will reduce the higher frequency components in the pulse. The second method is to step-up the modulation current on the rising edge. This will greatly reduce the overshoot and therefore improve the amount of chirp observed.

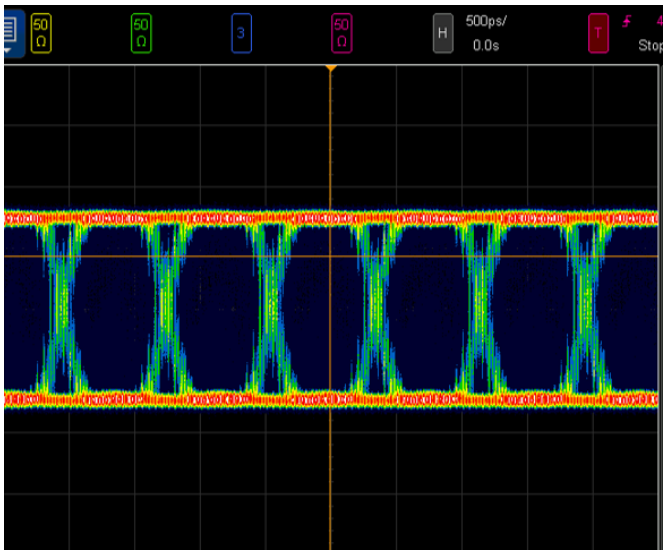

Figure 4.38: Eye Diagram generated at 1.25 Gbit s^{-1} and temperature of 23 °C

Operation at 1.25 Gbit s^{-1} is shown in Figure 4.38. It shows an open eye which is required for operation. When compared to Figure 4.36, it can be seen that the relaxation oscillations have been filtered out, showing what is achievable when the filtering is applied. Here the '1' bit voltage is 210.06 mV and the pk-pk voltage is 418.41 mV. From this the extinction ratio can be calculated to be 26.90 dB for NRZ-OOK modulation. Operation at 2.5 Gbit s^{-1} has not been measured due to limitations with the sampling rate of the measurement equipment and clock generation. As can be seen in the aliasing shown in the eye diagram due to a un-stable clock signal being used. As the clock signal in unstable, this will cause errors on the clock triggering both the PRBS and oscilloscope for eye diagram generation.

Minimum Allowed Data Rate

The minimum allowed data rate is limited by non-linear effects which cause damage at high optical powers. The main effect which is of interest is stimulated Brillouin

scattering (SBS). Brillouin scattering is caused by the 3rd order non-linearity term ($\chi^{(3)}$) of the guiding material. In most cases seen in the lab, this will be the silica glass core of the optical fibre. In this process an incident photon can be scattered so that it has a slightly lower energy (usually backwards) and a phonon being created. This energy in turn can be coupled to acoustic waves via the electro-striction effect, where acoustic waves are created by ions moving in the lattice due to the presence of EM fields, or by radiation pressure.

It is known that SBS can occur at low optical powers and at higher optical powers the acoustic waves created can become stimulated by the incident photons. Above a certain threshold (SBST), SBS can reflect most of the incident power. This involves a highly non-linear gain process for the reflected wave which can eventually lead to a refractive index grating becoming present in the fibre which will then reflect most of the incident power. SBST for operation in the CW regime is given by the equation [4.19]:

$$P_{cw} = 21\frac{A_e K}{g_b L_e} \tag{4.2}$$

Where A_e is the effective core area of the fibre, K is the polarization loss ($1 \leq K \leq 2$) and g_b is the Brillouin gain coefficient ($g_b = 4.6 \times 10^{-11}\ \mathrm{m\,W^{-1}}$). L_e is the effective interaction length which is given by:

$$L_e = \frac{1 - e^{-\alpha l}}{\alpha} \tag{4.3}$$

α is the fibre loss ($\mathrm{m^{-1}}$) and l is the length of the fibre. The polarization factor takes into account polarization scrambling between the incident waves and generated acoustic waves. I.e. in the case of a non-PM fibre, the polarization is completely scrambled and $K = 2$. By making the above calculation for the LTX and EDF absorption of 13 $\mathrm{dB\,m^{-1}}$, the SBS threshold is found to be 3.91 W. As the amplifier is core pumped, the fiber will exhibit a maximum pump power of 2 W. Therefore SBS will not be an issue and the LTX can be run in CW mode.

4.5.3 Temperature Testing (-5 to +50 °C)

With the test campaign at 25 °C successful, therefore testing at the extremes of the target operational temperature could be completed to prove that the module is at the target TRL of 5. The tests which were completed in Section 4.5.2 were repeated at ambient temperatures of -5 and +50 °C and results are presented below.

Output Power v Drive Current

Figure 4.39 and Figure 4.40 shows the L-I characteristics over the temperature range of -5 to +50 °C, respectively. It shows that at -5 °C that the output power target of 200 mW is reached at a current of 570 mA, which is the same as operation at room temperature. The power monitor is also showing stable operation at -5 °C.

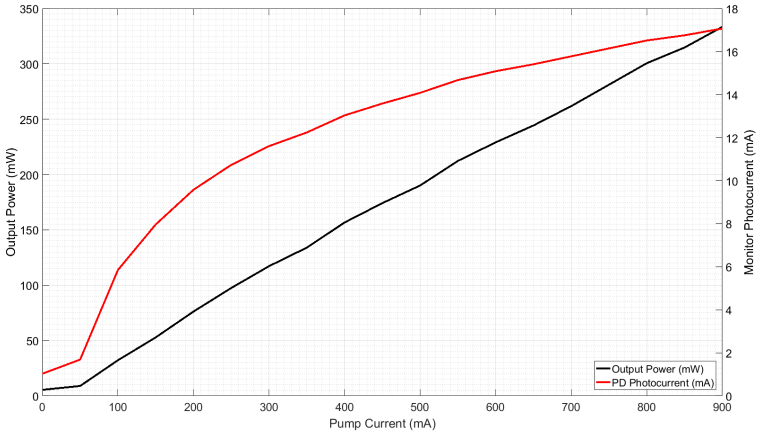

Figure 4.39: Output power and monitor photocurrent as a function of pump drive current of the fully assembled CubeCAT module measured at a temperature of -5 °C.

Operation at +50 °C is not as efficient as at +25 and -5 °C due to three reasons. The first reason is that the signal wavelength has shifted from 1543 nm to 1546 nm, a less efficient wavelength for the amplifier (Figure 4.40). The second reason is that the pump laser diodes are less efficient at a higher temperature. The result of this is that 200 mW output is met at a drive current of 750 mA which is still within the operational range of laser diode. In addition, the photodiode responsivity has dropped, showing that operation at 50 °C is limited. Finally, the DFB laser diode does become

less efficient at +50 °C, thus reducing the input power to the amplifier and therefore the output power.

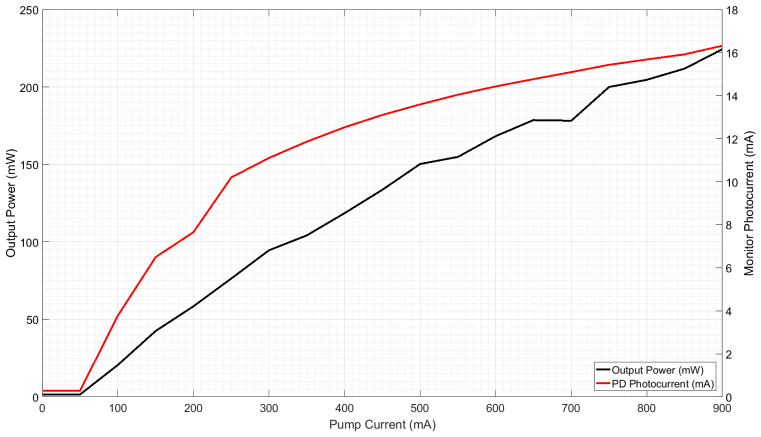

Figure 4.40: Output power and monitor photocurrent as a function of pump drive current of the fully assembled CubeCAT module measured at a temperature of +50 °C.

Optical Spectrum

Figure 4.41 shows the optical spectra at an output power of 200 mW and at temperatures of -5 °C (green) and +50 °C (blue). To generate the results at -5 °C, the TEC of the DFB needed to be switched because if the DFB is not warm enough, the output spectrum degrades and produces a broad band signal around 1517 nm (see Figure 4.42); outside of the operational wavelength range. With the TEC on, the laser reached a temperature of 20.0 °C (TEC set point) and could be used at the correct wavelength. The TEC was switched off for operation at +50 °C which caused the signal wavelength to shift to 1546 nm.

Based on an estimated ASE level of -66 dBm (+50 °C) and -67 dBm (-5 °C), the optical signal to noise ratio can be calculated for each temperature. The results of this calculation are shown in Table 4.9. It shows that the best place to operate is at -5 °C as this improves the OSNR. This in addition shows that the pay-off of using the TEC at cold temperatures is worth the slight performance increase.

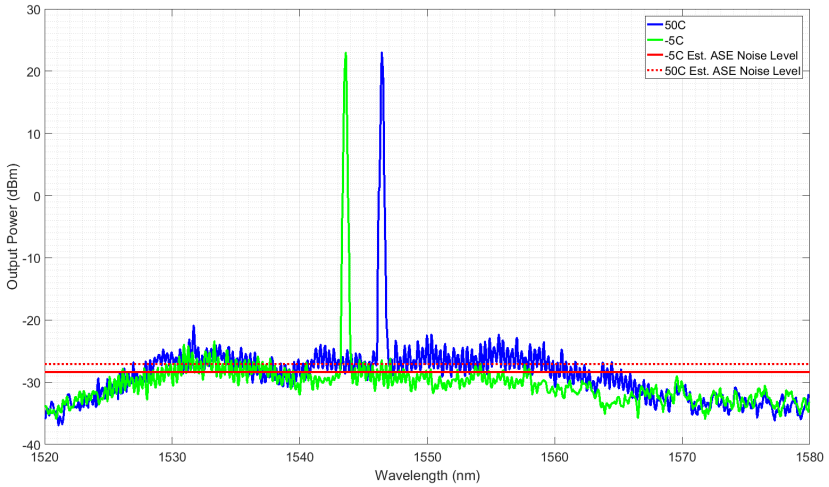

Figure 4.41: Output OSA trace at an output power of 200 mW and temperatures of -5 °C (green) and +50 °C (blue).

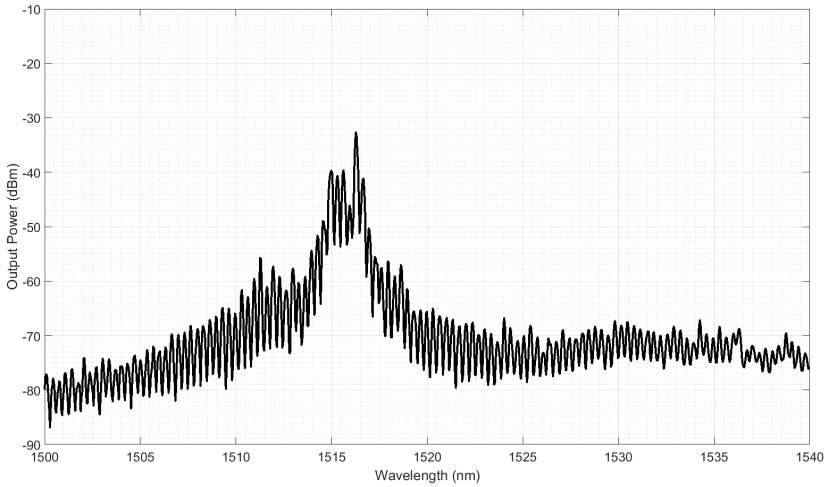

Figure 4.42: Output spectra of laser engine with amplifier off at a temperature of -5 °C, DFB biased at 100 mA and TEC disabled.

Eye Diagram

Eye diagrams were generated at -5 °C (Figure 4.43) and +50 °C (Figure 4.44) and at a data rate of 500 Mbit s^{-1}. Much like operation at 25 °C, it shows an open eye with some time jitter.

The main difference between the two eye diagrams is the amount of noise present

Temperature °C	OSNR (dB)
-5	51.39
+25	50.33
+50	50.08

Table 4.9: Table of calculated OSNR values as a function of temperature.

in both the '1' and '0' levels. As expected the amount of noise present at +50 °C is greater than the noise observed at -5 °C. This is because of three reasons. The first is the amount of thermal noise present. The second and more subtle reason, is the drift of the DFB threshold current.

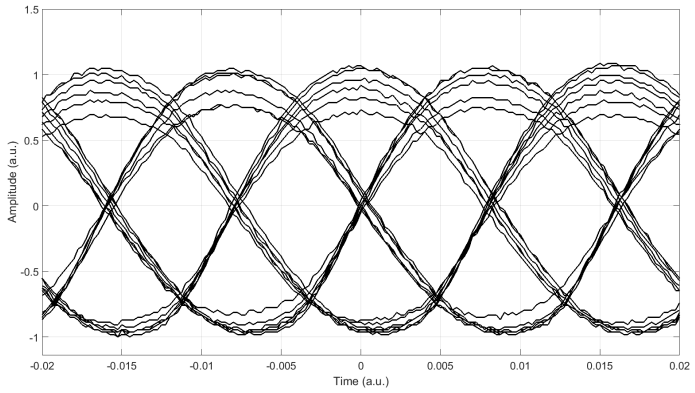

Figure 4.43: Generated Eye diagram at a data rate of 500 Mbit s^{-1} and temperature of -5 °C.

As the temperature of the DFB laser diode chip is varied, both the optical and electrical properties are changed. For example, the resistance across the chip is increased as temperature is increased and the intrinsic losses within the laser cavity are increased. As such for operation at +50 °C, the threshold current was changed to 81 mA (from 51 mA). This value was chosen as it was close to the threshold current of the DFB at this point. The threshold current was found by monitoring the back-facet monitor of the DFB whilst adjusting the DC drive current. Although this was a rough calculation, it proved to be adequate in creating an open eye. However, one degrading effect of this was the added noise to the eye due to the waveform being deformed by the unwanted effect of not switching below the threshold current at the '0' level. It is thought that

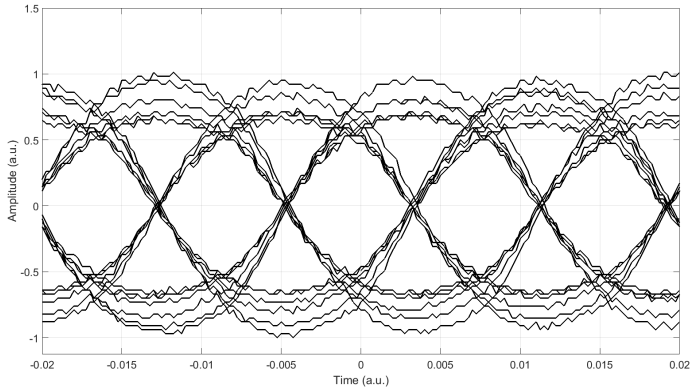

Figure 4.44: Generated Eye diagram at a data rate of 500 Mbit s^{-1} and temperature of +50 °C.

this can be counteracted by either tuning the DFB DC drive current such that the bias current can be found at +50 °C or that the TEC can be enabled to cool the laser chip to a suitable temperature.

The final reason is that with the efficiency of the DFB laser dropping, the modulation depth of the light exiting the DFB laser will decrease due to a shallower slope on the L-I curve of the DFB laser. This will close the eye, causing extra noise to appear in Figure 4.44 when the values are normalised.

4.5.4 Commentary and Test Conclusion

Based on the testing shown in Figures 4.33 -4.44, it can be seen that the best mode of operation is at 25 °C. This is because as soon as the temperature reaches the extremes of the operational temperature, it is recommended that the TEC is enabled. This can be seen the best in the data collected at -5 °C with the laser engine inoperable at this temperature unless the TEC is deployed. However, the TEC can be enabled and is usable at both +50 and -5 °C without damaging the laser diode. As such this module has been demonstrated to work in lab conditions and is now at TRL 5/6.

4.6 CubeSat Standard Variant and Further Work

With the TRL of the CubeCAT laser terminal raised to a level of TRL 5/6, the next steps of the module development should be laid out. There are two main paths this work can take in the future. The first is that of raising the TRL of the CubeCAT LTX to a higher level by applying rigorous FEA to the mechanics and thermals of the module and then placing the LTX though an environmental qualification campaign similar to those which the components have been tested to. The second path is to re-design the module to fit the CubeSat form-factor allowing for easier integration into different end users' systems.

4.6.1 CubeSat Standard

From Figure 4.17 it can be seen that the shape of the CubeCAT module does not lead to easy manufacture or integration into a CubeSat system due to it's unique shape. As such the next steps of the product development is to use the optical architecture and design described in Sections 4.3.1-4.3.2 and transfer it into a design which will fit within the standard CubeSat footprint of 96 x 96 mm.

In future applications these laser transmitters will be used in systems where a large volume will need to be manufactured due to the fact that it is anticipated that constellations of CubeSats will be needed to provide real-time downlinks from LEO. E.g. Welle et al. [4.20] expect that for complete coverage of LEO, a constellation numbering in the order of 100 nodes . If these nodes were built to the CubeSat standard, this can compare to the cost of launching one large GEO communications satellite. As such the motivation for redesigning the CubeCAT laser engine is three fold:

- As this laser transmitter is going to be manufactured in volume, redesigning the mechanical structure for ease of manufacture is essential. As this will reduce the build effort and therefore cost through both wastage and time.
- An easier integration method is needed so that the laser transmitter can be easily transferred from one CubeSat system to another. This both allows for a reduction

in time needed for spacecraft integration but also increases the marketability of the product to more end users.

- By increasing the complexity of the module by providing drive electronics and digital control, this reduces the impact of the laser transmitter on the spacecraft's SWaP restrictions by eliminating the need for extra control electronics and software.

From these design motivations the following improvements have been highlighted: Redesigning the mechanics to fit the CubeSat form factor of 96 x 96 mm, the addition of hybrid components, re-layout of the optical components to allow for ease of manufacture and lastly, addition of driver and digital control electronics. An initial concept design for the next generation of laser transmitter is shown in Figure 4.45.

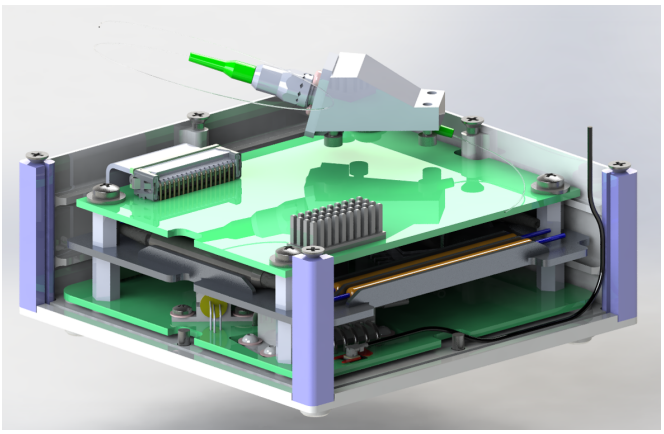

Figure 4.45: Early rendered CAD concept design of the upgraded CubeSat laser transmitter showing optical interface which is attached to the lid (not shown).

The possibility of using the hybrid components described in Section 3.1 has been investigated. At this stage, it would be of benefit in using these components as the component count is such that it is manageable on one layer of the module allowing for easier assembly. The next steps after developing the low-power module, is to design a high-power (3 W) LTX [4.21]. As this is a high-power LTX, the component count for the amplifier is effectively doubled.

Another change is that of the optical interface. In the module discussed in the previous sections, a bare fiber output has been provided to integrate into the satellite. This

bare fiber can then have a suitable ferrule fitted before being fixed into the telescope optics. For future models, as seen in Figure 4.45, an optical bulkhead shall be provided as this provides a fixed interface for the satellite. For space applications, typically the AVIM connector by Diamond is used as this has been previously flight proven [4.22]. Shown in Figure 4.45 is a mini-AVIM bulkhead and optical patch-cord. Although this part is still undergoing qualification, it has been used in modules at G&H which have undergone successful qualification campaigns [4.23].

Ease of manufacture and accessibility to components throughout the AIT process was one of key design drivers when designing these concepts. It is envisaged that this variant would be manufactured by building the PCB with the opto-electronics and drive electronics and fitting it to the base. The passive optical network can be built separately to the PCB. When spliced and ready, the two can be integrated together by fitting PCB stand-offs to the base. The active fiber would be placed on the central spool which can then be wound into the main fiber track around the edge of the fiber tray. If necessary, a ribbon cable running from the opto-electronics and drive electronics will be connected to the digital control board. At this point the module can be tested. With the testing complete the walls can be fitted and finally the lid.

4.6.2 The Path to Flight

With an eventual aim of flying the CubeCAT LTX, the TRL must be raised from 5/6 to 7/8. To raise the TRL to this level, the unit must pass a qualification campaign to ensure it's operation in space. The test levels for this campaign would be dependent on the launcher envisaged to be used in the future but will be similar to those used in Chapter 3.

However, before the qualification can take place, a rigorous simulation of the design must take place to ensure that the campaign would be a success. With a focus upon the mechanical and thermal design, this will ensure that the module can survive the harsh launch and operational environment.

4.7 Conclusion

In summary, this chapter has shown the design, development, integration and testing of a 200 mW, 1 Gbit s^{-1} CubeSat laser transmitter up to a TRL of 5/6. Difficulties were overcome in fitting all the optical components in the 24.75 cm cm^3 volume due to it's irregular shape. Operation has been shown over a temperature range of -5 to +50 °C with little degradation to performance.

An introduction to the CubeSat standard and capabilities of CubeSats have been discussed and how this can impact the laser transmitter design. From this the laser transmitter technical specification was described showing the

Also discussed is the future plan for the unit in terms of it's qualification and flight status. In addition to this an early design concept is shown, discussing the translation of the current optical design into a unit which fits the CubeSat standard footprint. From a commercial standpoint this is the path that should be followed as it allows for easy integration into as many CubeSat systems as possible and does not limit the unit to one laser terminal.

References

[4.1] E. Clements, R. Aniceto, D. Barnes, D. Caplan, J. Clark, I. del Portillo, *et al.*, "Nanosatellite optical downlink experiment: design, simulation, and prototyping," *Optical Engineering*, vol. 55, no. 11, p. 111 610, Sep. 2016. DOI: 10.1117/1.OE.55.11.111610.

[4.2] T. S. Rose, D. W. Rowen, S. Lalumondiere, N. I. Werner, R. Linares, A. Faler, *et al.*, "Optical Communications Downlink from a 1.5U CubeSat: OCSD Program," in *32nd Annual AIAA/USU Conference on Small Satellites*, 2018.

[4.3] M. Storm, S. Gupta, H. Cao, S. Litvinovitch, K. Puffenberger, M. M. Albert, *et al.*, "Cubesat Laser Communications Transceiver for Multi-Gbps Downlink," in *2017 Conference on Small Satellites*, 2017.

[4.4] D. Engin, J. Rudd, K. Le, K. Puffenberger, H. Cao, N. Sawruk, *et al.*, "51W, 1.5um, 7 WDM (25nm) channels PPM downlink Tx and 500W, 1um, uplink PPM Tx for deep space lasercom," *Free-Space Laser Communications XXXI*, no. March, p. 19, 2019. DOI: 10.1117/12.2513801.

[4.5] H. Heidt, J. Puig-Suari, A. Moore, S. Nakasuka, and R. Twiggs, "CubeSat: A new Generation of Picosatellite for Education and Industry Low-Cost Space Experimentation," *AIAA/USU Conference on Small Satellites*, vol. 14, 2000.

[4.6] A. Mehrparvar, D. Pignatelli, J. Carnahan, R. Munakata, W. Lan, A. Toorian, *et al.*, "CubeSat Design Specification," Cal. Poly, Tech. Rep., 2014.

[4.7] R. Limebear, "The AMSAT-UK FUNcube Handbook," AMSAT-UK, Tech. Rep., 2013.

[4.8] C. Clark, "Huge Power Demand...Itsy-Bitsy Satellite: Solving the CubeSat Power Paradox," *24th Annual AIAA/USU Conference on Small Satellites*, no. August, pp. 1–8, 2010.

[4.9] R. W. Kingsbury, K. Riesing, T. Nguyen, and K. Cahoy, "Two-Stage Control for CubeSat Optical Communications," in *CubeSat Developers' Workshop*, Cal. Poly, 2014.

[4.10] R. Saathof, S. Kuiper, W. Crowcombe, H. de Man, D. de Lange, N. van der Valk, *et al.*, "Opto-mechatronics system development for future intersatellite laser communications," in *Free-Space Laser Communications XXXI*, H. Hemmati and D. M. Boroson, Eds., SPIE, Mar. 2019, p. 47. DOI: 10.1117/12.2508870.

[4.11] B. Klofas and K. Leveque, "The Future of CubeSat Communications: Transitioning Away from Amateur Radio Frequencies for High-speed Downlinks," in *AMSAT Space Symposium*, AMSAT, 2012.

[4.12] J. Crabb, G. Stevens, C. Michie, W. Johnstone, and E. Kehayas, "Laser transmitter for CubeSat-class applications," in *Free-Space Laser Communications XXXI*, H. Hemmati and D. M. Boroson, Eds., SPIE, Mar. 2019, p. 54. DOI: 10.1117/12.2506967.

[4.13] E. Kehayas, J. Edmunds, M. Welch, M. Tuci, C. Palmer, K. Simpson, *et al.*, "Space qualification of multi-channel optical fiber amplifier for low Earth orbit satellite-to-ground direct downlinks," in *Free-Space Laser Communication and Atmospheric Propagation XXX*, H. Hemmati and D. M. Boroson, Eds., San Francisco: SPIE, Feb. 2018, p. 35. DOI: 10.1117/12.2289664.

[4.14] ECSS Executive Secretariat, "ECSS-Q-ST-70-08C Space product assurance - Manual soldering of high-reliability electrical connections," Noordwijk, 2009.

[4.15] E. Desurvire, *Erbium-doped fiber amplifiers: principles and applications*, Illustrate. Wiley-Interscience, 2002.

[4.16] J. M. Senior and M. Y. Jamro, *Optical Fiber Communications Principles and Practice*, Third. Pearson Education, 2009.

[4.17] T. Yamamoto, "High-Speed Directly Modulated Lasers," in *Optical Fiber Communication Conference*, Washington, D.C.: OSA, 2012, OTh3F.5. DOI: 10.1364/OFC.2012.OTh3F.5.

[4.18] R. Tucker, "High-speed modulation of semiconductor lasers," *IEEE Transactions on Electron Devices*, vol. 32, no. 12, pp. 2572–2584, Dec. 1985. DOI: 10.1109/T-ED.1985.22387.

[4.19] Y. Aoki, K. Tajima, and I. Mito, "Input Power Limits of Single-Mode Optical Fibers due to Stimulated Brillouin Scattering in Optical Communication Systems," *Journal of Lightwave Technology*, vol. 6, no. 5, pp. 710–719, 1988. DOI: 10.1109/50.4057.

[4.20] R. Welle, A. Utter, T. Rose, J. Fuller, K. Gates, B. Oakes, *et al.*, "A CubeSat-Based Optical Communication Network for Low Earth Orbit," in *AIAA/USU Conference on Small Satellites*, 2017.

[4.21] M. Welch, J. Edmunds, J. Crabb, E. Prowse, K. Hall, M. Kechagias, *et al.*, "High-power booster optical fibre amplifiers for satellite communications," in *Free-Space Laser Communications XXXII*, H. Hemmati and D. M. Boroson, Eds., San Francisco: SPIE, Mar. 2020, p. 32. DOI: 10.1117/12.2545570.

[4.22] F. Taugwalder, "ESCC standards, evaluation and qualification of optical fiber connectors for space application," in *International Conference on Space Optics — ICSO 2012*, E. Armandillo, N. Karafolas, and B. Cugny, Eds., SPIE, Nov. 2017. DOI: 10.1117/12.2309053.

[4.23] L. Stampoulidis, J. Edmunds, M. Kechagias, G. Stevens, J. Farzana, M. Welch, *et al.*, "Radiation-resistant optical fiber amplifiers for satellite communications," in *SPIE 10096, Free-Space Laser Communication and Atmospheric Propagation XXIX*, H. Hemmati and D. M. Boroson, Eds., Feb. 2017, 100960H. DOI: 10.1117/12.2252086.

Chapter 5

Development of a Multi-Channel Optical Amplifier for the Miniaturisation of RF Communications

As discussed in Chapter 2, RF communication terminals are very bulky and large. This is especially the case for satellites which use RF array beam-formers, a device that utilises constructive and destructive interference by the variance of the phase delay given by a single element in the beam-former. Highlighted as a key technology for providing small spot beams but over a large coverage area, phased-array beam-formers are known to be extremely heavy ($\geq$ 15 kg) [5.1] making it an area in which photonics can help reduce the SWaP of the communications payload.

This chapter will discuss the development and AIT of a multi-Channel erbium doped fiber amplifier (MC-EDFA) designed for use within a 4-element phased array antenna used for QPSK, Ka-Band beam-forming. This amplifier was developed as part of the BEACON project[1] an EU project focusing on developing the next generation of satellite communications components by leveraging photonics. For information on the overall project see [5.2], [5.3]. This chapter is split up into 5 sections:

[1] `http://www.space-beacon.eu/`.

- Section 5.1 introduces the BEACON amplifier by showing the overall optical architecture and MC-EDFA specification.
- Section 5.2 will discuss the testing completed on the MC-EDFA in terms of assessing the doped fiber for use in the radiation environment.
- Section 5.3 presents the BEACON amplifier assembly and integration process.
- Section 5.4 reports the module level testing completed on the BEACON amplifier.
- Section 5.6 will summarise the content of this chapter and discuss any further work.

5.1 Introduction

5.1.1 The BEACON Amplifier

As previously discussed, the development of the MC-EDFA is motivated by the need for future Telecom payloads with lower SWaP parameters. To achieve this the fiber and optical component count can be reduced by using a multi-core fiber amplifier which is presented in the chapter.

The focus of the work illustrated upon in this chapter is that of the design and AIT of a 7-channel booster amplifier providing output powers > 10 dBm with a gain > 20 dB over the optical C-band (1530-1565 nm). The amplifier's 7 channels come through the use of a multi-core optical fiber amplifier which was developed in partnership with InPhoTech (Warsaw, Poland). A concept of the optical circuit for the MC-EDFA is outlined in Figure 5.1 illustrating the various optical subsystems needed.

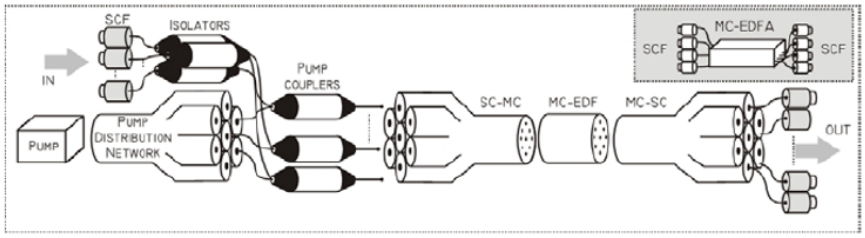

Figure 5.1: BEACON MC-EDFA optical circuit.

5.1.2 Design Specification

As part of the BEACON project, a set of design specifications were generated by project partners and are shown below in Table 5.1. It can be seen that with a gain > 15 dB, a single-stage amplifier is suitable for this application. Based on this conclusion, the overall optical architecture can be generated.

Specification	**Value**	**Notes**	**Units**
Type	MZM loss compensation		-
Wavelength	C-band (1530-1565)	-	nm
Input power	> -5	end-of-life (EOL)	dBm
Output power	10	Min.	dBm
Gain	> 15	Min	dB
Noise Figure	< 5	Typ.	dB
Fiber Type	Non-PM	-	-
No. of Channels	7	-	-

Table 5.1: BEACON MC-EDFA Specification.

5.1.3 Optical Architecture

The optical architecture for the BEACON amplifier is shown in Figure 5.2. It can be seen that the main bulk of fiber-optic components will be used to distribute pump power equally across all 7 channels. A bi-directional pumping scheme has been chosen such that the gain and NF can balanced correctly without degrading the performance of the module. 4 pump laser diodes have been used such that 2 pump lasers are used in each direction with a 90° splice for 1 pump such that both linear polarisation modes are pumped in the MC-EDFA. The pump power is distributed via an initial 15%/85% fiber-optic coupler followed by a 50%/50% coupler spliced to the 85% arm. Each output arm of the 50%/50% coupler is then spliced to the input of a 3-way 33%/33%/33% coupler. Therefore, approximately 6 channels will have 14.1% of the pump power in each channel with the final channel having the remaining 15%. A dual-channel fiber-optic isolator is used to reduce the component count, with each EDFA channel being assigned one

isolator.

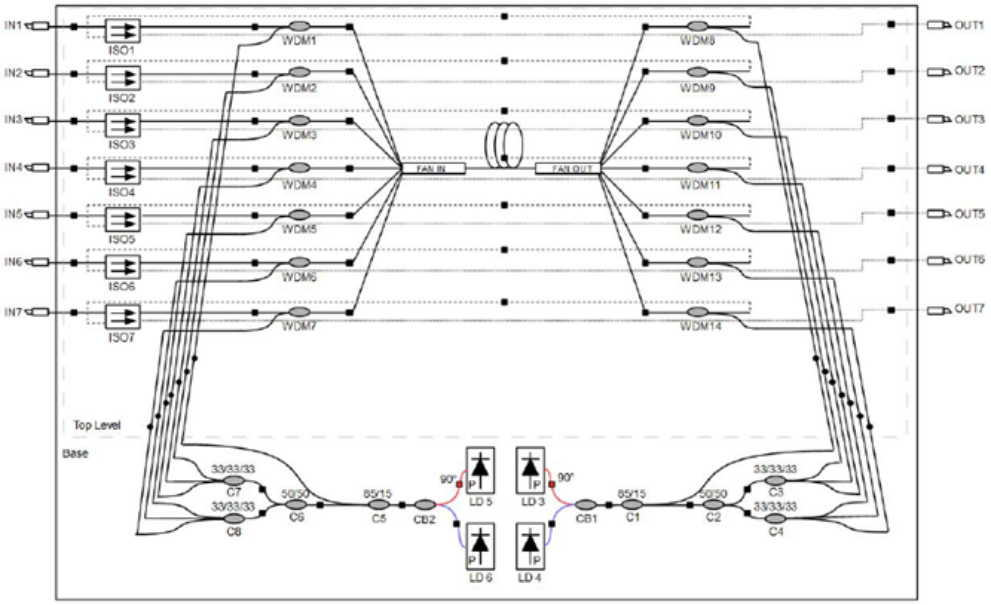

Figure 5.2: BEACON MC-EDFA optical architecture.

5.2 Multi-Core Fiber Amplifier Testing

By utilising a MC-EDFA, 7 channels can be miniaturised into one EDFA. This is achieved by utilising a 7-channel PCF arranged in a hexagonal structure. As part of the BEACON project, the PCF was developed by one of the project partners, InPhoTech (Warsaw, Poland) with feedback provided by G&H and the author of this thesis.

5.2.1 BEACON PCF Structure

The structure of the BEACON PCF is shown in Figure 5.3. The structure is created by the use of air holes and is of a hexagonal structure to provide a strong and tessellating structure to allow a single cell design to be scaled up to 7 channels.

As shown by Figure 5.4, the propagation in each core of multi-core fibre is independent. By simulation in Mode Solutions by Lumerical, the fiber supports the fundamental mode in the core. In addition, one higher order mode is also supported in the cladding but has a confinement loss which is quite large for both wavelengths

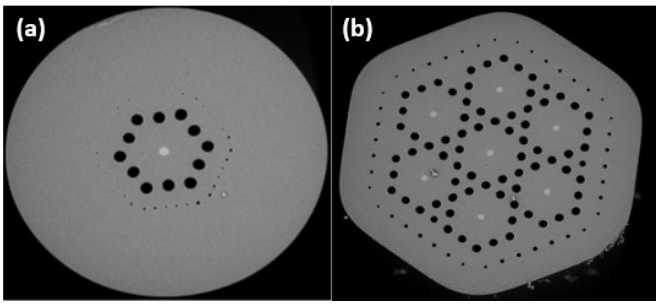

Figure 5.3: An electron microscope image of the cross section of the BEACON PCF. Shown is the structure of one elementary cell (channel) (a) and all 7 channels (b).

(7 dB/m and 27 dB/m for 980 nm and 1550 nm, respectively) and can therefore be ignored [5.4]. Therefore with independent propagation, features such as absorption, gain or bending loss can be measured only for a single core. With this approach, it allows for feedback of corrections into the fiber design. For more details see: [5.5] as the manufacture and optimisation of the PCF was not part of the scope of this thesis.

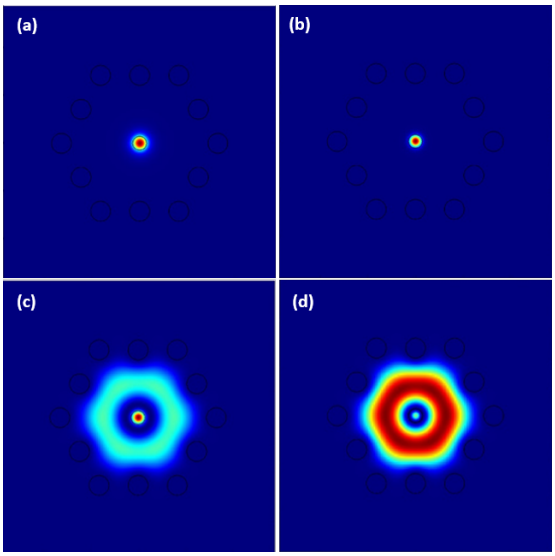

Figure 5.4: Cross sections of the 1550 nm (a) and 980 nm (b) simulated fundamental modes propagating in the elementary cell of the seven core fibre. Also shown are the one supported higher mode at 1550 nm (c) and 980 nm (d).

A fan in/out structure was created by InPhoTech to allow for splicing of standard SMF-28 fiber to the PCF. This was achieved by precisely etching fibers, inserting them into a capillary tube and tapering the capillary tube to provide proper filling of the

capillary tube and lastly splicing to the PCF. The exact details of the fan in/out will not be discussed as they are not covered by this thesis.

Information on the assembly and initial testing of the BEACON PCF has been published [5.4], [5.5]. However, more detailed information on the radiation testing of the fiber will now be presented.

5.2.2 Radiation Hardness Testing

To investigate the suitability of the rad-hard PCF, the aim of this test program was to investigate the influence of cerium as a co-dopant in the PCF. As discussed previously this has been used to a good effect and is seen as a possible solution to creating radiation-hardened EDFAs [5.6], [5.7] and in this case a radiation hardened PCFs.

The effect of introducing cerium has been initially investigated by observing the gain and NF for two sets of fiber before irradiation at 30 kRad and 100 kRad. The first fiber investigated is a single-core fiber (SCF) with the only active dopant being erbium. See Figure 5.3 (a) for an example of the fiber structure. The second fiber is a multi-core fiber (MCF) co-doped with cerium similar to that used in the amplifier module. To show similarity in gain and NF measurements with the SCF measurements, the extension splices used to interface with the MCF were only spliced to one core (channel 5, the central core).

Figures 5.5 and 5.6 show the gain and NF for both the SCF and MCF fibers over the C-band with a fixed input power of -6 dBm and fixed pump power of 300 mW. The fibers tested were un-irradiated; before the fiber is irradiated at 30 krad and 100 krad, simulating LEO and GEO radiation conditions. Once the two fiber batches have been irradiated the gain and NF deterioration will be measured.

It is shown that there is a drawback in the gain performance which is not ideal for applications such as a booster amplifier. However, it is expected for the SCF fiber to drop off in gain performance as the radiation dose increases. For example a gain drop of 6.5 dB is shown for a non-cerium doped fiber in [5.6] and a similar result is expected.

Following baseline testing with pristine fiber, the fiber samples were irradiated at room temperature (23 °C) in steps of 30 kRad and 100 kRad using a ^{60}Co at a dose

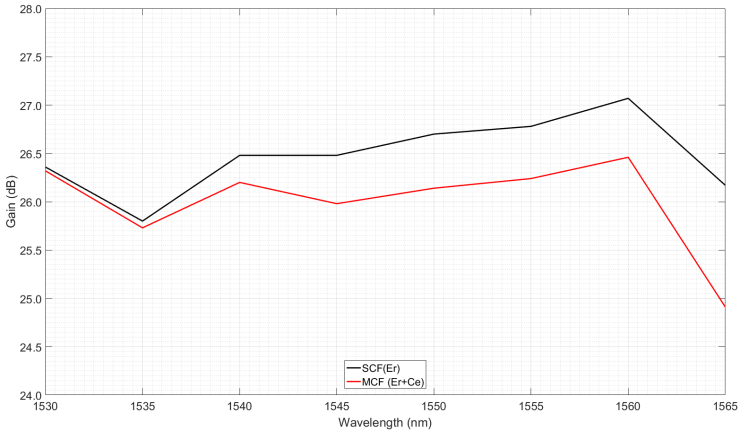

Figure 5.5: BEACON PCF gain as a function of signal wavelength for both the co-doped (Er+Ce) and un-doped PCF (Er).

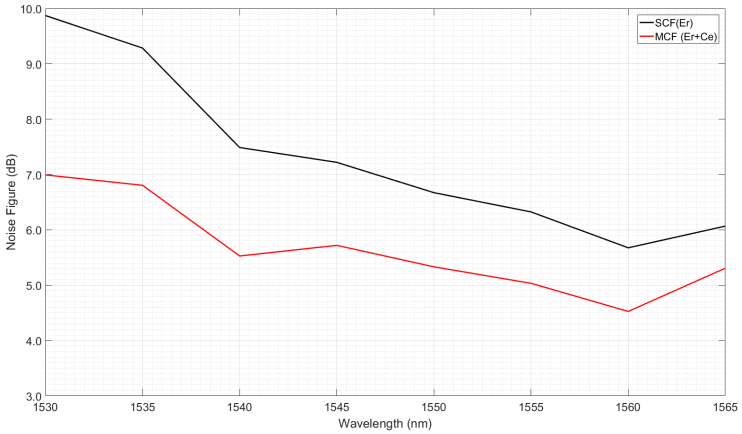

Figure 5.6: BEACON PCF noise figure as a function of signal wavelength for both the co-doped (Er+Ce) and un-doped PCF (Er).

rate of 210 Rad/h.

Shown in Figure 5.7 is the RIA for the two fibers developed. The signal power and wavelength was -6 dBm and 1550 nm, respectively and the bi-directional pump power was 300 mW. The SCF(Er) curve shows a gain degradation of 2.2 dB/100 kRad which is expected as this fiber is not designed to be radiation hard. The MCF curve shows a maximum gain degradation of 0.72 dB/100 kRad which is encouraging. It has shown that the influence of cerium co-doping has reduced the RIA by a considerable amount

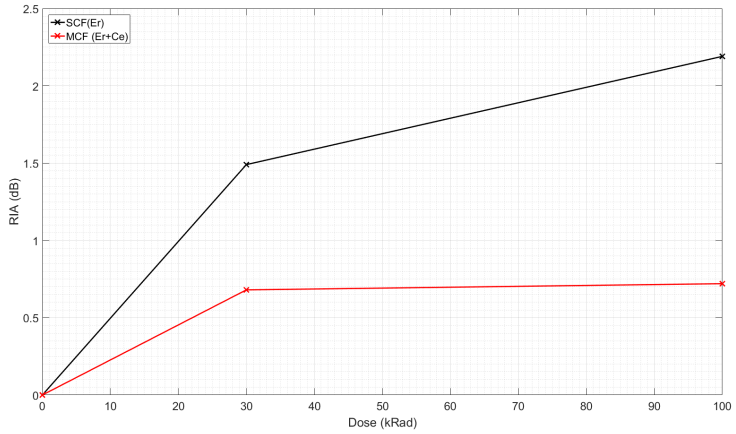

Figure 5.7: Measured RIA for the BEACON PCF for radiation doses of 30 and 100 kRad. Shown is the co-doped fiber (Er+Ce) and un-doped fiber (Er).

moving this fiber towards qualification for space.

Figure 5.8 and 5.9 show the wavelength dependency of the gain drop observed of the C-band for both the Er(only)-doped (Fig. 5.8) and Ce-co-doped fiber (Fig. 5.9). It shows that for the Ce-co-doped fiber that the RIA saturates past 30 kRad with the majority of colour centre formation occurring at low radiation doses. Furthermore, it can be seen that typically the gain curve shapes are the same. This suggests that RIA for this PCF is wavelength independent over the C-band.

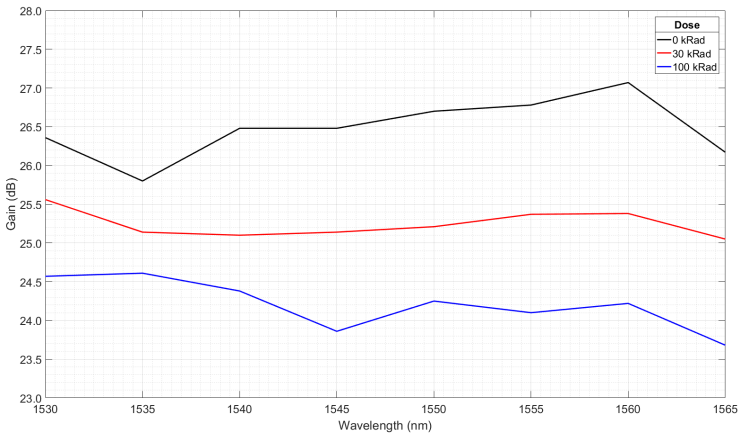

Figure 5.8: Measured gain for the BEACON Er-doped PCF at doses of 0, 30 and 100 kRad as a function of wavelength.

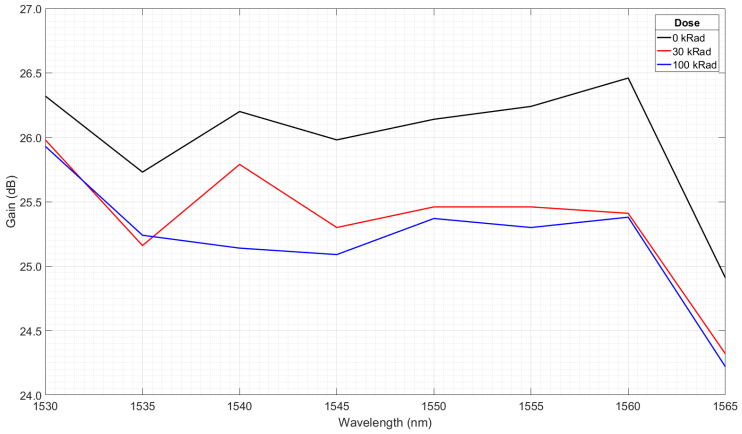

Figure 5.9: Measured gain for the BEACON Ce-co-doped PCF at doses of 0, 30 and 100 kRad as a function of wavelength.

Although currently IR-RIA is still under investigation [5.8], this provides some data towards showing it is independent over this key wavelength window for optical communications. This conclusion can be further supported by comparing the gain curves collected at different doses of 30 kRad and 100 kRad as shown in Section 3.5.1.

One point to note is that the RIA for the non-cerium doped fiber (SCF) is not as high as expected. This is most likely down to two reasons. The first is that the fiber was tested a while after irradiation (approx. 1 month). This would allow for some annealing to occur and in turn reduce the RIA level. The second, and main reason is that with pumping at 300 mW, photo-bleaching of the RIA is occurring which would mask the RIA levels at lower pump powers.

5.3 Module Assembly and Integration

With the PCF to be used within the module being verified for use in space, this section will discuss the assembly, integration and testing (AIT) of the BEACON module. Figure 5.10 shows the component of the BEACON module and how the unit shall be assembled. The pump distribution system (PSD) can be assembled in the base of the unit along with the PCB assembly (PCBA). The fiber optic amplifier path (FOAP) can be assembled independently before mating it to the rest of the module.

As shown in Figure 5.2 the component and splice count for this amplifier is unusually high, leading to challenges in assembling the unit. In total there are 47 optical components and 68 splices leading to issues such as the location of the various components and splice tubes.

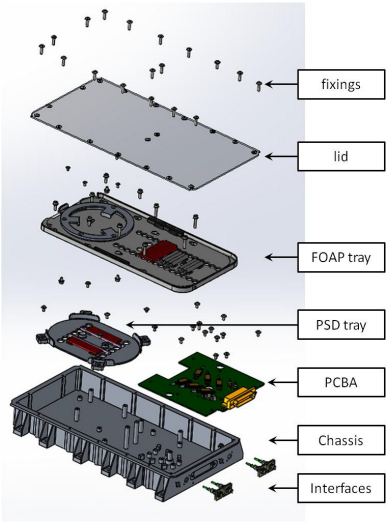

Figure 5.10: Exploded diagram of the BEACON module.

The assembly of the BEACON module is shown in Figure 5.11. Initially the PCBA and PSD were assembled and fitted into the base of the module (Figure 5.11a). The FOAP was assembled separately to the module and then integrated into the module. The fully assembled module is shown in Figure 5.11b. The one difference between the as-designed and as-built configurations is that the active fiber spool and radiation shield was not fitted. It was decided that this was not necessary for 2 reasons. The first is that the fiber had already been tested for it's response to radiation. The second is that no mechanical support, and therefore thermal path, is needed for the PCF due to the nature of the low output power of the amplifier. If any thermal effects were present they would become prevalent during temperature testing of the amplifier (see Section 5.4.

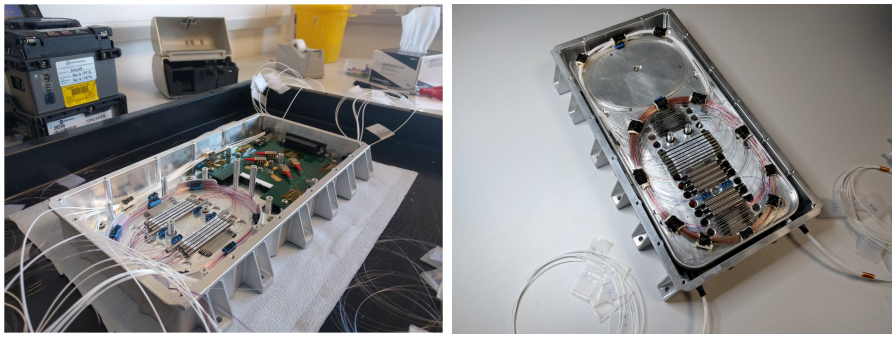

(a) (b)

Figure 5.11: BEACON module assembly. (a) shows the fully completed PCBA and PSD. (b) shows an assembled and integrated FOAP.

5.4 Design Verification

With the module assembled and integrated, a test campaign was commenced to test the functionality of the amplifier. The first initial functionality tests took place at room temperature (21 °C) and focused upon the C-band performance of the amplifier. In addition, the thermal performance of the pump laser diodes was recorded to ensure they do not overheat. A case thermistor was also present, the overall temperature rise of the module was also measured. The second stage of testing was to test the module between -10 & +60 °C to assess the module's gain and noise figure performance over temperature whilst at a fixed pump power and signal wavelength.

5.4.1 Initial Functionality Tests

The results of the 21 °C testing are shown in Figures 5.12-5.15. As shown in Figure 5.12, the temperature increase at an operating current of 500 mA is in the region of 9.97 °C with a maximum temperature of 37.77 °C. This validates the thermal design as the pump lasers will be operating well within their temperature range meaning that the unit can be reliably operated at a pump current of 500 mA.

Figure 5.13 shows the L-I curve for each of the 7 channels. Channel 7 has a higher output power than any other the other channels and this is shown throughout the rest of the data suggesting an issue with the doping profile of the MC-EDF. This test has also shown that a pump current of 500 mA is suitable for normal operations as at this

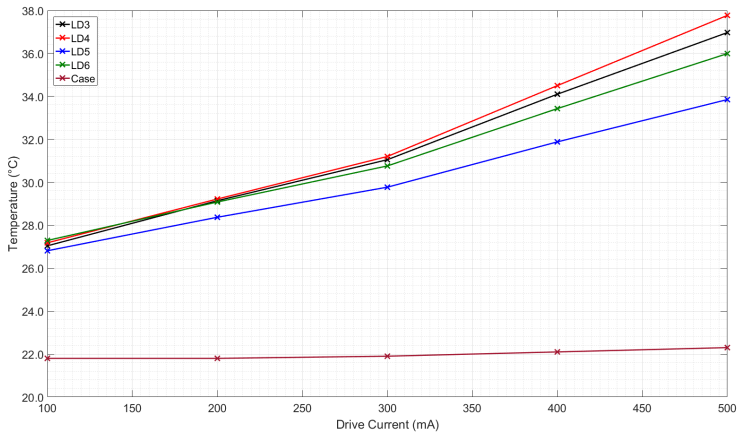

Figure 5.12: Temperature monitor measurements for varying pump drive currents.

operating point it can be seen that the amplifier has started to roll-off and saturate.

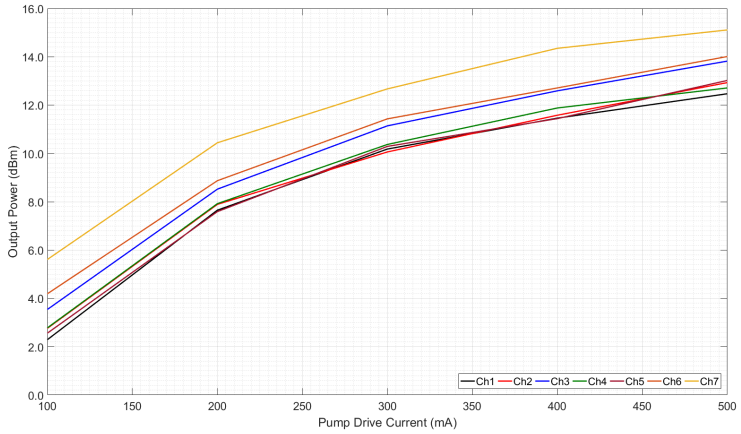

Figure 5.13: Output power as a function of pump drive current for each channel. Input power = 0dBm. Signal wavelength = 1550 nm. Ambient temperature = 21 °C

Figure 5.14 shows the gain spectra over the C-band showing the gain for each channel as a function of the seed wavelength. Performance is as expected with a gain curve which is in-line with the ASE curve for EDFAs. The maximum gain observed at 1550 nm (a typical operational signal wavelength for many amplifiers and used as a base wavelength for gain and noise figure measurements over temperature) is 22.86 dB produced by channel 7.

Figure 5.15 presents the NF measurements as a function of seed wavelength over

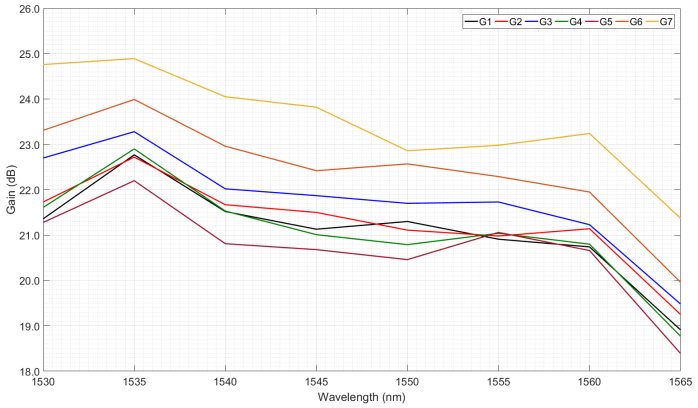

Figure 5.14: Gain as a function of signal wavelength for each channel. Input power = -10 dBm. Pump power = 500 mW. Ambient temperature = 21 °C

the C-band. The NF measurements were completed by using the standard ASE-interpolation subtraction method as shown in Appendix C. The results were as expected and follow the ASE curve found in most EDFAs.

It is positive to note that all the channels were following the same profile for each result showing the consistency of the result. However, the variations in values between the channels could be due to two reasons. The first possible reason is that the doping profile in the MC-EDFA is not uniform spatially, causing variations in gain and NF. The second reason is that the insertion losses for each channel vary causing the change in values of output power. In terms of the unit, this does not impact the overall performance as it is more than suitable for the requirements of the project.

5.4.2 Temperature Testing

The next stage of testing was completed by measuring the gain and NF at a fixed input wavelength (1550 nm), pump drive current (500 mW) and input power (-10 dBm) whilst varying the ambient temperature over a range of -10 to +60 °C. The main purpose of this test was to investigate the stability of the BEACON module as the ambient environment is changed.

Figure 5.16 shows that the gain is stable over a wide range of operating temperatures which are commonly seen on-board spacecraft. This is shown through a drop of 2 dB

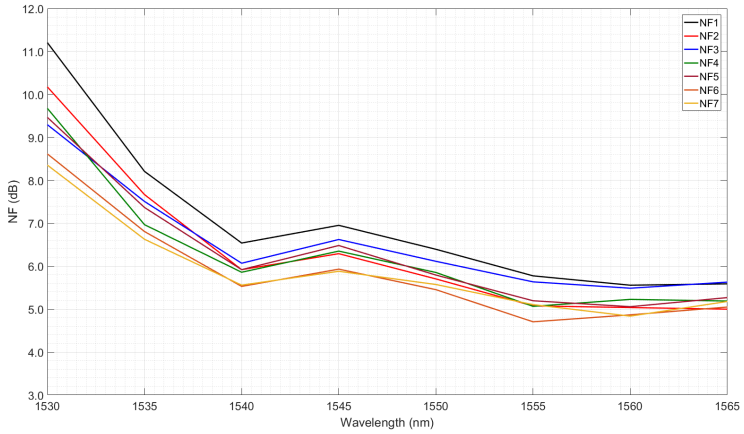

Figure 5.15: Noise figure as a function of seed wavelength for each channel. Input power = -10 dBm. Pump power = 500 mW. Ambient temperature = 21 °C

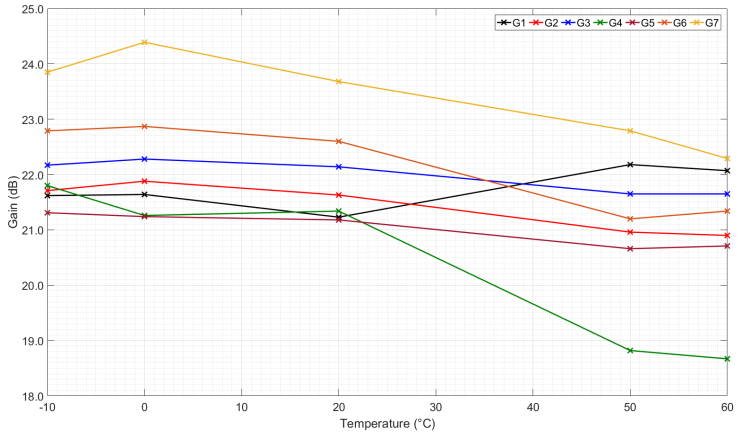

Figure 5.16: The temperature dependence of the gain for over all 7 channels for the BEACON module.

in gain over the temperature range. This variance in gain over temperature is common for most EDFA systems.

This pattern is repeated in the results for the variance in NF (Figure 5.17) over temperature with a variance of NF of no greater than 1 dB (apart from channel 4) over the temperature range. This is once again typical for EDFAs, highlighting the stability of the novel MC-PCF present in the amplifier and it's similarity to typical commercial systems.

One point of concern is the NF results for 60 °C as it does not follow the expected trend. This anomaly is mostly due to the measurement error for this method of NF and the estimation of the noise floor. It is commonly known that the ASE-interpolation subtraction method for measuring NF can produce erroneous results (NF $<$ 3 dB) or results with a large amount of uncertainty. This arises due to how the noise level is interpolated. If the ASE curve around the signal is distorted, the curve which is fitted to the ASE curve will be incorrect and therefore a wrong noise value predicted.

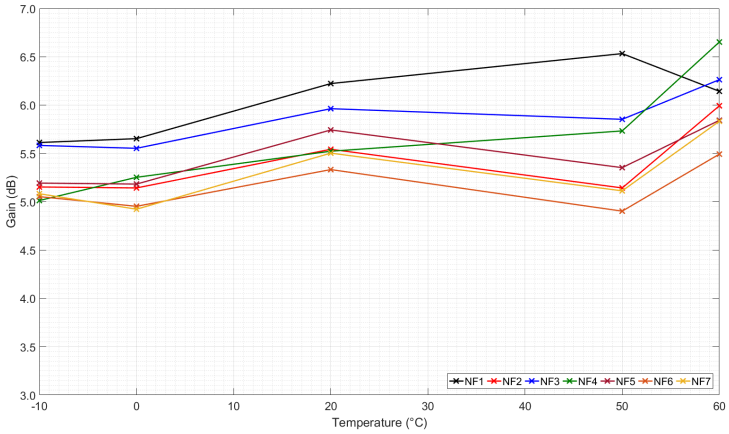

Figure 5.17: The temperature dependence of the NF for over all 7 channels for the BEACON module.

5.4.3 BEACON Demonstrator

With the amplifier demonstrated to work to it's specification as defined in Table 5.1, the unit was shipped such that it could be integrated into the project demonstrator. For detailed information the author points the reader towards publications describing the demonstrator and results [5.2], [5.3]. This sub-section shall briefly describe the demonstrator and the role that the BEACON amplifier described above had in the system.

The BEACON demonstrator was based at the Instituto de Telecomunicações, Aveiro, Portugal. Figure 5.19 shows a block diagram schematic of the demonstrator and the role that the BEACON amplifier had. The BEACON amplifier was used to amplify the signals exiting the MZM array to counteract the insertion loss of the MZMs. As

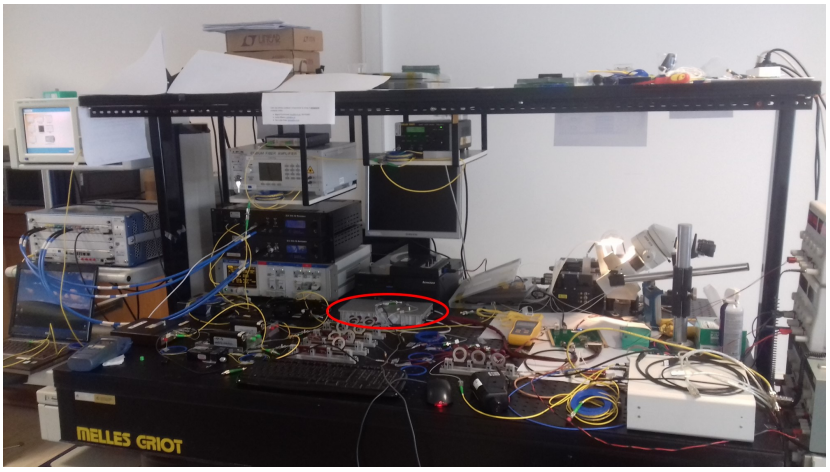

Figure 5.18: Photo of the BEACON demonstrator. The MC-EDFA is shown circled in red.

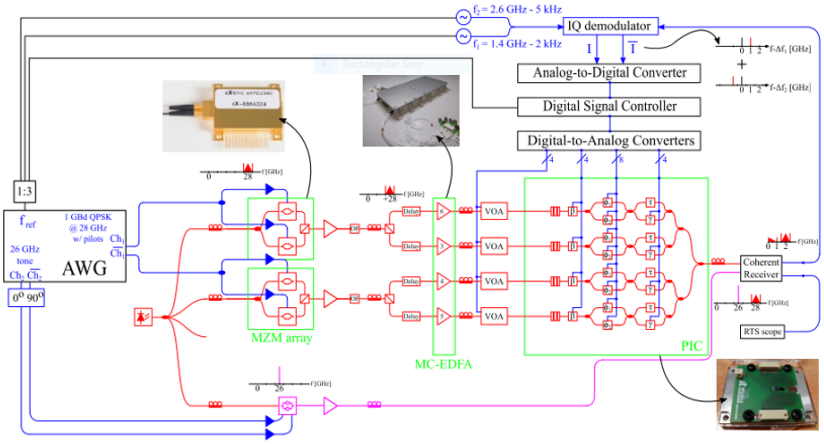

Figure 5.19: Schematic of the BEACON demonstrator.

this was a coherent based system, each fiber optic path had to be similar otherwise an unwanted phase delay would be added to the system; which in turn would cause a distortion in the beam-forming process.

Practically, trying to keep fiber optic paths the same is not feasible due to the variability of the splicing process. For example, if one splice is of a poor quality or breaks during AIT, the splice will have to be re-made. As the fiber would need to be re-cleaved, this would make one fiber path shorter than the others due to the wastage being caused by the cleaving process. To counteract this, a variable phase delay was added to each fiber channel such that the phases could be tuned such that all channels

are in phase before entering the beam-former.

5.5 BEACON Partner Contributions

The work in this chapter and BEACON demonstrator was the result of a consortium working together on the BEACON project. The overall project and demonstrator was overseen by the Instituto de Telecomunicações, Aveiro, Portugal. The MZM array was conceived and assembled by aXenic, Sedgefield, UK. The PIC chip was developed by a team based at the Instituto de Telecomunicações, Aveiro, Portugal and IHP, Frankfurt, Germany. InPhoTech, Warsaw, Poland manufactured and designed the PCF under guidance from the author and G&H. The radiation testing of the PCF was completed by the author. The amplifier design and AIT was completed by the author and G&H. Finally, end-user oversight was provided by Airbus Defence and Space, Stevenage, UK.

5.6 Conclusions and Further Work

In conclusion, this chapter reports the development and testing of a radiation-hardened PCF with a reported RIA of 0.72 dB/100 kRad which is currently better than a similar commercially available radiation-hardened Er-doped fiber (1.2 dB/100 kRad from IxFiber [5.9]).

Additionally, the radiation hardened PCF was assembled into a 7-channel MC-EDFA. The amplifier has a gain between 18.39-24.89 dB and NF ranging between 11.20-4.84 dB over the C-band and all 7 channels, thus showing it's suitability as a booster amplifier. The BEACON amplifier design was verified over temperatures between -10 and +60 °C with stable performance over the temperature range.

The next stage is to qualify this amplifier further was use in space applications through further environmental testing such as vibration, shock and TVAC. However, the maturity of the other technologies used within photonic satellite communication payloads are currently at a lower TRL. Therefore, the extra qualification can be suspended until the TRL of the other PICs are raised to a suitable level. However, this wait will not be too long as currently there is lots of active development in this field

[5.10].

The amplifier described in this chapter utilises space-division multi-plexing. Through the use of space-division multiplexing it is shown that all 7 channels can be communicated through, whilst maintaining performance characteristics when compared to regular EDFAs. Additionally, the radiation resistance performance for this class of fiber is proven with radiation testing showing it's suitability for space applications. Additionally, as one fiber is being used coherent communications can also be used as the path length for each channel is the same. In all, this amplifier is novel in expanding the design space for space-based EDFAs, and highlighting the opportunities for replacing standard RF payloads with photonics.

References

[5.1] W. Larson and J. R. Wertz, *Space Mission Analysis and Design*, 2nd, ser. Space Technology Library. Springer Netherlands, 1991.

[5.2] V. C. Duarte, J. G. Prata, C. Ribeiro, R. N. Nogueira, G. Winzer, L. Zimmermann, *et al.*, "Integrated Photonic True-Time Delay Beamformer for a Ka-band Phased Array Antenna Receiver," in *Optical Fiber Communication Conference*, Washington, D.C.: OSA, 2018, M2G.5. DOI: 10.1364/OFC.2018.M2G.5.

[5.3] V. C. Duarte, J. G. Prata, C. F. Ribeiro, R. N. Nogueira, G. Winzer, L. Zimmermann, *et al.*, "Modular coherent photonic-aided payload receiver for communications satellites," *Nature Communications*, vol. 10, no. 1, p. 1984, Apr. 2019. DOI: 10.1038/s41467-019-10077-4.

[5.4] M. Kechagias, J. Crabb, L. Stampoulidis, J. Farzana, E. Kehayas, M. Filipowicz, *et al.*, "Multi-core fiber amplifier arrays for intra-satellite links," in *International Conference on Space Optics — ICSO 2016*, N. Karafolas, B. Cugny, and Z. Sodnik, Eds., SPIE, Sep. 2017, p. 118. DOI: 10.1117/12.2296129.

[5.5] M. Filipowicz, M. Napierala, M. Murawski, L. Ostrowski, P. Mergo, M. Kechagias, *et al.*, "Radiation-hardened optical amplifier based on multicore fiber for telecommunication satellites," in *Technologies for Optical Countermeasures XIV*, D. H. Titterton, R. J. Grasso, and M. A. Richardson, Eds., SPIE, Oct. 2017. DOI: 10.1117/12.2278195.

[5.6] S. Girard, M. Vivona, A. Laurent, B. Cadier, C. Marcandella, T. Robin, *et al.*, "Radiation hardening techniques for Er/Yb doped optical fibers and amplifiers for space application," *Optics Express*, vol. 20, no. 8, pp. 8457–8465, Apr. 2012. DOI: 10.1364/OE.20.008457.

[5.7] M. Vivona, S. Girard, C. Marcandella, T. Robin, B. Cadier, M. Cannas, *et al.*, "Influence of Ce codoping and H2 pre-loading on Er/Yb-doped fiber: Radiation response characterized by Confocal Micro-Luminescence," *Journal of Non-Crystalline Solids*, vol. 357, no. 8-9, pp. 1963–1965, Apr. 2011. DOI: 10.1016/j.jnoncrysol.2010.10.039.

[5.8] S. Girard, A. Morana, A. Ladaci, T. Robin, L. Mescia, J.-J. Bonnefois, *et al.*, "Recent advances in radiation-hardened fiber-based technologies for space applications," *Journal of Optics*, vol. 20, no. 9, p. 093 001, Sep. 2018. DOI: 10.1088/2040-8986/aad271.

[5.9] S. Girard, Y. Ouerdane, T. Robin, B. Cadier, A. Boukenter, and L. H. Curien, "Recent Advances in Radiation Hardened Fiber-Based Technologies," in *OSA Frontiers in Optics*, Rochester, USA, 2016.

[5.10] M. A. Krainak, M. A. Stephen, E. Troupaki, S. A. Tedder, B. Reyna, J. Klamkin, *et al.*, "Integrated photonics for NASA applications," in *Components and Packaging for Laser Systems V*, A. L. Glebov and P. O. Leisher, Eds., SPIE, Mar. 2019, p. 14. DOI: 10.1117/12.2509808.

Chapter 6

Conclusions and Path to Flight

This chapter will summarise and conclude the work described within this thesis. The key developments will be discussed showing the path of qualifying components through to designing, assembling and verifying a compact laser transmitter and multi-channel optical amplifier. Secondly, the path towards qualifying and demonstrating in orbit the modules developed in this thesis will be discussed. Finally the thesis is closed with a view towards what future applications that the technology in this thesis has enabled.

6.1 Key Findings

This thesis has covered a wide range of topics from all levels of system design. This ranges from component selection and their suitability for space applications to verifying a fiber amplifier within a larger system. In a broader sense, although this thesis has been presented in a portfolio format, the work undertaken has shown how laser transmitters and optical amplifiers can be conceived from an optical schematic and initial specifications, to selecting and verifying key optical components and on to designing the overall module, and lastly verifying the performance of the module in a laboratory environment.

Three new classes of passive optical have been assessed for space use. Two classes of hybrid component were found to be suitable for LEO applications. The third class of optical component, a compact 1 µm isolator was also assessed. The outcome of

the 1 µm isolator testing was inconclusive so additional work is needed to assess this component for space use. Additionally a selection of COTS and specialist double-clad ErYb fibers were tested for their response to radiation doses of up to 100 kRad. These tests will ultimately drive the optical designs of the next generation of high power optical amplifier and transmitters for space applications.

A 0.2 W, 1 Gbit s^{-1}, laser transmitter designed for use within a CubeSat has also been presented. Challenges such as designing the mechanics and assembling the unit were overcome due to the unique footprint given by the system integrator. The unit's performance was verified an over temperatures of -5 °C to +50 °C and is now at a TRL of 5/6.

Finally, a multi-channel booster amplifier was developed for RF beam-forming applications using radiation hardened PCF fiber. The PCF fiber was tested to a radiation dose of up to 100 kRad and it was found that this fiber performed better than similar commercially available fiber (0.72 dB / 100 kRad). A multi-channel booster amplifier, based on this PCF was developed and assembled. The amplifier was assembled and verified to a TRL of 4/5 through lab-based testing between temperatures of -5 °C to +60 °C. Finally, the module was integrated into a demonstrator and the first demonstrated case of RF beam-forming via the use of photonics was demonstrated.

6.2 Future Work

As already alluded to within the thesis, the development of the next generation of laser transmitters and amplifiers for space-based laser communications is not complete until they are demonstrated in orbit and are commonplace on-board spacecraft. More specifically, for the components tested in Chapter 3 these components can now be considered for use in future designs.

By using hybrid components, the component count inside next-generation optical amplifiers and LTXs can be greatly reduced saving on the volume required for passive optical components. This is turn enables the next iteration of designs. E.g. The design currently being developed as shown in section 4.6.1. In addition to commercial grade high-power amplifiers for space can now be enabled and have in-fact already been

started to be developed [6.1].

For the currently assembled modules presented in Chapters 4 and 5, these are at a TRL of 5/6. A simple approach to future work for these modules would be to build a qualification model of the modules, qualify and demonstrate them in orbit by following the traditional method of raising TRL within the space industry.

However for CubeSats and micro-satellites, the focus of these spacecraft is that they are cheap and easy to replace. Therefore, they are typically flown without a rigorous qualification campaign [6.2]. For the CubeSat LTX shown in Chapter 4, a demonstrator is planned for Q4 2020. This is an aggressive plan to fly this LTX which would only be achieved through a limited qualification campaign.

For the multi-channel booster amplifier designed in Chapter 5, the way forward for this module is different. Although the unit was demonstrated to a TRL of 5/6, the overall system's TRL is much lower at approximately TRL 3/4. This is due to the nature of the technology within the demonstrator. E.g. The photonic integrated components (PIC) within the demonstrated such as the phase delay circuitry. In addition to this, currently a 4-element beam former has been demonstrated. Typically, GEO satellite have beam formers which have over 100 elements [6.3]. However, it will not be long until the TRL of PICs is raised sufficiently to be used in space missions [6.4]. Along with PICs being designed for space use, these devices will be inherently better system components than traditional fiber optics as fiber optical components were originally designed for terrestrial telecommunication applications and then adapted for space. The transfer of terrestrial technology to the space domain is no small undertaking; this is evidenced by this thesis playing a small part in the overall adoption process of using fiber optics in space.

6.3 Closing Remarks

Fundamentally this thesis has illustrated the design and development process required for designing the next generation of optical amplifiers and laser transmitters for satellite communications to a TRL of 5/6. The work described within has started and enabled

future laser communications systems for space applications by expanding the design space in which laser communication modules can be built. By pushing the design space larger this allows future space missions to start using space-based laser communications in different ways.

Looking forwards, space-based laser communications has a very exciting future. Already emerging as one of the key technologies to drive the next communication paradigm shift, laser communications has already shown it's potential to provide energy-efficient high-data rate communications from orbit. Future applications are more ambitious than those systems already in orbit. For example, laser communications has been highlighted as the cornerstone technology for interplanetary communications [6.5] and downlinking 1 $\mathrm{Tbit\,s^{-1}}$ from GEO [6.6]. However from a commercial context (which this thesis mainly addresses), more satellite constellations are being planned or already being launched into LEO. Unless RF regulations are significantly changed, spectrum congestion will soon become a very real problem. Thus diminishing the possibility of using RF solutions and enabling the optical revolution.

References

[6.1] M. Welch, J. Edmunds, J. Crabb, E. Prowse, K. Hall, M. Kechagias, *et al.*, "High-power booster optical fibre amplifiers for satellite communications," in *Free-Space Laser Communications XXXII*, H. Hemmati and D. M. Boroson, Eds., San Francisco: SPIE, Mar. 2020, p. 32. DOI: 10.1117/12.2545570.

[6.2] P. Fortescue, J. Stark, and G. Swinerd, *Spacecraft Systems Engineering*, 4th. Wiley, 2003.

[6.3] W. Larson and J. R. Wertz, *Space Mission Analysis and Design*, 2nd, ser. Space Technology Library. Springer Netherlands, 1991.

[6.4] M. A. Krainak, M. A. Stephen, E. Troupaki, S. A. Tedder, B. Reyna, J. Klamkin, *et al.*, "Integrated photonics for NASA applications," in *Components and Packaging for Laser Systems V*, A. L. Glebov and P. O. Leisher, Eds., SPIE, Mar. 2019, p. 14. DOI: 10.1117/12.2509808.

[6.5] D. M. Cornwell, "NASA's optical communications program for 2017 and beyond," in *2017 IEEE International Conference on Space Optical Systems and Applications (ICSOS)*, IEEE, Nov. 2017, pp. 10–14. DOI: 10.1109/ICSOS.2017.8357203.

[6.6] H. Hauschildt, C. Elia, L. Moeller, and J. M. Perdigués Armengol, "HydRON: High throughput optical network," in *Free-Space Laser Communications XXXI*, H. Hemmati and D. M. Boroson, Eds., SPIE, Mar. 2019, p. 18. DOI: 10.1117/12.2511391.

Appendix A

List of Publications

The work presented within this thesis has been published in peer-reviewed journals and conferences. A list of publications associated to this thesis can be found below and are referenced throughout the thesis.

- M. Kechagias, J. Crabb, L. Stampoulidis, J. Farzana, E. Kehayas, M. Filipowicz, M. Napierala, M. Murawski, T. Nasilowski, and J. Barbero, "Multi-core fiber amplifier arrays for intra-satellite links," in *International Conference on Space Optics — ICSO 2016*, N. Karafolas, B. Cugny, and Z. Sodnik, Eds., SPIE, Sep. 2017, p. 118. DOI: 10.1117/12.2296129

- M. Filipowicz, M. Napierala, M. Murawski, L. Ostrowski, P. Mergo, M. Kechagias, J. Farzana, L. Stampoulidis, E. Kehayas, J. Crabb, L. Szostkiewicz, and T. Nasilowski, "Radiation-hardened optical amplifier based on multicore fiber for telecommunication satellites," in *Technologies for Optical Countermeasures XIV*, D. H. Titterton, R. J. Grasso, and M. A. Richardson, Eds., SPIE, Oct. 2017. DOI: 10.1117/12.2278195

- V. C. Duarte, J. G. Prata, C. Ribeiro, R. N. Nogueira, G. Winzer, L. Zimmermann, R. Walker, S. Clements, M. Filipowicz, M. Napierała, T. Nasiłowski, J. Crabb, L. Stampoulidis, J. Anzalchi, and M. V. Drummond, "Integrated Photonic True-Time Delay Beamformer for a Ka-band Phased Array Antenna Receiver," in *Optical Fiber Communication Conference*, Washington, D.C.: OSA,

2018, M2G.5. DOI: 10.1364/OFC.2018.M2G.5

– J. Crabb, G. Stevens, C. Michie, W. Johnstone, and E. Kehayas, "Laser transmitter for CubeSat-class applications," in *Free-Space Laser Communications XXXI*, H. Hemmati and D. M. Boroson, Eds., SPIE, Mar. 2019, p. 54. DOI: 10.1117/12.2506967

– V. C. Duarte, J. G. Prata, C. F. Ribeiro, R. N. Nogueira, G. Winzer, L. Zimmermann, R. Walker, S. Clements, M. Filipowicz, M. Napierała, T. Nasiłowski, J. Crabb, M. Kechagias, L. Stampoulidis, J. Anzalchi, and M. V. Drummond, "Modular coherent photonic-aided payload receiver for communications satellites," *Nature Communications*, vol. 10, no. 1, p. 1984, Apr. 2019. DOI: 10.1038/s41467-019-10077-4

– M. Welch, J. Edmunds, J. Crabb, E. Prowse, K. Hall, M. Kechagias, R. Elliott, and E. Kehayas, "High-power booster optical fibre amplifiers for satellite communications," in *Free-Space Laser Communications XXXII*, H. Hemmati and D. M. Boroson, Eds., San Francisco: SPIE, Mar. 2020, p. 32. DOI: 10.1117/12.2545570

Appendix B

Definition of Technology Readiness Levels

In this thesis TRL has been used as an indicator as to how mature a technology or system is for use in space applications. Throughout, the thesis NASA definitions have been used. Below in Table B.1 is the definition of TRL as used by NASA [B.1]. NB: For brevity, this table has excluded some information. For the full table see: [B.1].

TRL	Definition	Completion criteria
1	Basic principles observed and reported.	Peer reviewed documented principles.
2	Technology concept and/or application formulated.	Documented description that addresses feasibility and benefit.
3	Analytical and experimental critical function and/or characteristic proof-of-concept.	Documented analytical/experimental results validating key predictions of key parameters.
4	Component and/or breadboard validation in laboratory environment.	Test performance demonstrated showing agreement with analytical predictions.
5	Component and/or breadboard validation in relevant environment.	Documented test performance demonstrating agreement with analytical predictions. Documented definition of scaling requirements.
6	System/subsystem model or prototype demonstration in a relevant environment.	Documented test performance demonstrating agreement with analytical predictions.
7	System prototype demonstration in an operational environment.	Documented test performance demonstrating agreement with analytical predictions.
8	Actual system completed and "flight qualified" through test and demonstration.	Documented test performance verifying requirements and analytical predictions.
9	Actual system flight proven through successful mission operations.	Documented mission operational results verifying requirements.

Table B.1: Definition of NASA TRL levels

References

[B.1] S. Hirshorn and S. Jefferies, "Final Report of the NASA Technology Readiness Assessment (TRA) Study Team," NASA, Tech. Rep. March 2016, 2016, pp. 42–43.

Appendix C

Derivation of Noise Figure Measurement

As discussed in Section 2.1.5, the derivation of noise figure (NF) such that it can be defined in terms of measurable variables. By starting with the definition given by the IEC standard, IEC 61291-1:2018 [C.1], NF is defined as:

$$NF = 10\log_{10}\left(\frac{SNR_{in}}{SNR_{out}}\right) \qquad \text{[dB]} \tag{C.1}$$

The signal-to-noise ratio (SNR) is defined for a received signal to be:

$$\begin{aligned} SNR_{out} &= \frac{\langle i_{sig,out}\rangle^2}{\langle \Delta^2 i_{n,out}\rangle} \\ SNR_{in} &= \frac{\langle i_{sig,in}\rangle^2}{\langle \Delta^2 i_{n,in}\rangle} \end{aligned} \tag{C.2}$$

Where i_sig is the received photocurrent and $< \Delta^2 i_n >$ is the variance of the photocurrent noise. For most communications systems, the main source of input noise is shot noise [C.2], [C.3]. This means that the input SNR can be defined as:

$$SNR_{in} = SNR_{shot} = \frac{\eta P_{in}}{2h\nu B} \tag{C.3}$$

Where η is the detector quantum efficiency, P_{in} is the input power, h is Planck's constant (6.63×10^{-34}J s), ν is the optical frequency and B is the noise bandwidth.

Assuming an ideal receiver and noise bandwidth of 1 Hz, Equation C.3 becomes:

$$SNR_{in} = \frac{P_{in}}{2h\nu} \tag{C.4}$$

The expression for the output SNR is given in Equation C.2 but the photocurrent term can be expressed as:

$$\langle i_{out} \rangle^2 = R^2 G^2 P_{in}^2 \tag{C.5}$$

Where G is the amplifier gain R is the detector responsivity. The determination of the noise variance of the output signal is not easy. The best way is to include all the different spectral noise densities over the noise bandwidth. To simplify the mathematics the noise power densities into two terms: Excess noise density, S_e and shot noise density, S_{shot}. By substituting Equation C.5 into C.2 and taking into account the noise densities, SNR_{out} is given by [C.3]:

$$SNR_{out} = \frac{R^2 G^2 P_{in}^2}{BR^2 \left(S_e + \eta^{-1} S_{shot}\right)} \tag{C.6}$$

Assuming an ideal receiver and noise bandwidth of 1 Hz, this becomes:

$$SNR_{out} = \frac{G^2 P_{in}^2}{S_e + S_{shot}} \tag{C.7}$$

Combining Equations (C.4), (C.7) and (C.1) yields the result:

$$NF = 10 \log_{10} \left[\frac{P_{in}}{2h\nu} \times \frac{S_e + S_{shot}}{G^2 P_{in}^2} \right]$$

$$\boxed{NF = 10 \log_{10} \left[\frac{S_e}{2h\nu G^2 P_{in}^2} + \frac{S_{shot}}{2h\nu G^2 P_{in}^2} \right]} \tag{C.8}$$

The result given above is the general noise figure equation from which either the NF can be measured optically or electrically. Most optical telecommunications test equipment completes measurements in the optical domain and this shall be focused upon. It is well known within the telecommunications industry that the main sources

of noise in an optical amplifier is the signal-spontaneous beat noise and shot noise [C.2], [C.3]. This modifies the noise densities to be [C.3]:

$$S_e = S_{sig-sp} = 4\rho_{ASE}GP_{in} \tag{C.9}$$

$$S_{shot} = 2h\nu GP_{in} \tag{C.10}$$

Where ρ_{ASE} is the ASE spectral density which can be measured by using an OSA. Substituting (C.9) and (C.10) into (C.8) gives:

$$NF = 10\log_{10}\left[\frac{4\rho_{ASE}GP_{in}}{2hG^2\nu} + \frac{2h\nu GP_{in}}{2h\nu G^2P_{in}}\right]$$

$$NF = 10\log_{10}\left[\frac{2\rho_{ASE}}{h\nu G} + \frac{1}{G}\right] \tag{C.11}$$

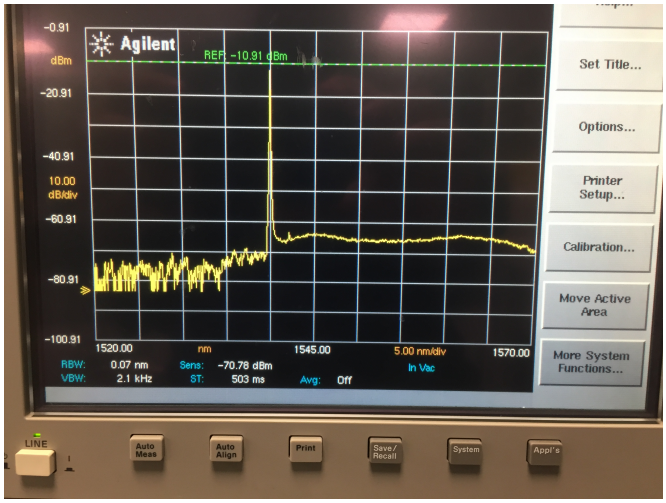

Figure C.1: A photo of a typical EDFA OSA scan in which the noise cannot be distinguished from the signal.

One major problem in measuring NF is the separation of ASE from the noise of the source. Figure C.1 shows a typical EDFA OSA scan showing the difficulties in measuring NF. Here it can be seen that the noise at the signal wavelength is masking both the ASE and signal noise making a NF measurement unreliable, if not impossible.

To waylay this issue, the source subtraction technique adjusts for this by including the source noise in the calculation [C.3]:

$$NF = 10\log_{10}\left[\frac{2\rho_{total}}{Gh\nu} + \frac{1}{G} - \frac{2\rho_{SSE}}{h\nu}\right] \tag{C.12}$$

The noise densities represented above relate to the polarised noise densities. However in practice measurements taken include the noise in both polarisation directions and it is assumed that these are equal. Equation C.12 can be translated into measurable quantities by replacing the un-polarised noise densities with the measured power over the measurement bandwidth (given by the OSA resolution and signal wavelength). i.e. $2\rho_{total} = P_{ASE}/B$ & $2\rho_{SSE} = P_{SSE}/B$. Where B is the measurement bandwidth given by $B = c\Delta\lambda/\lambda^2$. Where P_{ASE} is the measured ASE power, P_{SSE} is the measured source noise and $\Delta\lambda$ is the OSA scan resolution bandwidth. Both are measured at the signal wavelength. As shown in Figure C.2 these measurements must be derived from the spectrum shape of the signal after it has passed through the amplifier and signal. This is achieved by optically switching out the signal so that it can be measured separately from the amplifier. By using the interpolated noise powers, Equation C.12 can be rewritten as the final result:

$$\boxed{NF = 10\log_{10}\left[\frac{P_{ASE}\lambda^3}{Ghc^2\Delta\lambda} + \frac{1}{G} - \frac{P_{SSE}\lambda^3}{hc^2\Delta\lambda}\right] \quad \text{[dB]}} \tag{C.13}$$

However, there are a few caveats to this definition of NF. The first is that the method described above is largely dependent on having a signal with a stable SNR. Otherwise the accuracy of the measurement becomes compromised as it is assumed that the main sources of noise are from the amplifier, not the source. Another source of uncertainty in the source subtraction method is the when the amplifier is used in WDM systems as the noise contribution from the sources will be much higher, thus increasing the uncertainty in the measurement.

Secondly, there are more accurate and precise methods of measurement such as the time domain extinction (TDE) method. However, the source subtraction method is the simplest method which is easy to implement making it ideal for the rapid development

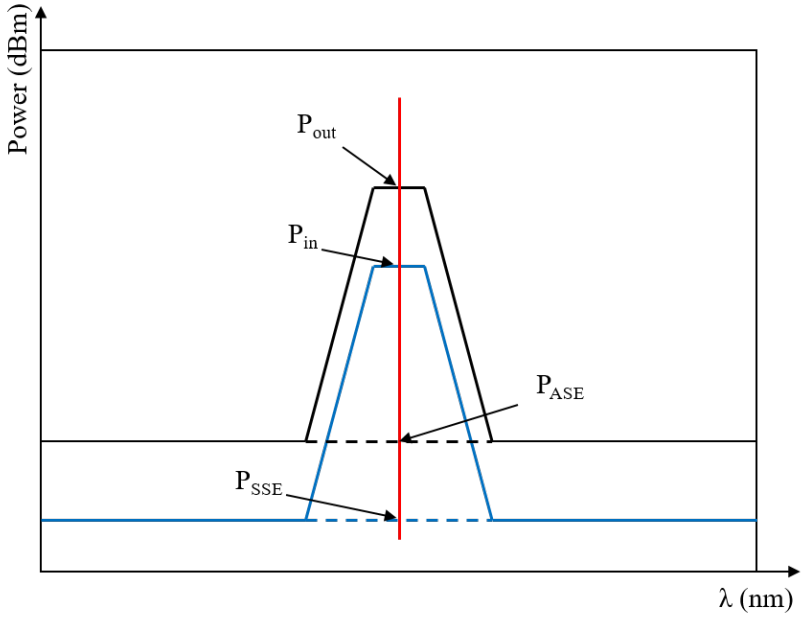

Figure C.2: A graphical representation of the measurements needed to measure NF. The signal wavelength is shown in red.

of optical amplifiers. In addition, the losses of the optical switches needed in the TDE method are not present in the source-noise subtraction method.

References

[C.1] BSI, *BS EN IEC 61291-1:2018*, 1st ed. BSI, 2018, pp. 13–14.

[C.2] E. Desurvire, *Erbium-doped fiber amplifiers: principles and applications*, Illustrate. Wiley-Interscience, 2002.

[C.3] D. M. Baney, P. Gallion, and R. S. Tucker, "Theory and Measurement Techniques for the Noise Figure of Optical Amplifiers," *Optical Fiber Technology*, vol. 6, no. 2, pp. 122–154, Apr. 2000. DOI: 10.1006/ofte.2000.0327.

Appendix C. Derivation of Noise Figure Measurement